Gamma-Ray Bursts within Fireshell Model

Dipartimento di Fisica

Dottorato di Ricerca in Astrofisica Relativistica, IRAP-PhD – XXX Ciclo

Candidate
Yerlan Aimuratov
ID number 1679167

Thesis Advisor
Prof. Remo Ruffini

A thesis submitted in partial fulfillment of the requirements
for the degree of Doctor of Philosophy in Relativistic Astrophysics

February 2020

Thesis is discussed on 25th of February, 2020
in front of a Board of Examiners composed by:

Prof. Roberto Capuzzo Dolcetta (Università di Roma "La Sapienza") (chairman)
Prof. Luigi Piro (Istituto Nazionale di Astrofisica INAF – IAPS Roma)
Prof. Marco Tavani (Istituto Nazionale di Astrofisica INAF – IAPS Roma)

The external evaluators of the thesis:

Prof. Francesco Longo (Università degli Studi di Trieste, Italy)
Dr. Bruce Grossan (Lawrence Berkeley National Laboratory, USA)

Abstract

This thesis is mainly focused on careful data analysis of different parts of high-energy (sub-keV–GeV) spectra of gamma-ray bursts. All the interpretation works are based on the theoretical ground of the *fireshell* paradigm which is being continuously developed for over 20 years.

The chapters in the main body of the thesis focus on current research and results obtained and published. A distinct emphasis on spectral bands is expressed through structural division of the thesis: soft gamma-ray emission, x-ray afterglow emission and high-energy gamma-ray emission.

In Chapter 2 we discuss theoretical and observational evidences which have been recently gained for a two-fold classification of short bursts within the *fireshell* working paradigm. We present three additional S-GRBs, 081024B, 090510 and 140402A, following the already identified S-GRBs, i.e., 090227B and 140619B.

In Chapter 3 we analyze the early X-ray flares in the GRB "flare-plateau-afterglow" (FPA) phase observed by *Swift*-XRT. We claim that the FPA occurs only in one of the subclasses—binary-driven hypernovae (BdHNe). This subclass consists of long GRBs with a carbon-oxygen core (CO_{core}) massive star and a neutron star (NS) binary companion as progenitors.

In Chapter 4 we examine a scenario when in binary system of neutron star (NS) and massive CO_{core} star, the latter undergoes a supernova (SN) explosion. A black hole (BH) subsequently originates from the gravitational collapse of the NS caused by hypercritical accretion of the SN ejecta. We infer a new asymmetric morphology for the BdHNe system where the GeV emission occurs within a cone of half-opening angle $\approx \pi/3$ normal to the orbital plane of the binary progenitor. We confirm that GeV luminosity light curves follow the universal power-law with index of -1.19 ± 0.04, and from this we further estimate the spin-down rate of the BH.

Acknowledgments

List of Tables

List of Figures

List of Publications

Journal Articles

- Rueda, J.; Ruffini, R.; Wang, Y.; Aimuratov, Y.; Barres de Almeida, U.; Bianco, C. L.; Chen, Y.-C.; Lobato, R. V.; Maia, C.; Primorac, D.; Moradi, R.; Rodriguez, J. GRB 170817A – GW170817 – AT 2017gfo and the observations of NS-NS, NS-WD and WD-WD mergers. Journal of Cosmology and Astroparticle Physics, Volume 10, article id. 006, 15pp, 2018.

- Ruffini, R.; Rodriguez, J; Muccino, M.; Rueda, J. A.; Aimuratov, Y.; Barres de Almeida, U.; Beccera, L. M.; Bianco, C. L.; Cherubini, C.; Filippi, S.; Gizzi, D.; Kovacevic, M.; Moradi, R.; Oliveira, F. G.; Pisani, G. B.; Wang, Y. On the Rate and on the Gravitational Wave Emission of Short and Long GRBs. The Astrophysical Journal, Volume 859, Issue 1, article id. 30, 17pp, 2018.

- Ruffini, R.; Wang, Y.; Aimuratov, Y.; Barres de Almeida, U.; Beccera, L. M.; Bianco, Chen, Y.-C.; Karlica, M.; Kovacevic, M.; Li, L.; Melon Fuksman, J. D.; Moradi, R.; Muccino, M.; Penacchioni, A.V.; Pisani, G. B.; Primorac, D.; Rueda, J. A.; Shakeri, S.; Vereshchagin, G.V.; Xue, S.-S. Early X-Ray Flares in GRBs. The Astrophysical Journal, Volume 852, Issue 1, article id. 53, 27pp, 2018.

- Aimuratov, Y.; Ruffini, R.; Muccino, M.; Bianco, C. L.; Penacchioni, A.V.; Pisani, G. B.; Primorac, D.; Rueda, J. A.; Wang, Y. GRB 081024B and GRB 140402A: Two Additional Short GRBs from Binary Neutron Star Mergers. The Astrophysical Journal, Volume 844, Issue 1, article id. 83, 15pp, 2017.

- Ruffini, R.; Aimuratov, Y.; Beccera, L. M.; Bianco, C. L.; Karlica, M.; Kovacevic, M.; Melon Fuksman, J. D.; Moradi, R.; Muccino, M.; Penacchioni, A.V.; Pisani, G. B.; Primorac, D.; Rueda, J. A.; Shakeri, S.; Vereshchagin, G. V.; Wang, Y.; Xue, S.-S. The Cosmic Matrix in 50th Anniversary of Relativistic Astrophysics. International Journal of Modern Physics D, Volume 26, Issue 10, article id. 1730019, 47pp, 2017.

- Rueda, J. A.; Aimuratov, Y.; Barres de Almeida, U.; Beccera, L. M.; Bianco, C. L.; Cherubini, C.; Filippi, S.; Karlica, M.; Kovacevic, M.; Melon Fuksman, J. D.; Moradi, R.; Muccino, M.; Penacchioni, A.V.; Pisani, G. B.; Primorac, D.; Ruffini, R.; Sahakyan, N.; Shakeri, S.; Wang, Y. The Binary Systems Associated with Short and Long Gamma-Ray Bursts and Their Detectability.

International Journal of Modern Physics D, Volume 26, Issue 9, article id. 1730016, 19pp, 2017.

- Pisani, G. B.; Ruffini, R.; Aimuratov, Y.; Bianco, C. L.; Kovacevic, M.; Moradi, R.; Muccino, M.; Penacchioni, A.V.; Rueda, J. A.; Wang, Y. On the Universal Late X-Ray Emission of Binary-driven Hypernovae and Its Possible Collimation. The Astrophysical Journal, Volume 833, Issue 2, article id. 159, 12pp, 2016.

- Ruffini, R.; Rueda, J. A.; Muccino, M.; Aimuratov, Y.; Beccera, L. M.; Bianco, C. L.; Kovacevic, M.; Moradi, R.; Oliveira, F. G.; Pisani, G. B.; Wang, Y. On the Classification of GRBs and Their Occurrence Rates. The Astrophysical Journal, Volume 832, Issue 2, article id. 136, 24pp, 2016.

- Ruffini, R.; Muccino, M.; Aimuratov, Y.; Bianco, C. L.; Cherubini, C.; Enderli, M.; Kovacevic, M.; Moradi, R.; Penacchioni, A.V.; Pisani, G. B.; Rueda, J. A.; Wang, Y. GRB 090510: A Genuine Short GRB from a Binary Neutron Star Coalescing into a Kerr-Newman Black Hole. The Astrophysical Journal, Volume 831, Issue 2, article id. 178, 17pp, 2016.

- Ruffini, R.; Aimuratov, Y.; Bianco, C. L.; Enderli, M.; Kovacevic, M.; Moradi, R.; Muccino, M.; Penacchioni, A. V.; Pisani, G. B.; Rueda, J. A.; Wang, Y. Induced gravitational collapse in FeCO Core-Neutron star binaries and Neutron star-Neutron star binary mergers. International Journal Of Modern Physics A, Volume 30, Issue: 28-29, article id. 1545023, 28pp, 2015.

Conference Proceedings

- Primorac, D.; Ruffini, R.; Pisani, G. B.; Aimuratov, Y.; Bianco, C. L.; Karlica, M.; Melon Fuksman, J.D.; Moradi, R.; Muccino, M.; Penacchioni, A.V.; Rueda, J. A.; Wang, Y. GRB 110731A within the IGC Paradigm. EPJ Web of Conferences, Volume 168, pp. 04008. Published: online January 2018.

- Muccino, M.; Ruffini, R.; Aimuratov, Y.; Becerra, L.; Bianco, C. L.; Karlica, M.; Kovacevic, M.; Melon Fuksman, J.D.; Moradi, R.; Penacchioni, A.V.; Pisani, G. B.; Primorac, D.; Rueda, J. A.; Shakeri, S.; Vereshchagin, G.V.; Xue, S.-S.; Wang, Y. What can we learn from GRBs? EPJ Web of Conferences, Volume 168, pp. 01015. Published: online January 2018.

- Pisani, G. B.; Ruffini, R.; Aimuratov, Y.; Bianco, C. L.; Karlica, M.; Kovacevic, M.; Moradi, R.; Muccino, M.; Penacchioni, A.V.; Primorac, D.; Rueda, J. A.; Wang, Y. The First ICRANet Catalog of Binary-driven Hypernovae. EPJ Web of Conferences, Volume 168, pp. 04002. Published: online January 2018.

- Rueda, J. A.; Ruffini, R.; Rodriguez, J.F.; Muccino, M.; Aimuratov, Y.; Barres de Almeida, U.; Becerra, L.; Bianco, C. L.; Cherubini, C.; Filippi, S.; Kovacevic, M.; Moradi, R.; Pisani, G. B.; Wang, Y. The Binary Progenitors of Short and Long GRBs and Their Gravitational-Wave Emission. EPJ Web of Conferences, Volume 168, pp. 01006. Published: online January 2018.

- Wang, Y.; Aimuratov, Y.; Moradi, R.; Peresano, M.; Ruffini, R.; Shakeri, S. Revisiting the statistics of x-ray flares in gamma-ray bursts. Memorie della Societa Astronomica Italiana, Volume 89, pp. 293. Published: January 2018.

- Muccino, M.; Ruffini, R.; Kovacevic, M.; Oliveira, F.G.; Rueda, J. A.; Aimuratov, Y.; Bianco, C. L.; Enderli, M.; Izzo, L.; Moradi, R.; Penacchioni, A. V.; Pisani, G. B.; Wang, Yu; Zaninoni, E. GRB 140619B: A short GRB from a binary neutron star merger leading to black hole formation. The 14th MG Meeting. Conference Proceedings, pp. 2969-2974. Published: online 2017.

- Aimuratov, Y.; Muccino, M.; Bianco, C. L.; Enderli, M.; Izzo, L.; Kovacevic, M.; Moradi, R.; Penacchioni, A. V.; Pisani, G. B.; Rueda, J. A.; Wang, Yu; Zaninoni, E. and Ruffini, R. Analysis of the GRB 081024B. The 14th MG Meeting. Conference Proceedings, pp. 2975-2980. Published: online 2017.

- Ruffini, R.; Aimuratov, Y.; Belinski, V.; Bianco, C. L.; Enderli, M.; Izzo, L.; Kovacevic, M.; Mathews, G. J.; Moradi, R.; Muccino, M.; Penacchioni, A. V.; Pisani, G. B.; Rueda, J. A.; Vereshchagin, G. V.; Wang, Y.; Xue, S.-S. Cosmic matrix in the jubilee of relativistic astrophysics. AIP Conference Proceedings, Volume 1693, Issue 1, id.020001, 22pp, 2015.

Preprints

- Ruffini, R.; Moradi, R.; Rueda, J. A.; Wang, Y.; Aimuratov, Y.; Becerra, L.; Bianco, C. L.; Chen, Y. -C.; Cherubini, C.; Filippi, S.; Karlica, M.; Mathews, G. J.; Muccino, M.; Pisani, G. B.; Primorac, D.; Xue, S. -S. On the role of the Kerr-Newman black hole in the GeV emission of long gamma-ray bursts. ArXiv e-prints, 1803.05476, March, 2018.

- Ruffini, R.; Muccino, M.; Aimuratov, Y.; Amiri, M.; Bianco, C. L.; Chen, Y. -C.; Eslam Panah, B.; Mathews, G. J.; Moradi, R.; Pisani, G. B.; Primorac, D.; Rueda, J. A.; Wang, Y. On the Short GRB GeV emission from a Kerr Black hole. ArXiv e-prints, 1802.07552, February, 2018.

Contents

Chapter 1

Introduction

We give a brief historical overview and introduce the reader to past and current challenges. Further we outline main goals and objectives. The philosophy and methods of the investigation follow in general and detailed description.

In order to make an attempt to understand the phenomenon called a cosmological *gamma-ray burst* (GRB) one should keep in mind that we need to deal with a whole complex of astrophysical processes generalized and named so due to the explosion as a main initial characteristic for energy generation and high-energy domain in which most of this energy is being released, transformed, transfered and detected in the form of the photons.[1]

1.1 Observational approach

Indeed, what we finally detect on Earth and its orbit directly or indirectly are photons[2] with specific properties. The properties are *temporal*, *spatial* and *spectral*. Only they are responsible to define some observed event to belong to a particular celestial phenomenon and differ from the ones we knew before. Let's get a closer look at each of these three characteristics with an emphasis on gamma-ray bursts.

Temporal properties

Gamma-ray bursts are phenomena discovered by *Vela* satellite in 1967 [256]. They can last from fractions of a second to thousands of seconds [11]. Consequently, the bursts were classified as transient astrophysical gamma-ray events.

Improving methods of detection revealed the abundance of gamma-ray bursts occurring almost on a daily base.[3] Gradually increasing population of events allowed

---

[1]An experienced reader can skip the entire Section 1.1 as the information given there is mostly of historical character.

[2] Here we refer to what is called as "classical" astrophysics dealing with *quanta* of electromagnetic radiation, namely photons. However, the situation is never be the same since inevitable progress in technology made other forms—neutrino and gravitational waves—break into the area.

[3] Gamma-Ray Coordinate Network `https://gcn.gsfc.nasa.gov/`

one to search for statistical patterns.

Early attempts of classification based on the total duration of events defined as the time from onset of a burst to the latest time when a significant flux was detected. The first evidences of temporal *bimodal* nature of gamma-ray bursts were given, see, e.g., Figure 164 in Mazets et al. (1981) [328] based on a distribution for 143 events obtained by *Konus* experiment onboard of *Venera 11* and *Venera 12* satellites. Some other reported evidences of clustering in time were given in articles [89, 359, 255] on the ground of data acquired by various space experiments. It was suggested that domains are separated with a minimum at 0.5–4 s range. Here it is worth noting that the duration of bursts is a detector-dependent parameter[4] and the lack of universal algorithm for the duration resulted in applying various techniques by different authors hence making difficult the quantitative assessment on bimodality.

The phenomenology of bimodal structure in temporal distribution was further studied with a growing number of bursts. Two classes have been also found for a distribution of 260 events detected by *Burst and Transient Source Experiment* (BATSE) instrument [151] onboard of *Compton Gamma-Ray Observatory* (CGRO) [170]. The separation line marked at ≈ 2 s. Moreover, it was pointed out that a distribution based on *spectral hardness ratio* supports the above classification showing anticorrelating association with temporal bimodality [258].

In the same publication a convention about GRB duration called T_{90} was introduced being a time during which the cumulative counts increase from 5% to 95% above the background level. Thus the time period encompasses 90% of total counts being an intensity-independent measure of duration. Currently the method is also widely practiced and energy band 50–300 keV is conventionally used to determine the burst duration by a successor of *CGRO* mission—*Fermi Gamma-Ray Space Telescope* mission.

An easier one was a naming convention,[5] although it was implemented in two stages. In the case of multiple detections on a single day the format GRB YYMMDDX is adopted, where YY is a year, MM is a month, DD is a day and X is a letter: "A" for the first official announcement during the day, "B" for the second, "C" for the third, etc. Since January 1 of 2010, all GRB names follow the YYMMDDX convention [26], always including the final letter, even if only one GRB is detected and announced on a given day.

Currently detectors are able to resolve every single photon. The quantitative measurement of incident light is made possible owing to the development of observational tools. This ability opens up the following possibilities: we know arrival time of each photon, hence we are able to fix the specific period of emission and say how long the phenomenon under interest lasts.

Above-mentioned high resolution on arrival time of the photons manifested that GRBs display very diverse temporal structure. There are no two absolutely similar

---

[4] We highly rely on the operating energy range of our detectors and their sensitivity. Consequently, all the specific definitions and terms should be understood as following from existed level of technology, conventionally used or historically adopted by the professional community.

[5] In contrast to star naming with celestial coordinates, i.e., right ascension (R.A.) and declination (Dec) (`https://www.iau.org/public/themes/naming/`), the initial difficulties in spatial localization due to transiency of the gamma-ray bursts naturally proposed the naming by a date of detection.

light curves, and obviously, there is no typical time profile for gamma-ray bursts.

The morphology of temporal structures given as a light curve of the photons' count rate makes one to have some important inferences. For instance, it is believed that one of the simplest composition of the light curve[6] consists of a *fast rise and exponential decay* (FRED) pulse, see, e.g., the study [404]. But most commonly the time profiles exhibit the ovelapping behavior with multiple peaks, and statistically significant fine structure is as short as few milliseconds in width.

According to the temporal characteristics one can divide each GRB having *prompt* phase and *afterglow* phase. The former stands out by the most of energy release which received by instruments in keV–MeV range and associated to T_{90}, the latter exhibits activity in eV–keV and MeV–GeV ranges being less energetic and associated to the counterparts of the first.

In some bursts there is a *precursor* element—a weak excess in photon counts— occurring prior to the main intense episode. An early of the few systematic studies [281] has shown that the precursors have typical delay of tens of seconds and in some cases up to two hundred seconds. Later study [55] evidences no correlation between that quiescent time and the energetics of the precursor. However, it was concluded that the precursors are tightly connected to the events being just a factor less energetic than the entire bursts. To the date there is no clear mechanism creating the precursor episode in gamma-ray bursts [77].

Among many other studies focused on temporal properties of GRBs we should also mention the ones resulting in temporal asymmetry of the pulses [360] and the reflection of spectral variability by the time profile, the so-called hard-to-soft spectral evolution [188].

Indeed, the signatures of the burst evolution should be hidden in the time evolution of the multipeaked pattern. Pulses represent individual emission episodes and reflect the behavior of emitting substances. The latter can be interpreted by a wide range of physical models with different level of complexity.

At the date, the rapidity and transient nature of gamma-ray bursts required the improvement of the methods for instantaneous detection and reliable measurement of coordinates. This task has been solved gradually by the launches of constantly improving missions[7] since the discovery in 1967 and over the next thirty years.

Spatial properties

Gamma-ray bursts emit across whole electromagnetic spectrum, predominantly in keV–MeV range. It is a band of x-ray and gamma-ray astronomy which is quite different to implement from the experimental perspective due to impossibility of the direct ground-based observations, see, e.g., extensive early reviews by Fazio (1967) [148] and Oda (1965) [374].

There is a production of photons and charged particles while high-penetrative gamma-rays are absorbed by matter.[8] This is a general principle for measuring of primary high-energy photons implemented in early balloon-borne and present space

---

[6] From the point of interpretation by physical model.

[7] High-energy missions `https://heasarc.gsfc.nasa.gov/docs/heasarc/missions/time.html`

[8] There are three processes: the photoelectric effect, Compton scattering, and pair production.

experiments. We give a hardware overview on an example of detectors for gamma-radiation onboard of currently operative *Fermi* space observatory and slightly touch few others.

The *Gamma-Ray Burst Monitor* (GBM) [335] is the instrument using an array of 12 thallium activated sodium iodide NaI[Tl] scintillators and 2 bismuth germanate BGO scintillators to detect gamma-ray photons from ~ 8 keV to ~ 40 MeV over the full unocculted sky. The NaI detectors on *Fermi* are used to measure low-energy spectrum (8 keV–1 MeV) and to determine the direction[9] to GRBs. The latter is achieved by their positioning such that the direction where the burst comes from can be derived from relative flux ratios, see the description and reference in the following paragraphs. Hence, the big number of sensors used in order to increase the precision and, on the other hand, to cover full sky. The *Fermi's* BGO detectors (200 keV–40 MeV) are mainly used for cross-correlation between low-energy NaI detectors and high-energy LAT instrument by means of the overlap between energy ranges on both edges.

The *Large Area Telescope* (LAT) [21], on the contrary, is an imaging (although not without some limitations) gamma-ray instrument with wide field of view covering the energy range from ~ 20 MeV to > 300 GeV. The detection principle is based on a pair-conversion and its hardware consists of a precision converter-tracker and calorimeter, each consisting of 4×4 array of 16 modules. The tungsten converter planes are alternated with layers of silicon strip detectors used to reconstruct the direction of the incident gamma-ray, later used to produce the image. The *Fermi*-LAT calorimeter is used to measure the energy deposition due to the shower and to image the shower development profile. Each colorimeter module consists of 96 optically isolated CsI[Tl] crystals and arranged in a tower of 8 layers with 12 crystals each. A scintillation light signals from every crystal are read out by photodiodes of two types (large area 147 mm^2 for the range 2 MeV–1.6 GeV and small area 25 mm^2 for the range 100 MeV–70 GeV) from both edges. Due to construction features there are presented the techniques for energy reconstruction, energy resolution and measurement up to very high values, and also many others.

There are several techniques implemented in space gamma-ray telescopes for measuring a position of a burst. The first one is based on a measurement of the relative intensities of orthogonally oriented detectors onboard of a spacecraft, see, e.g., Figure 1 in Mazets & Golenetskii (1981) [325]. The principal advantage of the method is a localization over a very wide field of view. An improved modern protocol requires the production of three types of location [53]: automatic location by a software onboard the satellite, automatic location by a ground software, and a human-guided location. In this case the positioning accuracy highly depends on general stabilization of the spacecraft, proper modeling of the signal and the background, and can be measured with error boxes of few square degrees.

The second localization technique is determined by arrival-time differences between widely separated detectors [256]. In astronomy this practice is named as a *parallax* method (or simply as a triangulation method). The criteria for positioning

---

[9] One should know that scintillation detectors are not imaging instruments and individually provide no directional information. The principle stands on the properties of a scintillator—a substance (here crystal) that has an ability to emit light while absorbing ionizing radiation—coupled to an electronic sensor for light collection, here the photomultiplier tube.

accuracy are determined by increase of the distance between detectors and more accurate timing of the reception. The resulting error boxes can be as small as a square arcminute. In this case the usage of detectors of similar construction and characteristic is desirable although not necessary.

We should mention here the *InterPlanetary Network* (IPN) as a successful attempt of international collaboration between different ongoing space experiments, see, e.g., the first catalog [254]. Apart the above mentioned analysis—an arrival-time difference from two satellites resulting to an annulus by two concentric circles on the celestial sphere—there implemented an alternative localization method by one or two irregularly shaped error boxes. This is made possible due to three and more satellites including also the ones blocked by Earth or satellite's construction parts to extract the information about the region of the sky to be excluded. As a result we have an improvement of localization by triangulation technique; the IPN annuli and error boxes have 3σ areas with an average value of 27.1 square degrees and median value of 5.6 square degrees, see recent publication [232]. Depending on the current space fleet[10] the IPN consists of, there can be many other combinations for positioning accuracy [20] based on a triangulation method.

Another technique called a *coded-aperture mask* is successfully used in x-ray and gamma-ray astronomy. Interestingly, it was developed on the base of a disadvantage such as the impossibility to focus high energy photons with lenses and mirrors. The method (originally proposed by Oda (1965) [373] and broadened by Ables (1968) [8] and Dicke (1968) [136]) uses a specifically patterned grating installed above the detectors in a way that radiation creates a shadow on the receiver array which can then be mathematically reconstructed back to the position on sky. One of the modern coded-aperture masks is embodied in the *Burst Alert Telescope* (BAT) [25] onboard of the *The Neil Gehrels Swift Observatory* mission [171]. The mask has an area of 2.7 m^2 with field of view of 1.4 sr. Within the first 10 s BAT is able to calculate the source position with an uncertainty of 4 arcminutes. When a GRB is detected, the celestial coordinates together with the measured intensity will be automatically sent to the ground and distributed to the community to follow-up.

All the above mentioned detectors and techniques are primarily aimed for the localization and the proper measurement of the intensities. The progress depended significantly on the development of observational technology. It had to answer the major questions on whether GRBs are either of galactic origin or of extragalactic one and what are the distances to them?

Already the early guesses [88, 328, 186, 221] based on a small number of detected sources showed a substantial scatter from the galactic plane. However, it was not possible to definitively answer the questions. Moreover, it revealed [91, 328, 326], that some of the transient gamma-ray sources show the *recurrence* in time though being small in number. Yet again, more statistics and improved methods were needed. So by the beginning of the last decade of the twentieth century there were more than 500 transient gamma-ray events which could be divided into two distinct classes [223]: the classical bursts and the soft repeaters. The latter were further allocated to a separate class of astrophysical objects as *soft gamma repeaters* (SGR) [327, 187, 277] and currently are associated with magnetars of galactic origin [378].

---

[10] IPN progress report `https://ipnpr.jpl.nasa.gov/index.cfm?force_external=0`

Turning to the classical bursts, a progress in describing their spatial properties resulted in a uniform distribution over a celestial sphere [336]. It has been shown decisively [54] by *CGRO*-BATSE instrument whose operational era had in total 2704 GRB detections. These results on isotropic distribution catalogued in [152, 337, 387] were independently confirmed and extended by instruments on succeeding space missions such as *Swift*-BAT [484, 486, 289], *AGILE*-MCAL [168], *Fermi*-GBM [388, 564, 355] and others.

At mid-90s all this in turn allowed to make two mutually exclusive assumptions: either the bursts localized in an extended galactic halo [273, 272] or they have an extragalatic origin [389, 390]. The argument in favor of the first assumption was a typical estimation of the *isotropic-equivalent energy* E_{iso}, being comparable with the power of *supernovae*, whereas the cosmological origin would point to larger values, making gamma-ray bursts the most energetic(!) objects in the universe. And as one may notice, at that time the distance to GRB events left as the only open problem regarding the spatial properties. A thorough answer to this question was possible only with the help of counterparts in other spectral ranges. The observations at other wavelengths would also reveal important properties such as the host galaxy and the structure of the part of universe the light propagates through.

The attempts on searching the counterparts at longer wavelengths were made since the GRBs' discovery, but the problem, as was mentioned above, lay in the impossibility to get the accurate angular position by gamma-ray telescopes for follow-up observations. The impossibility is primarily caused by two factors: the rapidity of events with an intensity decreasing steeply in time [428] and the fuzzy image due to instrumental difficulties in working with gamma radiation [224].

As it is always the case in such situations, the faster operative solution was found not through the endless improvement of technology, but with the help of an original approach. This was a combination of a gamma-ray telescope with x-ray telescope[11] embodied in *BeppoSAX* mission [45]. The wide spectral coverage 0.1–300 keV of the spacecraft stood on a transition range[12] between x-ray and gamma-ray. The instruments onboard of *BeppoSAX* were of two kinds: 1) two units of the *Wide Field Camera* (WFC) with coded-aperture mask, working energy band of 2–30 keV and a field of view of $20° × 20°$ with best resolution of $5'$; and 2) the *Narrow Field Instruments* (NFI) consisting of *Medium Energy Concentrator Spectrometers* (MECS) 1.3–10 keV, *Low Energy Concentrator Spectrometer* (LECS) 0.1–10 keV, *High Pressure Gas Scintillation Proportional Counter* (HPGSPC) 4–120 keV, *Phoswich Detector System* (PDS) 15–300 keV. The PDS were used as a monitor for GRBs with fluence $\gtrsim 10^{-6}$ erg cm^{-2} in the range 60–600 keV with 1 ms temporal resolution.

The turning point in this "Odyssey for the counterparts" happened on February 28, 1997 with the detection of GRB 970228 by *BeppoSAX*-WFC, which further allowed the *BeppoSAX*-NFI repoint to the location of the burst leading to the

---

[11] For the principles and construction of the x-ray telescope, the reader is referred to the conceptual article of x-ray imaging telescope by Giacconi & Rossi (1960) [174], and for the development of x-ray astronomy one can have a pleasure to look at autobiographical note by Giacconi (2005) [173].

[12] It is conventionally defined in astrophysics that gamma range of the electromagnetic spectrum starts at 100 keV and beyond being the subject of gamma-ray astronomy while the radiation below 100 keV is classified as x-rays being the subject of x-ray astronomy.

successful detection of the first x-ray afterglow from a GRB [100]. The peak of precise positioning was conquered! What expected next is the identification on other wavelengths. And it was literally not long in coming too.

Three days later *BeppoSAX* observed the same burst with greater precision which allowed an optical follow-up by Hubble Space Telescope (HST) on 26$^{\text{th}}$ day and 39$^{\text{th}}$ day post-trigger [483], but even before ~ 20.8 hours after the GRB occurred there was a measurement by ground-based William Herschel Telescope (WHT) with the second imaging on March 8 together with Isaac Newton Telescope (INT) [548]. A rapidly fading optical counterpart was revealed. Thus GRBs gained an optical afterglow.

Here we mention the role of *Gamma-Ray Burst Coordinates Network* (`GCN`) as a system[13] that distributes information (notices) on the location of a new GRB given these coordinates by various spacecraft. There is also a possibility to distribute messages (circulars) on follow-up observations by ground-based and other space telescopes of all kind with information on details found. Altogether the service makes the GRB follow-up community to optimize usage of limited resources such as labor and telescope time. It was the prompt dissemination of coordinates and other information that made possible the successful solving of the main observational issues that demand a quick response.

An accurate burst position somewhat accelerated GRB observation and follow-up radio [162] detection was not long in coming.

The distance estimation—crucial for any meaningful physical quantities—consists of identifying emission/absorption lines in spectrum and measuring the amount of how lines are stretched. Taking into the account that there is a particular physical effect when an expansion of the Universe stretches the SED as $(1 + z)$ then it is possible to derive the redshift. The relation of the redshift to a proper distance is possible through the assumption based on a cosmological model.

Many efforts were put on early spectroscopy of GRB 970228 during the hunt for a redshift but initially resulted with no emission/absorption lines [522, 267]. More successful was an observational campaign with optical spectroscopy for the second GRB 970508 [167, 343]. The burst was associated to faint host galaxy [43] and spectra revealed a redshift of $z = 0.8349 \pm 0.0003$ being a firm prove of the cosmological origin of GRBs.

In the light of above the location of GRB 970228 was revisited in the course of several runs and spectra of the host galaxy were obtained. These revealed a prominent emission line [O II] 3727 Å at $z = 0.695 \pm 0.002$ together with [Ne III] 3869 Å and [O III] 5007 Å at the same redshift [139].

Therefrom a modern epoch started with a possibility to observe the value of a redshift in spectral lines.

To the present there are several thousand bursts detected and around half of a thousand[14] redshift values identified ranging from the smallest $z = 0.0085^{+0.0002}_{-0.0002}$ [520] to the biggest $z = 8.23^{+0.06}_{-0.07}$ [513] (maximum photometric redshift is $z \sim 9.4$ [106]), which uncompromisingly points to the cosmological origin of gamma-ray

---

[13] Gamma-Ray Coordinate Network `https://gcn.gsfc.nasa.gov/`

[14] The spectroscopy while being precise is however requires resource-expensive alert observations by large aperture ground-based telescopes which are in turn usually fully-loaded.

bursts.

With known distance to an object the estimates of its isotropic-equivalent energy range from 10^{46} to 10^{55} erg. Indeed, GRBs are the most powerful objects in Universe!

Spectral properties

The spectral properties of gamma-ray bursts should be attributed with the quantity and quality of the radiation received, and, consequently, they are in a tight relation with temporal and spatial properties. To be more precise, it is necessary to answer the following questions: how many photons arrived in a certain amount of time from a particular location and what is the energy distribution of the radiation received?

Since γ-rays are at the upper edge of electromagnetic scale they possess higher energy per photon due to shorter wavelength, hence, higher frequency; this brings some particularity in the study and representation of results. Because the energy of each photon is proportional to its frequency, the photons have sufficient energy to be resolved individually while detected by gamma-ray spectrometer, producing the so-called *photon count* spectrum $C(E)$ in units of $[\,\text{counts} \cdot \text{s}^{-1} \cdot \text{keV}^{-1}\,]$. Being in essence an energy histogram it needs to be corrected for Instrument Response Function (IRF) and consequently transformed to *photon number* spectrum $N(E)$ in units of $[\,\text{photons} \cdot \text{cm}^{-2} \cdot \text{s}^{-1} \cdot \text{keV}^{-1}\,]$. The latter represents the true specific flux received by instrument and for GRB analysis the photon number spectrum is the most straightforward to obtain. When there is no possibility to resolve individual photons the *specific flux density* spectrum is used, F_ν or $E\,N(E)$ in units of $[\,\text{erg} \cdot \text{cm}^{-2} \cdot \text{s}^{-1} \cdot \text{keV}^{-1}\,]$. This manner of representation was used on early stages of GRB investigation.

The above-mentioned *Spectral Energy Distribution* (SED or simply *spectrum*) itself is a graph also showing the intensity of a radiation over a range of energies. Its usual representation is $\log(\nu F_\nu)$ *vs.* $\log(\nu)$ called the *energy* spectrum νF_ν or $E^2 N(E)$ in units of $[\,\text{erg} \cdot \text{cm}^{-2} \cdot \text{s}^{-1}\,]$. Since the SED directly shows the relative energy output per frequency band its usage is the most preferable for multiwavelength astronomy including a domain probing the GRBs. The inquiring reader is referred to a short but very useful article on equations for manipulating the SEDs by Gehrels (1997) [169].

The time profiles of the bursts differ noticeably from one to another what not to say about their spectra. Despite a presence on entire electromagnetic spectrum the SED shape of a typical GRB implies that most of the energy is received in γ-rays. The main radiation during the *prompt* phase falls within the energy range from few keV to hundreds of MeV. And if one analyzes the GRB study evolution over decades through series of articles then it should be noticed that spectra of bursts have had similar appearance.

Early work by Cline et al. (1973) [90] revealed pulse spectra of 6 GRBs well described by exponentials in photon flux over 100–1200 keV region with a maximum intensity appearing at ~ 150 keV and then followed by softer decay.

A larger catalog of 143 GRBs by Mazets et al. (1981) [328, 329, 330] declares two groups of spectrum: the first fraction can be roughly described by a power law, $dN \propto E^{-\alpha} dE$ with $\alpha = 1.3$–2.5 where values of a range 1.5–1.7 are met most

frequently; the second fraction is more numerous and manifests a gradual steepening at higher energies. Such spectra are best fit with $dN/dE \propto \exp(-E/E_0)$ with $E_0 = 100$–200 keV, the so-called *cutoff* in the spectrum. A strong spectral evolution in time was also observed for several prominent events consisting of the formation of essentially softer distribution later on. An apparently weak relation between the type of time profile and the spectral distribution was further emphasized.

The succeeding 72 gamma-ray burst events measured by *Solar Maximum Mission Satellite* (SMM) were examined by Matz (1985) [321] and revealed that high-energy emission > 1 MeV is a common and energetically important feature. Therefore, the results contradict with spectra of thermal model, being harder to achieve using blackbody profile. Not all of events follow a power law behavior in spectra. Regarding the cutoff they did not find a steepening below ~ 6 MeV.

Norris et at. (1986) [361] evidenced a spectral variability on timescales shorter than the burst duration. They confirm previously seen spectral softening: within single pulse the high-energy emission has a tendency to peak earlier than its low-energy counterpart with a typical time delay of a range ~ 0.5–3 s. This softening of the pulse structure acquired a name of *hard-to-soft* spectral evolution.

The modern epoch of GRB spectral properties is based on data obtained by *CGRO*-BATSE, and its first spectral results were summarized by Band et al. (1993) [23]. They studied a sample of 54 strong bursts and found that the spectra at lower energies are best fit by a power law with exponential cutoff, $N_E(E) \propto E^\alpha \exp(-E/E_0)$, and at higher energies by power law of steeper behavior, $N_E(E) \propto E^\beta$, with $\alpha > \beta$. Moreover, they found no typical set of parameters α, β and E_0, evidencing them to vary from burst to burst, and the spectral energy break E_0 tending to occur at very wide range of energies from $\lesssim 100$ keV to $\gtrsim 1$ MeV, with whole distribution prevalence at < 200 keV. Additionally the authors did not find any correlation between spectral hardness and the spatial distribution of GRBs, while confirming that events exhibit significant spectral evolution, usually evolving from hard to soft.

Capabilities offered by *CGRO*-EGRET made use of study the spectra of bursts at high energies 30 MeV–30 GeV. Such an analysis with regard to the earliest three bright GRBs was done by Dingus et al. (1994) [137]. In particular the article states that intensities of high-energy emission is of the same order (or similar) as its low-energy counterpart, thereby indicating a significant contribution in the energy budget. Furthermore, the GeV energy photons show seconds-to-minutes delayed arrival with respect to the keV–MeV photons and last as long as main radiation episode. All of these put an uncertainty on high-energy cutoff in the spectra of gamma-ray bursts and rise a set of new issues to investigate.

To summarize the above written, the spectra[15] of gamma-ray bursts are similar in shape with energy distribution having a prominent peak though not fixed to particular value and varies around 1 MeV after correcting for $(1 + z)$ cosmological redshift [241, 179]. There is also a trend for bursts of higher luminosity to have a higher value for E_{peak}. The spectra are highly variable in time and have a complex variability. The SED are the hardest initially and soften to later phases, the hard-to-soft spectral evolution. The shape of the spectra differ significantly depending on the energy domain and tend to be a power law at the high energies

---

[15] Here we speak about continuum spectra with no features of emission/absorption lines.

and almost exponential at the low energies. The high-energy tail found later on made adjustments in description of the spectral shape, thus the burst spectra have been typically defined as $N_E(E) \propto E^\alpha \exp(-E/E_0)$ and flattening out smoothly to $N_E(E) \propto E^\beta$. Overall the shape of spectra cannot be represented by single law of a simple character.

As can be noticed the GRB spectra are described by several observational characteristics. Among them there are *Energy Fluence* in units of $[\,\mathrm{erg\,cm^{-2}}]$, *Peak Energy Flux* in units of $[\,\mathrm{erg\,cm^{-2}\,s^{-1}}]$ and *Spectral Hardness*. They define many properties, tell immediately how intense a given event and together with a redshift and a total duration serve to derive the energy component. Therefore these values become essential in any spectral catalog of bursts. Here we just list these spectral catalogs in a time sequence of space missions: *CGRO*-BATSE [241, 177], *HETE-2* [401], *BeppoSAX* [163], *Swift*-BAT [484, 486, 289], and *Fermi*-GBM [179, 201]. The information provided there is a very wide field for analysis and inferences.

A purely astronomical problem with focus to GRB spectra is a search of the correct interpretation in terms of physical properties. Regarding the above question "what is the energy distribution of the radiation received?", the one working with the spectrum—a quantitative characteristic—should answer the further qualitative question: what is the origin of incident radiation?

Spectroscopy offers a view on the origin of radiative processes fueling a source and its vicinity. While a time-integrated spectrum demonstrates a general picture,[16] a time-resolved spectroscopy shows how the processes might change over moments. A natural will to resolve the high variability by decreasing time bin leads to direct disadvantage. A trade-off is needed due to poor statistics caused by small number of photons while moving towards an infinitely small time bin.[17]

In general the radiative processes concentrate on well-studied mechanisms, which are not numerous and they are especially few in the subject of high-energy astrophysics.[18] The only changes that create a variety of results are initial and boundary conditions together with a handful of physical effects.

A reproduction of a particular GRB spectrum (distribution of photons by energy) requires a primary assumption of a distribution of some sort of radiating particles—in our case the most popular assumption is a plasma of various composition. Given the radiation mechanism (or mechanisms) applied on plasma we are able to calculate an outcome, namely the synthetic spectrum that further needs to be compared with the authentic one.

It is nothing but the comparison (or the so-called *fitting*, widely used in data analysis) of two spectral data—original and synthetic—serving as initial step on interpretation of GRB spectra. One of these spectra is coming from observation, another—its best reproduction—is an attempt utilizing our accumulated experience on the subject.

The most popular fitting models in GRB study are Band model [23], cutoff power law (CutoffPL or CPL) and simple power law (PL). The first two are characterized

---

[16] Due to the highly transient nature of bursts it should always be of a particular caution to completely trust in time-integrated spectra for subsequent inferences.

[17] Currently, the best time resolution available is $2\ \mu s = 2 \times 10^{-6}$ s or two millionths of a second.

[18] One should always remember that the higher we climb on energy scale the more efficient mechanisms we are required to use in order to reproduce the observed spectrum.

by the peak energy E_p (or equivalently the break energy E_0) and two indices before and after the peak in the distribution. It was noticed by Zhang (2018) [590] that photon-rich GRBs detected by *CGRO*-BATSE, *INTEGRAL*-SPI or *Fermi*-GBM, trace such a change in spectral behavior—different spectral regimes separated by break—due to relatively wide energy coverage, hence favoring the Band and CutoffPL models. The PL fitting model instead is suitable for describing the spectra shot by narrow bandpass instruments, e.g., *HETE-2* and *Swift*-BAT.

Overall, a prevalent type of the burst spectrum is non-thermal. From the point of analysis it means that the spectrum of GRB is not fitted by a blackbody model (BB), i.e., the spectral shape is of another form. From the physical point the blackbody model (also known as *thermal* or *Planck* spectrum) works as indication for fundamental mechanism—thermal radiation—where the resulting spectral shapes of similar appearance depend exclusively on temperature of the emitting substance. Thus, the radiative processes should be examined among other mechanisms. Being sub-dominant BB model was however found to contribute a substantial amount of energy [481, 482], therefore still present in some spectra and resolvable[19] by specific "bump" additionally nested to non-thermal model.

Technically speaking the broad-band spectrum can be synthetically reproduced by three components, namely two non-thermal and one thermal, where one of the non-thermal components (usually PL) serves for extension of the distribution to high energies. An imperfection of this approach lies in difficulties of subsequent interpretation. Mainly the reasons lie in physics behind, the microphysics and the macrophysics.

From the above written the GRB spectra seem to be as of *optically thin* emission. This is a direct consequence of the best fitting models, thus giving the preference to non-thermal radiative processes. While referring the reader to a textbook on *radiative transfer* [480] it worths to say that in general the processes responsible for the continuous spectrum—the one we deal with in x-ray and γ-ray bands of GRB radiation—are those where plasma is left free to vary in energy without significant restrictions. And the above mentioned *optically thin* or its opposite the *optically thick* emission are directly related to properties of radiating plasma, namely geometrical (size, relativistic effects) and composite (particles and photons of various energy) features.

The *afterglow* of GRB deserves a separate consideration because it is equally important part of an event. But saying the "afterglow" in Chapter 3 we focus on x-ray band emission. However, the afterglow includes as well optical, radio and high-energy afterglows. A common feature for all of them being rather conventional is an occurrence after the *prompt* phase. Nevertheless there were many evidences when a simultaneous observational campaign has taken with a success of detecting GRB during *prompt* phase by x-ray and optical telescopes.

Currently, *x-ray afterglow* observations are carried out routinely, mainly by *The Neil Gehrels Swift Observatory*. Around 95% of GRBs have x-ray afterglows detected. A collection sample made possible to reveal a general structure for the x-ray light curve called "canonical" afterglow, having three distinct PL segments [362] which

---

[19] The BB component is especially conspicuous in time-resolved analysis of the *prompt* spectrum.

later had been completed to a prototype with five distinctive components [591]. The motivation for such a division caused by interpretation needs as well as by structures themselves showing the unlike spectral features. They are *steep* decay, a *plateau*, a *flare*, *normal* decay and *late* decay. The characteristic equation describing the afterglow flux density is $F_\nu(t, \nu) \propto t^{-\alpha} \nu^{-\beta}$, where indices α and β denote the *temporal decay* rate and *spectral index* respectively. Consequently, each episode of x-ray afterglow is defined by range of index values typical for it.

A time-resolved analysis of separate episode can reveal many interesting features of GRB physics, see our approach on early x-ray *flares* in Chapter 3. And as one notices in literature there is an abundance of articles dedicated to different components of the *canonical* x-ray afterglow. The interpretation scenarios use a variety of mechanisms and geometries, but the majority agree the synchrotron process to be the most preferable. Not the last role is due to PL model (note the above equation) as best-fitting the single component data. We will come to brief discussion of this matter in the following theoretical approach section.

Around 70% of GRBs have *optical afterglows* detected. Typically ground-based optical/near-infrared telescopes start their observational challenge after receiving celestial coordinates of a GRB provided by narrow-field x-ray telescope—*Swift*-XRT—so accounting for the delay of ten-to-hundred of seconds after the trigger.[20] But as was stated few paragraphs before there are evidences (also between other bands) for co-living observation of keV–MeV (*prompt*) and eV (optical) emission, see, e.g. articles [46, 340]. These occasions give means to conditionally split the optical observations into "late" time and "early" time afterglows. The prospect of such a division is supported by temporal and spectral properties of the radiation received. A synthetic scheme for optical afterglow obtained by Li et al. (2012) [288] illustrates richer and more complicated behavior for early optical light curve while late regime follows by gradual decay trend. Consequently, the late time data are best-fit by simple PL model with decay index ~ -1, sometimes showing a steepening break [371]. Spectra of late time optical radiation most probably represent an environment where the GRBs are placed and what initial high energy plasma and photons interacts with in order to be re-emitted in the form of low energy optical afterglow. The early afterglows of the first few hours post-trigger show an active energy release through optical flares some of which are claimed to correlate with ones of x-ray and even γ-ray bands, the so-called "chromaticity" of behavior, see among others the articles [110, 263]. These studies come to a connection between inner activities of energy production site for the correlated bands including early radiation in the optical range.

The *radio afterglow* can last as long as hours to years after the initial outburst. A consensus regarding the radio emission tells us that the longer wavelength radiation originates in the environment of GRBs. Similar to optical the radio observations reveal early rise with peaking 3–6 days after the trigger then followed by decay, all curves are fit by PL model. There was noticed a presence of the clear dependence between energy of a GRB and its detectability in radio waves showing for long

---

[20] In practice one should understand the complexity of ground-based alert observations as many factors should come together at right moment: nighttime, weather, sky location availability, Moon, instrument itself, etc.

duration bursts a peak luminosity an order of magnitude brighter than for short bursts [75]. A statistics shows around 30% of GRB have radio afterglows detected. Additionally, radio bright GRBs are significantly longer in prompt duration than radio quiet events but at the same time an absence of radio afterglow was claimed in recent study to be due to circumburst density profile and not due to energetics [294].

In *high-energy emission* of MeV–GeV order the number of detected photons from GRBs becomes extremely small. So the observation is still carried out as photon counting experiment but now every quantum should be carefully treated and studied. Interestingly it was found that more energetic bursts have more high-energy photons. As these photons are arriving on time intervals longer ($\sim 10^3$ s and more) than main T_{90} duration of the *prompt* radiation then the naming *high-energy afterglow* was adapted.

The key question appeared during the observational campaign of previous space missions is a true physical nature of high-energy emission. Regarding the spectral properties of MeV–GeV radiation from GRBs there are three possibilities pointed in [24]: an extrapolation of the low-energy spectrum, an additional spectral component coexisting with the main low-energy *prompt* emission, and an afterglow. Moreover, the extrapolation assumes the presence of a spectral cutoff due to different physical processes either in a formation region or during the intergalactic propagation or both.

To the present moment there are several publications giving the analysis of a whole population of GRBs with observed gigaelectronvolt (GeV) emission, see e.g., The First *Fermi*-LAT Catalog of GRBs [10] or recent publication [356] as well as new The Second *Fermi*-LAT Catalog of GRBs [13]. There are also a big number of publications focusing on the analysis of one or two (or a small number of) objects with presence of high-energy photons. Latter ones make an effort for interpretation of the phenomenon within a paradigm of their developing model, hence some data selection according to the parameters of interest is necessary. We also will choose this path and interpret the results within the framework of a *fireshell* model [471]. We dedicate Chapter 4 for high-energy emission from gamma-ray bursts. It should only be noted that to the date an interpretation of the whole burst population with high-energy emission is an open question [13].

There are only improving upper limits regarding the neutrinos detection from GRBs [1, 2, 3, 4, 5].

There are few detections of gravitational waves. One of these detections is temporally and spatially coincident with a *Fermi*-GBM trigger on short duration GRB 170817A.[21]

---

[21] The reader is referred to the entire journal issue dedicated to GW 170817-GRB 170817A event—*The Astrophysical Journal Letters*, Volume 848, Number 2.

1.2   Theoretical approach

An interpretation is always in a very close relationship with observations, and for the case of gamma-ray bursts the experimental difficulties were both an accelerator and a decelerator. The latter case means that the observations under a certain angle could be represented as restrictions. And the restrictions are precisely the very determining factor for the development of certain ideas, and, like the vessel, determine the form that the theory must take, which is playing the role of a water here, completely filling the volume offered to it.

Following above concept we notice from previous chapter that the chronicles of theoretical ideas are essentially shaped by their contemporary observational constraints. The only should be mentioned is that GRB enigma has many branch connections not only in astronomy but also in physics.

Here we are adapting probably one of the most generic formulation given in [418], noticing that modern theoretical developments on GRBs are conducted in three main directions:[22]

- Central engine;

- Dynamics of extending plasma;

- Radiation processes.

Methodologically, searches and studies are conducted both in direct and reverse directions, which implies the development of models from a central object through plasma expansion and emission by radiative processes, or the search for mechanisms responsible for a particular phenomenon of observational activity.

In the present thesis we will exclusively focus on and work within the *fireshell* paradigm.[23] Its foundation as model is given in series of three conceptual articles [458, 457, 456], although the essential physical processes has been already given in 1970s [84, 112] and used a black hole as central engine powering the whole process. Effects of the dynamics of plasma around the black hole is also studied at the time [466, 111] being further developed in the beginning of the third millennium for needs of GRB interpretation [429, 461, 463, 428]. Since then the fireshell model have been extensively evolving with an attempt [471] to give an exhaustive answer to the problem of Gamma-Ray Bursts.

Fireshell model

In the present section we describe a working model which will be used further for interpretation of the observational data. The model is built on the basis of fundamental physical principles, the model is self-consistent, and it is not devoid

---

[22] Such a division is of course conditional and can in no way limit the study of an object as a whole phenomenon.

[23] Other GRB models and especially the widely used *fireball* model can be found elsewhere in the literature. The most recent and comprehensive description of the physics of gamma-ray bursts is given in the manuscript "The Physics of Gamma-Ray Bursts" by Bing Zhang [590].

of variability which makes it adaptable to continuous improvement, including the property of extracting qualitative conclusions about the object of study.

It is generally accepted that gamma-ray bursts are related to compact astrophysical objects, namely they are agreed to be connected with the black hole formation process. The model we are going to describe in this chapter consistently approach the issues of extracting energy from a black hole, conversion of extracted energy into a plasma of electrons and positrons, propagation and expansion of the plasma, and the interaction processes both within the plasma itself and the interaction of the plasma with an environment. For these purposes a system with initial and boundary conditions was defined. Further we defined and fixed the dynamics and by exactly solving the equations of motion we got the final results in the form of light curve and spectrum that are ready for comparison with observational data.

In the fireshell model [458, 457, 456], the GRB acceleration process consists in the dynamics of an optically thick e^+e^- plasma of total energy $E_{e^+e^-}^{\rm tot}$—the *fireshell*. Its expansion and self-acceleration is due to the gradual e^+e^- annihilation, which has been described in [462]. The effect of baryonic contamination on the dynamics of the fireshell has been then considered in [463], where it has been shown that even after the engulfment of a baryonic mass $M_{\rm B}$, quantified by the baryon load $B = M_{\rm B}c^2/E_{e^+e^-}^{\rm tot}$, the fireshell remains still optically thick and continues its self-acceleration up to ultrarelativistic velocities [14, 15]. The dynamics of the fireshell in the optically thick phase up to the transparency condition is fully described by $E_{e^+e^-}^{\rm tot}$ and B [463]. In the case of long bursts, it is characterized by $10^{-4} \lesssim B < 10^{-2}$ [235, 400, 403, 402], while for short bursts we have $10^{-5} \lesssim B \lesssim 10^{-4}$ [351, 469, 470].

The fireshell continues its self-acceleration until the transparency condition is reached; then the first flash of thermal radiation, the Proper-GRB (hereafter P-GRB), is emitted [462, 463, 457]. The spectrum of the P-GRB is determined by the geometry of the fireshell which is dictated, in turn, by the geometry of the pair-creation region. In the case of the spherically symmetric dyadosphere, the P-GRB spectrum is generally described by a single thermal component in good agreement with the spectral data, see, e.g., [351, 469]. In the case of an axially symmetric dyadotorus, the resulting P-GRB spectrum is a convolution of thermal spectra of different temperatures which resembles more a power-law spectral energy distribution with an exponential cutoff [470].

After transparency, the accelerated baryons (and leptons) propagates through the *circumburst medium* (CBM). The collisions with the CBM, assumed to occur in fully radiative regime, give rise to the prompt emission [457]. The spectrum of these collisions, in the comoving frame of the shell, is modeled with a modified BB spectrum, obtained by introducing an additional power-law at low energy with a phenomenological index $\bar{\alpha}$ which describes the departure from the purely thermal case, see [400] for details. The structures observed in the prompt emission of a GRB depend on the CBM density $n_{\rm CBM}$ and its inhomogeneities [459], described by the fireshell filling factor $\mathcal{R}$. This parameter is defined as the ratio between the effective fireshell emitting area $A_{\rm eff}$ and the total visible area $A_{\rm vis}$ [455, 454]. The $n_{\rm CBM}$ profile determines the temporal behavior (the *spikes*) of the light curve. The observed prompt emission spectrum results from the convolution of a large number of modified BB spectra over the surfaces of constant arrival time for photons at the detector (EQuiTemporal Surfaces, EQTS; [38, 37]) over the entire observation time.

Each modified BB spectrum is deduced from the interaction with the CBM and it is characterized by decreasing temperatures and Lorentz and Doppler factors.

The duration and, consequently, the moment at which the burst emission stops are determined by the dynamics of the e^+e^- plasma. The short duration is essentially due to the low baryon load of the plasma and the high Lorentz factor $\Gamma \approx 10^4$, see Figure 2 in [457] and Figure 4 in [351].

The description of both the P-GRB and the prompt emission, requires the appropriate relative spacetime transformation paradigm introduced in [458]: it relates the observed GRB signal to its past light cone, defining the events on the worldline of the source that is essential for the interpretation of the data. This requires the knowledge of the correct equations relating the comoving time, the laboratory time, the arrival time, and the arrival time at the detector corrected by the cosmological effects.

It is interesting to compare and contrast the masses, densities, thickness and distances from the BH of the CBM clouds, both in short and long bursts. In S-GRBs we infer CBM clouds with masses of 10^{22}–10^{24} g and size of $\approx 10^{15}$–10^{16} cm, at typical distances from the BH of $\approx 10^{16}$–10^{17} cm, see [470], indeed very similar to the values inferred in long GRBs, see, e.g., [235]. The different durations of the spikes in the prompt emission of S-GRBs and long bursts depend, indeed, only on the different values of Γ of the accelerated baryons and not on the structure of the CBM: in long bursts we have $\Gamma \approx 10^2$–10^3, see, e.g., [235], while in S-GRBs it reaches the value of $\Gamma \approx 10^4$, see, e.g., [470].

The evolution of an optically thick baryon-loaded pair plasma, is generally described in terms of $E_{e^+e^-}^{\mathrm{tot}}$ and B and it is independent of the way the pair plasma is created. This general formalism can also be applied to any optically thick e^+e^- plasma, like the one created via $\nu\bar{\nu} \leftrightarrow e^+e^-$ mechanism in a NS merger as described in Narayan (1992) [354], Salmonson & Wilson (2002) [488], and Rosswog (2003) [447].

Only in the case in which a BH is formed, an additional component to the fireshell emission occurs both in S-GRBs and in the binary-driven hypernovae (BdHNe, long GRBs with $E_{\mathrm{iso}} > 10^{52}$ erg, details in [472] at the end of the P-GRB phase: the GeV emission observed currently by *Fermi*-LAT and *AGILE*. This component has a Lorentz factor $\Gamma > 300$, and it appears to have an universal behavior common to S-GRBs and BdHNe. It is however important to recall that the different geometry present in S-GRBs and BdHNe leads, in the case of BdHNe, to the absorption of the GeV emission in some specific cases, see [472] and Chapter 4.

1.3   Thesis outline

The principal interest for the research that formed the basis of this work is a comprehensive study of the gamma-ray bursts. The main goal of the thesis is a search of common trends and patterns and an interpretation of the observational effects in the character of gamma-ray bursts.

General description

The chapters in the main body of the thesis focus on current research and results obtained and published. A distinct emphasis on spectral bands is expressed through structural division of the thesis: soft gamma-ray emission, x-ray afterglow emission and high-energy gamma-ray emission.

The following articles are included in this thesis:

- R. Ruffini, M. Muccino, Y. Aimuratov, C. L. Bianco, C. Cherubini, M. Enderli, M. Kovacevic, R. Moradi, A. V. Penacchioni, G. B. Pisani, J. A. Rueda, and Y. Wang. GRB 090510: A Genuine Short GRB from a Binary Neutron Star Coalescing into a Kerr–Newman Black Hole. The Astrophysical Journal, Volume 831, 178 (2016)—**Chapter 2**

- Y. Aimuratov, R. Ruffini, M. Muccino, C. L. Bianco, A. V. Penacchioni, G. B. Pisani, D. Primorac, J. A. Rueda, Y. Wang. GRB 081024B and GRB 140402A: Two Additional Short GRBs from Binary Neutron Star Mergers. The Astrophysical Journal, Volume 844, 83 (2017)—**Chapter 2**.

- R. Ruffini, Y. Wang, Y. Aimuratov, U. Barres de Almeida, L. Becerra, C. L. Bianco, Y. C. Chen, M. Karlica, M. Kovacevic, L. Li, J. D. Melon Fuksman, R. Moradi, M. Muccino, A. V. Penacchioni, G. B. Pisani, D. Primorac, J. A. Rueda, S. Shakeri, G. V. Vereshchagin, and S.-S. Xue. Early X-Ray Flares in GRBs. The Astrophysical Journal, Volume 852, 53 (2018)—**Chapter 3**.

- R. Ruffini, R. Moradi, J. A. Rueda, Y. Wang, Y. Aimuratov, L. Becerra, C. L. Bianco, Y.-C. Chen, C. Cherubini, S. Filippi, M. Karlica, G. J. Mathews, M. Muccino, G. B. Pisani, D. Primorac, S. S. Xue. On the role of the Kerr-Newman black hole in the GeV emission of long gamma-ray bursts. arXiv:1803.05476 (2018)—**Chapter 4**.

Each of the chapters contains in a self-consistent way most of the arguments from each of the above-mentioned articles [470, 12, 472, 475]. The text was intentionally reduced to the present shape in order to maximally demonstrate author's contribution in each of the publications as requested by thesis supervisor.

Author's Contribution

In Ruffini et al. (2016, ApJ, 831, 178) [470] the author of the current thesis implemented data reduction and data analysis of GRB 090510 from *Fermi*-GBM and *Fermi*-LAT under supervision of the project's leading data analysts (M. Muccino, M. Enderli). After familiarizing himself with analysis techniques as a co-author he

independently reconstructed the analysis, revised and confirmed the results obtained. Following the *fireshell* paradigm the author performed simulation of the prompt phase emission deriving the basic parameters of the model: total energy of electron-positron plasma $E_{e^+e^-}^{\text{tot}}$, baryon load factor B, filling factor $\mathcal{R}$, theoretical redshift z_{theor}, etc. The author was involved into the discussion of results and theoretical interpretation.

In Aimuratov et al. (2017, ApJ, 844, 83) [12] the author of the current thesis carried out data reduction and data analysis of GRB 081024B and GRB 140402A from *Fermi*-GBM, *Fermi*-LAT and *Swift*-XRT being one of the project's leading data analysts (together with M. Muccino). Following the *fireshell* paradigm the author run simulation of the prompt phase emission deriving basic parameters of the model, performed likelihood analysis of *Fermi*-LAT data, then derived and built luminosity time evolution dependence. As the first author he was responsible for writing and revising the text, did the correspondence with journal editor together with project's leading scientists (R. Ruffini, M. Muccino), was involved into the discussion of the results and theoretical interpretation.

In Ruffini et al. (2018, ApJ, 852, 53) [472] the author of the current thesis did data reduction and data analysis of x-ray emission of GRBs from *Swift*-XRT under supervision of the project's leading data analyst (Y. Wang). Together with other project's data analysts (R. Moradi, M. Peresano, S. Shakeri) as a co-author he was responsible for analysis of 16 GRBs with focus on early x-ray flare emission. His contribution includes derivation of light curves and spectra both time-integrated and time-resolved, calculation of GRB parameters, writing part of the text, discussion of the results and theoretical interpretation.

In the preprint Ruffini et al. (2018, arXiv:1803.05476) [475] the author of the current thesis conducted data reduction and data analysis of γ-ray emission from *Fermi*-LAT being one of the project's data analysts (together with M. Muccino, R. Moradi, Y. Wang, D. Primorac and Y.-C. Chen). His contribution includes data collection, sample selection and sample updates, likelihood analysis, derivation of light curves and spectra, calculation of GRB parameters, writing part of the text, discussion of the results and theoretical interpretation.

There are other co-authored articles not included in the text [471, 421, 474, 451] which were published during author's PhD course. There the author of present thesis contributed mainly by collecting and analyzing data of various GRBs and by participating in the discussion of results. Most of the published results were prior presented and discussed at conferences, meetings, workshops and seminars and the contribution have been reflected as well in conference materials and proceedings.

Detailed description

In **Chapter** 2 "Short Bursts: GRB 090510, GRB 081024B, GRB 140402A" we discuss theoretical and observational evidences which have been recently gained for a two-fold classification of short bursts within the *fireshell* working paradigm: 1) short gamma-ray flashes (S-GRFs), with isotropic energy $E_{\text{iso}} < 10^{52}$ erg and no BH formation, and 2) the authentic short gamma-ray bursts (S-GRBs), with isotropic energy $E_{\text{iso}} > 10^{52}$ erg evidencing a BH formation in the binary neutron star merging process. The signature for the BH formation consists in the on-set

of the high energy (0.1–100 GeV) emission, coeval to the prompt emission, in all S-GRBs. No GeV emission is expected nor observed in the S-GRFs.

We present three additional S-GRBs, 081024B, 090510 and 140402A, following the already identified S-GRBs, i.e., 090227B and 140619B. All the correctly identified S-GRBs correlate to the high energy emission, implying no significant presence of beaming in the GeV emission.

The existence of a common power-law behavior in the GeV luminosities, following the BH formation, when measured in the source rest-frame, points to a commonality in the mass and spin of the newly-formed BH in all S-GRBs.

In **Chapter** 3 "X-ray flares in GRBs" we analyze the early X-ray flares in the GRB "flare-plateau-afterglow" (FPA) phase observed by Swift-XRT. We claim that the FPA occurs only in one of the subclasses—binary-driven hypernovae (BdHNe). This subclass consists of long GRBs with a carbon-oxygen core (CO_{core}) massive star and a neutron star (NS) binary companion as progenitors.

We consider a scenario when the CO_{core} star undergoes a supernova (SN) explosion. The hypercritical accretion of the SN ejecta onto the NS can lead to the gravitational collapse of the NS into a black hole. Consequently, one can observe a GRB emission with isotropic energy $E_{iso} \gtrsim 10^{52}$ erg, as well as the associated GeV emission and the FPA phase.

Previous work had shown that gamma-ray spikes in the prompt emission occur at $\sim 10^{15}$–10^{17} cm with Lorentz gamma factor $\Gamma \sim 10^2$–10^3. Using a novel data analysis we show that the time of occurrence, duration, luminosity and total energy of the X-ray flares correlate with E_{iso}. A crucial feature is the observation of thermal emission in the X-ray flares that we show occurs at radii $\sim 10^{12}$ cm with $\Gamma \lesssim 4$.

We show that in BdHNe a collision between the GRB and the SN ejecta occurs at $\simeq 10^{10}$ cm reaching transparency at $\sim 10^{12}$ cm with $\Gamma \lesssim 4$. The agreement between the thermal emission observations and these theoretically derived values validates our model and opens the possibility of testing each BdHN episode with the corresponding Lorentz gamma factor.

In **Chapter** 4 "High-energy emission from GRBs" we examine a scenario when in binary system of neutron star (NS) and massive CO_{core} star, the latter undergoes a supernova (SN) explosion. A black hole subsequently originates from the gravitational collapse of the NS caused by hypercritical accretion of the SN ejecta. Alternatively there is a case when hypercritical accretion occurs on already existed BH.

As inverse problem we address the role of the Kerr BH in explaining the GeV emission of long gamma-ray bursts (GRBs) with a model characterized by the process occurring in the binary-driven hypernova (BdHN) system. We assume that high-energy emission from GRBs observed by *Fermi*-LAT originates from the rotational energy of the Kerr BH. The integrated GeV emission of sample GRBs allows to estimate the initial mass and spin of the BH.

We infer a new asymmetric morphology for the BdHNe system where the GeV emission occurs within a cone of half-opening angle $\approx \pi/3$ normal to the orbital plane of the binary progenitor. We confirm that GeV luminosity light curves follow the universal power-law with index of -1.19 ± 0.04, and from this we further estimate the spin-down rate of the BH.

Chapter 2

Short bursts: GRB 090510, GRB 081024B, GRB 140402A

Based on the high-energy extended emission from three short gamma-ray bursts, GRB 090510, GRB 081024B and GRB 140402A, we identify their progenitors as binary neutron star mergers that undergo collapse to a black hole.

2.1 Observation and data analysis

We have collected information on observations and analyzed data from three Short Gamma-Ray Bursts (hereafter SGRBs) following the standard procedure and using the packages provided by *Fermi Science Support Center*.[1]

Short GRB 090510

Observation

The *Fermi*-GBM instrument [335] was triggered at $T_0 =$00:22:59.97 UT on May 10, 2009 by the short and bright burst GRB 090510 ([211], trigger 263607781 / 090510016). The trigger was set off by a precursor emission of duration 30 ms, followed ~ 0.4 s later by a hard episode lasting ~ 1 s. This GRB was also detected by *Swift* [229], *Fermi*-LAT [377], *AGILE* [298], *Konus*-WIND [183], and *Suzaku*-WAM [375]. The position given by the GBM is consistent with that deduced from *Swift* and LAT observations.

During the first second after LAT trigger at 00:23:01.22 UT, *Fermi*-LAT detected over 50 events (respectively over 10) with an energy above 100 MeV (respectively above 1 GeV) up to the GeV range, and more than 150 (respectively more than 20) within the first minute [384]. This makes GRB 090510 the first bright short GRB with an emission detected from the keV to the GeV range.

Observations of the host galaxy of GRB 090510, located by VLT/FORS2, provided a measurement of spectral emission lines. This led to the determination of a redshift $z = 0.903 \pm 0.003$ [439]. The refined position of GRB 090510 obtained from the Nordic Optical Telescope [382] is offset by 0.7" relative to the center of

---

[1] https://fermi.gsfc.nasa.gov/ssc/

the host galaxy in the VLT/FORS2 image. At $z = 0.903$, this corresponds to a projected distance of 5.5 kpc. The identified host galaxy is a late-type galaxy of stellar mass $5 \times 10^9 \ M_\odot$, with a rather low star-forming rate SFR $= 0.3 \ M_\odot \ \mathrm{yr}^{-1}$ ([35] and references therein).

Data analysis

Our analysis focused on *Fermi* (GBM and LAT) and *Swift*-XRT data. The *Fermi*-GBM signal is the most luminous in the NaI-n6 (8–900 keV, dropping the overflow high-energy channels and cutting out the K-edge between ~ 30 and ~ 40 keV) and BGO-b1 (260 keV–40 MeV, again dropping the overflow high-energy channels) detectors. We additionally considered *Fermi*-LAT data in the 100 MeV– 100 GeV energy range. We made use of standard software in our analysis: GBM time-tagged data—suitable in particular for short GRBs—were analyzed with the `rmfit` package;[2] LAT data were analyzed with the Fermi Science tools.[3] The data were retrieved from the Fermi Science Support Center.[4]

We use C-Statistic option recommended in a standard RMFit package for spectral fitting because it is advantageous for non-Gaussian counting statistics (hence, preferable over χ^2), which is the case in most of short duration bursts. The Castor C-Statistic is a modified log-likelihood statistic based on Cash statistic, see Cash (1979) [64], and is used for fitting a model to data through minimization. The C-Stat does not envisage a goodness-of-fit test like the χ^2 minimization since there is by definition no standard probability distribution for likelihood statistics, see, e.g., discussion by Protassov et al. (2002) [432].

We use a difference between C-Stat values of two models fitted to the same data set, we mark it as ΔC-Stat. Since the models have different number of degrees of freedom (DoF) then there exists minimum value of ΔC-Stat for every additional DoF equal or over which one model (with less parameter numbers, hence, higher DoF) is considered to be preferable than another, see, e.g., Table 2.1 further in the text.

Time-integrated analysis

Using GBM time-tagged event data binned in 16 ms intervals, the best fit in the T_{90} interval $T_0 + 0.528$ s to $T_0 + 1.024$ s is a CPL+PL model (see Figure 2.1). Using this spectral model we find an isotropic energy $E_{\mathrm{iso}} = (3.95 \pm 0.21) \times 10^{52}$ erg. The observed peak energy of the best-fit model of the time-integrated GBM data is 4.1 ± 0.4 MeV, which corresponds to a rest-frame value of 7.89 ± 0.76 MeV.

Time-resolved analysis

Taking into account that the structure of spikes are time resolution dependent we first look at burst count rate of the detector with the strongest signal (NaI-n6) at different time resolution from 128 s down to 4 ms, see Figure 2.2. As should be obvious for short bursts the largest resolution of 128 ms is the least informative. Nevertheless,

---

[2]`http://fermi.gsfc.nasa.gov/ssc/data/analysis//rmfit/vc_rmfit_tutorial.pdf`
[3]`http://fermi.gsfc.nasa.gov/ssc/data/analysis//documentation/Cicerone/`
[4]`http://fermi.gsfc.nasa.gov/ssc/data/access/`
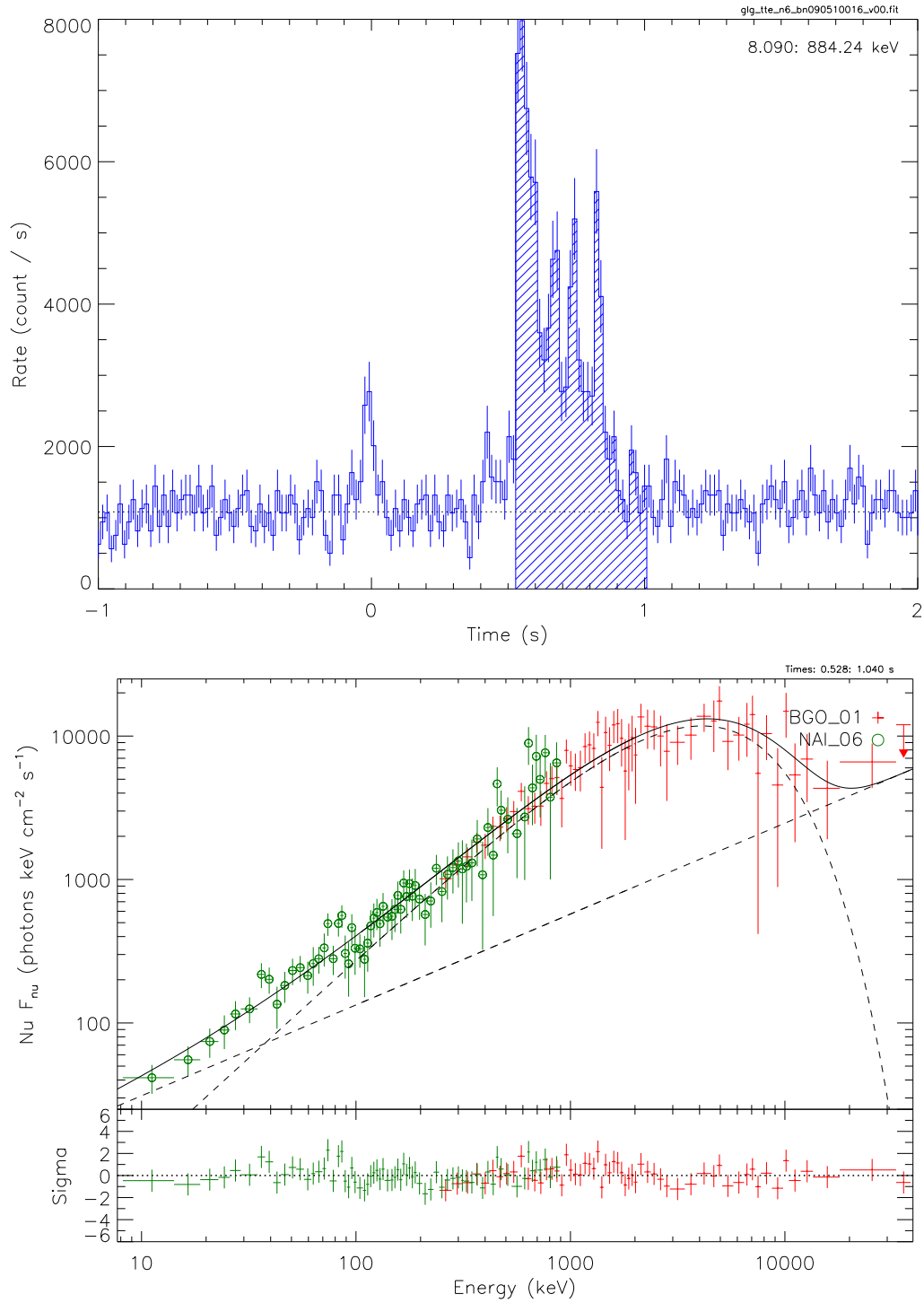
Figure 2.1. Upper panel: *Fermi*-GBM NaI-n6 light curve of GRB 090510 binned in 16 ms with dashed T_{90} interval from $T_0 + 0.528$ to $T_0 + 1.024$ s considered to compute $E_{\rm iso}$. Lower panel: CPL+PL best fit of the spectrum corresponding to T_{90} interval. Plot reproduced from [470].

going down in time scale we are able to resolve fine structures and already at time binning of 32 ms there are prominent spikes seen. Further than binning of 16 ms all the main spikes keep their presence at higher resolution just becoming sharper, but now without additional fine structure being uncovered. Therefore, we analyze the structure of short GRB 090510 at 16 ms time resolution.

A weak increase at $T_0 = 0$ occurred 0.4 s before main episode is a precursor, see definition in Chapter 1. It was already examined by Muccino et al. (2013) [351] and its spectrum is well-fit by BB+PL model with temperature of 34.2 ± 7.5 keV, and estimate of isotropic-equivalent energy gives a value of $E_{\mathrm{iso},\gamma} = (2.28 \pm 0.39) \times 10^{51}$ erg.

The precursor may be interpreted within a model of coalescing compact objects, namely binary neutron star. It was suggested that emission we see as the precursor can be generated by resonant fragmentation of neutron star crust [534] or alternatively as a result of NS magentospheres interaction [219]. Our model supposes there is no significant emission before the first pulse at transparency of the expanding plasma— the fireshell. Nevertheless, a delay between precursor and P-GRB is still consistent with pre-merger activity of the binary progenitor

We do time-resolved analysis of all the major structures so fit spikes one by one giving a table of results with different models used, the fitting statistics are summarized in Table 2.1. In the case of GRB 090510 there are five spikes but apart the first one others do not show the predominance of either model.

The best-fit model during the first pulse (from $T_0 + 0.528$ s to $T_0 + 0.640$ s) in the 8 keV–40 MeV range is also a CPL+PL, preferred over a power law (PL, ΔC-STAT= 100), a blackbody plus PL (BB+PL, ΔC-STAT= 41), or a Band model (ΔC-STAT= 12). The peak energy E_{peak} of the CPL component is 2.6 MeV. The total isotropic-equivalent energy contained in this time interval is $\sim 1.77 \times 10^{52}$ erg, while the isotropic-equivalent energy contained in the CPL part reaches $\sim 1.66 \times 10^{52}$ erg.

The above spike represents itself (according to fireshell paradigm) a Proper-GRB emission (P-GRB). Its identification is especially relevant to the fireshell analysis, since it marks the reaching of the transparency of the fireshell. The P-GRB is followed by the prompt emission [458]. It is suggested in [469] that the GeV emission is produced by the newborn BH and starts only after the P-GRB is emitted, at the beginning of the prompt emission. Here, the bulk of the GeV emission is detected after the first main spike is over. Therefore, we identify the spike (from $T_0 + 0.528$ to $T_0 + 0.644$ s, see Figure 2.3) with the P-GRB. The results of the analysis within the fireshell theory (presented hereafter) also offer an *a posteriori* confirmation of this identification of the P-GRB.

The best-fit model of the P-GRB spectrum consists of a CPL+PL model. We note that a CPL component may be viewed as a convolution of BB (see Figure 2.4 and Table 2.2, for details).

The geometry of the fireshell is dictated by the geometry of the pair-creation region. It is in general assumed to be a spherically symmetric dyadosphere, which leads to a P-GRB spectrum generally described by a single thermal component in good agreement with the spectral data. In the following approximation [78] it was found that the region of pair-creation in a Kerr-Newman geometry becomes axially symmetric, thus effectively becoming a dyadotorus. Qualitatively, one expects a pure thermal spectrum resulting from the dyadosphere while a convolution of thermal
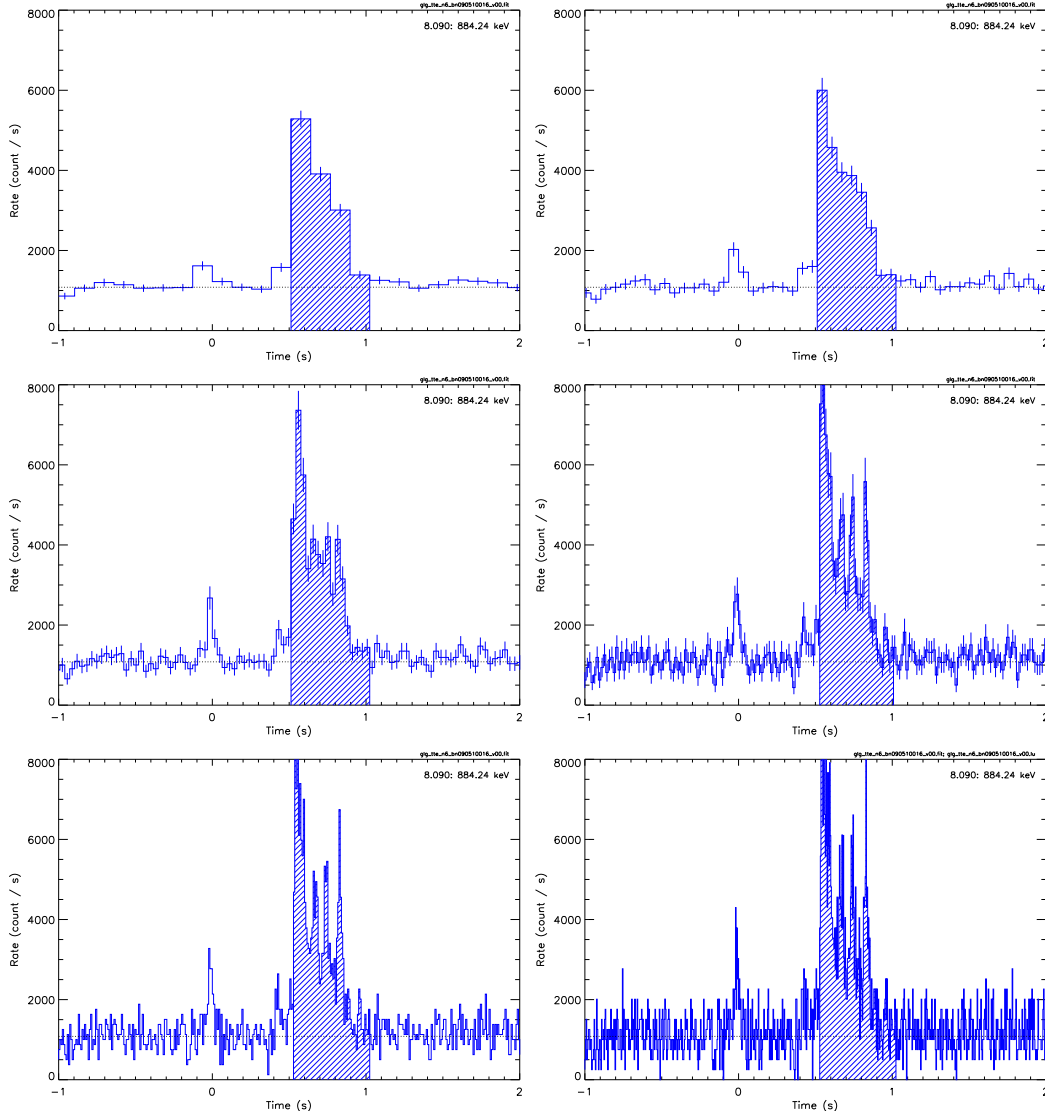
Figure 2.2. *Fermi*-GBM NaI-n6 light curve of GRB 090510 at different time resolution (from left to right and from top to down): 128 ms, 64 ms, 32 ms, 16 ms, 8 ms, 4 ms. Dashed T_{90} interval from $T_0 + 0.528$ to $T_0 + 1.024$ s was considered to compute E_{iso} isotropic-equivalent energy.

1st spike from $T_0 + 0.528$ s to $T_0 + 0.640$ s

Model	C-STAT/DoF	E_{peak} (keV)	α	β	γ	kT (keV)
Band	221.46/237	2987 ± 343	-0.64 ± 0.05	-3.13 ± 0.42	$\cdots$	$\cdots$
CPL	392.65/238	3020 ± 246	-0.64 ± 0.05	$\cdots$	$\cdots$	$\cdots$
CPL+PL	**209.26/236**	2552 ± 233	-0.26 ± 0.14	$\cdots$	-1.45 ± 0.07	$\cdots$
PL	492.83/239	$\cdots$	$\cdots$	$\cdots$	-1.20 ± 0.02	$\cdots$
BB+PL	250.09/237	$\cdots$	$\cdots$	$\cdots$	-1.38 ± 0.04	477.5 ± 24.9
BB	510.15/239	$\cdots$	$\cdots$	$\cdots$	$\cdots$	360.5 ± 13.4

2nd spike from $T_0 + 0.640$ s to $T_0 + 0.704$ s

Model	C-STAT/DoF	E_{peak} (keV)	α	β	γ	kT (keV)
Band	275/237	4627 ± 576	-0.24 ± 0.11	-2.99 ± 0.50	$\cdots$	$\cdots$
CPL	277/238	5261 ± 428	-0.33 ± 0.08	$\cdots$	$\cdots$	$\cdots$
CPL+PL	273/236	4668 ± 446	-0.09 ± 0.19	$\cdots$	-1.24 ± 0.12	$\cdots$
PL	436/239	$\cdots$	$\cdots$	$\cdots$	-1.02 ± 0.03	$\cdots$
BB+PL	292/237	$\cdots$	$\cdots$	$\cdots$	-1.15 ± 0.05	812.9 ± 47.1
BB	373/239	$\cdots$	$\cdots$	$\cdots$	$\cdots$	934.9 ± 32.3

3rd spike from $T_0 + 0.704$ s to $T_0 + 0.800$ s

Model	C-STAT/DoF	E_{peak} (keV)	α	β	γ	kT (keV)
Band	268/237	9755 ± 5890	-1.11 ± 0.01	-1.97 ± 0.58	$\cdots$	$\cdots$
CPL	269/238	13320 ± 4250	-1.13 ± 0.05	$\cdots$	$\cdots$	$\cdots$
CPL+PL	268/236	*unconstrained*	-1.12 ± 0.07	$\cdots$	*unconstrained*	$\cdots$
PL	278/239	$\cdots$	$\cdots$	$\cdots$	-1.27 ± 0.03	$\cdots$
BB+PL	275/237	$\cdots$	$\cdots$	$\cdots$	-1.32 ± 0.05	1135.0 ± 344.0
BB	515/239	$\cdots$	$\cdots$	$\cdots$	$\cdots$	746.1 ± 40.7

4th spike from $T_0 + 0.800$ s to $T_0 + 0.944$ s

Model	C-STAT/DoF	E_{peak} (keV)	α	β	γ	kT (keV)
Band	237/237	*unconstrained*	-1.13 ± 0.14	-1.99 ± 0.58	$\cdots$	$\cdots$
CPL	238/238	5120 ± 2200	-1.19 ± 0.08	$\cdots$	$\cdots$	$\cdots$
CPL+PL	237/236	*unconstrained*	-1.16 ± 0.24	$\cdots$	*unconstrained*	$\cdots$
PL	248/239	$\cdots$	$\cdots$	$\cdots$	-1.38 ± 0.05	$\cdots$
BB+PL	243/237	$\cdots$	$\cdots$	$\cdots$	-1.44 ± 0.07	343.4 ± 190.0
BB	295/239	$\cdots$	$\cdots$	$\cdots$	$\cdots$	33.7 ± 2.9

5th spike from $T_0 + 0.944$ s to $T_0 + 1.024$ s

Model	C-STAT/DoF	E_{peak} (keV)	α	β	γ	kT (keV)
Band	217/237	*unconstrained*	-1.15 ± 0.37	-1.64 ± 1.38	$\cdots$	$\cdots$
CPL	217/238	*unconstrained*	-1.22 ± 0.23	$\cdots$	$\cdots$	$\cdots$
CPL+PL	217/236	3654 ± 3480	*unconstrained*	$\cdots$	*unconstrained*	$\cdots$
PL	217/239	$\cdots$	$\cdots$	$\cdots$	-1.32 ± 0.13	$\cdots$
BB+PL	217/237	$\cdots$	$\cdots$	$\cdots$	-1.25 ± 0.20	*unconstrained*
BB	232/239	$\cdots$	$\cdots$	$\cdots$	$\cdots$	5651 ± 3350

Table 2.1. Results of time-resolved spectral analysis on the S-GRB 090510. Fitting parameters of the first spike with time interval $T_0 + 0.528$ s to $T_0 + 0.640$ s is identified with the P-GRB and best-fit by CPL+PL model. There columns denote: α is the low-energy index of the CPL or Band component, β is the high-energy index of the Band component, E_{peak} is the peak energy of the CPL or Band component, γ is the power law index, and kT is the temperature of the BB component. Other four time intervals (spikes 2–5) do not show the predominance of any model. Unconstrained values are due to model non convergence when fitted to data.
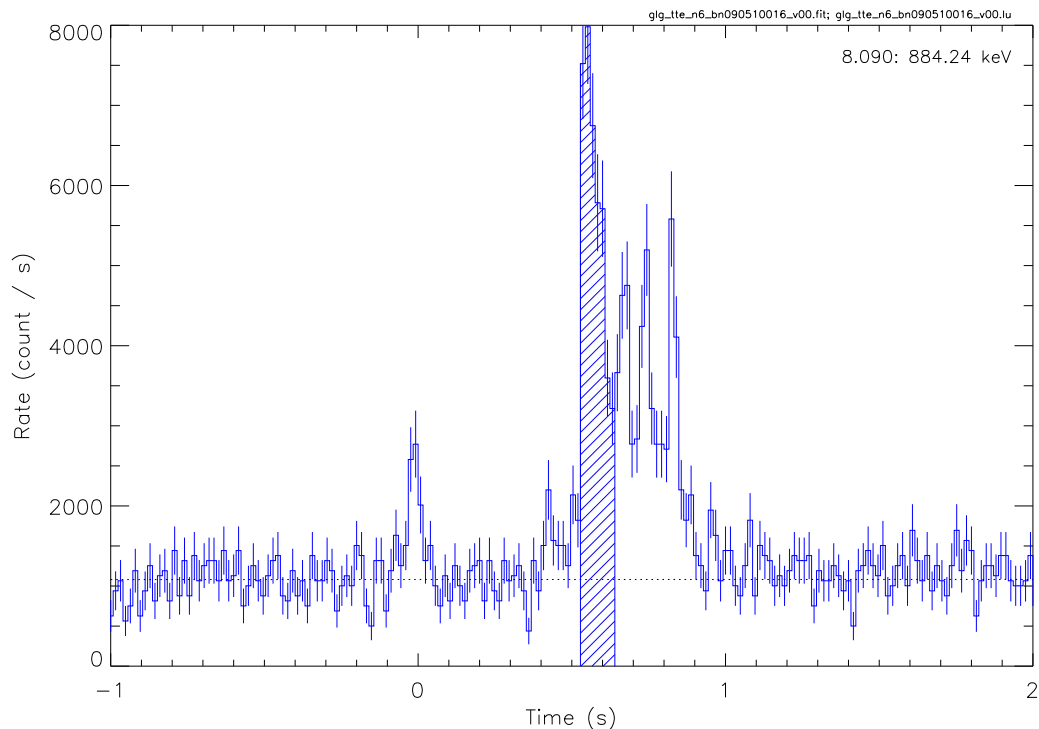
Figure 2.3. Counts rate of GRB 090510 as seen by the NaI-n6 detector of *Fermi*-GBM with a 16 ms binning. The dashed area represents the interval in which the P-GRB is identified. The small peak at T_0 represents a precursor emission, see details in the text. Plot reproduced from [470].

BB	kT (keV)	$E_{\mathrm{BB}}/E_{\mathrm{P-GRB}}$ (%)
1	1216	8.8
2	811	43.6
3	405	31.8
4	203	9.6
5	101	4.4
6	51	1.2
7	25	0.4
8	13	0.2

Table 2.2. The parameters of the blackbody (BB) spectra used in the convolution shown in Figure 2.4. The columns list the number of BB, their temperatures and their energy content with respect to the P-GRB energy computed from the CPL model.
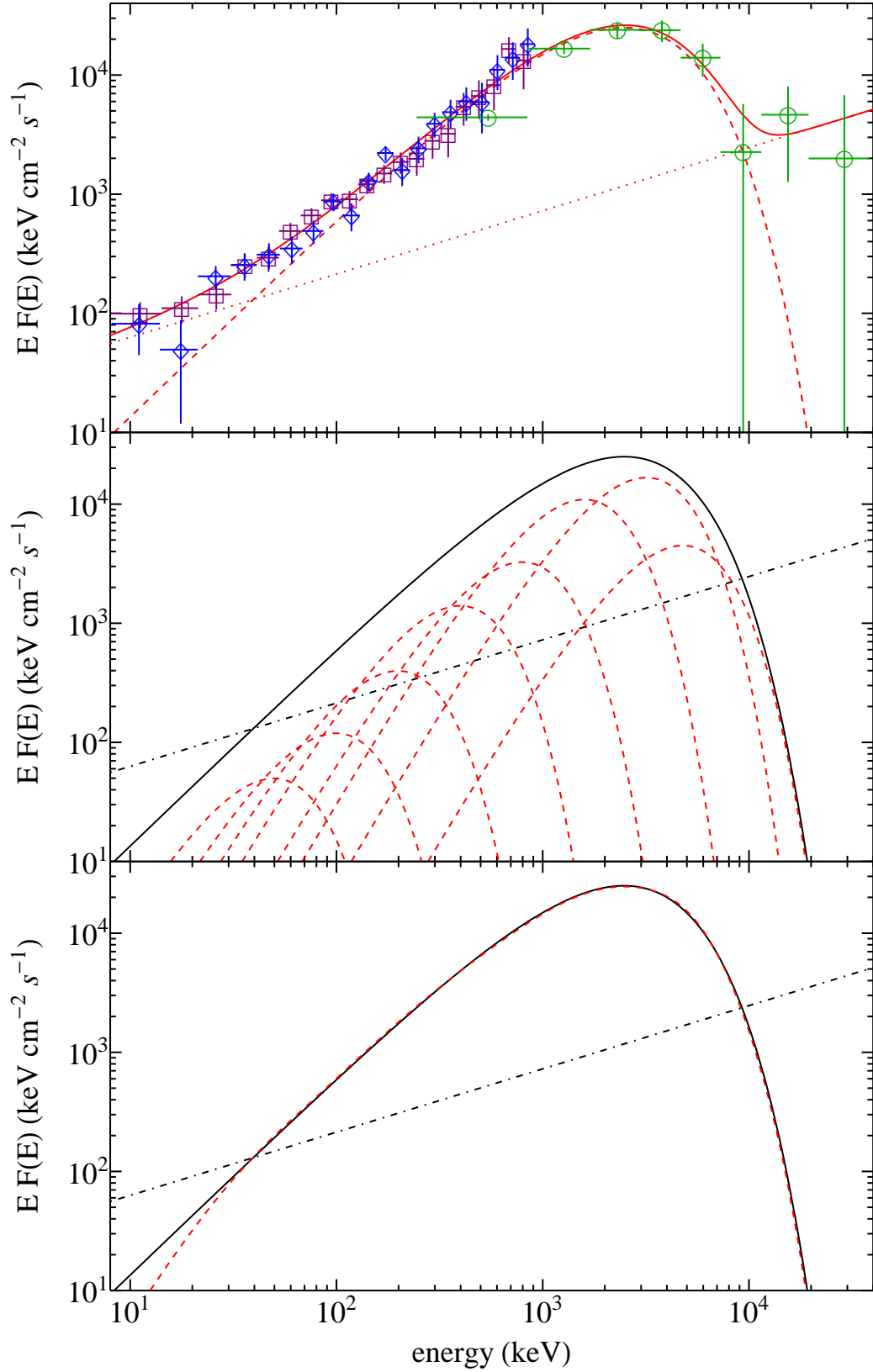
Figure 2.4. Upper panel: P-GRB spectrum of GRB 090510 from NaI-n6 (purple squares) and n7 (blue diamonds), and the BGO-b1 (green circles) detectors, obtained from $T_0 + 0.528$ to $T_0 + 0.640$ s. The best fit (solid red) is composed of PL (dotted red) and CPL (dashed red) models. Middle panel: the above CPL model (here solid black), viewed as a convolution of BB components (dashed red). Lower panel: the resulting shape (dashed red) produced by BB convolution. The PL component is given in dot-dashed black in both middle and lower panels. Plot reproduced from [470].

spectra of different temperatures is expected for a dyadotorus. One should remember that in Kerr-Newman metric with associated electromagnetic field the mass, total charge and total angular momentum characterize the spacetime.

In the present case of GRB 090510, also in view of the good quality of the γ-ray data, the P-GRB is best fitted by above mentioned convolution of thermal spectra. The theoretically expected temperatures of the thermal components in the dyadotorus are a function of the polar angle [78]. Knowing that the final spectrum at the transparency condition is a convolution of such thermal spectra at different angles, we adopted for simplicity a discrete number of thermal components (see Table 2.2). Infinitely increasing number of such thermal components, leading in principle to a continuum, is a function of the quality of the data. This provides an indication that indeed the mass, total charge and total angular momentum play a role in the dyadotorus, where the latter being a consequence of the merging of two NSs [78]. This opens a new window of research which is not going to be addressed in the present chapter. We just notice that previous identifications of pure thermal components in the P-GRB of other GRBs (e.g., [235, 469]) nevertheless evidence that the angular momentum of the BH formed by GRB 090510 should be substantially large in order to affect the P-GRB spectrum.

Finally, the extra power-law component observed in the P-GRB spectrum is very likely related with a mildly jetted component necessary to fulfill the conservation of the energy and angular momentum of the system.

There is a strong observational point on usual delay by high-energy photons with regard to GBM trigger moment and this line of presenting LAT observations were widely supported in early works [24, 6]. However evidences on non consistency of that generalization cast a shadow of doubt on whole vision of LAT GRBs even being few in occurrence. A vivid example of such inconsistency is high-energy emission of GRB 090510. According to our analysis and also results given in Table 3 of [13] photons in [100 MeV–100 GeV] band were detected simultaneously with GBM trigger, therefore the front of bulk radiation consisted of keV–MeV–GeV photons. This interesting case (another two cases are GRB 110721A and GRB 131108A) creates some difficulties not only for the fireshell model, which states P-GRB being the first flash of radiation escaped at transparency radius and especially its end marking the start of GeV radiation, but also for other models using above mentioned universal delay by LAT detection as well as models interpreting high-energy photons coming from external shock mechanisms. We improve our model in a direction of interpreting GeV photons [479, 350] as coming from activity of the central object—the black hole, see Chapter 4.

Short GRB 081024B

Observation

The short hard GRB 081024B was detected on 2008 October 24 at 21:22:41 (UT) by the *Fermi*-GBM [97]. It has a duration $T_{90} \approx 0.8$ s and exhibits two main peaks in its light curve structure, the first peak is lasting ≈ 0.2 s. Its location $(\mathrm{RA, Dec}) = (322°.9, 21°.204)$ (J2000) is consistent with that reported by the *Fermi*-LAT [383]. The LAT recorded 11 events with energy above 100 MeV within 15°

from the position of the burst and within 3 s from the trigger time [7]. Emission up to 3 GeV was seen within $\sim$ 5 s after the trigger [383].

GRB 081024B also triggered the *Suzaku*-WAM instrument, showing double peaked light curve with a duration of $\sim$ 0.4 s [215]. *Swift*-XRT instrument began observing the field of the *Fermi*-LAT $\sim$ 70.3 ks after the trigger in Photon Counting (PC) mode for 9.9 ks [208]. Initially three uncatalogued sources were detected within the *Fermi*-LAT error circle [208], but a series of follow-up observations established that none of them could be the X-ray counterpart because they were not fading in time [207, 206, 203].

The above possible associations have been also discarded by the optical observations performed in the R_c-band [147]. Similar non-detection were with optical and radio counterparts [491, 73]. Consequently, no host galaxy has been associated to this burst and, therefore, no spectroscopic redshift has been determined.

Time-integrated analysis

We analyzed data from the *Fermi*-GBM detectors, i.e., the NaI-n6 and n9 (8–900 keV) and the BGO-b1 (0.25–40 MeV), and LAT data[5] in the energy range 0.1–100 GeV. In order to obtain detailed *Fermi*-GBM light curves we analyzed the `TTE` (Time-Tagged Events) files[6] with the `RMFIT` package.[7]

In Figure 2.5 we reproduced the 50 ms binned GBM light curves corresponding to the NaI-n9 (8–260 keV, top panel) and the BGO-b1 (0.26–40 MeV, the second panel) detectors. We also reproduced the 100 ms binned LAT light curve (0.1–100 GeV, third panel) and the corresponding high energy detected photons (bottom panel), both consistent with those reported in previous publication by *Fermi* team [7]. All the light curves are background subtracted. The GBM light curves show one narrow spike of about 0.1 s, followed by a longer pulse lasting around $\sim$ 0.7 s.

The time-integrated analysis was performed in the time interval from $T_0 - 0.064$ s to $T_0 + 0.768$ s which corresponds to T_{90} duration of the burst and T_0 is the trigger time. We have fitted the corresponding spectrum with two spectral models: Cutoff Power-law (CPL, i.e., a power-law model with an exponential cutoff) and Band [23], Figure 2.6. The CPL and the Band models provide similar values of the C-STAT, see Table 2.3. Therefore, the best-fit is the CPL model because for the fitting it requires one parameter less than the Band one.

Time-resolved analysis

We have also performed the time-resolved analysis by using 16 ms bins. After rebinning the GBM light curves still exhibit two pulses: the first pulse observed before the LAT emission on-set, from $T_0 - 0.064$ s to $T_0 + 0.128$ s, and the following emission, from $T_0 + 0.128$ s to $T_0 + 0.768$ s, hereafter dubbed as ΔT_1 and ΔT_2 time intervals, respectively.

As proposed in [469], the emission before the on-set of the LAT emission corresponds to the P-GRB emission, while the following emission is attributed to the

---

[5] `http://fermi.gsfc.nasa.gov/ssc/data/analysis/documentation/Cicerone/`

[6] `ftp://legacy.gsfc.nasa.gov/fermi/data/gbm/bursts`

[7] `http://fermi.gsfc.nasa.gov/ssc/data/analysis/rmfit/vc_rmfit_tutorial.pdf`
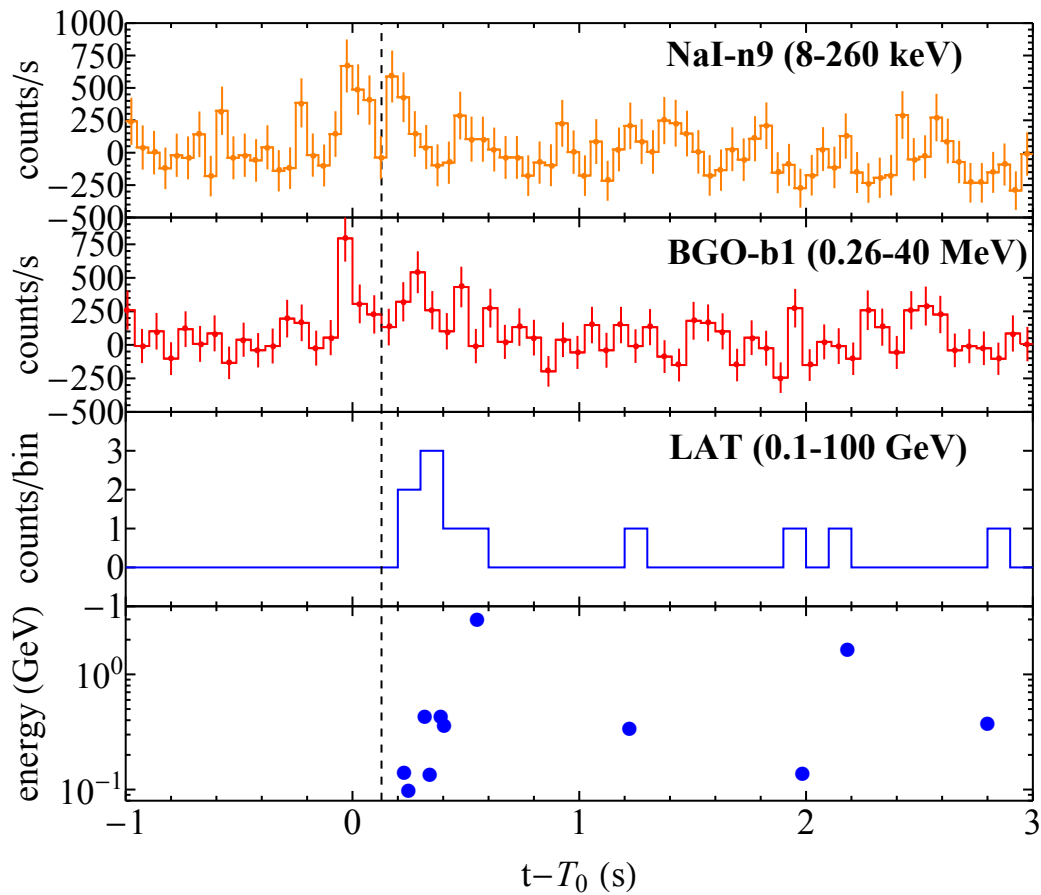
Figure 2.5. Background subtracted light curves and high energy photons of GRB 081024B: the 50 ms binned light curves from the NaI-n9 (8–260 keV, top panel) and BGO-b1 (0.26–40 MeV, the second panel) detectors, the 100 ms binned high-energy channel light curve (0.1–100 GeV, third panel, without error bars), and the high energy photons detected by the of the *Fermi*-LAT (bottom panel). The vertical dashed line marks the end of the first *Fermi*-GBM light curve pulse, before the on-set of the LAT light curve. Plot reproduced from [12].

GRB 081024B

ΔT sec	Model	K (ph keV^{-1} cm^{-2}s^{-1})	kT (keV)	E_p (MeV)	α	β	F (erg cm^{-2}s^{-1})	C-STAT/DOF
T_{90}	CPL	$(6.39\pm0.69)\times10^{-3}$		2.3 ± 1.2	-1.02 ± 0.11		$(2.27\pm0.87)\times10^{-6}$	383.89/356
	Band	$(6.51\pm0.92)\times10^{-3}$		1.9 ± 1.7	-1.01 ± 0.15	-2.2 ± 1.1	$(2.9\pm1.5)\times10^{-6}$	383.23/355
ΔT_1	BB	$(4.0\pm1.7)\times10^{-7}$	152 ± 20				$(2.24\pm0.40)\times10^{-6}$	343.54/357
	CPL	$(9.8\pm1.9)\times10^{-3}$		1.33 ± 0.59	-0.48 ± 0.27		$(3.8\pm1.4)\times10^{-6}$	333.78/356
ΔT_2	PL	$(4.60\pm0.53)\times10^{-3}$			-1.37 ± 0.07		$(5.0\pm1.5)\times10^{-6}$	392.2/357
	CPL	$(4.80\pm0.59)\times10^{-3}$		10.95(unc)	-1.28 ± 0.11		$(3.5\pm2.0)\times10^{-6}$	390.57/356

GRB 140402A

ΔT sec	Model	K (ph keV^{-1} cm^{-2}s^{-1})	kT (keV)	E_p (MeV)	α	β	F (erg cm^{-2}s^{-1})	C-STAT/DOF
T_{90}	BB	$(2.43\pm0.75)\times10^{-7}$	173 ± 18				$(2.26\pm0.31)\times10^{-6}$	527.65/483
	CPL	$(7.0\pm1.4)\times10^{-3}$		0.94 ± 0.24	0.12 ± 0.37		$(2.77\pm0.62)\times10^{-6}$	521.66/482
ΔT_1	BB	$(1.67\pm0.69)\times10^{-7}$	242 ± 34				$(6.0\pm1.1)\times10^{-6}$	441.01/483
	CPL	$(7.1\pm2.6)\times10^{-3}$		1.20 ± 0.32	0.43 ± 0.51		$(6.9\pm1.8)\times10^{-6}$	439.61/482
ΔT_2	BB	$(5.0\pm2.2)\times10^{-7}$	122 ± 18				$(1.17\pm0.22)\times10^{-6}$	500.42/483
	CPL	$(7.5\pm2.0)\times10^{-3}$		0.70 ± 0.25	0.07 ± 0.54		$(1.52\pm0.46)\times10^{-6}$	497.57/482

Table 2.3. Results of the spectral analyses on the S-GRBs 081024B and 140402A. Each column lists: the GRB, the time interval ΔT, the spectral model, the normalization constant K, the BB temperature kT, the CPL peak energy E_p, the low-energy α and the high-energy β photon indexes, the 8 keV–40 MeV energy flux F, and the value of the C-STAT over the number of degrees of freedom (DOF).

GRB	z	$E_{\rm p,i}$ (MeV)	$E_{\rm iso}$ (10^{52} erg)	$E_{\rm GeV}^{\rm max}$ (GeV)	$\Gamma_{\rm GeV}^{\rm min}$	$E_{\rm LAT}$ (10^{52} erg)	$M_{\rm acc}^{\eta+}$ (M$_\odot$)	$M_{\rm acc}^{\eta-}$ (M$_\odot$)
081024B	3.12 ± 1.82	9.56 ± 4.94	2.64 ± 1.00	3	$\gtrsim779$	2.79 ± 0.98	$\gtrsim0.04$	$\gtrsim0.41$
090227B	1.61 ± 0.14	5.89 ± 0.30	28.3 ± 1.5	—	$\gtrsim2.79$	—	—	—
090510	0.903 ± 0.003	7.89 ± 0.76	3.95 ± 0.21	31	$\gtrsim551$	5.78 ± 0.60	$\gtrsim0.08$	$\gtrsim0.86$
140402A	5.52 ± 0.93	6.1 ± 1.6	4.7 ± 1.1	3.7	$\gtrsim354$	$\gtrsim4.5\pm2.2$	$\gtrsim0.06$	$\gtrsim0.66$
140619B	2.67 ± 0.37	5.34 ± 0.79	6.03 ± 0.79	24	$\gtrsim471$	$\gtrsim2.34\pm0.91$	$\gtrsim0.03$	$\gtrsim0.35$

Table 2.4. S-GRB prompt and GeV emission properties. Columns list the redshift z, the spectral peak energy $E_{\rm p,i}$, the maximum GeV photon observed energy $E_{\rm GeV}^{\rm max}$, the minimum Lorentz factor of the GeV emission $\Gamma_{\rm GeV}^{\rm min}$, the isotropic-equivalent energy $E_{\rm iso}$, the energy in GeV domain $E_{\rm LAT}$, and the amount of infalling accreting mass co-rotating (counter-rotating) with the BH $M_{\rm acc}^{\eta+}$ ($M_{\rm acc}^{\eta-}$), needed to explain $E_{\rm LAT}$.
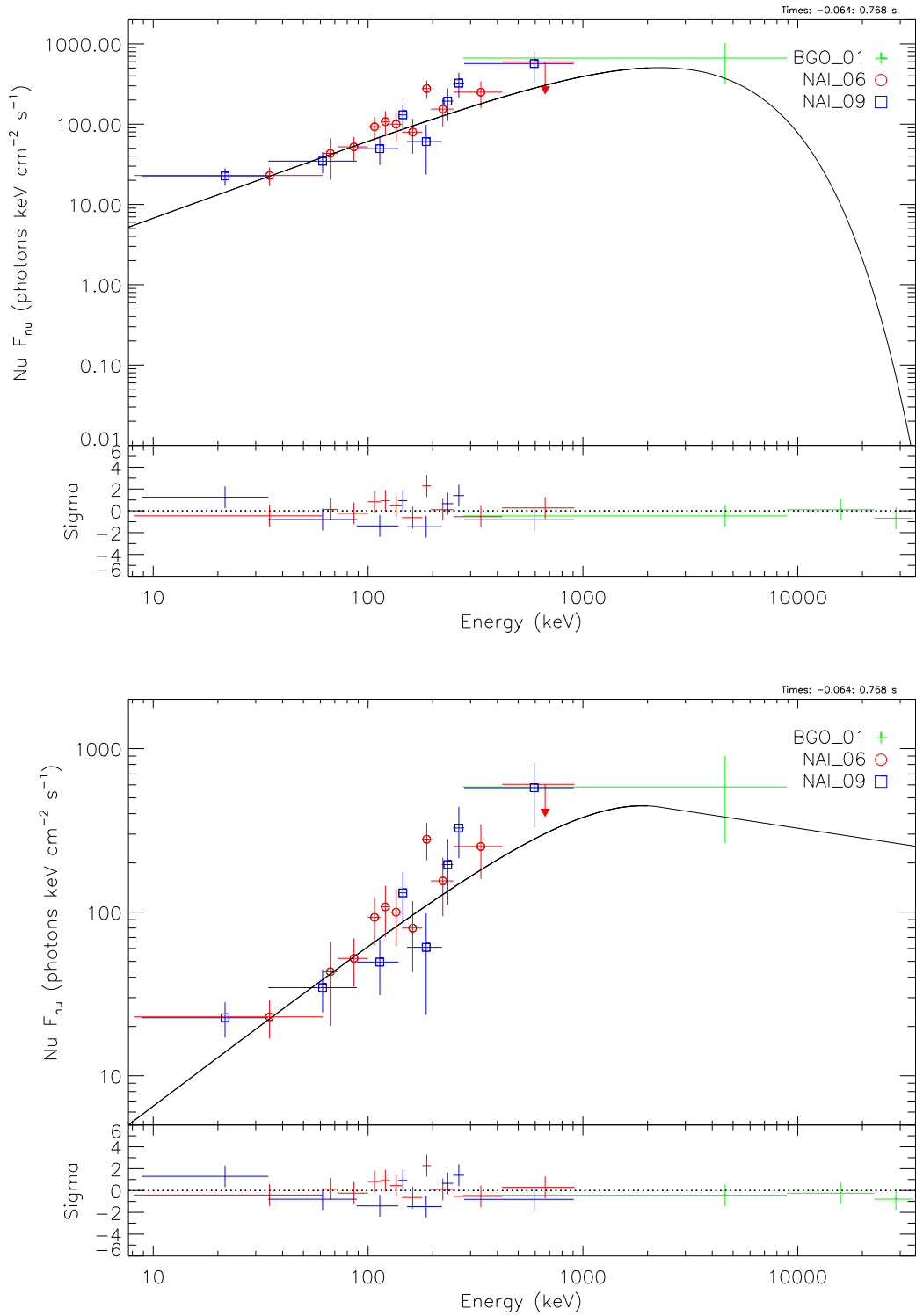
Figure 2.6. The CPL (upper plot) and the Band (lower plot) spectral fits on the combined NaI-n6, NaI-n9 and BGO-b0 νF_ν data of GRB 081024B in the T_{90} time interval. Plot reproduced from [12].

prompt emission, Sec. 2.2.

The spectrum of the ΔT_1 time interval, which can be interpreted as the P-GRB emission, is equally best-fit, among all the possible models, by a Blackbody (BB) and a CPL spectral models. Figure 2.7 and Table 2.3 illustrate the results of this time-resolved analysis. From the difference in the C-STAT values between the BB and the CPL models (ΔC-STAT= 9.88, Table 2.3), we conclude that the simpler BB model can be excluded at $> 3\sigma$ confidence level. Therefore the best fit is the CPL model.

As in the case of GRB 090510, a CPL spectrum for the P-GRB emission can be interpreted as the result of the convolution of BB spectra at different Doppler factors arising from the a spinning BH [470].

The spectrum of the ΔT_2 time interval, which can be interpretated as the prompt emission, is equally best-fit by a power-law (PL) and a CPL spectral models (see Figure 2.8 and Table 2.3). The PL and the CPL models are equivalent, though CPL model slightly improves the C-STAT statistic. However, because of the unconstrained value for the peak energy of the CPL model E_p, we conclude that the PL model represents an acceptable fit to the data.

Short GRB 140402A

Observation

The short hard GRB 140402A was detected on 2014 April 2 at 00:10:07.00 (UT) by the *Fermi*-GBM [239]. The duration of this S-GRB in the 50–300 keV is $T_{90} = 0.3$ s. It was also detected by the *Fermi*-LAT [42] with a best on-ground location $(RA, Dec) = (207°.47, 5°.87)$ (J2000), consistent with the GBM. More than 10 photons were detected above 100 MeV and within $10°$ from the GBM location, which spatially and temporally correlates with the GBM emission with high significance [42].

This burst was also detected by the *Swift*-BAT [107], with a best location $(RA, Dec) = (207°.592, 5°.971)$ (J2000). No source was detected in the *Swift*-XRT data [391] after two pointings in PC mode, from 33.3 ks to 51.2 ks and from 56 ks to 107 ks, respectively. These two observation sets are within the 3σ upper limit of the count rate of 3.6×10^{-3} counts/s and 3.0×10^{-3} counts/s, respectively [391]. Optical exposures at the full refined BAT position [107] took by the *Swift*-UVOT (during both the XRT pointings, [49]) and by Magellan (at 1.21 days after the burst, [157]) showed no optical afterglow. This allowed to set, respectively, 3σ upper limits of $v > 19.8$ mag and of $r > 25.0$ mag. Consequently, no host galaxy has been associated to this burst and, therefore, no spectroscopic redshift has been determined.

Time-integrated analysis

In Figure 2.9 we reproduced the 16 ms binned GBM light curves corresponding to detectors NaI-n3 (8–260 keV, top panel) and BGO-b0 (0.26–20 MeV, the second panel), and the 0.2 s binned high-energy light curve (0.1–100 GeV, bottom panel). Also for this burst all the light curves are background subtracted.

The NaI light curve shows a very weak and short pulse, almost at the background level, while the BGO signal exhibit two sub-structures with a total duration of ≈ 0.3 s.
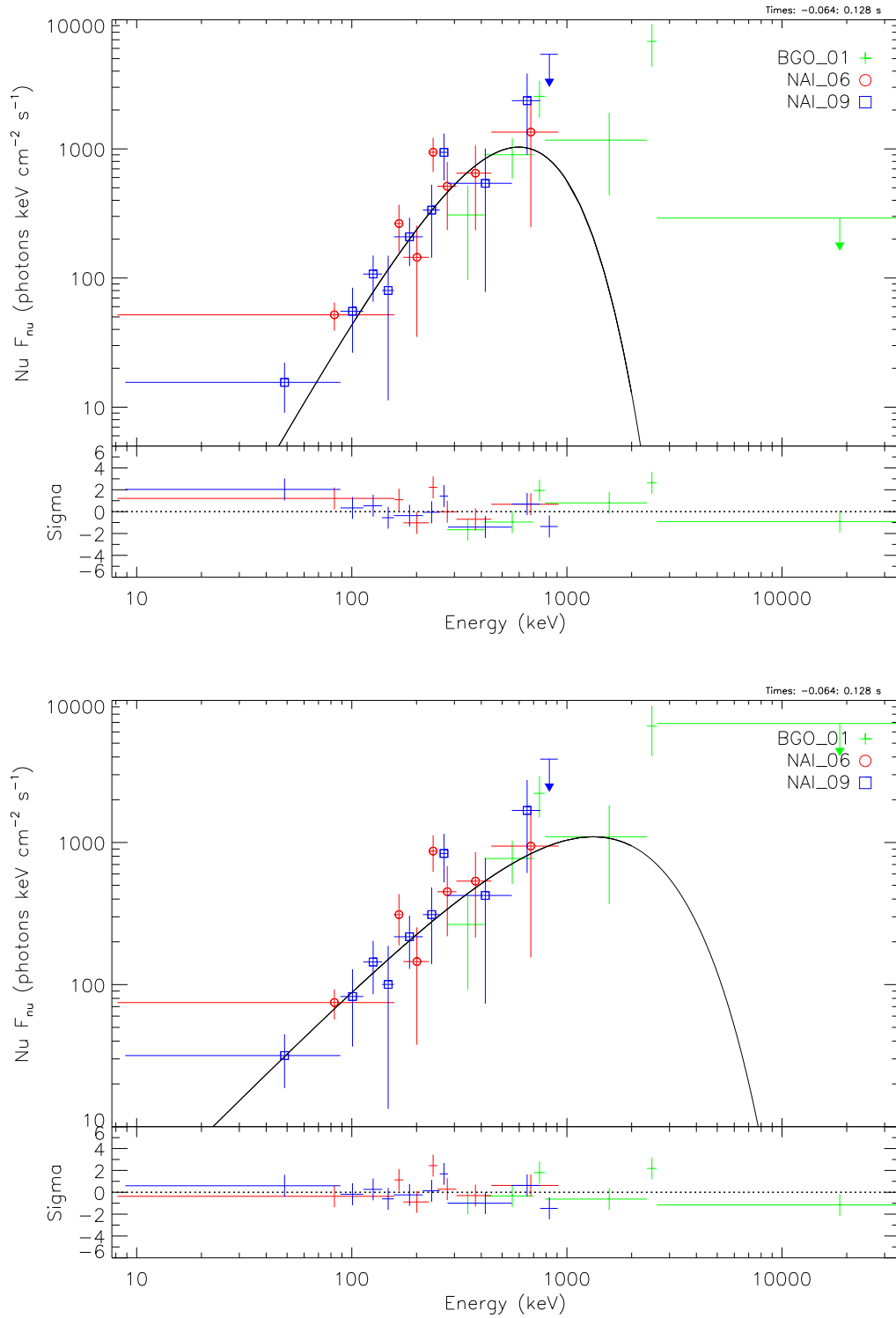
Figure 2.7. The same as in Figure 2.6, in the ΔT_1 time interval for GRB 081024B. A comparison between BB (upper plot) and CPL (lower plot) models. Plot reproduced from [12].
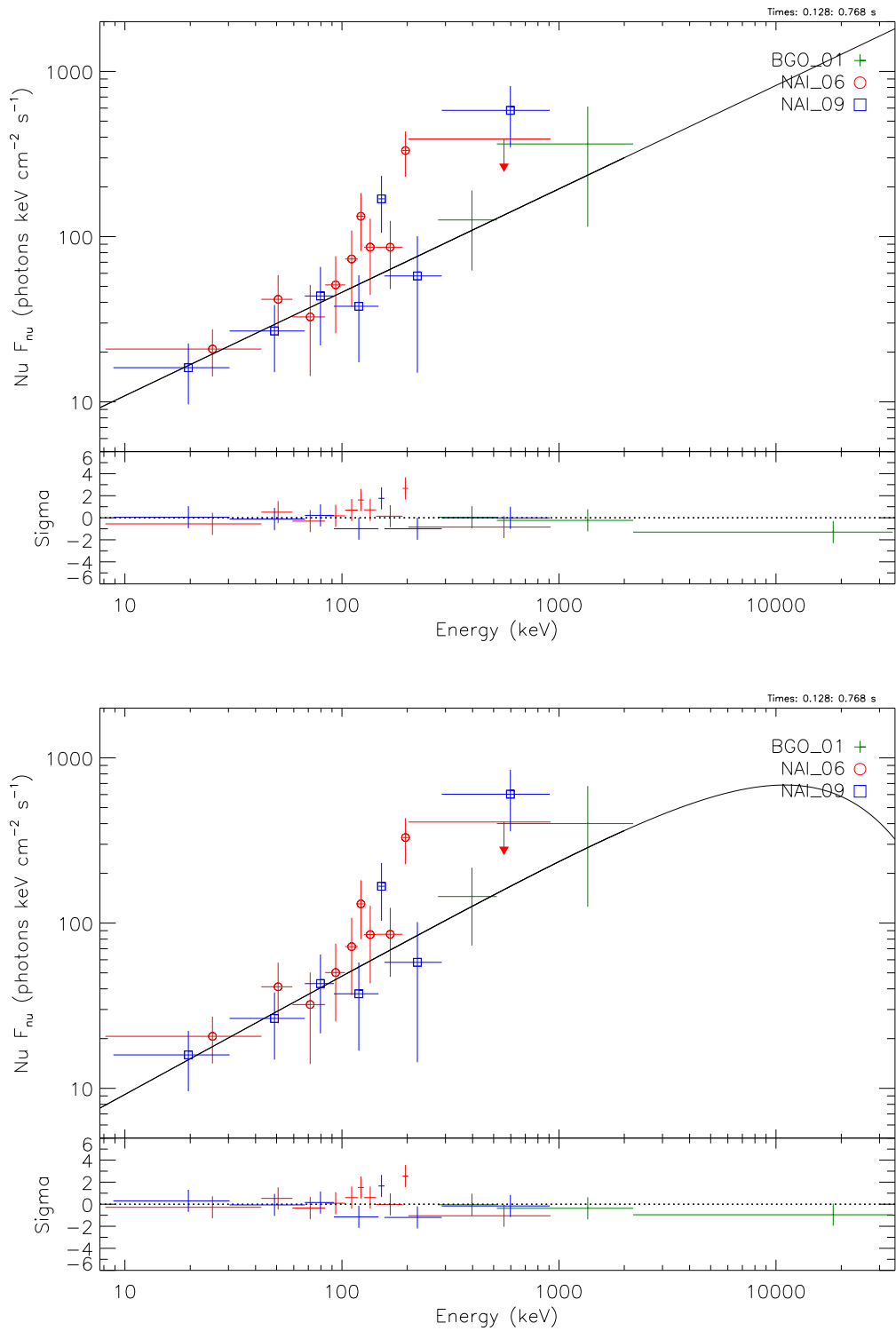
Figure 2.8. The same as in Figure 2.7, in the ΔT_2 time interval for GRB 081024B. A comparison between PL (upper plot) and CPL (lower plot) models. Plot reproduced from [12].
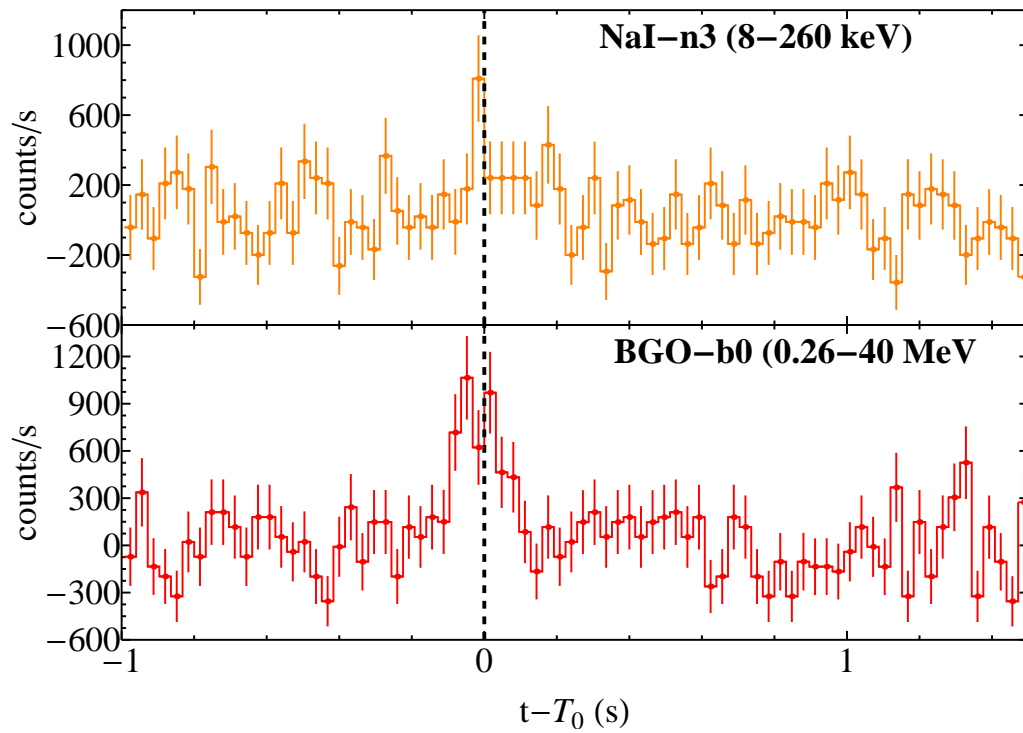
Figure 2.9. Background subtracted light curves of GRB 140402A: the 16 ms binned light curves from the NaI-n3 (8–260 keV, upper panel) and BGO-b0 (0.26–20 MeV, lower panel) detectors. The vertical dashed line marks the on-set of the LAT light curve (see Figure 2.10). Plot reproduced from [12].
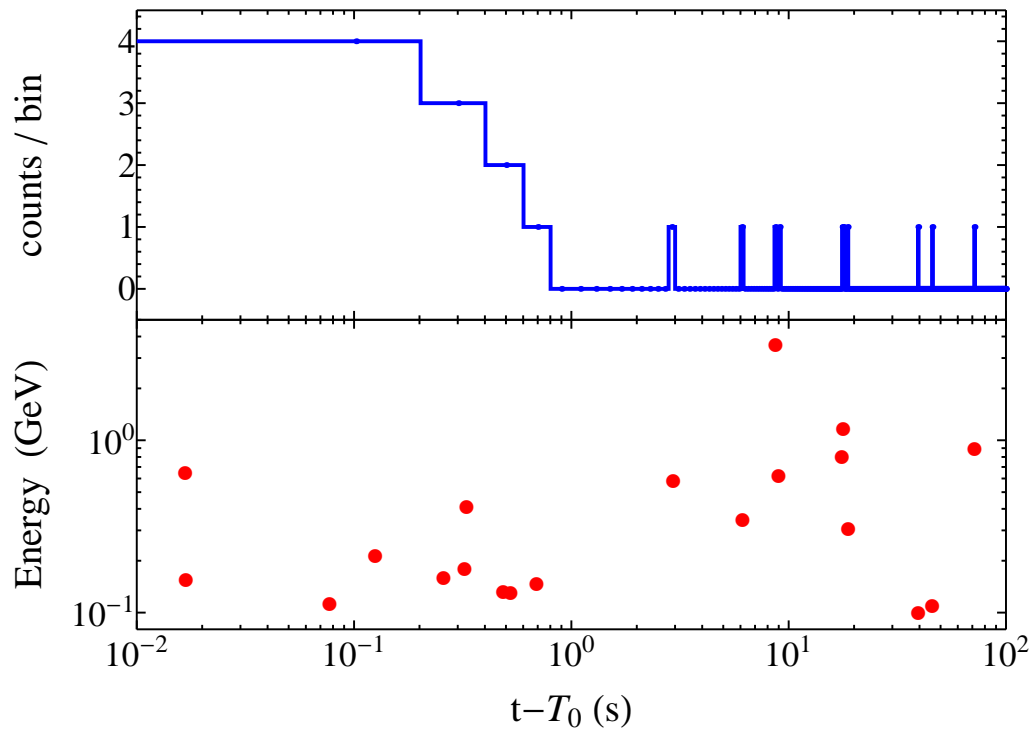
Figure 2.10. Upper panel: the background subtracted 200 ms binned high-energy (0.1–100 GeV) light curve, without error bars of GRB 140402A. Lower panel: the energy of detected high energy photons. Plot reproduced from [12].

The vertical dashed line in Figure 2.9 represents the on-set of the LAT emission, soon after the first pulse seen in both the GBM light curves. The background subtracted LAT light curve within 100 s after the GBM trigger and the corresponding 20 photons with energies higher than 0.1 GeV are shown in Figure 2.10.

We performed the time-integrated spectral analysis in the time interval from $T_0 - 0.096$ s to $T_0 + 0.288$ s (hereafter T_{90}). To increase the poor statistics at energies $\lesssim 260$ keV, we included also the data from the NaI-n0 and n1 detectors to the spectral analysis. Among all the possible models, BB and CPL equally best-fit the above data (see Figure 2.11 and the results listed in Table 2.3). From the value ΔC-STAT$= 5.99$ between the above two models, we conclude that the CPL model is an acceptable fit to the data. Similar to the GRB 140619B [469], also in the case of GRB 140402A the low-energy index of the CPL model is consistent with $\alpha \sim 0$. From theoretical and observational considerations on the on-set of the GeV emission (see Section 2.3 and Figure 2.10), we investigate the presence of a spectrum consistent with a BB one, which corresponds to the signature of the P-GRB emission for moderately spinning BH [470].

Time-resolved analysis

The first spike (Figure 2.9), observed before the on-set of the GeV, emission extends from $T_0 - 0.096$ s to T_0 (hereafter ΔT_1). Again BB and CPL spectral models equally best-fit the above data. As it is shown in Figure 2.12 and Table 2.3, the above two models are almost indistinguishable, with the low-energy index of the CPL model $\alpha = 0.43 \pm 0.51$ being consistent within almost 1σ level with the low energy index of a BB ($\alpha = 1$). We conclude that the BB model is an acceptable fit to the data and identify the first pulse in the light curve with the P-GRB emission.

The spectrum of the emission in the time interval from T_0 to $T_0 + 0.288$ s (hereafter ΔT_2) reveals that a CPL model fits slightly better the data points at ≈ 1 MeV and its low-energy index $\alpha = 0.07 \pm 0.54$ indicates that the energy distribution is somehow broader than that of a BB model (Figure 2.13 and Table 2.3). The CPL model is consistent with the modified BB spectrum adopted in the fireshell model for the prompt emission [400]. Therefore we identify the ΔT_2 time interval with the prompt emission.

2.2   Prompt emission and theoretical redshift estimate

GRB 090510

The estimate of the redshift

An interesting feature of the fireshell model is the possibility to infer a theoretical redshift from the observations of the P-GRB and the prompt emission. In the case of GRB 090510, a comparison is therefore possible between the measured redshift $z = 0.903 \pm 0.003$ and its theoretical derivation. An agreement between the two values would in particular strengthen the validity of our P-GRB choice, which would in turn strengthen our results obtained with this P-GRB.

The feature of redshift estimate stems from the relations, engraved in the fireshell theory, between different quantities computed at the transparency point: the radius
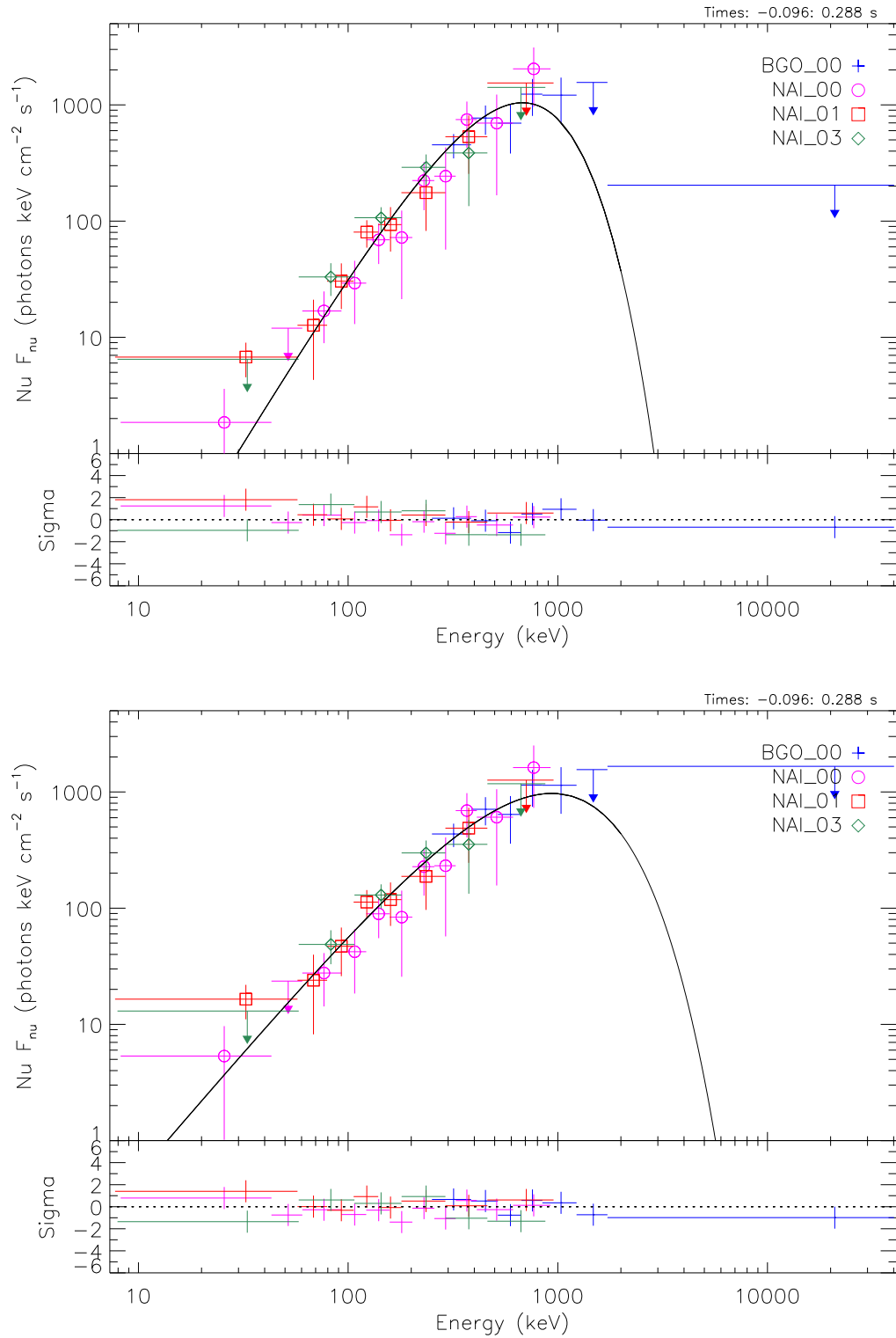
Figure 2.11. The BB (upper plot) and the CPL (lower plot) spectral fits on the combined
NaI-n0, NaI-n1, NaI-n3 and BGO-b1 νF_ν data of GRB 140402A in the T_{90} time interval.
Plot reproduced from [12].
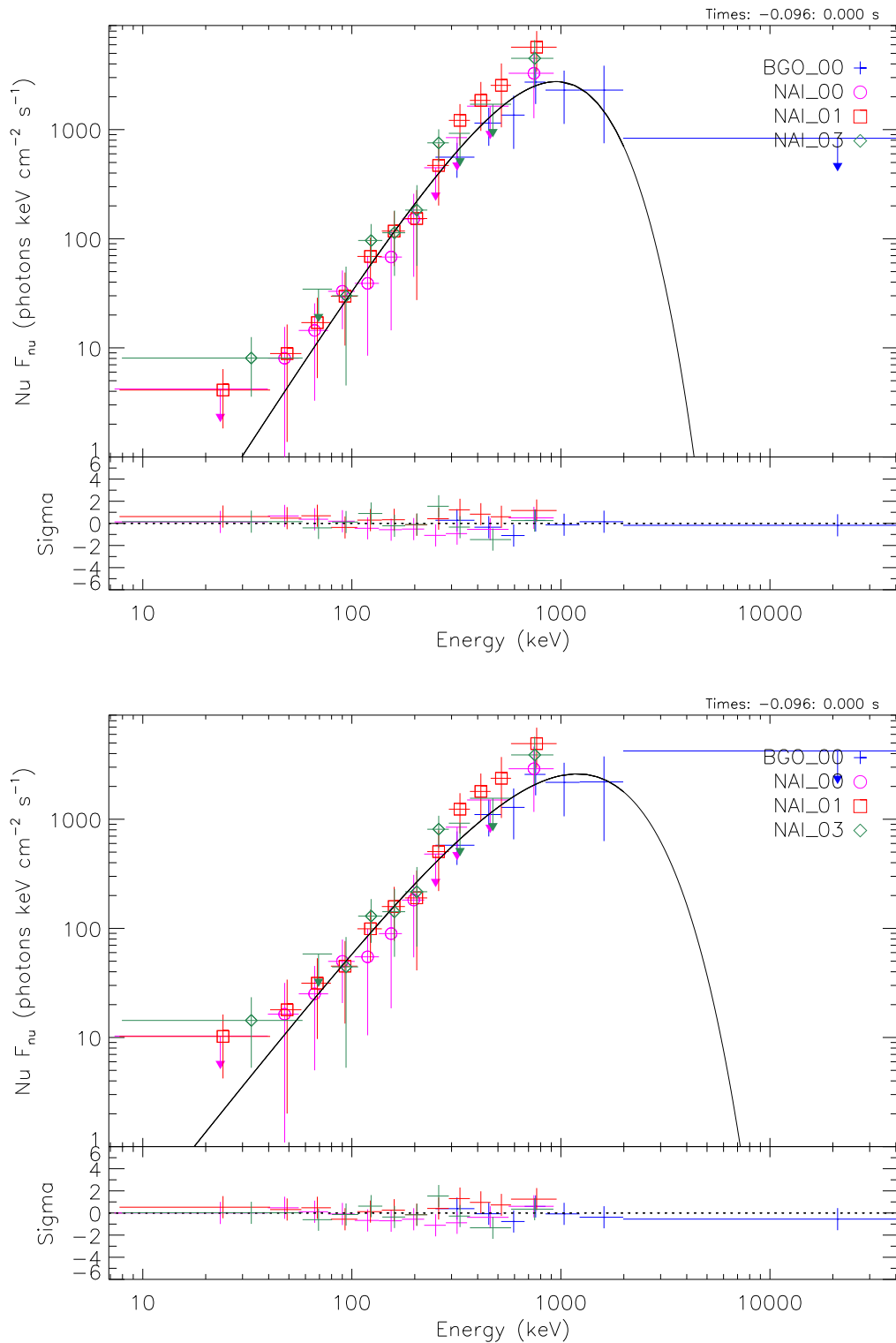
Figure 2.12. The same as in Figure 2.11, in the ΔT_1 time interval for GRB 140402A. A comparison between BB (upper plot) and CPL (lower plot) models. Plot reproduced from [12].
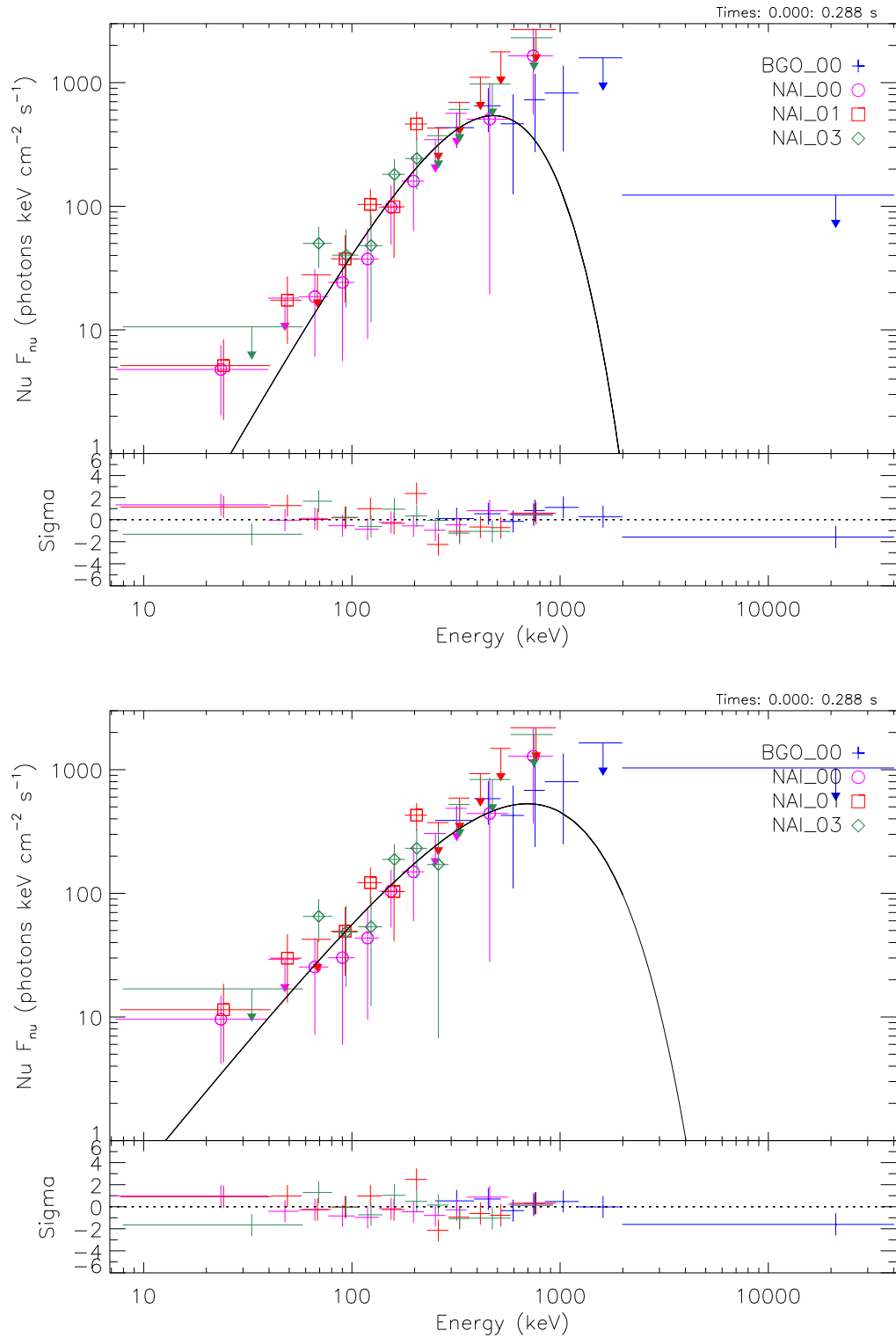
Figure 2.13. The same as in Figure 2.11, in the ΔT_2 time interval for GRB 140402A. A comparison between BB (upper plot) and CPL (lower plot) models. Plot reproduced from [12].

in the laboratory frame, the co-moving frame and blue-shifted temperatures of the plasma, the Lorentz factor, and the fraction of energy radiated in the P-GRB and in the prompt emission as functions of B (see Figure 4 in [469]). Thus, the ratio $E_{\mathrm{P-GRB}}/E_{e^+e^-}^{\mathrm{tot}}$ implies a finite range for the coupled parameters $E_{e^+e^-}^{\mathrm{tot}}$ and B (last panel of Figure 4 in [469]). Assuming $E_{e^+e^-}^{\mathrm{tot}} = E_{\mathrm{iso}}$, this ratio is known since it is equal to the ratio between the observed fluences of the respective quantities:

$$\frac{E_{\mathrm{P-GRB}}}{E_{e^+e^-}^{\mathrm{tot}}} \approx \frac{4\pi S_{\mathrm{P-GRB}} d_l^2(z)/(1+z)}{4\pi S_{e^+e^-}^{\mathrm{tot}} d_l^2(z)/(1+z)} = \frac{S_{\mathrm{P-GRB}}}{S_{e^+e^-}^{\mathrm{tot}}} \tag{2.1}$$

With the measured values $S_{\mathrm{P-GRB}} = (9.31 \pm 0.76) \times 10^{-6}$ erg cm^{-2} and $S_{e^+e^-}^{\mathrm{tot}} = (2.19 \pm 0.18) \times 10^{-5}$ erg cm^{-2}, we find $E_{\mathrm{P-GRB}}/E_{e^+e^-}^{\mathrm{tot}} = (42.1 \pm 3.8)\%$.

In addition, knowing the couple $[E_{e^+e^-}^{tot}, B]$ gives the (blue-shifted towards the observer) temperature of the fireshell at transparency kT_{blue} (Figure 4 in [469], the second panel). But we also have the following relation between kT_{blue} and the observed temperature at transparency kT_{obs}, linking their ratio to the redshift:

$$\frac{kT_{\mathrm{blue}}}{kT_{\mathrm{obs}}} = 1 + z \ . \tag{2.2}$$

Finally, since we assume that $E_{e^+e^-}^{\mathrm{tot}} = E_{\mathrm{iso}}$, we also have an expression of $E_{e^+e^-}^{\mathrm{tot}}$ as a function of z using the formula of the K-corrected isotropic energy:

$$E_{\mathrm{iso}} = 4\pi d_l^2(z) \frac{S_{\mathrm{tot}}}{1+z} \frac{\int_{1/(1+z)\ \mathrm{keV}}^{10000/(1+z)\ \mathrm{keV}} EN(E)dE}{\int_{8\ \mathrm{keV}}^{40000\ \mathrm{keV}} EN(E)dE} \tag{2.3}$$

where $N(E)$ is the photon spectrum of the GRB and the fluence S_{tot} is obtained in the full GBM energy range 8–40000 keV.

The use of all these relations allows a redshift to be determined by an iterative procedure, testing at every step the value of the parameters $E_{e^+e^-}^{\mathrm{tot}}(z)$ and kT_{blue}. The procedure successfully ends when both values are consistent according to the relations described above. In the case of GRB 090510, we find $z = 0.75 \pm 0.17$, which provides a satisfactory agreement with the measured value $z = 0.903 \pm 0.003$.

Analysis of the prompt emission

In order to simulate the light curve and spectrum of the prompt emission of GRB 090510, we assume that the initial fireshell energy $E_{e^+e^-}^{\mathrm{tot}}$ is equal to E_{iso}. Since the P-GRB spectrum is not purely thermal, we derive an effective BB temperature from the peak energy of the CPL component. We obtain a temperature $kT_{\mathrm{obs}} = (633 \pm 62)$ keV.

The fireshell theory allows the determination of all essential quantities of the model from the total pair plasma energy $E_{e^+e^-}^{\mathrm{tot}}$ and from the ratio of the energy contained in the P-GRB to $E_{e^+e^-}^{\mathrm{tot}}$. This ratio directly leads to the baryon load B, which in conjunction with $E_{e^+e^-}^{\mathrm{tot}}$ and the relation between the predicted and observed temperatures gives the Lorentz factor at transparency, the temperature of the fireshell at transparency, and the radius at transparency.

Given $E_{\mathrm{iso}} = 3.95 \times 10^{52}$ erg and $E_{\mathrm{P-GRB}} = (42.1 \pm 3.8)\% E_{e^+e^-}^{\mathrm{tot}}$, we deduce a baryon load $B = 5.54 \times 10^{-5}$, a Lorentz factor $\gamma = 1.04 \times 10^4$, a temperature at

Parameter	Value
B	$(5.54 \pm 0.70) \times 10^{-5}$
γ_{tr}	$(1.04 \pm 0.07) \times 10^{4}$
r_{tr}	$(7.60 \pm 0.50) \times 10^{12}$ cm
$E_{e^{+}e^{-}}^{\mathrm{tot}}$	$(3.95 \pm 0.21) \times 10^{52}$ erg
kT_{blue}	$(1.20 \pm 0.11) \times 10^{3}$ keV
$\langle n \rangle$	$(8.7 \pm 2.1) \times 10^{-6}$ cm^{-3}

Table 2.5. Parameters derived from the fireshell analysis of GRB 090510: the baryon load B, the Lorentz factor at transparency γ_{tr}, the fireshell radius at transparency r_{tr}, the total energy of the electron-pair plasma $E_{e^{+}e^{-}}^{\mathrm{tot}}$, the blue-shifted temperature of the fireshell at transparency kT_{blue}, and the CBM average density $\langle n \rangle$.

transparency $kT = 1.2$ MeV, and a radius at transparency $r_{\mathrm{tr}} = 7.60 \times 10^{12}$ cm (cf. Table 2.5).

In order to determine the profile of the CBM, a simulation of the prompt emission following the P-GRB has been performed. The simulation starts at the transparency of the fireshell with the parameters that we determined above. A trial-and-error procedure is undertaken, guided by the necessity to fit the light curve of GRB 090510. The results of this simulation (reproduction of the light curve and spectrum, in the time interval from $T_0 + 0.644$ to $T_0 + 0.864$ s, and CBM profile) are shown in Figure 2.14 and Figure 2.15. The average CBM density is found to be $\langle n_{\mathrm{CBM}} \rangle = 8.7 \times 10^{-6}$ cm^{-3}. This low value, typical of galactic halo environments [35, 158, 431], is consistent with the large offset from the center of the host [155] and further justifies the interpretation of GRB 090510 as a short GRB originating in a binary NS merger [354, 589, 30].

Our theoretical fit of the prompt emission (see red line in the plot of Figure 2.15) predicts a cut-off at ~ 10 MeV. The spectrum at energy $\gtrsim 10$ MeV could be affected by the onset of the high energy power-law component manifested both in the data of the Mini-Calorimeter on board *AGILE* (see top panel of Figure 4 in [176]) and in the data points from the *Fermi*-GBM BGO-b1 detector.

GRB 081024B

The estimate of the redshift

After having identified of the P-GRB emission of the S-GRB 081024B, we follow the same loop procedure as for S-GRB 090510 recalled in Section 2.2 to infer the redshift, $E_{e^{+}e^{-}}^{\mathrm{tot}}$ and B of the source. The theoretical redshift for GRB 081024B is $z_{\mathrm{theor}} = 3.12 \pm 1.82$, all the other quantities so far determined are summarized in Table 2.6.

Analysis of the prompt emission

In the fireshell model, the prompt emission light curve is the result of the interaction of the accelerated baryons with the Circumburst Medium (hereafter CBM) [455, 453, 400]. After the determination of the initial conditions for the fireshell, i.e., $E_{e^{+}e^{-}}^{\mathrm{tot}}$ and B (Table 2.6), to simulate the prompt emission light curve of the S-GRB
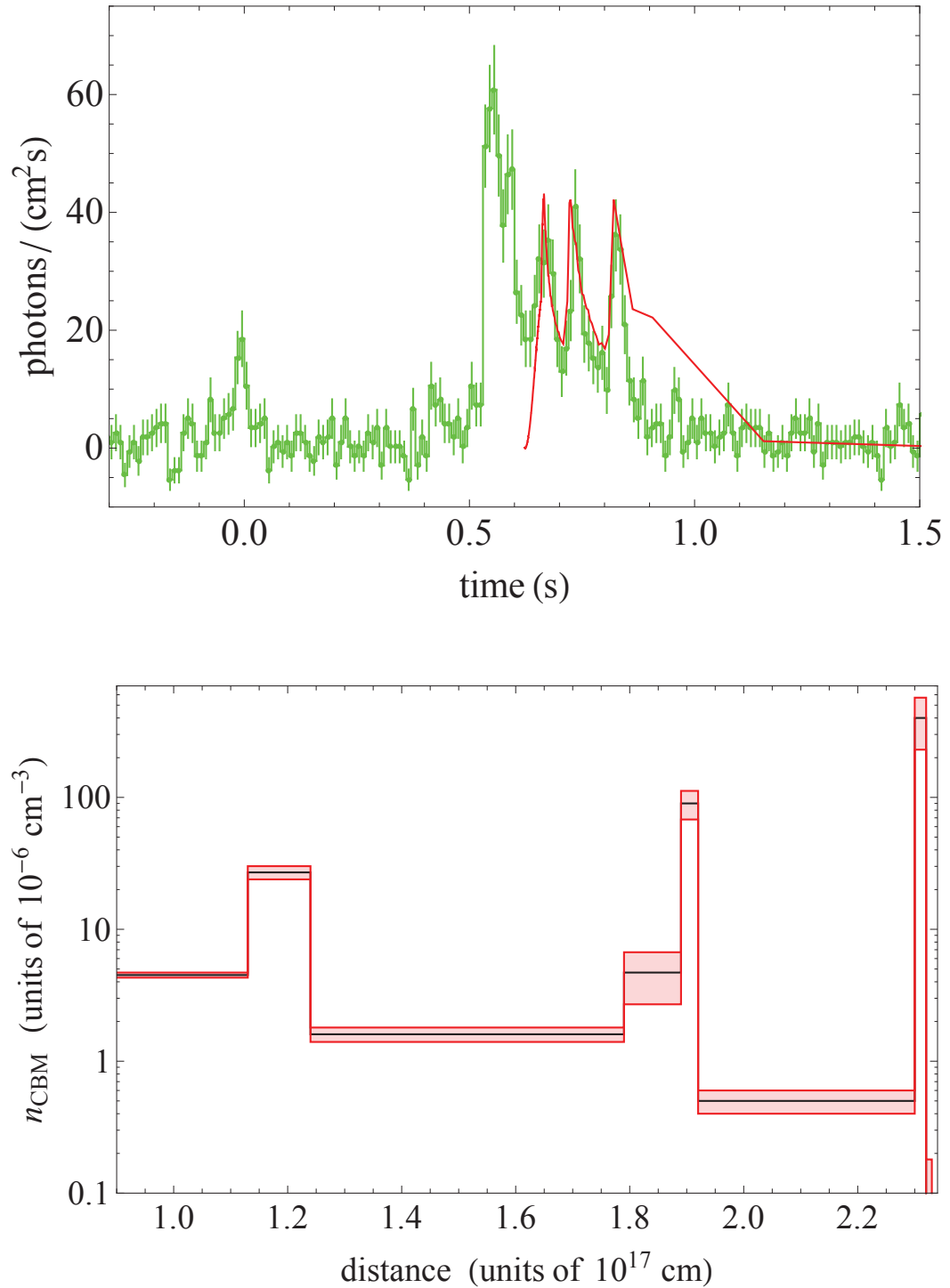
Figure 2.14. Results of the fireshell light curve simulation of GRB 090510. Upper panel: fit of the prompt emission *Fermi*-GBM NaI-n6 light curve. Lower panel: density profile of the CBM inferred from the simulation of CBM clouds of $\sim 10^{22}$ g. Plot reproduced from [470].
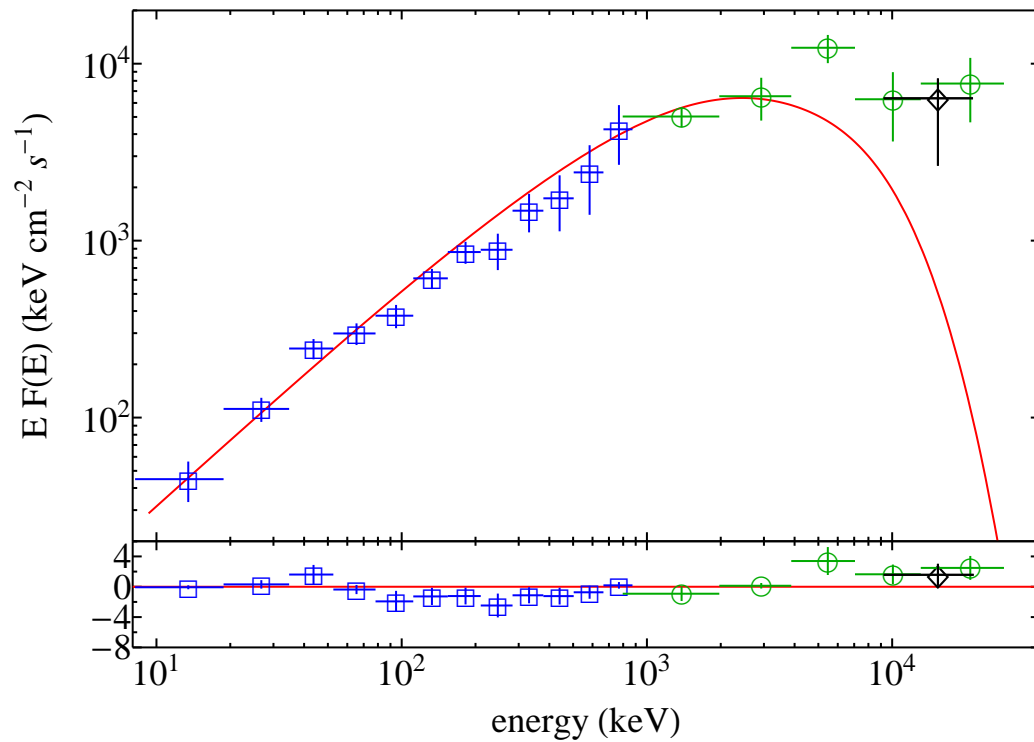
Figure 2.15. Results of the fireshell spectral simulation of GRB 090510. Fit of the prompt emission spectrum including the *Fermi*-NaI-6 (blue squares) and BGO-b1 (green circles) data in the time interval from $T_0 + 0.644$ to $T_0 + 0.864$ s. A single data point obtained from the Mini-Calorimeter on board *AGILE*, in the range 10–20 MeV and in the first 0.2 s of the *AGILE* light curve (from $T_0 + 0.5$ to $T_0 + 0.7$ s in the *Fermi* light curve), is shown for comparison (reproduced from Figure 4 in [176]). Plot reproduced from [470].

081024B (see Figure 2.5) and its corresponding spectrum, we derived the CBM number density and the filling factor $\mathcal{R}$ distributions and the corresponding attached errors (Table 2.6 and Figure 2.16, top panel). The average CBM number density inferred from the prompt emissions of GRB 081024B is $\langle n_{\mathrm{CBM}} \rangle = (3.18 \pm 0.74) \times 10^{-4}$ and it is larger than those of GRB 140619B, $\langle n_{\mathrm{CBM}} \rangle = (4.7 \pm 1.2) \times 10^{-5}$ cm^{-3} [469], and GRB 090227B, $\langle n_{\mathrm{CBM}} \rangle = (1.90 \pm 0.20) \times 10^{-5}$ cm^{-3} [351], but still typical of the S-GRB galactic halo environments.

The simulation of the prompt emission light curve of the NaI-n9 (8–900 keV) data of GRB 081024B is shown in Figure 2.16 (middle panel). The short time scale variability observed in the S-GRB light curves is the result of the large values of the Lorentz factor ($\Gamma \approx 10^4$, Table 2.6). Under these conditions the total transversal size of the fireshell visible area, d_v, is smaller than the thickness of the inhomogeneities ($\approx 10^{16}$ cm, see the values indicated in Table 2.6), justifying the spherical symmetry approximation [455, 453, 400] and explaining the absence of significant "broadening" in arrival time of the luminosity peaks.

The corresponding spectrum is simulated by using the spectral model described in [400] with phenomenological parameters $\bar{\alpha} = -1.99$. The rebinned data within the ΔT_2 time interval agree with the simulation, as shown by the residuals around the fireshell simulated spectrum on Figure 2.17.

GRB 140402A

The estimate of the redshift

After having identified of the P-GRB emission of the S-GRB 140402A, we follow the same loop procedure recalled in Section 2.2 to infer the redshift, $E_{e^+e^-}^{\mathrm{tot}}$ and B of the source. The results of this method are summarized in Table 2.6. In particular the theoretically derived redshift for this source is $z_{\mathrm{theor}} = 5.52 \pm 0.93$.

Being model-dependent these high values are certainly not something to propose casually, because the highest measured redshift of a short event is the one of S-GRB 092426 at $z = 2.609$. Nevertheless we cross-checked obtained values of E_{iso} and E_{peak} by plotting them on Zhang's E_{peak}-E_{iso} relation for short GRBs [593] (analogue of Amati's relation for long bursts) and got a good agreement within 1σ, see Figure 1 in [471].

Currently we are working on improving the analysis in a way that an estimate of the redshift will be independently made from different approaches, including the whole population analysis, see Section 4.5.2 and Section 4.5.3.

Analysis of the prompt emission

Similarly to the case of the S-GRB 081024B (see Section 2.2), to simulate the prompt emission light curve of the S-GRB 140402A (Figure 2.9) and its corresponding spectrum, we derived the CBM number density and the filling factors $\mathcal{R}$ distributions (Table 2.6 and Figure 2.18, top panel). Also in this case the inferred values fully justify the adopted spherical symmetry approximation and explain the negligible "dispersion" in arrival time of the luminosity peak.

The average CBM number density in the case of GRB 140402A is $\langle n_{\mathrm{CBM}} \rangle = (1.54 \pm 0.25) \times 10^{-3}$ (Table 2.6), which is similar to that inferred for GRB 081024B.

GRB 081024B

P-GRB

z_{theor}	$E^{\text{tot}}_{e^+e^-}$ (10^{52} erg)	B (10^{-5})	M_{B} (10^{-7} M$_\odot$)	$E_{\text{P−GRB}}/E_{e^+e^-}$ (%)	Γ_{tr} (10^4)	r_{tr} (10^{12} cm)	kT_{blue} (MeV)
3.12 ± 1.82	2.64 ± 1.00	4.6 ± 2.8	6.7 ± 4.8	50 ± 26	1.10 ± 0.24	5.6 ± 2.1	1.39 ± 0.76

Prompt

Cloud	r (cm)	Δr (cm)	n_{CBM} (10^{-4} cm^{-3})	M_{CBM} (10^{22} g)	$\mathcal{R}$ (10^{-12})	Γ (10^4)	d_{v} (cm)
1st	5.5×10^{16}	0.5×10^{16}	0.90 ± 0.70	3.1 ± 2.4	9.0 ± 7.0	1.10	2.90×10^{10}
2nd	6.0×10^{16}	0.8×10^{16}	0.10 ± 0.02	0.69 ± 0.14		0.52	6.60×10^{14}
3rd	6.8×10^{16}	0.7×10^{16}	1.00 ± 0.20	7.5 ± 1.5		0.51	7.68×10^{14}
4th	7.5×10^{16}	0.3×10^{16}	3.5 ± 0.70	12.9 ± 2.6	98 ± 53	0.40	1.08×10^{15}
5th	7.8×10^{16}	0.7×10^{16}	20.0 ± 4.00	196 ± 39		0.29	1.55×10^{15}
average			3.18 ± 0.74				

GRB 140402A

P-GRB

z_{theor}	$E^{\text{tot}}_{e^+e^-}$ (10^{52} erg)	B (10^{-5})	M_{B} (10^{-7} M$_\odot$)	$E_{\text{P−GRB}}/E_{e^+e^-}$ (%)	Γ_{tr} (10^4)	r_{tr} (10^{12} cm)	kT_{blue} (MeV)
5.52 ± 0.93	4.7 ± 1.1	3.6 ± 1.0	9.5 ± 3.4	54 ± 16	1.30 ± 0.13	6.66 ± 0.91	1.58 ± 0.22

Prompt

Cloud	r (cm)	Δr (cm)	n_{CBM} (10^{-4} cm^{-3})	M_{CBM} (10^{22} g)	$\mathcal{R}$ (10^{-12})	Γ (10^4)	d_{v} (cm)
1st	1.0×10^{16}	1.4×10^{16}	6.0 ± 2.0	5.4 ± 1.8	4.7 ± 0.45	1.30	6.64×10^{10}
2nd	2.4×10^{16}	2.6×10^{16}	24.0 ± 3.0	187 ± 23		0.92	1.49×10^{14}
average			15.4 ± 2.5				

Table 2.6. The P-GRB and Prompt emission parameters of the S-GRBs 081024B and S-GRB 140402A within the fireshell model. The P-GRB list of parameters (upper part of the table) are: the inferred redshift z_{theor}, the e^+e^- plasma energy $E^{\text{tot}}_{e^+e^-}$, the baryon load B and the corresponding baryonic mass M_{B}, the P-GRB energy $E_{\text{P−GRB}}$ over $E^{\text{tot}}_{e^+e^-}$, and the Lorentz factor Γ_{tr}, the radius of the fireshell r_{tr}, and the temperature blue-shifted toward the observed kT_{blue} computed at the transparency point. The CBM properties inferred from the prompt emission simulation (lower part of the table) are: the number of CBM clouds, the distance r from the BH, the thickness Δr, the number density distribution n_{CBM}, the total mass M_{CBM}, the filling factors $\mathcal{R}$, the Lorentz factor after each collision Γ, and the total transversal sizes d_{v} of the fireshell visible area. The average number density is indicated at the end of the n_{CBM} column.
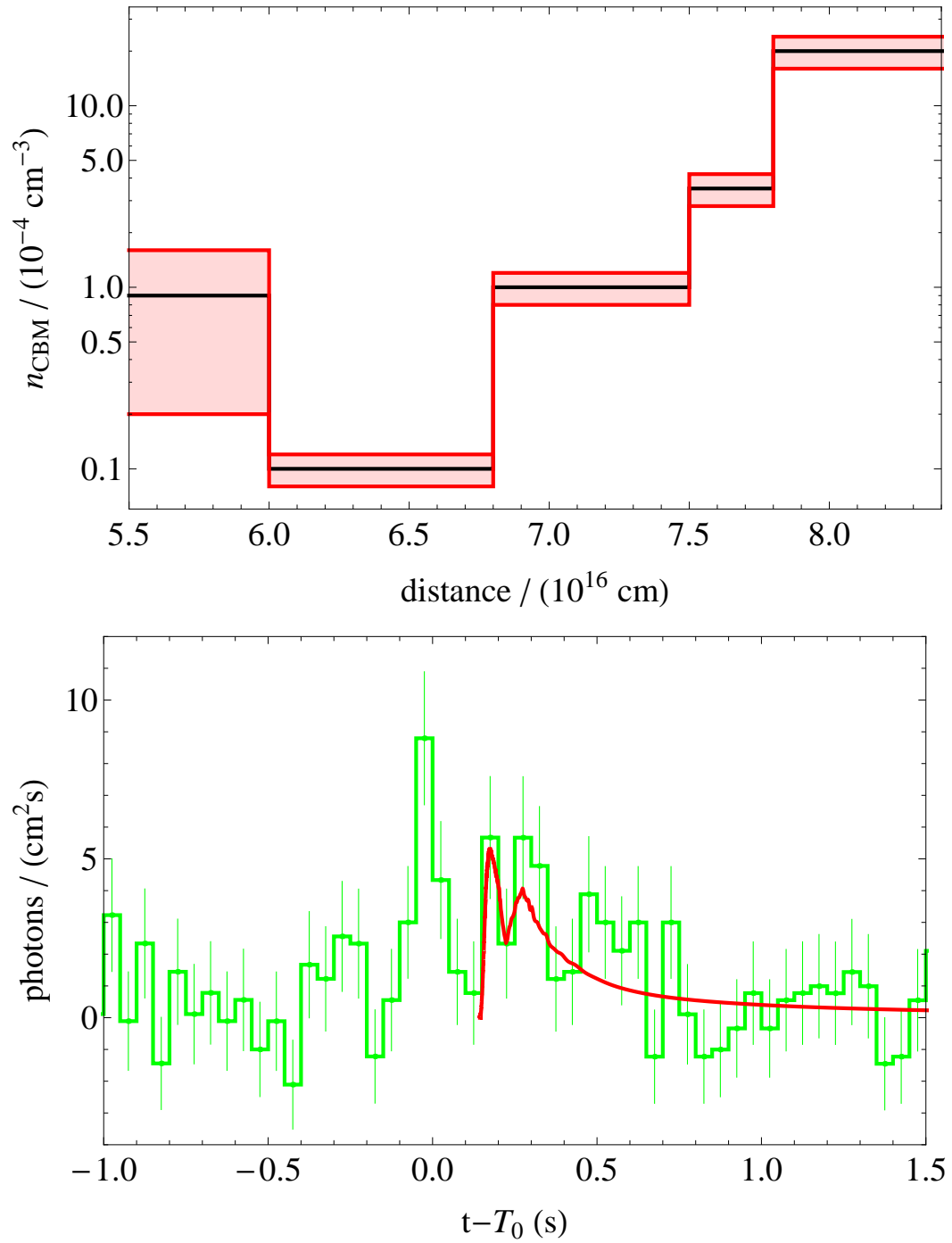
Figure 2.16. Results of the prompt emission simulation of the S-GRB 081024B. Top: the CBM number density (black line) and errors (red shaded region). Bottom: comparison between the simulated prompt emission light curve (solid red curves) and the NaI-n9 (8–900 keV) data. Plot reproduced from [12].
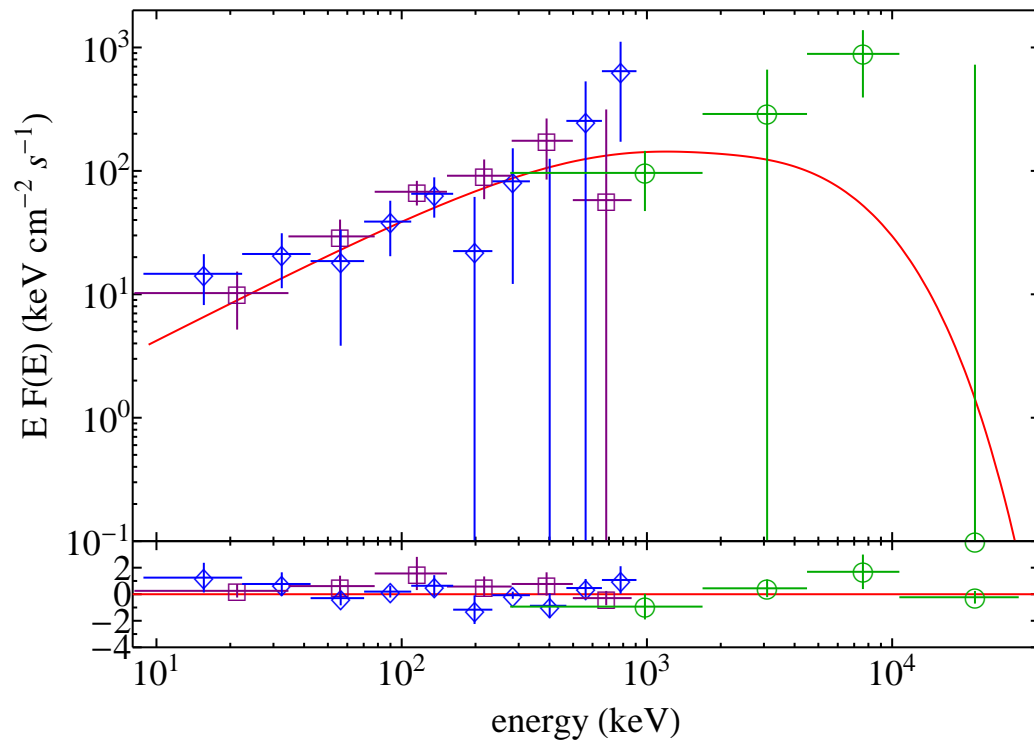
Figure 2.17. Results of the prompt emission simulation of the S-GRB 081024B. Comparison between the simulated spectrum (solid red curve) and the NaI-n6 (purple squares), NaI-n9 (blue diamonds), and the BGO-b1 (green circles) spectra within the ΔT_2 time interval. The residuals are shown in the sub-plot. Plot reproduced from [12].
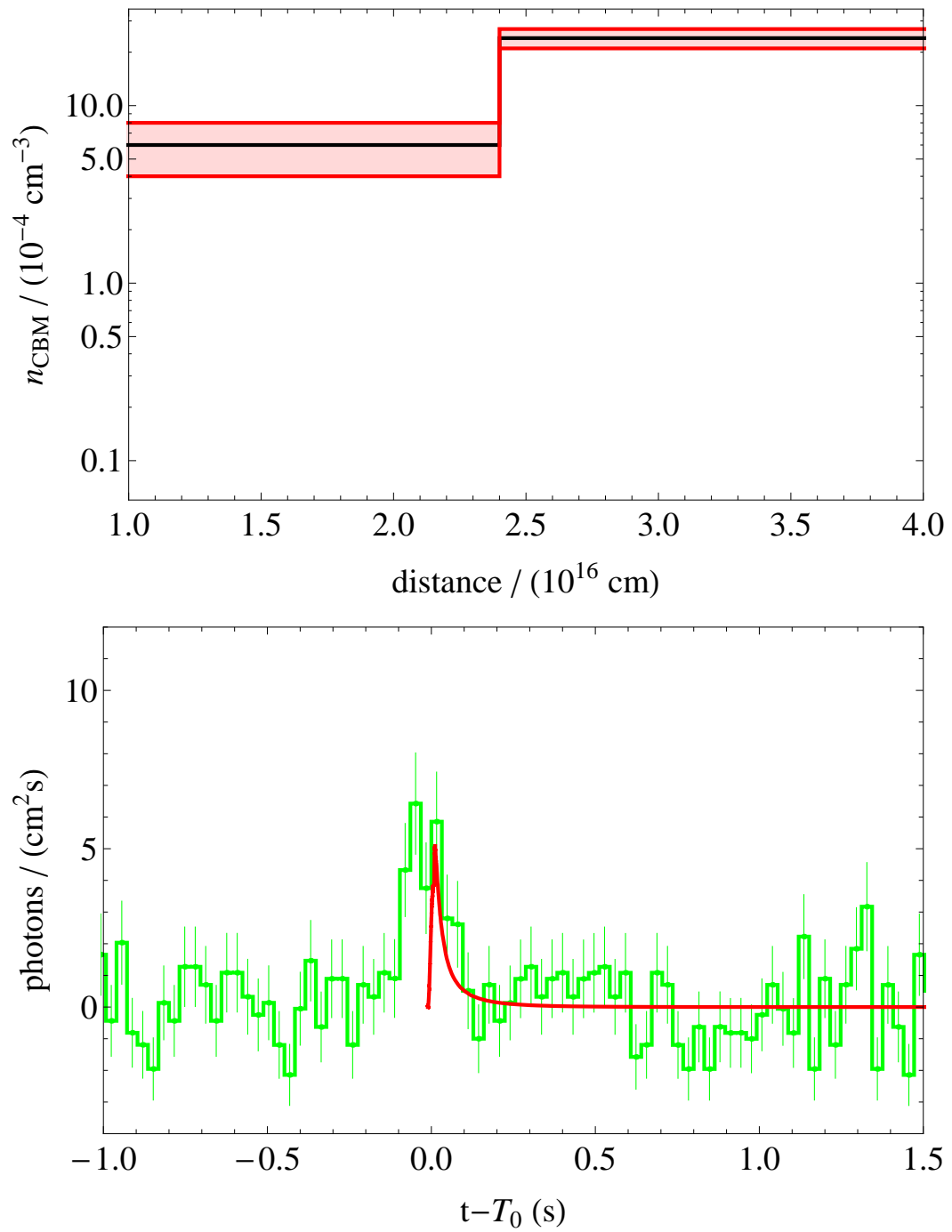
Figure 2.18. Results of the prompt emission simulation of the S-GRB 140402A. Top: the CBM number density (black line) and errors (red shaded region). Bottom: comparison between the simulated prompt emission light curve (solid red curves) and the BGO-b0 (0.26–40 MeV) data. Plot reproduced from [12].
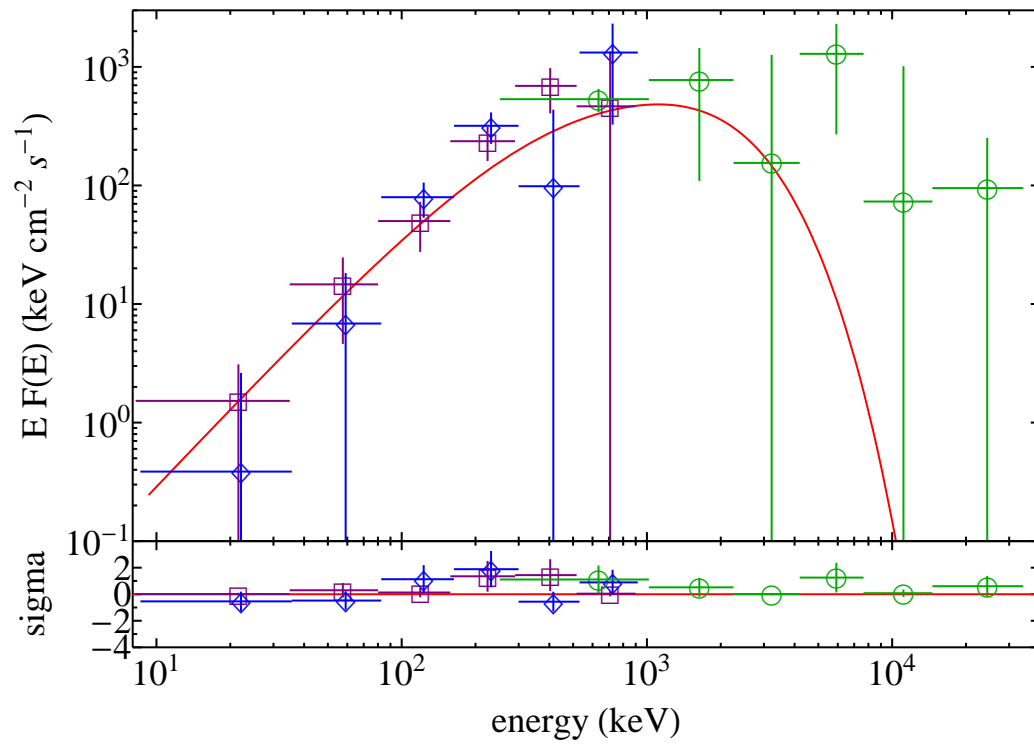
Figure 2.19. Results of the prompt emission simulation of the S-GRB 140402A. Comparison between the simulated spectrum (solid red curve) and the NaI-n1 (purple squares), NaI-n3 (blue diamonds), and the BGO-b0 (green circles) spectra within the ΔT_2 time interval. The residuals are shown in the sub-plot. Plot reproduced from [12].

The simulation of the prompt emission light curve of the BGO-b0 (0.26–40 MeV) data of GRB 140402A is shown in Figure 2.18 (lower panel). The simulation of the corresponding spectrum requires a phenomenological parameter $\bar{\alpha} = -0.9$. Figure 2.19 displays the agreement between the rebinned data from the ΔT_2 time interval with the simulation.

2.3 High-energy emission from S-GRBs

2.3.1 Clustering of luminosity light curves

We downloaded the LAT event and spacecraft data[8] selecting the observational time, the energy range and the source coordinates [42]. We then made cuts on the dataset time and energy range, position, region of interest (ROI) radius (typically 10º), and maximum zenith angle.[9] Within the event selection recommendations for the analysis of LAT data using the *Pass 8 Data* (`P8R2`) we adopted the *Transient* analysis (for events lasting < 200 s) with an energy selection of 0.1–500 GeV, a ROI-based zenith angle cut of 100º, an event class 16, and the instrument response function `P8R2_TRANSIENT020_V6`.[10] The additional selection of the good time intervals (GTIs) when the data quality is good (`DATA_QUAL>0`) is introduced to exclude time periods when some spacecraft event has affected the quality of the data (in addition to the time selection to the maximum zenith angle cut introduced above). Additionally to event selection we have used the standard Galactic interstellar emission model `gll_iem_v06` and isotropic model `iso_P8R2_SOURCE_V6_v06` to describe the diffuse background emission in gamma range.[11]

In the case of the S-GRB 081024B, we obtained the GeV light curve and the observed photon energies showed in Figure 2.5 (third and fourth panels), which are in agreement with those reported by *Fermi*-LAT group [10]. In the case of the S-GRB 140402A, we obtained the GeV light curve showed in Figure 2.10 (upper panel). About 20 photons with energies higher than 0.1 GeV have been detected within 100 s after the GBM trigger (Figure 2.10, lower panel). The highest energy photon is a 3.7 GeV event which is observed at $T_0 + 8.7$ s.

Then, using the values of theoretically derived redshift we built up the rest-frame 0.1–100 GeV light curves of the S-GRBs 081024B and 140402A. For the S-GRB 081024B, we rebinned its GeV emission luminosity light curve into two bins, as displayed in [10]. For the S-GRB 140402A, we rebinned it into two time bins with number of photons enough to perform a spectral analysis: from T_0 to $T_0 + 0.6$ s, and from $T_0 + 0.6$ s to $T_0 + 20$ s. The resulting luminosity light curves follow a common power-law trend with the rest-frame time which goes as $t^{-1.29 \pm 0.06}$ (dashed black line in Figure 2.20). All the light curves are shown from the burst trigger times on, while in the case of the S-GRB 090510 it starts after the precursor emission, i.e., from the P-GRB emission on, see [470]. The GeV emission of the S-GRB 140402A is the second longest in time duration after GRB 090510, which exhibits a common behavior with the light curves of the other S-GRBs after ~ 1 s in the rest-frame.

Table 2.4 lists the redshift z, the spectral peak energy $E_{\mathrm{p,i}}$, the isotropic-equivalent energy E_{iso} (1–10 000 keV), and the GeV isotropic emission energy E_{LAT} (0.1–100 GeV) of the five authentic S-GRBs discussed here. These values of E_{LAT} are simply obtained by multiplying the average luminosity in each time bin by the corresponding rest-frame duration and, then, by summing up all the contributions

---

[8] `http://fermi.gsfc.nasa.gov/cgi-bin/ssc/LAT/LATDataQuery.cgi`

[9] The maximum zenith angle selection excludes any portion of the ROI which is too close to the Earth's limb, resulting in elevated background levels.

[10] `http://fermi.gsfc.nasa.gov/ssc/data/analysis/documentation/Cicerone/Cicerone_Data_Exploration/Data_preparation.html`

[11] `https://fermi.gsfc.nasa.gov/ssc/data/access/lat/BackgroundModels.html`
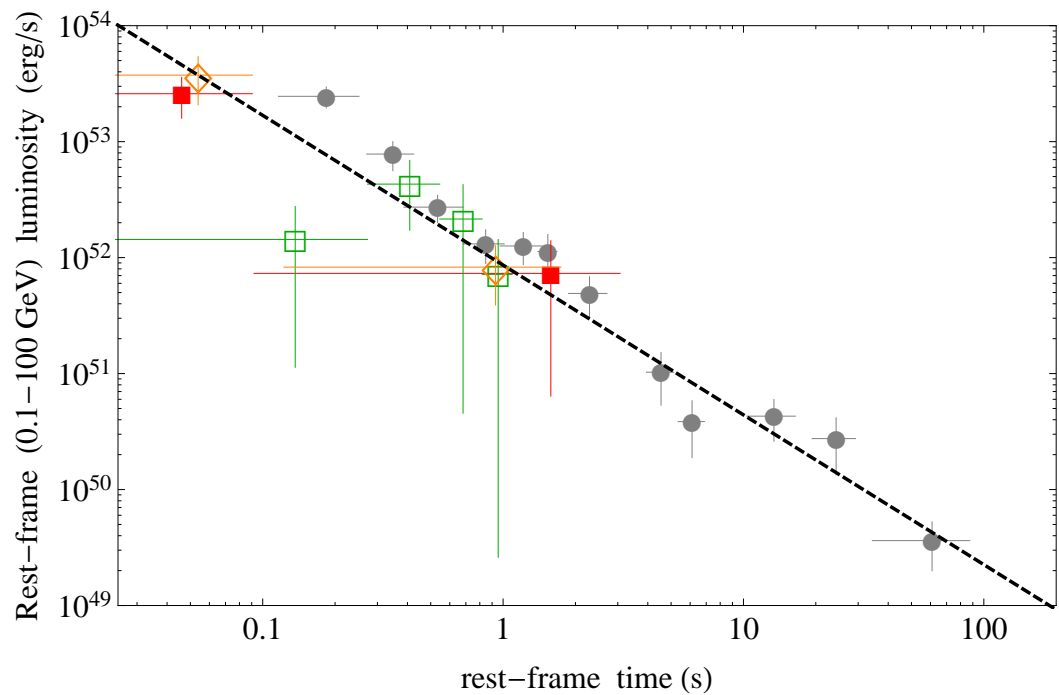
Figure 2.20. The rest-frame 0.1–100 GeV luminosity light curves of the S-GRBs: 081024B (orange empty diamonds), 090510 (gray filled circles), 140402A (red filled squares), and 140619B (green empty squares). All the light curves are shown from the burst trigger times on, while in the case of the S-GRB 090510 it starts after the precursor emission, i.e., from the P-GRB emission on (see for details [470]). The dashed black line marks the common behavior of all the S-GRB light curves which goes as $t^{-1.29\pm0.06}$. Plot reproduced from [12].

for each bin. However, these estimates represent lower limits to the actual GeV isotropic emission energies, since at late times the observations of GeV emission could be prevented due to instrumental threshold of the LAT instrument.

2.3.2 Lower limits on the Lorentz factors in S-GRBs

Following Lithwick & Sari (2001) [292], it is possible to derive a lower limit on the Lorentz factor of the GeV emission $\Gamma_{\mathrm{GeV}}^{\mathrm{min}}$. The basic idea is that photon pairs have energies sufficient to annihilate and create pairs of electron and positron.

By requiring the optical depth τ for the observed photon with maximum energy $E_{\mathrm{GeV}}^{\mathrm{max}}$ to be smaller than unity we have a lower limit of Lorentz factor:

$$\Gamma_{\mathrm{GeV}}^{\mathrm{min}} \gtrsim \hat{\tau}^{\frac{1}{2\alpha+2}} \left(\frac{E_{\mathrm{GeV}}^{\mathrm{max}}}{m_e c^2} \right)^{\frac{\alpha-1}{2\alpha+2}} (1+z)^{\frac{\alpha-1}{\alpha+1}} \, , \tag{2.4}$$

where the index α of the photon spectrum $fE^{-\alpha}$ has typical value between 2 and 3. Here m_e is a mass of electron, c is a speed of light, z is a redshift of the object. The factor $\hat{\tau}$ is defined as

$$\hat{\tau} \equiv \frac{(11/180)\sigma_{\mathrm{T}} \, d^2 (m_e c^2)^{-\alpha+1} f}{c^2 \, \delta T (\alpha-1)} \, , \tag{2.5}$$

where the factor $(11/180)\sigma_{\mathrm{T}}$ is an averaged cross section, d is a luminosity distance, f is a normalization factor of the photon spectrum.

Using the maximum GeV photon observed energy $E_{\mathrm{GeV}}^{\mathrm{max}}$ in Table 2.4, for each S-GRB various lower limits on the GeV Lorentz factors can be derived from the time resolved spectral analysis. For each S-GRB we estimate lower limits in each time interval of the GeV luminosity light curves in Figure 2.20. Then, $\Gamma_{\mathrm{GeV}}^{\mathrm{min}}$ for each S-GRB has been then determined as the largest among the inferred lower limits (see Table 2.4). The GeV photons are produced in ultrarelativistic outflows with $\Gamma_{\mathrm{GeV}}^{\mathrm{min}} \gtrsim 300$.

2.4 Discussion

2.4.1 Sufficiency of energy budget for high-energy emission

It was proposed in [470] that the 0.1–100 GeV emission in S-GRBs (Figure 2.20) is produced by the mass accretion onto the newborn KNBH. The amount of mass that remains bound to the BH is given by the conservation of energy and angular momentum from the merger moment to the BH birth. We can estimate lower limits of the needed mass to explain the energy requirements for E_{LAT} in Table 2.4 by considering the above accretion process onto a maximally rotating Kerr BH. In this case, depending whether the infalling material is in co- or counter-rotating orbit with the spinning BH, the maximum efficiency of the conversion of gravitational energy into radiation is $\eta_+ = 42.3\%$ or $\eta_- = 3.8\%$, respectively (see book Ruffini & Wheeler 1969, in problem 2 of § 104 in [274]). Therefore, E_{LAT} can be expressed as

$$E_{\mathrm{LAT}} = f_{\mathrm{b}}^{-1} \eta_{\pm} M_{\mathrm{acc}}^{\eta_{\pm}} c^2 \, , \tag{2.6}$$

where $f_{\rm b}$ is the beaming factor which depends on the geometry of the GeV emission, and $M_{\rm acc}^{\eta\pm}$ is the amount of accreted mass corresponding to the choice of the efficiency $\eta_\pm$.

The claim that energetic S-GRBs should exhibit GeV emission follows from the central engine activity [478]. That means nothing but the fact that we consider GeV photons as coming from central engine directly, and not as a propagation of initial fireball plasma with beaming factor which further creates GeV photons on the go through burst environment via forward shock mechanism. Further we claim that the absence of GeV photons for some energetic bursts with LAT boresight $\theta < 75°$ is due to geometrical effects of the GeV photons production site, i.e., there is in fact some kind of geometrical/colimation effect, but again not coming from the main prompt emission. Then it will be possible to calculate half-opening angle for such a "beaming" and it will be a conservative point to say that "in some cases we do not see GeV photons due to geometrical effects of the emission site". And this independence between prompt emission and GeV emission sites will go in accordance with non-observability of the latter in some, at first sight, plausible conditions, see Chapter 4. This suggests that no beaming is necessary in Equation (2.6). Therefore, in the following we set fb $\equiv$ 1. The corresponding estimates of $M_{\rm acc}^{\eta\pm}$ in our sample of S-GRBs are listed in Table 2.4

2.4.2   On the detectability of the X-ray emission of S-GRBs

Since *Swift* launch in 2004 there were over one thousand events followed[12] by its XRT instrument. In general the population of long bursts forms a significant majority of that list. Short GRBs have fewer x-ray afterglow follow-ups and the reasons are mainly thought to be due either to instrumental difficulties such as a fast slewing or reflection of local properties such as low explosion energies and low circumburst densities or their combination. Fong et al. (2015) [156] report on 71 x-ray detections within a time span 2004–2015. So we can estimate that around 10% of observed x-ray afterglows belong to short bursts and the rest consists of counterparts of long duration events.

In our approach we gradually frame the efforts towards a problem of high-energy emission from GRBs. Hence, individual bursts we peak to analyze, in general, should manifest a presence of GeV energy photons. Making this as a sampling criterion we can look again at detection statistics. Then regarding the x-ray afterglow of short GRBs with high-energy emission we find the following: there are 17 short events within a decade of *Fermi* operation [13], see Table 2.7. Nearly half of them were observed by *Swift*-XRT instrument either in trigger mode or by ToO request from other telescopes. Only three cases show x-ray afterglow detection while others get upper limit. Systematically cases with a positive detection are correlated with early observation of a still strong signal and contrary non-detections are probably due to the signal decayed below threshold at late observations.

GRB 090510 is the only S-GRB with high-energy emission having a complete X-ray afterglow [470], Figure 2.21(a). Only upper limits exist for the X-ray afterglow emission of the other S-GRBs with GeV photons and no special features are

---

[12] https://www.swift.ac.uk/xrt_products/index.php?year=ALL

GRB	T_{90}	X-ray	Obs time	GRB	T_{90}	X-ray	Obs time
	(s)		T_0+ ($\times 10^3$ s)		(s)		T_0+ ($\times 10^3$ s)
180703B	1.54	–	–	110728A	0.70	–	–
171011C	0.48	–	–	110529A	0.51	–	–
170127C	0.13	N	61.2–77.4	090531B	0.77	Y	6.1–26.5
160829A	0.51	N	37.4–61.4	090510A	0.96	Y	0.09–25.0
160702A	0.20	–	–	090228A	0.45	–	–
141113A	0.45	–	–	090227B	0.30	–	–
140402A	0.32	N	33.3–51.2	081102B	1.73	Y	0.1–16.0
120915A	0.58	–	–	081024B	0.64	N	70.3–1304.6
120830A	0.90	N	60.0–133.0			–	

Table 2.7. Short GRBs with high-energy photons within 2008–2018 and with information on x-ray afterglow observations. Signs "Y", "N" and "–" stand respectively for "detected", "not detected" and "not observed" regarding x-ray afterglow by XRT instrument. Observation time is indicated from T_0 trigger moment. Numbers were retrieved from online *Fermi*-GBM Burst Catalog, The second *Fermi*-LAT GRB Catalog, UK *Swift* Data Centre website, webpage by Jochen Greiner and `GCN` Circulars.

identifiable.

As an example to evidence the difficulty of measuring the X-ray afterglow in S-GRBs, we computed the observed X-ray flux light curve of GRB 090510, actually observed at $z_{\text{in}} = 0.903$, as if it occurred at the redshifts of the other S-GRBs, i.e., $z_{\text{fin}} = 1.61, 2.67, 3.12$, and 5.52. This can be attained through four steps.

(1) In each time interval of the X-ray flux light curve $f_{\text{obs}}^{\text{in}}$ of GRB 090510, we assume that the best fit to the spectral energy distribution is a power-law function with photon index γ, i.e., $N(E) \sim E^{-\gamma}$.

(2) In the rest-frame of GRB 090510, we identify the spectral energy range for a source at redshift z_{fin} which corresponds to the 0.3–10 keV observed by *Swift*-XRT, i.e.,

$$\text{from} \;\; 0.3 \times \left(\frac{1+z_{\text{fin}}}{1+z_{\text{in}}} \right) \text{keV} \;\; \text{to} \;\; 10 \times \left(\frac{1+z_{\text{fin}}}{1+z_{\text{in}}} \right) \text{keV} \;.$$

(3) We rescale the fluxes for the different luminosity distance d_{l}. Therefore, the observed 0.3–10 keV X-ray flux light curve $f_{\text{obs}}^{\text{fin}}$ for a source at redshift z_{fin} is given by

$$
\begin{aligned}
f_{\text{obs}}^{\text{fin}} &= f_{\text{obs}}^{\text{in}} \left[\frac{d_{\text{l}}(z_{\text{in}})}{d_{\text{l}}(z_{\text{fin}})} \right]^2 \frac{\displaystyle\int_{0.3\frac{1+z_{\text{fin}}}{1+z_{\text{in}}} \text{keV}}^{10\frac{1+z_{\text{fin}}}{1+z_{\text{in}}} \text{keV}} N(E) E \, dE}{\displaystyle\int_{0.3\,\text{keV}}^{10\,\text{keV}} N(E) E \, dE} = \\
&= f_{\text{obs}}^{\text{in}} \left[\frac{d_{\text{l}}(z_{\text{in}})}{d_{\text{l}}(z_{\text{fin}})} \right]^2 \left(\frac{1+z_{\text{fin}}}{1+z_{\text{in}}} \right)^{2-\gamma} .
\end{aligned}
\tag{2.7}
$$

(4) We transform the observational time t_{in} of GRB 090510 at z_{in} into the observational time t_{fin} for a source at z_{fin} by taking into account the time dilation
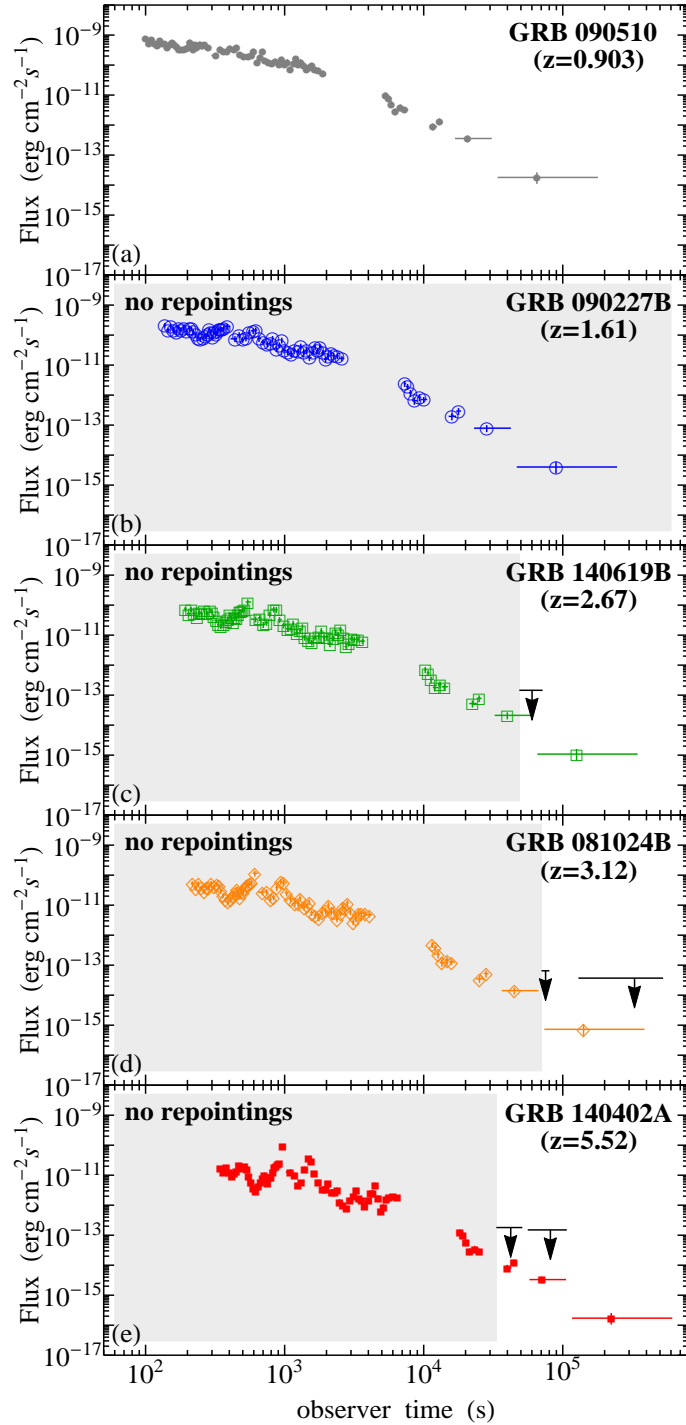
Figure 2.21. The observed 0.3–10 keV energy flux light curves of (a) the S-GRB 090510, located at $z_{in} = 0.903$, and the corresponding predicted ones for the S-GRBs (b) 090227B at $z_{in} = 1.61$, (c) 140619B at $z_{in} = 2.67$, (d) 081024B at $z_{in} = 3.12$, and (e) 140402A at $z_{in} = 5.52$ (same symbols as in Figure 2.20. The shaded areas correspond to the epochs before the observational upper limits set by the available *Swift*-XRT repointings (black arrows, see text for details). Plot reproduced from [12].

due to the cosmological redshift effect, i.e.,

$$t_{\text{fin}} = \left(\frac{1 + z_{\text{fin}}}{1 + z_{\text{in}}} \right) t_{\text{in}}. \tag{2.8}$$

Figure 2.21 shows that all the computed flux light curves are well below the observational upper limits provided by the *Swift*-XRT repointings.

- S-GRB 090227B, no repointings, Figure 2.21(b).

- S-GRB 140619B, a repointing from 48.7 to 71.6 ks after the GBM trigger with an upper limit of 2.9×10^3 count/s, see [319] and Figure 2.21(c).

- S-GRB 081024B, two repointings within the flux light curve in Figure 2.21(d). Each upper limit was set by using the lowest count rate among those of the uncatalogued sources within the LAT FoV, later on confirmed as not being the burst X-ray counterparts: the first one at ~ 70.3 ks after the trigger for ~ 9.9 ks with a count rate of 1.3×10^{-3} counts/s [208]; the second one from 1.5 to 6.1 days with an average count rate of 7.4×10^{-4} counts/s [206].

- S-GRB 140402A, two repointings [391]: the first from 33.3 to 51.2 ks with a count rate upper limit of 3.6×10^{-3} counts/s; the second from 56 to 107 ks with an upper limit of 3.0×10^{-3} counts/s, Figure 2.21(d).

We converted the above count rate upper limits in fluxes by multiplying for a typical conversion factor 5×10^{-11} erg/cm^2/counts [392].

We conclude that there is no evidence in favor or against a common behavior of the X-ray afterglows of the S-GRBs in view of the limited observations.

These aspects are noteworthy since in the case of long GRBs the X-ray emission has a very crucial role [421, 472], which is not testable in the case of S-GRBs.

Chapter 3

X-Ray Flares in GRBs

We deal with fits to the flares—a non-regular structural features in early X-ray afterglow—in a sample of GRBs and argue that the origin of these flares is a collision between GRB emission and supernova ejecta. A key results of this section are the presence, location, and associated Lorentz factor of the X-ray flares and their subsequent interpretation.

An emission from gamma-ray bursts that occurs within the x-ray band (0.1–100 keV) is traditionally named as an *afterglow*, since typical time of detection delayed by seconds to minutes with respect to trigger-causing soft γ-ray emission (> 100 keV), and what is more important the afterglow emission lasts minutes to hours after the main burst.

The investigation on x-ray afterglow structure arose with a possibility to actually see that structural dependencies and follow their temporal and spectral patterns.

We analyze the early X-ray flares in the "Flare-Plateau-Afterglow" (FPA) phase of GRBs observed by XRT instrument onboard of *The Neil Gehrels Swift Observatory*. Previous work had shown that gamma-ray spikes in the prompt emission occur at $\sim 10^{15}$–10^{17} cm with Lorentz gamma factor $\Gamma \sim 10^2$–10^3. Using a novel data analysis we show that the time of occurrence, duration, luminosity and total energy of the X-ray flares correlate with $E_{\rm iso}$. A crucial feature is the observation of thermal emission in the X-ray flares that occurs at radii $\sim 10^{12}$ cm with $\Gamma \lesssim 4$.

Context and aim

With the increase in the number of observed GRBs, an attempt was made to analyze the X-ray flares and other processes considered to be similar in the observer reference frame, independent of the nature of GRB type and of the value of their cosmological redshift or the absence of such a value. The goal was to identify their properties, following a statistical analysis methodology often applied in classical astronomy ([82, 146, 312] as well as the review articles [418, 419, 341, 342, 35, 270]). We now summarize our approach, the background for the observational identification and the theoretical interpretation of the X-ray flares.

As the first step, we only consider GRBs with an observed cosmological redshift. Having ourselves proposed the classification of all GRBs into seven different subclasses

[471], we have given preliminary attention to verifying whether X-ray flares actually occur preferentially in some of these subclasses and if so, to identify the physical reasons determining such a correlation. We have analyzed all X-ray flares and found *a posteriori* that X-ray flares only occur in BdHNe. No X-ray flare has been identified in any other GRB subclass, either long or short.

As the second step, since all GRBs have a different redshift values z, in order to compare them we need a description of each one of them in its own cosmological rest frame. The luminosities have to be estimated after doing the necessary K-correction and the time coordinate in the observer frame has to be corrected by the cosmological redshift $t_a^d = (1 + z)t_a$.

As a third step, we recall an equally important distinction from the traditional fireball approach with a single ultra relativistic jetted emission. Our GRB analysis envisages the existence of different episodes within each GRB, each one characterized by a different physical process and needing the definition of its own world-line and corresponding gamma factors, essential for estimating the time parametrization in the rest-frame of the observer (see Sec.).

These three steps are applied specifically to the study of the early X-ray flares and their fundamental role in establishing the physical and astrophysical nature and in distinguishing our binary model from the traditional one.

3.1   Sample selection and analysis

The early x-ray flares

We turn now to the selection procedure for the early X-ray flares. We take the soft X-ray flux light curves of each source with known redshift from the *Swift*-XRT repository [143, 144]. We then apply the K-correction (see Appendix A) to obtain the corresponding luminosity light curves in the rest frame 0.3–10 keV energy band. Starting from 421 *Swift*-XRT light curves, we found in 50 sources X-ray flare structures in the early 200 s. We further filter our sample by applying the following criteria:

1. We exclude GRBs with flares having low (< 20) signal to noise ratio (SNR), or with an incomplete data coverage of the early X-ray light curve—14 GRBs are excluded (see, e.g., Figure 3.1).

2. We consider only X-ray flares and do not address here the gamma-ray flares—8 GRBs having only gamma-ray flares are temporarily excluded (see, e.g., Figure 3.3). In Figure 3.2 we show an illustrative example of the possible co-existence of a X-ray flare and a gamma-ray flare, and a way to distinguish them.

3. We also neglect here the late X-ray flare, including the ultra-long GRBs—6 GRBs are consequently excluded.

4. We neglect the GRBs for which the soft X-ray energy observed by *Swift*-XRT (0.3–10 keV) before the plateau phase is higher than the gamma-ray energy observed by *Swift*-BAT (15–150 keV) during the entire valid *Swift*-BAT
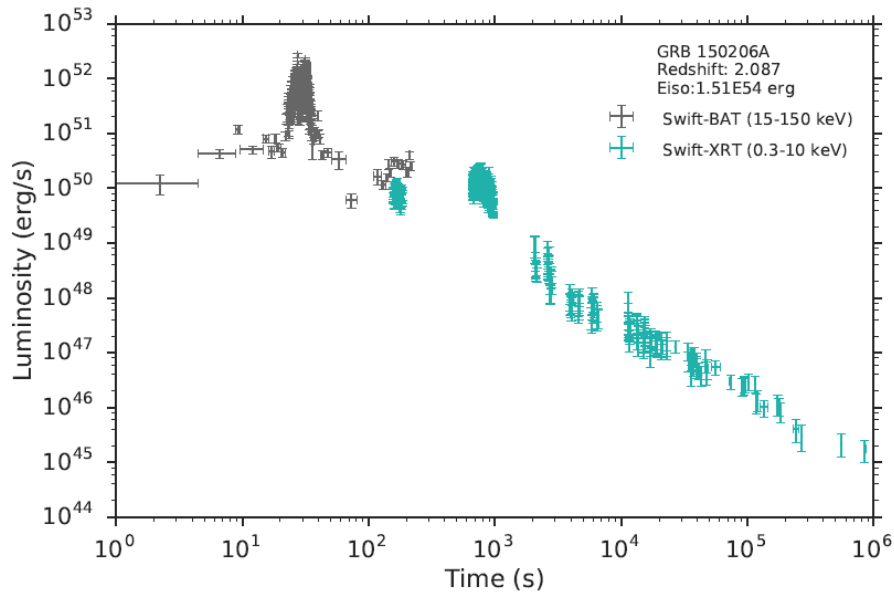
Figure 3.1. GRB 150206A is an example of a GRB with incomplete data, which therefore must be excluded. It only has 30 s *Swift*-XRT observations in the early 300 s. The flare determination is not possible under these conditions. Plot reproduced from [472].
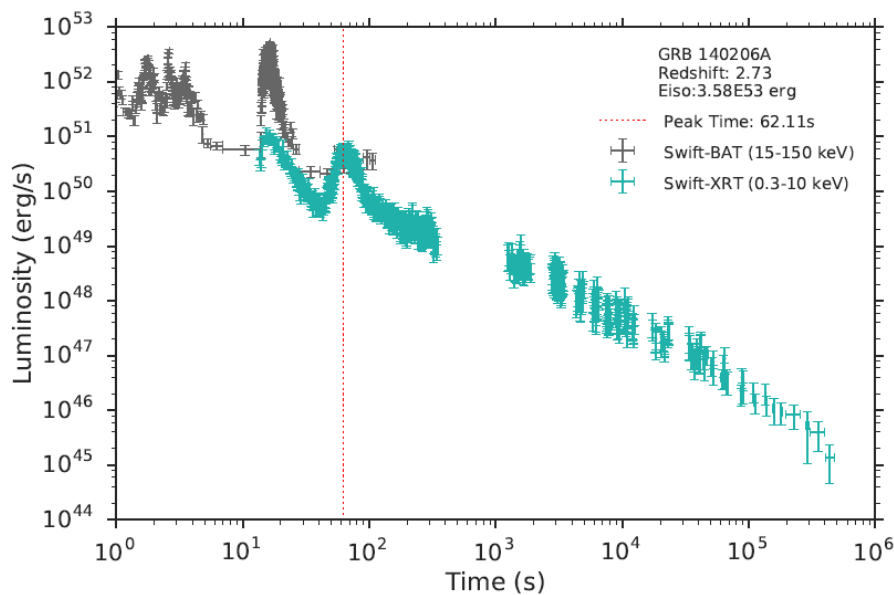
Figure 3.2. GRB 140206A has two flares. A gamma-ray flare coincides with the first flare while it is dim in the second one. The spectral analysis, using both *Swift*-XRT and *Swift*-BAT data, indicates a power-law index -0.88 ± 0.03 for the first flare. While the second flare requires an additional blackbody component; its power-law index is -1.73 ± 0.06 and its blackbody temperature is 0.54 ± 0.07 keV. Clearly, the energy of the first flare is contributed mainly by gamma-ray photons—it is a gamma-ray flare, and the second flare is an X-ray flare that we consider in this article. Plot reproduced from [472].
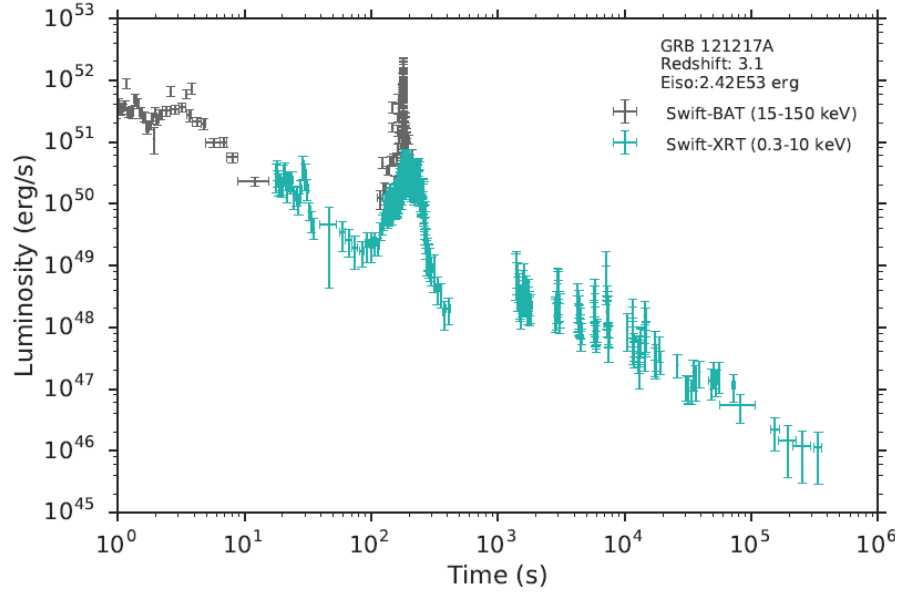
Figure 3.3. GRB 121217A shows a gamma-ray flare observed by *Swift*-BAT which coincides with a soft X-ray component observed by *Swift*-XRT. From the spectral analysis, it has a soft power-law photon index, and most of the energy deposited in high energy gamma-rays. This is an indication that the soft X-ray component is likely the low energy part of a gamma-ray flare. For these reasons, we neglect it in our sample. Plot reproduced from [472].
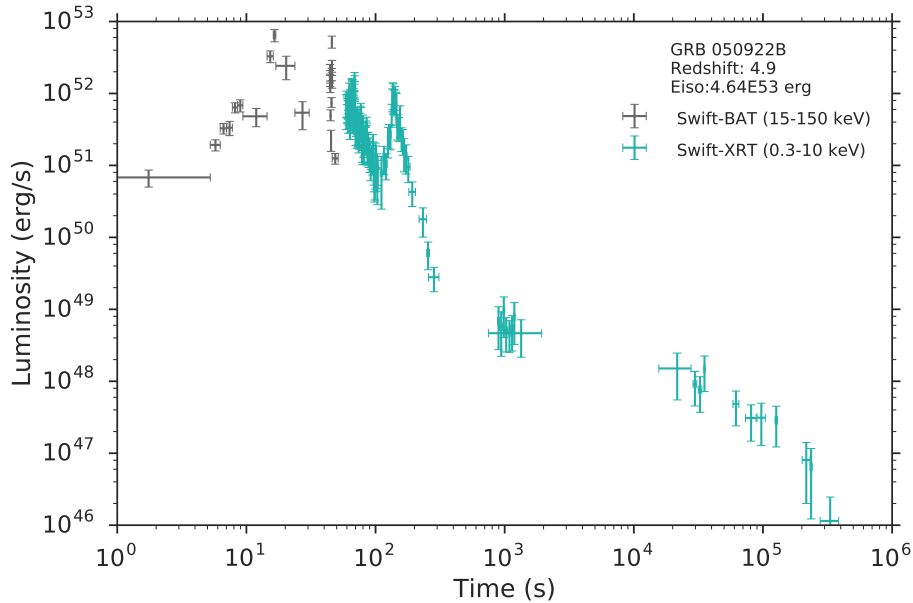
Figure 3.4. The *Swift*-BAT data of GRB 050922B has poor resolution, it cannot provide valid information after 50 s; the energy observed in its energy band 15–150 keV during this 50 s duration is 1.19×10^{53} erg. The energy observed by *Swift*-XRT is higher; the energy of the flares $(60 - 200$ s) in the *Swift*-XRT band 0.3–10 keV is 3.90×10^{53} erg. These results imply that the *Swift*-BAT observations may not cover the entire prompt emission phase; the isotropic energy computed from the *Swift*-BAT data is not reliable, consequently the *Swift*-XRT observed partial prompt emission which brings complexity to the X-ray light curve and makes the identification of the authentic X-ray flare more difficult. Plot reproduced from [472].

observation. This *Swift*-BAT anomaly points to an incomplete coverage of the prompt emission—6 GRBs are excluded (see, e.g., Figure 3.4).

Finally, we have found 16 GRBs satisfying all the criteria to be included in our sample. Among them, 7 objects show a single flare. The other 9 contain two flares: generally we exclude the first one, which appears to be a component from the gamma-ray spike or gamma-ray flare, and therefore select the second one for analysis (see, e.g., Figure 3.2).

These 16 selected GRBs cover a wide range of redshifts. The closest one is GRB 070318 with redshift $z = 0.84$, and the farthest one is GRB 090516A with redshift $z = 4.11$. Their isotropic energy is also distributed over a large range: 5 GRBs have energies of the order of 10^{52} erg, 9 GRBs of the order of 10^{53} erg, and 2 GRBs have extremely high isotropic energy $E_{\rm iso} > 10^{54}$ erg. Therefore, this sample is well-constructed although the total number is limited.

3.2 Luminosity light curves with flare emission

We now turn to the light curves of each one of the 16 GRBs composing our sample (Figures 3.5–3.20). Blue curves represent the X-rays observed by *Swift*-XRT, and green curves are the corresponding optical observations when available. All the values are in the rest-frame and the X-ray luminosities have been K-corrected. The red vertical lines indicate the peak time of the X-ray flares. The rest-frame luminosity light curves of some GRBs show different flare structures compared to the observed count flux light curves. An obvious example is GRB 090516A, as follows by comparing Figure 3.14 in this paper with Figure 1 in [525]. The details of the FPA, as well as their correlations or absence of correlation with $E_{\rm iso}$, are given in the next section.

We then conclude that in our sample, there are *Swift* data for all 16 GRBs, *Konus*-WIND observed 7 of them GRB 080607, 080810, 090516A, 131030A, 140419A, 141221A and 151027A, while Fermi detected 4 of them GRB 090516A, 140206, 141221A, 151027A. The energy coverage of the available satellites is limited: *Fermi* detects the widest photon energy band, from 8 keV to 300 GeV, *Konus*-WIND observes from 20 keV to 15 MeV, *Swift*-BAT has a narrow coverage from 15 keV to 150 keV.

No GeV photons were observed, though GRB 090516A and 151027A were in the *Fermi*-LAT field of view (FoV) [331, 521]. This contrasts with the observations of S-GRBs for which, in all of the sources so far identified and within the *Fermi*-LAT field of view, GeV photons were always observed [470, 471] and can always freely reach a distant observer. This observational fact could suggest that NS-NS (or NS-BH) mergers leading to the formation of a BH leave the surrounding environment poorly contaminated by the material ejected in the merging process ($\lesssim 10^{-2}$–$10^{-3}\ M_\odot$) and therefore the GeV emission, originating from accretion on the BH formed in the merger process [470] can be observed (see Section 2.3). On the other hand, BdHNe originate in $CO_{\rm core}$-NS binaries in which the material ejected from the $CO_{\rm core}$ explosion ($\approx M_\odot$) greatly pollutes the environment where the GeV emission has to propagate to reach the observer. This together with the asymmetries of the SN ejecta, see [33] lead to the possibility that the GeV emission in BdHNe can be
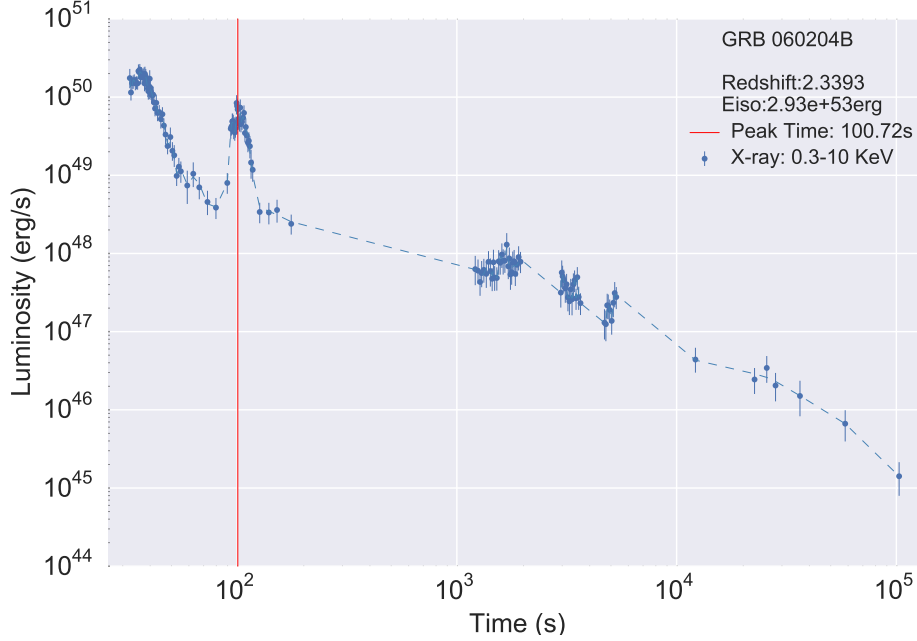
Figure 3.5. **GRB 060204B**: source has been detected by *Swift*-BAT [145]; *Swift*-XRT began observing 28.29 s after the BAT trigger. There is no observation from the *Fermi* satellite. X-shooter found its redshift at $z = 2.3393$ based on the host galaxy [414]. The isotropic energy of this GRB reaches $E_{\mathrm{iso}} = 2.93 \times 10^{53}$ erg computed from *Swift*-BAT data. Plot reproduced from [472].
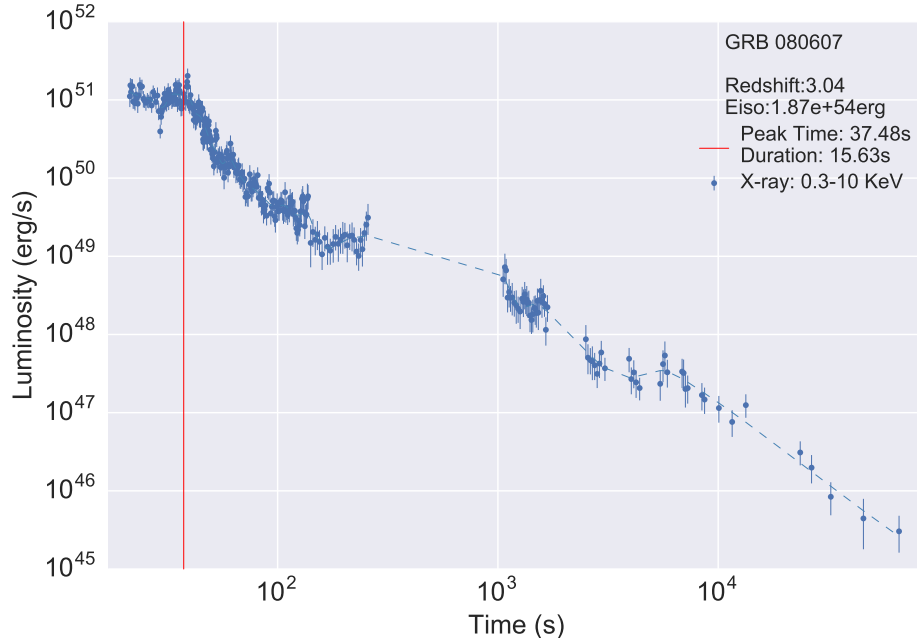
Figure 3.6. X-ray afterglow of GRB 080607: source has been observed by *AGILE* [313], *Konus*-WIND [182] and *Swift*-BAT [309]. *Swift*-UVOT detected only a faint afterglow, since the source is located at a redshift $z = 3.04$. The BAT prompt light curve shows a very pronounced peak that lasts ~ 10 s, followed by several shallow peaks until 25 s. The isotropic energy is $E_{\mathrm{iso}} = 1.87 \times 10^{54}$ erg. The *Swift* localization was at 113° off-axis with respect to the *AGILE* pointing, so well out of the FoV of the *AGILE* Gamma-Ray Imaging Detector (GRID), which does not show any detection. The *Konus*-WIND light curve (50–200 keV) shows a multiple peak emission lasting 15 s. Plot reproduced from [472].
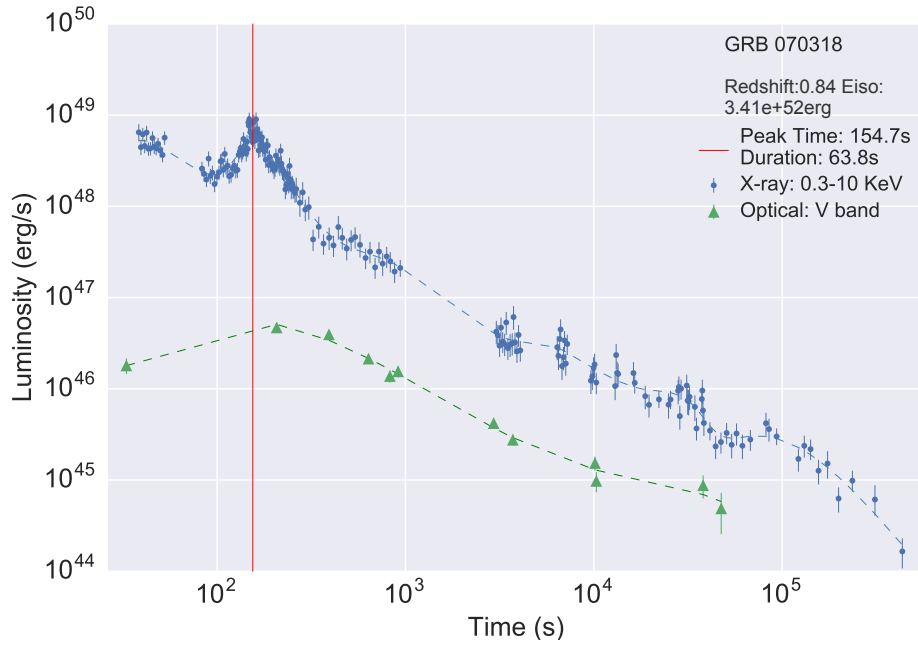
Figure 3.7. GRB 070318: source has been detected by the *Swift*-BAT [108]. It has a spectroscopic redshift of $z = 0.836$ [237]. The prompt light curve shows a peak with a typical fast-rise exponential-decay (FRED) behavior lasting ~ 55 s. The isotropic energy is $E_{\mathrm{iso}} = 3.64 \times 10^{52}$ erg. XRT began observation 35 s after the BAT trigger. From the optical observation at ~ 20 days, no source or host galaxy is detected at the position of the optical afterglow, indicating that the decay rate of the afterglow must have steepened after some hours [92]. Optical data is from [80]. Plot reproduced from [472].
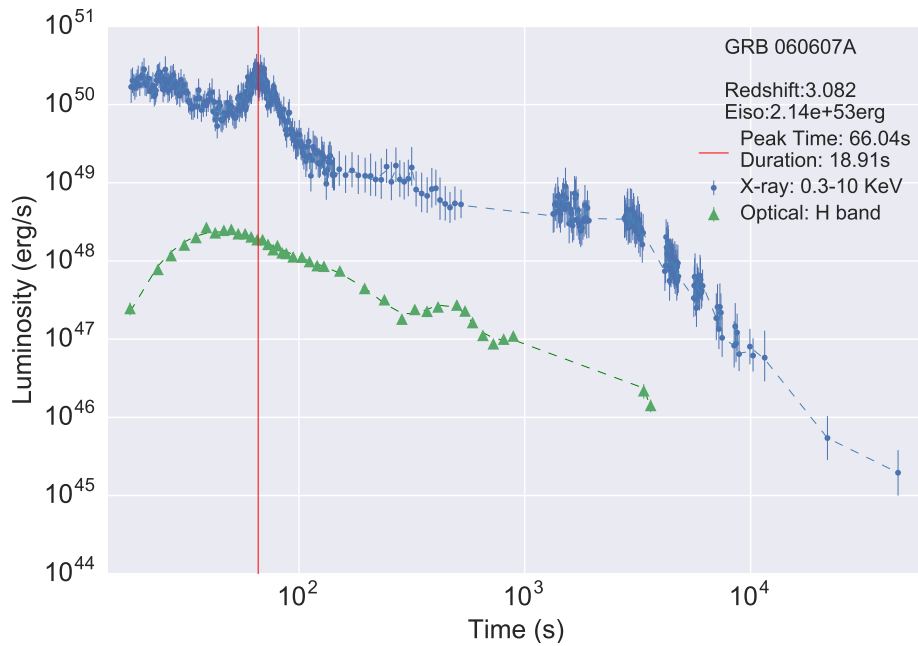
Figure 3.8. GRB 060607A: source has been detected by the Swift-BAT [596]. It has a bright optical counterpart. It is located at a redshift $z = 3.082$ [282]. The prompt light curve displays a double-peaked emission that lasts ~ 10 s, plus the second emission at ~ 25 s with 2.5 s duration. The isotropic energy is $E_{\mathrm{iso}} = 2.14 \times 10^{53}$ erg. Optical data is from [363]. Plot reproduced from [472].
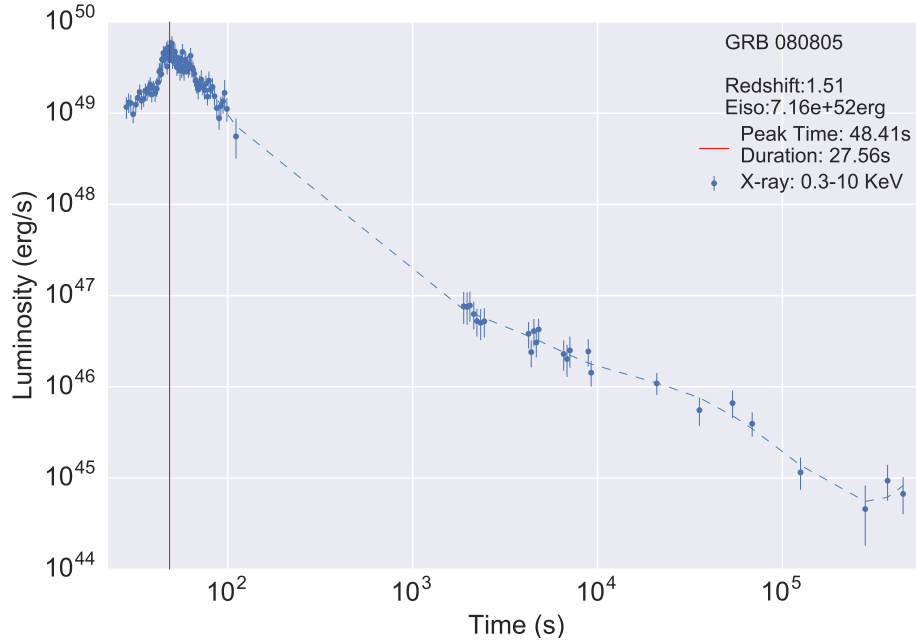
Figure 3.9. GRB 080805: source was detected by *Swift*-BAT [393]. The prompt light curve shows a peak with a FRED behavior lasting about 32 s. The redshift is $z = 1.51$, as reported by VLT [236], and the isotropic energy is $E_{\rm iso} = 7.16 \times 10^{52}$ erg. Plot reproduced from [472].
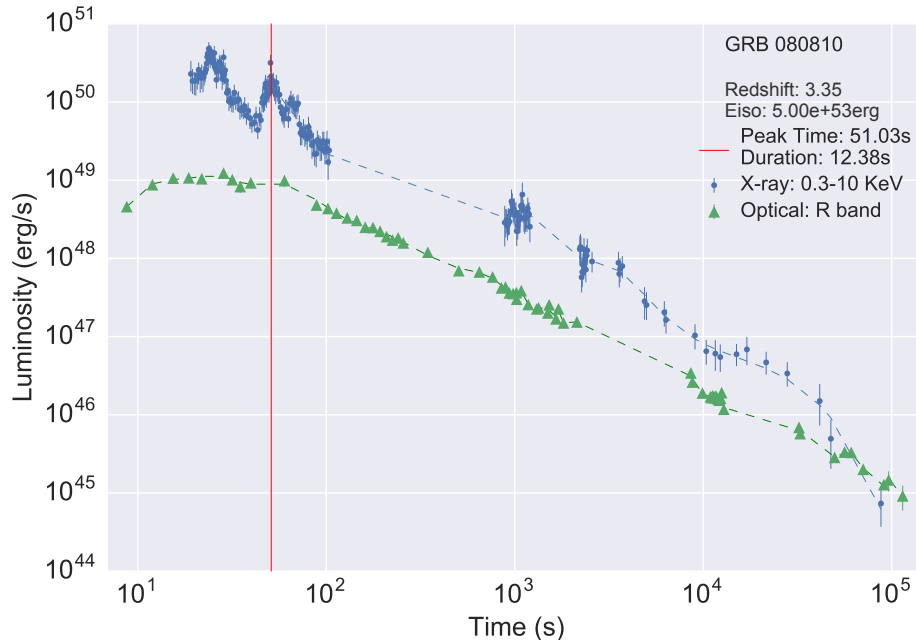
Figure 3.10. GRB 080810: source was detected by *Swift*-BAT [182]. The BAT light curve shows a multiple-peaked structure lasting ~ 23 s. XRT began observing the field 76 s after the BAT trigger. The source is located at a redshift of $z = 3.35$ and has an isotropic energy $E_{\rm iso} = 3.55 \times 10^{53}$ erg. Optical data is taken from [397]. Plot reproduced from [472].
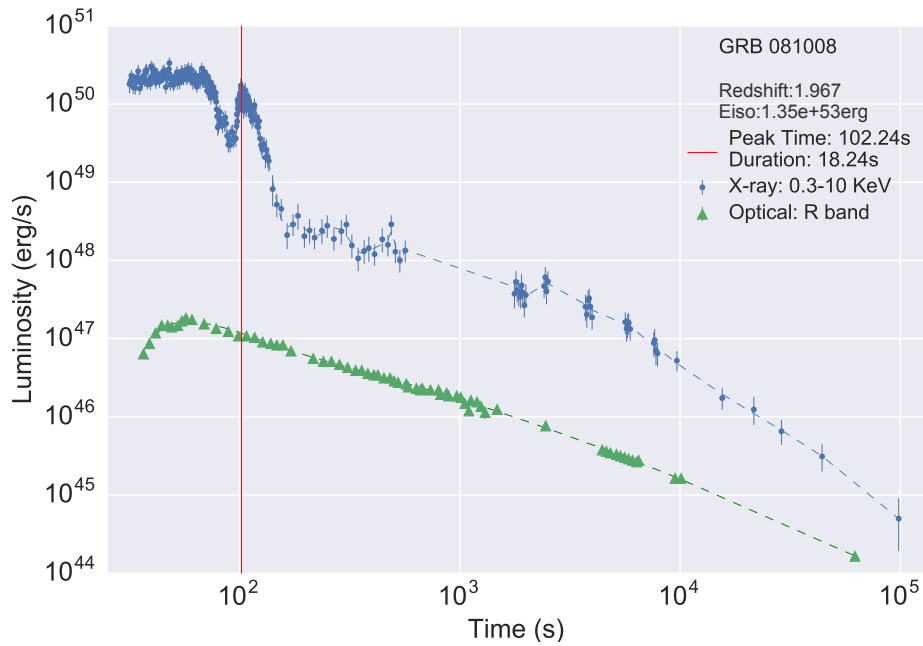
Figure 3.11. **GRB 081008**: source was detected by *Swift*-BAT [436]. The prompt emission lasts ~ 60 s and shows two peaks separated by 13 s. It is located at $z = 1.967$, as reported by VLT [114], and has an isotropic energy $E_{\mathrm{iso}} = 1.07 \times 10^{53}$ erg. Optical data is from [586]. Plot reproduced from [472].
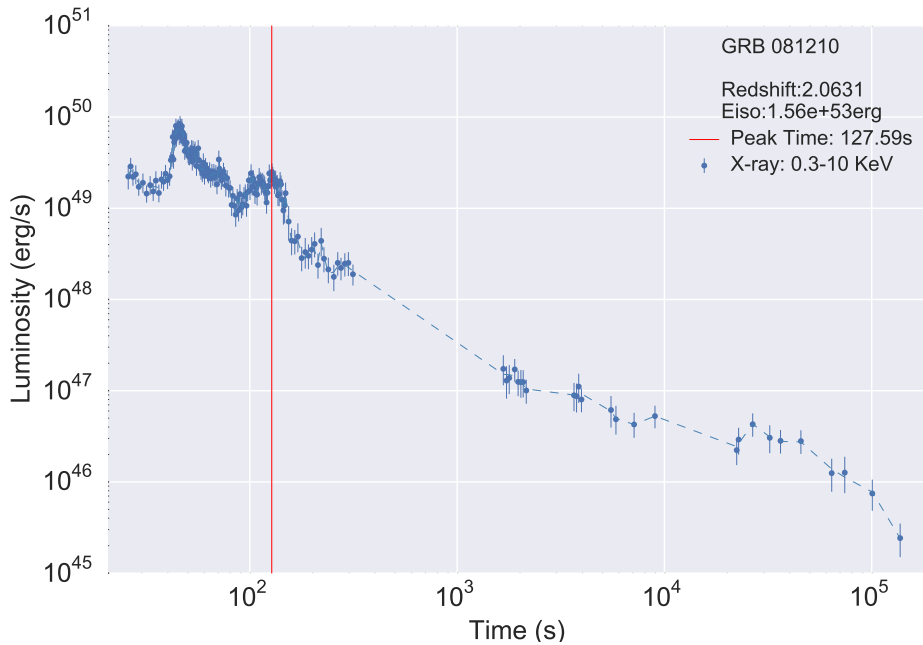
Figure 3.12. GRB 081210: source was detected by *Swift*-BAT [259], *Swift*-XRT began observing at 23.49 s after the BAT trigger. The BAT light curve begins with two spikes with a total duration ~ 10 s, and an additional spike at 45.75 s. There is no observation from the *Fermi* satellite. X-shooter found its redshift to be $z = 2.0631$ [414]. The isotropic energy of this GRB is $E_{\mathrm{iso}} = 1.56 \times 10^{53}$ erg. Plot reproduced from [472].
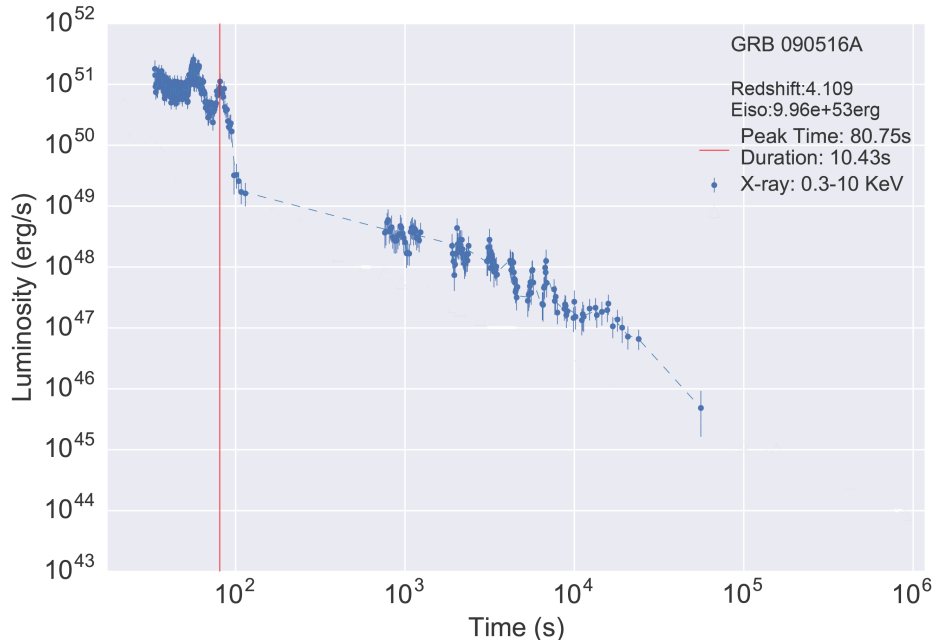
Figure 3.13. GRB 090516A: source was observed by *Swift*-BAT [449], *Konus*-WIND [485] and *Fermi*-GBM [331]. The BAT prompt light curve is composed of two episodes, the first starting 2 s before the trigger and lasting up to 10 s after the trigger, while the second episode starts at 17 s and lasts ~ 2 s. The GBM light curve consists of about five overlapping pulses from $T_{F,0} - 10$ s to $T_{F,0} + 21$ s (where $T_{F,0}$ is *Fermi*-GBM trigger time). The VLT redshift is $z = 4.109$ [129], in agreement with the photometric redshift by GROND [445]. The isotropic energy is $E_{iso} = 6.5 \times 10^{53}$ erg. GRB was inside FoV of *Fermi*-LAT, the standard likelihood analysisgives the upper limit of observed count flux is 4.76×10^{-6} photons cm^{-2} s^{-1}, no GeV photon was found for such a high redshift. Plot reproduced from [472].
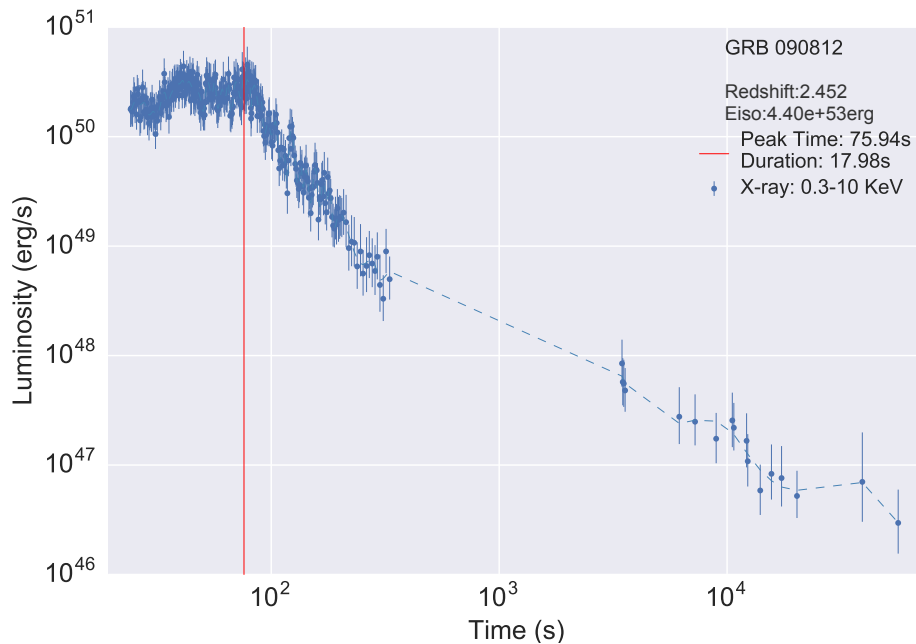
Figure 3.14. GRB 090812: source was detected by *Swift*-BAT [502]. The VLT redshift is $z = 2.452$ [129]. An isotropic energy $E_{iso} = 4.75 \times 10^{53}$ erg. The BAT light curve shows three successive bumps lasting ~ 20 s in total. XRT began observation 22 s after the BAT trigger. Plot reproduced from [472].
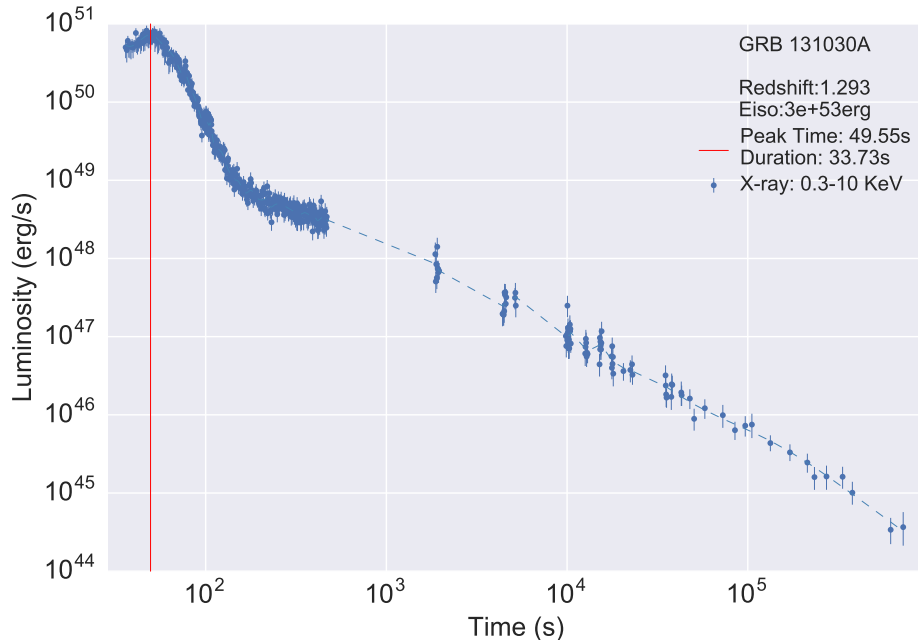
Figure 3.15. GRB 131030A: source was observed by *Swift*-BAT [528] and *Konus*-WIND [180]. The BAT light curve shows two overlapping peaks starting (with respect to the Swift-BAT trigger $T_{B,0}$) at $\sim T_{B,0} - 3.5$ s and peaking at $\sim T_{B,0} + 4.4$ s [27]. The duration is 18 s in the 15–350 keV band. The *Konus*-WIND light curve shows a multi-peaked pulse from $\sim T_{KW,0} - 1.3$ s till $\sim T_{KW,0} + 11$ s (where $T_{KW,0}$ is the *Konus*-WIND trigger time). The redshift of this source is $z = 1.293$, as determined by NOT [576]. The isotropic energy is $E_{iso} = 3 \times 10^{53}$ erg. Plot reproduced from [472].
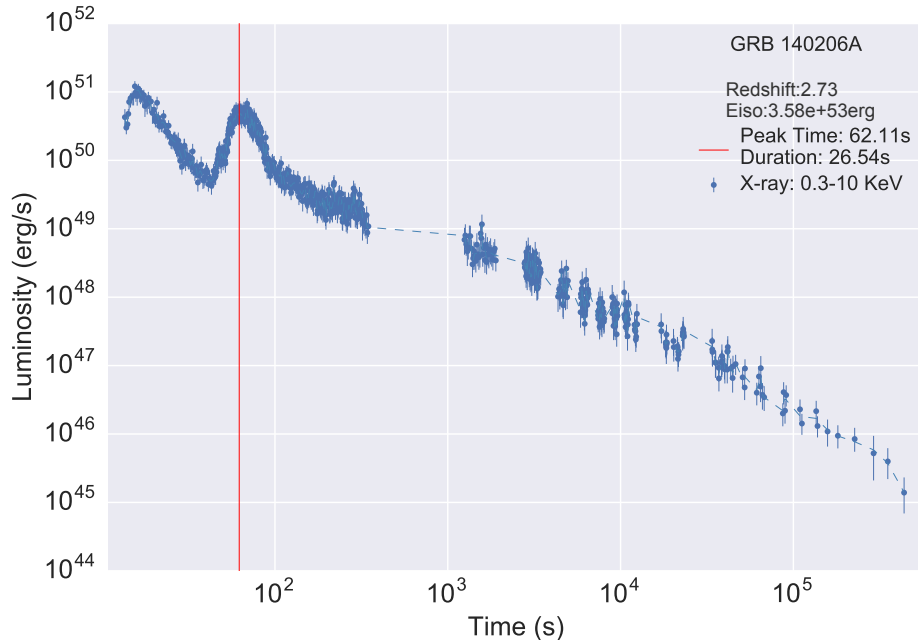
Figure 3.16. GRB 140206A: source was detected by *Swift*-BAT [290] and by *Fermi*-GBM [563]. The GBM light curve shows a single pulse with a duration of ~ 7 s (50–300 keV). The source was outside of *Fermi*-LAT FoV at the trigger time (boresight angle $\theta = 123°$). The BAT light curve shows a multi-peaked structure with roughly three main pulses [487]. The source duration is 25 s (15–350 keV). The NOT redshift is $z = 2.73$ [306], and the isotropic energy is $E_{iso} = 4.3 \times 10^{53}$ erg. Plot reproduced from [472].
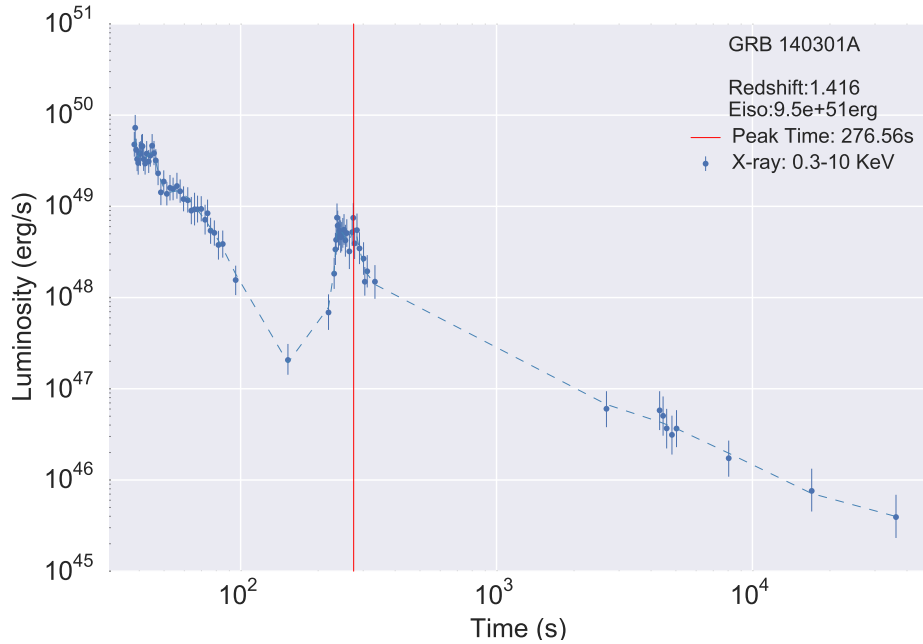
Figure 3.17. GRB 140301A: source was triggered by *Swift*-BAT [395]; the BAT light curve has a single spike with a duration ~ 4 s. XRT started observation 35.63 s after the BAT trigger. There is no observation by *Fermi* satellite. From the X-Shooter spectral analysis, redshift was revealed as $z = 1.416$ [262]. The isotropic energy is 9.5×10^{51} erg. Plot reproduced from [472].
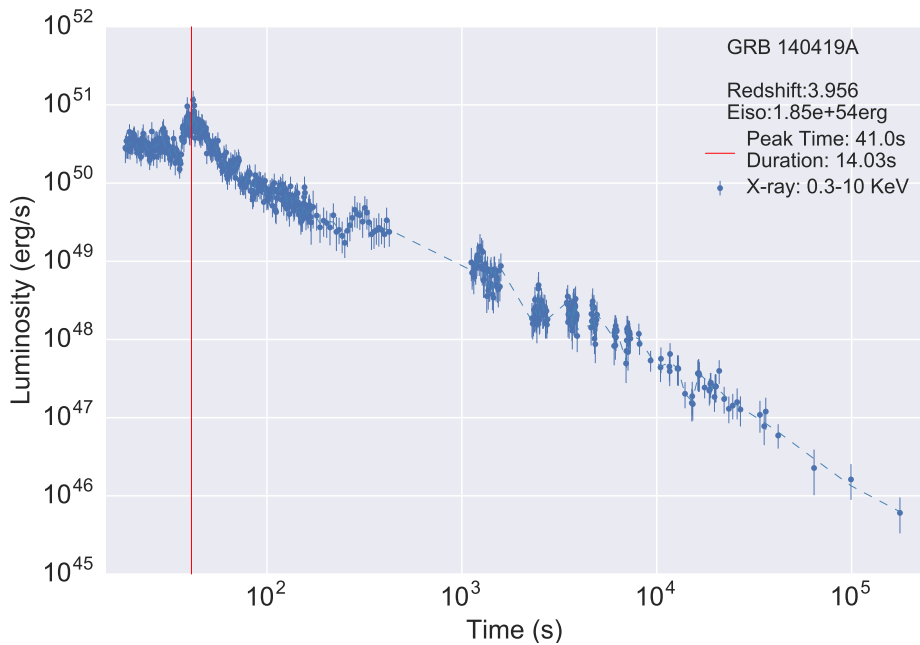
Figure 3.18. GRB 140419A: this source was detected by *Konus*-WIND [181] and *Swift*-BAT [315]. The *Konus*-WIND light curve shows a broad pulse ($\sim T_{\mathrm{KW},0} - 2$ s; $\sim T_{\mathrm{KW},0} + 8$ s), followed by softer pulses ($\sim T_{\mathrm{KW},0} + 10$ s). The total duration is ~ 16 s. The BAT light curve shows two slightly overlapping clusters of peaks, starting at $\sim T_{\mathrm{B},0} - 2$ s, peaking at $\sim T_{\mathrm{B},0} + 2$ s and $\sim T_{\mathrm{B},0} + 10$ s, and ending at $\sim T_{\mathrm{B},0} + 44$ s [29]. The total duration is 19 s (15–350 keV). The Gemini redshift is $z = 3.956$ [516] and isotropic energy is $E_{\mathrm{iso}} = 1.85 \times 10^{54}$ erg. Plot reproduced from [472].
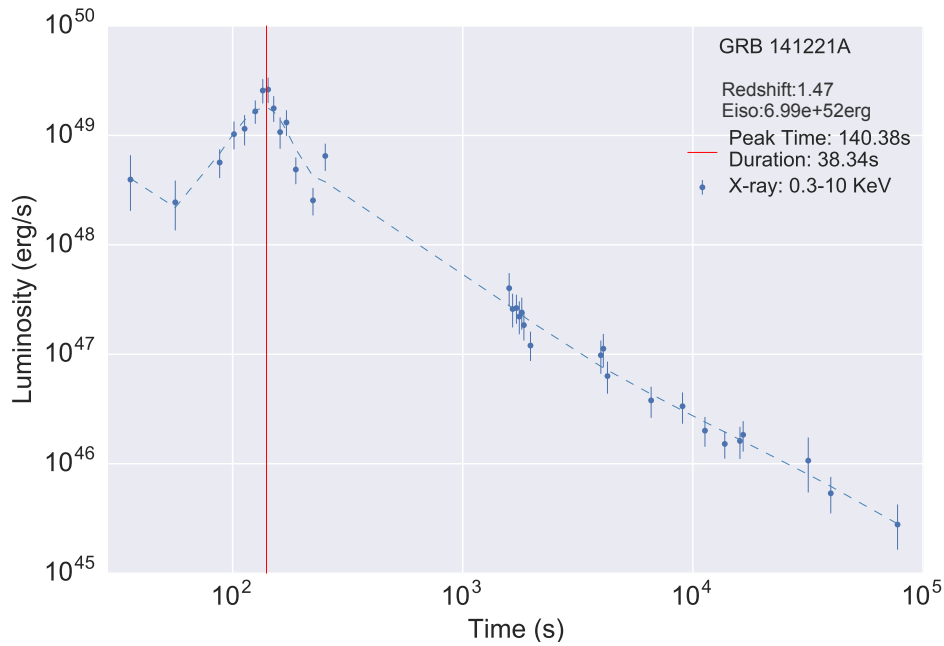
Figure 3.19. GRB 141221A: source was detected by *Swift*-BAT [500] and by *Fermi*-GBM [584]. The Keck spectroscopic redshift $z = 1.47$ [409]. The GBM light curve consists of two pulses lasting ~ 10 s (50–300 keV). Its isotropic energy is $E_{\rm iso} = 1.91 \times 10^{52}$ erg. The source was 76° from the LAT boresight at the trigger time. The BAT light curve showed a double-peaked structure with a duration ~ 8 s. XRT began observation 32 s after the BAT trigger. Plot reproduced from [472].
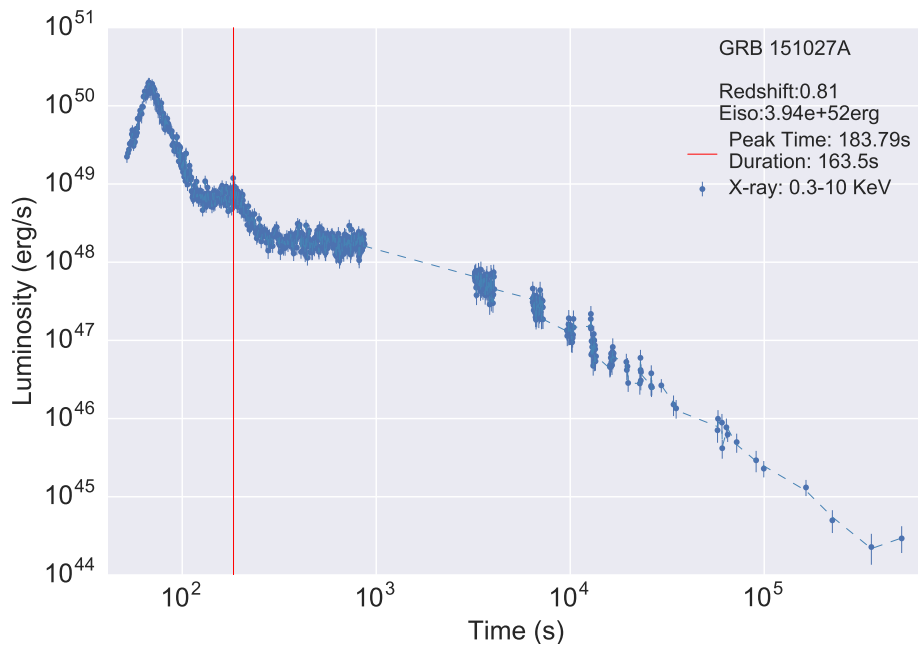
Figure 3.20. GRB 151027A: source was detected by MAXI [320], *Konus*-WIND [185], *Swift*-XRT [318] and *Fermi*-GBM [521]. The *Keck*/HIRES redshift is $z = 0.81$ [410]. The GBM light curve consists of three pulses with a duration ~ 68 s (50–300 keV). The isotropic energy is $E_{\rm iso} = 3.94 \times 10^{52}$ erg. The LAT boresight of the source was 10°, no clearly associated high energy photons; an upper limit of observed count flux is 9.24×10^{-6} photons cm^{-2} s^{-1}. The BAT light curve shows a complex peaked structure lasting at least 83 seconds. XRT began observation 48 s after the BAT trigger. Plot reproduced from [472].

"obscured" by the material of the SN ejecta, explaining the absence of GeV photons in the above cases of GRB 090516A and 151027A.

We derive the isotropic-equivalent energy E_{iso} by assuming the prompt emission to be isotropic and by integrating the prompt photons in the rest-frame energy range from 1 keV to 10 MeV [44]. None of the satellites is able to cover the entire energy band of E_{iso}, so we need to fit the spectrum and find the best-fit function, then extrapolate the integration of energy by using this function. The method is relatively safe for GRBs observed by *Fermi* and *Konus*-WIND, but 6 GRBs in our sample have been observed only by *Swift*-BAT, so we uniformly fit and extrapolate these 6 GRBs by Power-Law (PL) and Cutoff Power-Law (CPL) functions; then we take the average value as E_{iso}. In general, our priority in computing E_{iso} is *Fermi*-GBM, *Konus*-WIND, then *Swift*-BAT. In order to take into account the expansion of the universe, all of our computations consider *K*-correction (see Appendix A). The formula of *K*-correction for E_{iso} varies depending on the best-fit function. The energy in the X-ray afterglow is computed in the cosmological rest-frame energy band from 0.3 keV to 10 keV.

We smoothly fit the luminosity light curve using an algorithm named Locally Weighted Regression (LWR) [87] which provides a sequence of PL functions. The corresponding energy in a fixed time interval is obtained by summing up all of the integrals of the power-laws within it. This method is applied to estimate the energy of the flare E_f, as well as the energy of the FPA phase up to 10^9 s, E_{FPA}. An interesting alternative procedure was used in [507] to fit the light curve and determine the flaring structure with a Bayesian Information Criterion method (BIC). On this specific aspect the two treatments are equally valid and give compatible results.

Table 3.1 contains the relevant energy and time information of the 16 BdHNe of the sample: the cosmological redshift z, the isotropic-equivalent energy E_{iso}, the flare peak time t_p, the corresponding peak luminosity L_p, the flare duration Δt, and the energy of the flare E_f. To determine t_p we apply LWR algorithm, which results in a smoothed light curve composed of power-law functions: the flare peak is localized where the power-law index is zero. Therefore t_p is defined as the time interval between the flare peak and the trigger time of *Swift*-BAT.[1] Correspondingly, we find the peak luminosity L_p at t_p and its duration Δt which is defined as the time interval between start time and end time at which the luminosity is half of L_p. We have made public the entire details including the codes online.[2]

Statistical Correlations

We then establish correlations between the quantities characterizing each luminosity light curve of the sample with the E_{iso} of the corresponding GRB. We have relied heavily on the Markov Chain Monte Carlo (MCMC) method and iterated 10^5 times for having the best fit of the PL function and its correlation coefficient. The main results are summarized in Figures 3.21–3.24. All the codes are publicly

---

[1] In reality, the GRB occurs earlier than the trigger time, since there is a short period when the flux intensity is lower than the satellite trigger threshold [149].

[2] https://github.com/YWangScience/AstroNeuron

GRB	z	T_{90} (s)	$E_{\rm iso}$ (erg)	t_p (s)	L_p (erg/s)	Δt (s)	E_f (erg)	α_f
060204B	2.3393	40.12	$2.93(\pm0.60) \times 10^{53}$	100.72 ± 6.31	$7.35(\pm2.05) \times 10^{49}$	17.34 ± 6.83	$8.56(\pm0.82) \times 10^{50}$	2.73
060607A	3.082	24.49	$2.14(\pm1.19) \times 10^{53}$	66.04 ± 4.98	$2.28(\pm0.48) \times 10^{50}$	18.91 ± 3.84	$3.33(\pm0.32) \times 10^{51}$	1.72
070318	0.84	28.80	$3.41(\pm2.14) \times 10^{52}$	154.7 ± 12.80	$6.28(\pm1.30) \times 10^{48}$	63.80 ± 19.82	$3.17(\pm0.37) \times 10^{50}$	1.84
080607	3.04	21.04	$1.87(\pm0.11) \times 10^{54}$	37.48 ± 3.60	$1.14(\pm0.27) \times 10^{51}$	15.63 ± 4.32	$1.54(\pm0.24) \times 10^{52}$	2.08
080805	1.51	31.08	$7.16(\pm1.90) \times 10^{52}$	48.41 ± 5.46	$4.66(\pm0.59) \times 10^{49}$	27.56 ± 9.33	$9.68(\pm1.24) \times 10^{50}$	1.25
080810	3.35	18.25	$5.00(\pm0.44) \times 10^{53}$	51.03 ± 6.49	$1.85(\pm0.53) \times 10^{50}$	12.38 ± 4.00	$1.80(\pm0.17) \times 10^{51}$	2.37
081008	1.967	62.52	$1.35(\pm0.66) \times 10^{53}$	102.24 ± 5.66	$1.36(\pm0.33) \times 10^{50}$	18.24 ± 3.63	$1.93(\pm0.16) \times 10^{51}$	2.46
081210	2.0631	47.66	$1.56(\pm0.54) \times 10^{53}$	127.59 ± 13.68	$2.23(\pm0.21) \times 10^{49}$	49.05 ± 6.49	$8.86(\pm0.54) \times 10^{50}$	2.28
090516A	4.109	68.51	$9.96(\pm1.67) \times 10^{53}$	80.75 ± 2.20	$9.10(\pm2.26) \times 10^{50}$	10.43 ± 2.44	$7.74(\pm0.63) \times 10^{51}$	3.66
090812	2.452	18.77	$4.40(\pm0.65) \times 10^{53}$	77.43 ± 16.6	$3.13(\pm1.38) \times 10^{50}$	17.98 ± 4.51	$5.18(\pm0.61) \times 10^{51}$	2.20
131030A	1.293	12.21	$3.00(\pm0.20) \times 10^{53}$	49.55 ± 7.88	$6.63(\pm1.12) \times 10^{50}$	33.73 ± 6.55	$3.15(\pm0.57) \times 10^{52}$	2.22
140206A	2.73	7.24	$3.58(\pm0.79) \times 10^{53}$	62.11 ± 12.26	$4.62(\pm0.99) \times 10^{50}$	26.54 ± 4.31	$1.04(\pm0.59) \times 10^{51}$	1.73
140301A	1.416	12.83	$9.50(\pm1.75) \times 10^{51}$	276.56 ± 15.5	$5.14(\pm1.84) \times 10^{48}$	64.52 ± 10.94	$3.08(\pm0.22) \times 10^{50}$	2.30
140419A	3.956	16.14	$1.85(\pm0.77) \times 10^{54}$	41.00 ± 4.68	$6.23(\pm1.45) \times 10^{50}$	14.03 ± 5.74	$7.22(\pm0.88) \times 10^{51}$	2.32
141221A	1.47	9.64	$6.99(\pm1.98) \times 10^{52}$	140.38 ± 5.64	$2.60(\pm0.64) \times 10^{49}$	38.34 ± 9.26	$7.70(\pm0.78) \times 10^{50}$	1.79
151027A	0.81	68.51	$3.94(\pm1.33) \times 10^{52}$	183.79 ± 16.43	$7.10(\pm1.75) \times 10^{48}$	163.5 ± 30.39	$4.39(\pm2.91) \times 10^{51}$	2.26

Table 3.1. Sample properties of the Prompt and Flare phases. This table contains: the redshift z, the T_{90} in the rest frame, the isotropic-equivalent energy $E_{\rm iso}$, the flare peak time t_p in the rest frame, the flare peak luminosity L_p, the flare duration of which the starting and ending time correspond to half of the peak luminosity Δt, the flare energy E_f within the time interval Δt, and α_f power-law index from the fitting of the flare's spectrum.
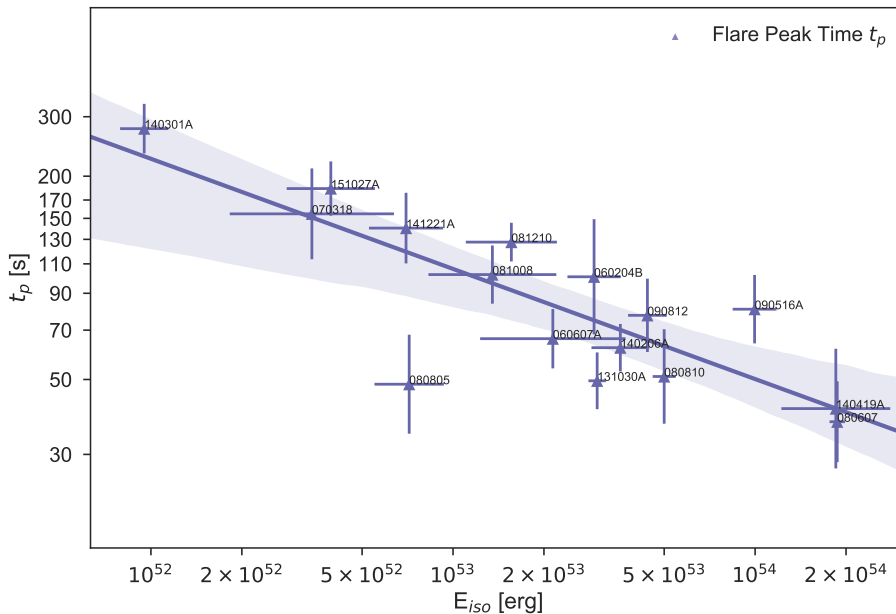
Figure 3.21. Relation between E_{iso} and t_p fit by a power-law. The shaded area indicates the 95% confidence level. Plot reproduced from [472].

Correlation	Power-Law Index	Coefficient
$E_{\mathrm{iso}} - t_p$	$-0.290(\pm 0.010)$	$-0.764(\pm 0.123)$
$E_{\mathrm{iso}} - \Delta t$	$-0.461(\pm 0.042)$	$-0.760(\pm 0.138)$
$E_{\mathrm{iso}} - L_p$	$1.186(\pm 0.037)$	$0.883(\pm 0.070)$
$E_{\mathrm{iso}} - E_f$	$0.631(\pm 0.117)$	$0.699(\pm 0.145)$

Table 3.2. Power-law correlations among the quantities in Table 3.1. The values and uncertainties (at 1σ confidence level) of the power-law index and of the correlation coefficient are obtained from 10^5 MCMC iterations. All relations are highly correlated.

available online.[3] We conclude that the peak time and the duration of the flare, as well as the peak luminosity and the total energy of flare, are highly correlated with E_{iso}, with correlation coefficients larger than 0.6 (or smaller than -0.6). The average values and the 1σ uncertainties are shown in Table 3.2.

3.3 Discussion

3.3.1 The partition of electron-positron plasma energy between the prompt emission and the Flare–Plateau–Afterglow phases

The energy of the prompt emission is proportional to E_{iso} if and only if spherical symmetry is assumed: this clearly follows from the prompt emission time integrated

---

[3] https://github.com/YWangScience/MCCC
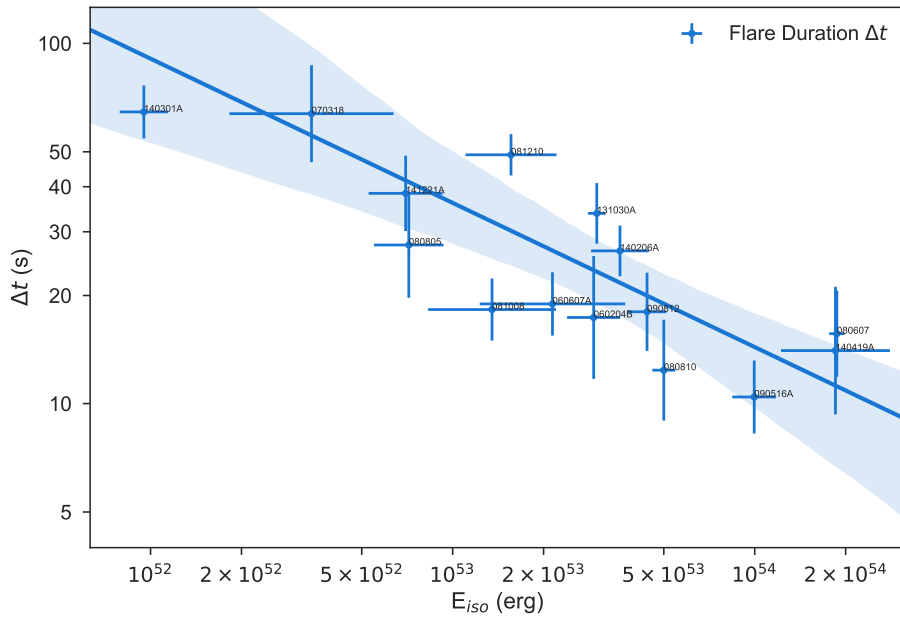
Figure 3.22. Relation between E_{iso} and Δt fit by a power-law. The shaded area indicates the 95% confidence level. Plot reproduced from [472].
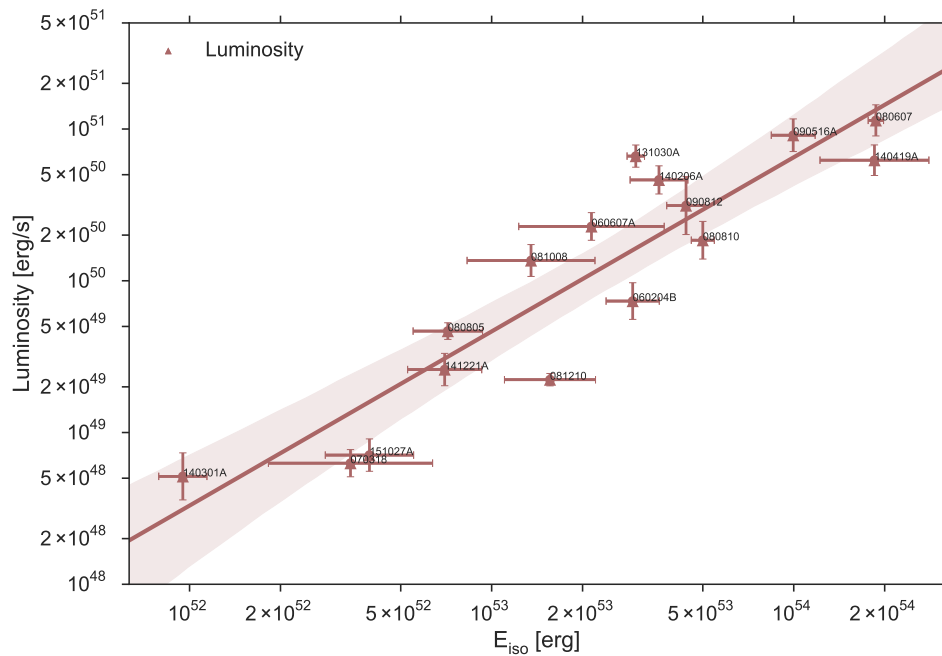
Figure 3.23. Relation between E_{iso} and L_p fit by a power-law. The shaded area indicates the 95% confidence level. Plot reproduced from [472].
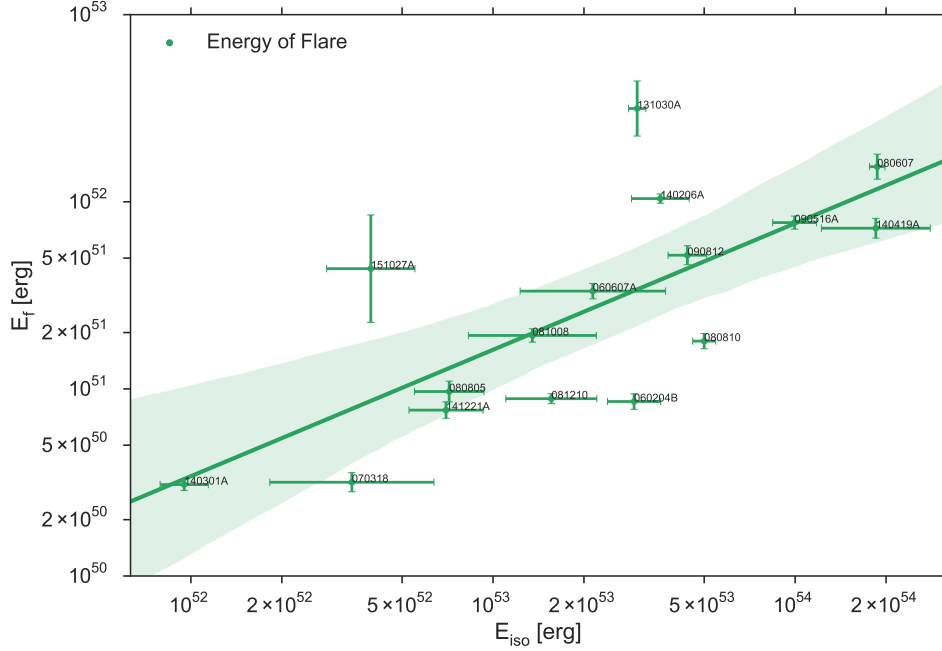
Figure 3.24. Relation between E_{iso} and E_f fit by a power-law. The shaded area indicates the 95% confidence level. Plot reproduced from [472].

luminosity. We are now confronted with a new situation: the total energy of the FPA emission up to 10^9 s (E_{FPA}) is also proportional to E_{iso}, following the correlation given in Table 3.3, Table 3.4, and Figure 3.25. What is clear is that there are two very different components where the energy of the dyadosphere $E_{e^+e^-}$ is utilized: the energy E_{prompt} of the prompt emission and the energy E_{FPA} of the FPA, i.e., $E_{e^+e^-} = E_{\mathrm{iso}} = E_{\mathrm{prompt}} + E_{\mathrm{FPA}}$. Figure 3.26 shows the distribution of $E_{e^+e^-} = E_{\mathrm{iso}}$ among these two components.

As a consequence of the above, in view of the presence of the companion SN remnant ejecta ([33] for more details), we assume here that the spherical symmetry of the prompt emission is broken. Part of the energy due to the impact of the e^+e^- plasma on the SN is captured by the SN ejecta, and gives origin to the FPA emission as originally proposed by [452].

It can also be seen that the relative partition between E_{prompt} and E_{FPA} strongly depends on the value of $E_{e^+e^-}$: the lower the GRB energy, the higher the FPA energy percentage and consequently the lower is the prompt energy percentage.

In [33] we indicate that both the value of $E_{e^+e^-}$ and the relative ratio of the above two components can in principle be explained in terms of the geometry of the binary nature of the system: the smaller the distance is between the CO_{core} and the companion NS, the shorter the binary period of the system, and the larger the value of $E_{e^+e^-}$ energy.

GRB	z	E_{iso} (erg)	E_{FPA} (erg)
060204B	2.3393	$2.93(\pm 0.60) \times 10^{53}$	$6.02(\pm 0.20) \times 10^{51}$
060607A	3.082	$2.14(\pm 1.19) \times 10^{53}$	$2.39(\pm 0.12) \times 10^{52}$
070318	0.84	$3.41(\pm 2.14) \times 10^{52}$	$4.76(\pm 0.21) \times 10^{51}$
080607	3.04	$1.87(\pm 0.11) \times 10^{54}$	$4.32(\pm 0.96) \times 10^{52}$
080805	1.51	$7.16(\pm 1.90) \times 10^{52}$	$6.65(\pm 0.42) \times 10^{51}$
080810	3.35	$5.00(\pm 0.44) \times 10^{53}$	$1.67(\pm 0.14) \times 10^{52}$
081008	1.967	$1.35(\pm 0.66) \times 10^{53}$	$6.56(\pm 0.60) \times 10^{51}$
081210	2.0631	$1.56(\pm 0.54) \times 10^{53}$	$6.59(\pm 0.60) \times 10^{51}$
090516A	4.109	$9.96(\pm 1.67) \times 10^{53}$	$3.34(\pm 0.22) \times 10^{52}$
090812	2.452	$4.40(\pm 0.65) \times 10^{53}$	$3.19(\pm 0.36) \times 10^{52}$
131030A	1.293	$3.00(\pm 0.20) \times 10^{53}$	$4.12(\pm 0.23) \times 10^{52}$
140206A	2.73	$3.58(\pm 0.79) \times 10^{53}$	$5.98(\pm 0.69) \times 10^{52}$
140301A	1.416	$9.50(\pm 1.75) \times 10^{51}$	$1.42(\pm 0.14) \times 10^{50}$
140419A	3.956	$1.85(\pm 0.77) \times 10^{54}$	$6.84(\pm 0.82) \times 10^{52}$
141221A	1.47	$6.99(\pm 1.98) \times 10^{52}$	$5.31(\pm 1.21) \times 10^{51}$
151027A	0.81	$3.94(\pm 1.33) \times 10^{52}$	$1.19(\pm 0.18) \times 10^{52}$

Table 3.3. Sample properties for the Prompt and Flare-Plateau-Afterglow (FPA) phases. This table lists: the redshift z, the isotropic-equivalent energy E_{iso}, and the FPA energy E_{FPA} from the start of the flare and up to 10^9 s.

Correlation	Power-Law Index	Coefficient
E_{iso}-E_{FPA}	$0.613(\pm 0.041)$	$0.791(\pm 0.103)$
E_{iso}-$E_{\mathrm{FPA}}/E_{\mathrm{iso}}$	$-0.005(\pm 0.002)$	$0.572(\pm 0.178)$

Table 3.4. Power-law correlations among the quantities in Table 3.3. The statistical considerations of Table 3.2 are valid here as well.
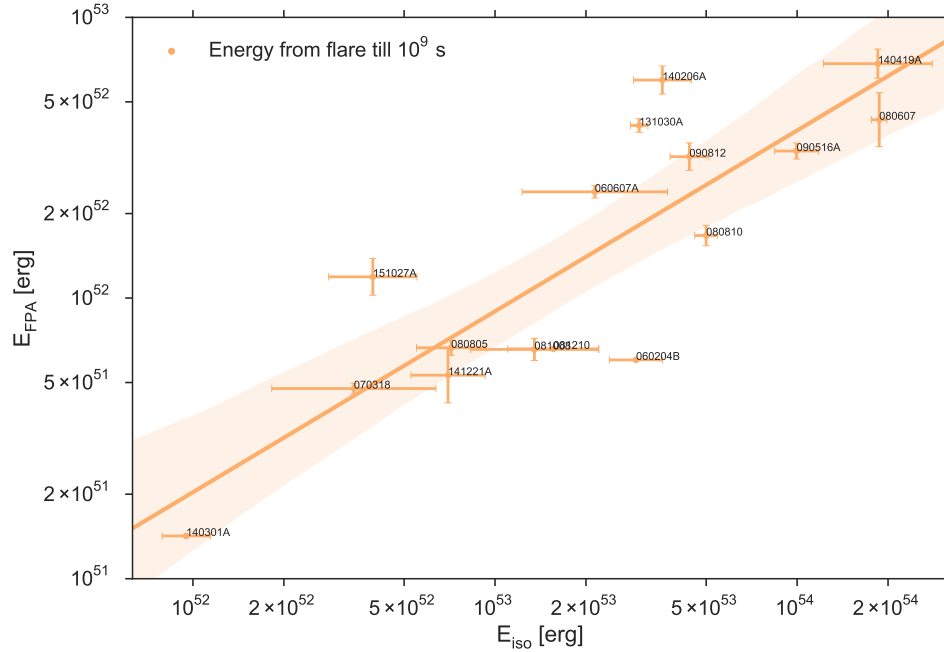
Figure 3.25. Relation between E_{iso} and E_{FPA} fit by Power-Law function. The shaded area indicates the 95% confidence level. Plot reproduced from [472].
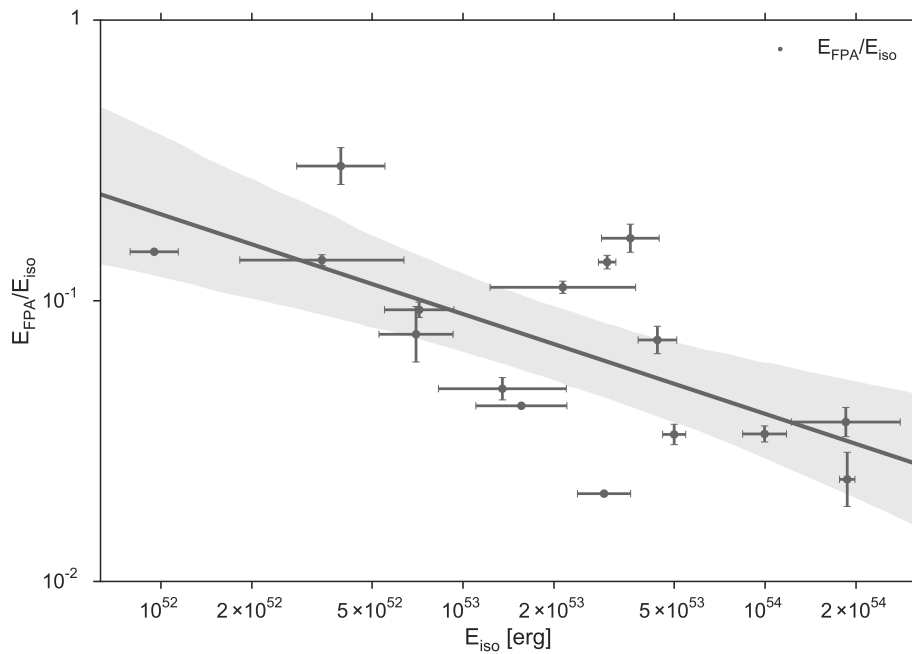
Figure 3.26. Relation between the percentage of $E_{e^+e^-}$ going to the SN ejecta and accounting for the energy in FPA, i.e., $E_{\text{FPA}}/E_{\text{iso}} \times 100\%$, and E_{iso} fit by a Power-Law function. The shaded area indicates the 95% confidence level. Plot reproduced from [472].

GRB	Radius (cm)	kT_{obs} (keV)	Significance
060204B	$\mathbf{1.80(\pm1.11)\times10^{11}}$	$\mathbf{0.60(\pm0.15)}$	**0.986**
060607A	$\mathbf{1.67(\pm1.01)\times10^{11}}$	$\mathbf{0.92(\pm0.24)}$	**0.991**
070318	*unconstrained*	$1.79(\pm1.14)$	0.651
080607	$\mathbf{1.52(\pm0.72)\times10^{12}}$	$\mathbf{0.49(\pm0.10)}$	**0.998**
080805	$1.12(\pm1.34)\times10^{11}$	$1.31(\pm0.59)$	0.809
080810	$\mathbf{2.34(\pm4.84)\times10^{11}}$	$\mathbf{0.61(\pm0.57)}$	**0.999**
081008	$\mathbf{1.84(\pm0.68)\times10^{12}}$	$\mathbf{0.32(\pm0.03)}$	**0.999**
081210	*unconstrained*	$0.80(\pm0.51)$	0.295
090516A	*unconstrained*	$1.30(\pm1.30)$	0.663
090812	$1.66(\pm1.84)\times10^{12}$	$0.24(\pm0.12)$	0.503
131030A	$\mathbf{3.67(\pm1.02)\times10^{12}}$	$\mathbf{0.55(\pm0.06)}$	**0.999**
140206A	$\mathbf{9.02(\pm2.84)\times10^{11}}$	$\mathbf{0.54(\pm0.07)}$	**0.999**
140301A	*unconstrained*	*unconstrained*	0.00
140419A	$1.85(\pm1.17)\times10^{12}$	$0.23(\pm0.05)$	0.88
141221A	$1.34(\pm2.82)\times10^{12}$	$0.24(\pm0.24)$	0.141
151027A	$1.18(\pm0.67)\times10^{12}$	$0.29(\pm0.06)$	0.941

Table 3.5. Radii and temperatures of the thermal components detected within the flare duration Δt. The observed temperatures kT_{obs} are inferred from fitting with a Power-Law plus Blackbody (PL+BB) spectral model. The significance of a blackbody is computed by the maximum likelihood ratio for comparing nested models and its addition improves a fit when the significance is > 0.95. The radii are calculated assuming mildly relativistic motion ($\beta = 0.8$) and isotropic radiation. The GRBs listed in boldface have prominent Blackbody components, with radii of the order of $\sim 10^{11}$–10^{12} cm. Uncertainties are given at 1σ confidence level.

3.3.2 On the flare thermal emission, its temperature and dynamics

We discuss now the profound difference between the prompt emission, which we recall is emitted at distances of the order of 10^{16} cm away from the newly-born BH with $\Gamma \approx 10^2$–10^3, and the FPA phase. We focus on a further fundamental set of data, which originates from a thermal emission associated with the flares.[4] Only in some cases this emission is so clear and prominent that it allows the estimation of the flare expansion speed, and the determination of its mildly relativistic Lorentz factor $\Gamma \lesssim 4$, which creates a drastic separatrix, both in the energy and in the gamma factor between the astrophysical nature of the prompt emission and of the flares.

Following the standard data reduction procedure of *Swift*-XRT [444, 143, 144], X-ray data within the duration of flare are retrieved from the *United Kingdom Swift Science Data Centre* (UKSSDC)[5] and analyzed by HEASoft.[6] Table 3.5 shows the fit of the spectrum within the duration Δt of the flare for each GRB of the sample. As the first approximation, in computing the radius we have assumed a constant expansion velocity of $0.8c$ indicated for some bursts, such as GRB 090618

---

[4] The late afterglow phases have been already discussed in [420, 421].

[5] `http://www.swift.ac.uk`

[6] `http://heasarc.gsfc.nasa.gov/lheasoft/`

[468] and GRB 130427A [465]. Out of 16 sources, 7 objects have highly confident thermal components (significance > 0.95, see boldface in Table 3.5), which means that the addition of a blackbody spectrum improves a single Power-Law fit (which is, conversely, excluded at 2σ of confidence level). These blackbodies have fluxes in a range from 1% to 30% of the total flux and share similar order of magnitude radii, i.e., $\sim 10^{11}$–10^{12} cm. In order to have a highly significant thermal component, the blackbody radiation itself should be prominent, as well as its ratio to the non-thermal part. Another critical reason is that the observable temperature must be compatible with the satellite bandpass. For example, *Swift*-XRT observes in the 0.3–10 keV photon energy band, but the hydrogen absorption affects the lower energy part (~ 0.5 keV), and data is always not adequate beyond 5 keV, due to the low effective area of satellite for high energy photons. The reliable temperature only ranges from 0.15 keV to 1.5 keV (since peak photon energy is equal to the temperature multiplied by a factor of 2.82), so the remaining 9 GRBs may contain a thermal component in the flare but outside the satellite bandpass.

We now attempt to perform a more refined analysis to infer the value of β from the observations. We assume that during the flare the Blackbody emitter has spherical symmetry and expands with a constant Lorentz gamma factor. Therefore, the expansion velocity β is also constant during the flare. The relations between the comoving time t_{com}, the laboratory time t, the arrival time t_a, and the arrival time t_a^d at the detector, given as

$$t_a^d = (1+z)t_a = (1+z)\left(t - \frac{r(t)}{c}\cos\vartheta\right) = (1+z)\left(\Gamma t_{com} - \frac{r(\Gamma t_{com})}{c}\cos\vartheta\right), \quad (3.1)$$

in this case become:

$$t_a^d = t_a(1+z) = t(1 - \beta\cos\vartheta)(1+z) = \Gamma t_{com}(1 - \beta\cos\vartheta)(1+z) . \quad (3.2)$$

We can infer an effective radius R of the Blackbody emitter from: i) the observed Blackbody temperature $T_{\rm obs}$, which comes from the spectral fit of the data during the flare; ii) the observed bolometric Blackbody flux $F_{\rm bb,obs}$, computed from $T_{\rm obs}$ and the normalization of the Blackbody spectral fit; and iii) the cosmological redshift z of the source [235]. We recall that $F_{\rm bb,obs}$ by definition is given by:

$$F_{\rm bb,obs} = \frac{L}{4\pi D_L(z)^2} , \quad (3.3)$$

where $D_L(z)$ is the luminosity distance of the source, which in turn is a function of the cosmological redshift z, and L is the source bolometric luminosity, i.e., the total emitted energy per unit time. Bolometric luminosity L is Lorentz invariant, so we can compute it in the comoving frame of the emitter using the usual Blackbody expression:

$$L = 4\pi R_{\rm com}{}^2\sigma T_{\rm com}{}^4 , \quad (3.4)$$

where $R_{\rm com}$ and $T_{\rm com}$ are the comoving radius and the comoving temperature of the emitter, respectively, and σ is the Stefan-Boltzmann constant. We recall that $T_{\rm com}$ is constant over the entire shell due to our assumption of spherical symmetry. From Equation (3.3) and Equation (3.4) we then have:

$$F_{\rm bb,obs} = \frac{R_{\rm com}{}^2\sigma T_{\rm com}{}^4}{D_L(z)^2} . \quad (3.5)$$

We now need the relation between T_com and the observed Blackbody temperature T_obs. Considering both the cosmological redshift and the Doppler effect due to the velocity of the emitting surface, we have:

$$T_\text{obs}(T_\text{com}, z, \Gamma, \cos\vartheta) = \frac{T_\text{com}}{(1+z)\,\Gamma\,(1-\beta\cos\vartheta)} = \frac{T_\text{com}\mathcal{D}(\cos\vartheta)}{1+z}\,, \qquad (3.6)$$

where we have defined the Doppler factor $\mathcal{D}(\cos\vartheta)$ as:

$$\mathcal{D}(\cos\vartheta) \equiv \frac{1}{\Gamma\,(1-\beta\cos\vartheta)}\,. \qquad (3.7)$$

Equation (3.6) gives us the observed Blackbody temperature of the radiation coming from different points of the emitter surface, corresponding to different values of $\cos\vartheta$. However, since the emitter is at a cosmological distance, we are not able to resolve spatially the source with our detectors. Therefore, the temperature that we actually observe corresponds to an average of Equation (3.6) computed over the emitter surface:[7]

$$
\begin{aligned}
T_\text{obs}(T_\text{com}, z, \Gamma) &= \frac{1}{1+z}\frac{\int_\beta^1 \mathcal{D}(\cos\vartheta)T_\text{com}\cos\vartheta\,d\cos\vartheta}{\int_\beta^1 \cos\vartheta\,d\cos\vartheta}\\[2mm]
&= \frac{2}{1+z}\frac{\beta\,(\beta-1)+\ln(1+\beta)}{\Gamma\beta^2\,(1-\beta^2)}T_\text{com}\\[2mm]
&= \Theta(\beta)\frac{\Gamma}{1+z}T_\text{com} \qquad (3.8)
\end{aligned}
$$

where we defined

$$\Theta(\beta) \equiv 2\,\frac{\beta\,(\beta-1)+\ln(1+\beta)}{\beta^2}\,, \qquad (3.9)$$

we have used the fact that due to relativistic beaming, we observe only a portion of the surface of the emitter defined by:

$$\beta \leq \cos\vartheta \leq 1\,. \qquad (3.10)$$

Therefore, inverting Equation (3.8), the comoving Blackbody temperature T_com can be computed from the observed Blackbody temperature T_obs, the source cosmological redshift z and the emitter Lorentz gamma factor Γ in the following way:

$$T_\text{com}(T_\text{obs}, z, \Gamma) = \frac{1+z}{\Theta(\beta)\Gamma}T_\text{obs}\,. \qquad (3.11)$$

We can now insert Equation (3.11) into Equation (3.5) to obtain:

$$F_\text{bb,obs} = \frac{R_\text{com}{}^2}{D_L(z)^2}\sigma T_\text{com}^4 = \frac{R_\text{com}{}^2}{D_L(z)^2}\sigma\left[\frac{1+z}{\Theta(\beta)\Gamma}T_\text{obs}\right]^4\,. \qquad (3.12)$$

---

[7] From the point of view of the observer the spectrum is not a perfect Blackbody, coming from a convolution of Blackbody spectra at different temperatures. The Blackbody component we obtain from the spectral fit of the observed data is an effective Blackbody of temperature T_obs, analogously to other cases of effective temperatures in cosmology [464].

Since the radius R_{lab} of the emitter in the laboratory frame is related to R_{com} by:

$$R_{\mathrm{com}} = \Gamma R_{\mathrm{lab}}, \tag{3.13}$$

we can insert Equation (3.13) into Equation (3.12) and obtain:

$$F_{\mathrm{bb,obs}} = \frac{(1+z)^4}{\Gamma^2} \left(\frac{R_{\mathrm{lab}}}{D_L(z)} \right)^2 \sigma \left[\frac{T_{\mathrm{obs}}}{\Theta(\beta)} \right]^4 . \tag{3.14}$$

Solving Equation (3.14) for R_{lab} we finally obtain the thermal emitter effective radius in the laboratory frame:

$$R_{\mathrm{lab}} = \Theta(\beta)^2 \Gamma \frac{D_L(z)}{(1+z)^2} \sqrt{\frac{F_{\mathrm{bb,obs}}}{\sigma T_{\mathrm{obs}}^4}} = \Theta(\beta)^2 \Gamma \phi_0 , \tag{3.15}$$

where we have defined ϕ_0:

$$\phi_0 \equiv \frac{D_L(z)}{(1+z)^2} \sqrt{\frac{F_{\mathrm{bb,obs}}}{\sigma T_{\mathrm{obs}}^4}} . \tag{3.16}$$

In astronomy the quantity ϕ_0 is usually identified with the radius of the emitter. However, in relativistic astrophysics this identity cannot be straightforwardly applied, because the estimate of the effective emitter radius R_{lab} in Equation (3.15) crucially depends on the knowledge of its expansion velocity β and, correspondingly, of its Γ.

It must be noted that Equation (3.15) above gives the correct value of R_{lab} for all values of $0 \leq \beta \leq 1$ by taking all the relativistic transformations properly into account. In the non-relativistic limit ($\beta \to 0$, $\Gamma \to 1$) we have respectively:

$$\Theta \xrightarrow[\beta \to 0]{} 1, \qquad\qquad\qquad \Theta^2 \xrightarrow[\beta \to 0]{} 1, \tag{3.17}$$

$$T_{\mathrm{com}} \xrightarrow[\beta \to 0]{} T_{\mathrm{obs}}(1+z), \qquad\qquad R_{\mathrm{lab}} \xrightarrow[\beta \to 0]{} \phi_0, \tag{3.18}$$

as expected.

3.3.3 Implications on the dynamics of the flares from their thermal emission

An estimate of the expansion velocity β can be deduced from the ratio between the variation of the emitter effective radius ΔR_{lab} and the emission duration in laboratory frame Δt, i.e.,

$$\beta = \frac{\Delta R_{\mathrm{lab}}}{c \Delta t} = \Theta(\beta)^2 \Gamma (1 - \beta \cos \vartheta)(1+z) \frac{\Delta \phi_0}{c \Delta t_a^d}, \tag{3.19}$$

where we have used Equation (3.15) and the relation between Δt and Δt_a^d given in Equation (3.2). We then have:

$$\beta = \Theta(\beta)^2 \frac{1 - \beta \cos \vartheta}{\sqrt{1 - \beta^2}} (1+z) \frac{\Delta \phi_0}{c \Delta t_a^d}, \tag{3.20}$$
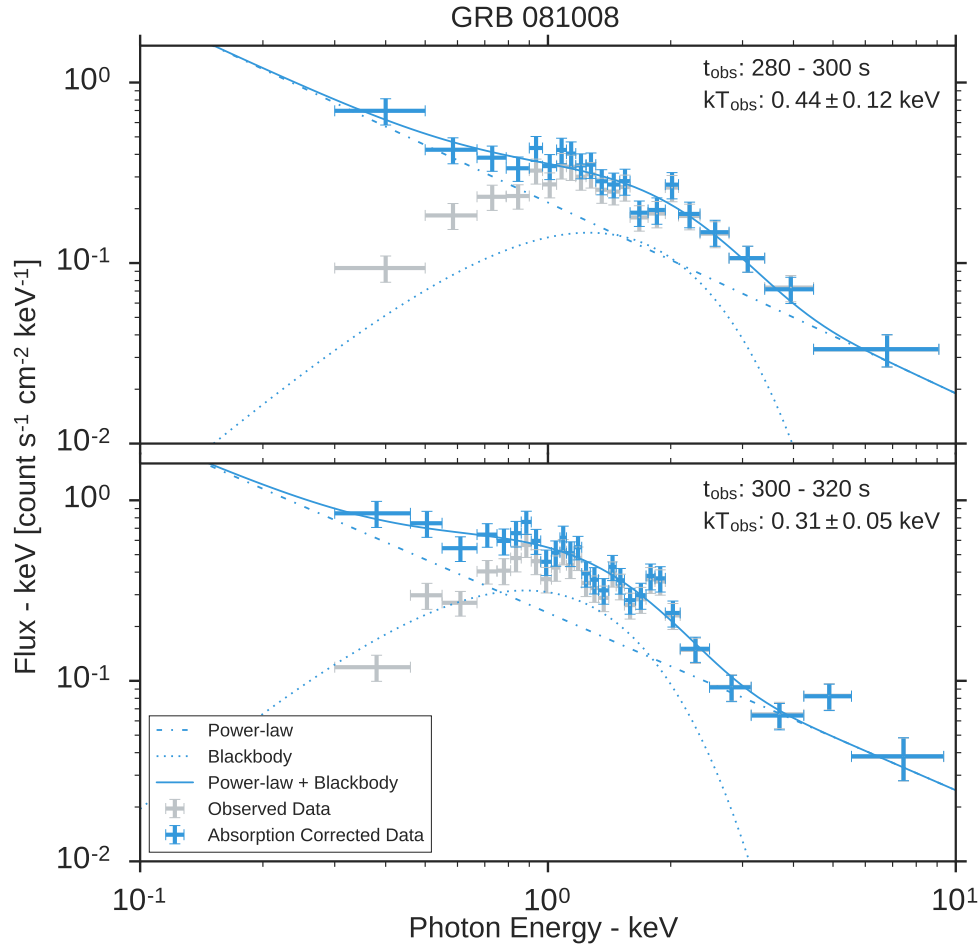
Figure 3.27. Thermal evolution of GRB 081008 ($z = 1.967$) in the observer frame. The X-ray flare of this GRB peaks at $304(\pm17)$ s. **Upper panel**: *Swift*-XRT spectrum from 280 s to 300 s. **Lower panel**: *Swift*-XRT spectrum from 300 s to 320 s. The grey points are the observed data markedly absorbed at low energies, while the blue points are absorption corrected ones. The data is fit with a combination of Power-Law (PL dot-dashed lines) and Blackbody (BB dotted line curves) spectra. The PL+BB spectra are shown as solid curves. Clearly, the temperature decreases with time from ~ 0.44 keV to ~ 0.31 keV, but the ratio of thermal component goes up from $\sim 20\%$ to $\sim 30\%$. This is a remarkable high percentage among our sample. Plot reproduced from [472].

Physical quantities	Time interval $280\,\mathrm{s} \leq t_a^d \leq 300\,\mathrm{s}$	Time interval $300\,\mathrm{s} \leq t_a^d \leq 320\,\mathrm{s}$
T_obs (keV)	0.44 ± 0.12	0.31 ± 0.05
ϕ_0 (cm)	$(5.6 \pm 3.2) \times 10^{11}$	$(1.44 \pm 0.48) \times 10^{12}$
$\langle\beta\rangle_{(\cos\vartheta=1)}$	$0.19^{+0.10}_{-0.11}$	$0.42^{+0.10}_{-0.12}$
$\langle\Gamma\rangle$	$1.02^{+0.03}_{-0.02}$	$1.10^{+0.07}_{-0.05}$
R_lab (cm)	$(7.1 \pm 4.1) \times 10^{11}$	$(2.34 \pm 0.78) \times 10^{12}$

Table 3.6. List of the physical quantities inferred from the thermal components observed during the flare of GRB 081008. For each time interval we summarize: the observed temperature T_obs, ϕ_0, the average expansion speed $\langle\beta\rangle$ computed from the beginning up to the upper bound of the considered time interval, and the corresponding average Lorentz factor $\langle\Gamma\rangle$ and laboratory radius R_lab.

where we used the definition of Γ given in previously.

For example, in GRB 081008 we observe a temperature of $T_\mathrm{obs} = (0.44\pm0.12)$ keV between $t_a^d = 280$ s and $t_a^d = 300$ s, i.e., 20 s before the flare peak time, and a temperature of $T_\mathrm{obs} = (0.31 \pm 0.05)$ keV between $t_a^d = 300$ s and $t_a^d = 320$ s, i.e., 20 s after the flare peak time, see the corresponding spectra in Figure 3.27. In these two time intervals we can infer ϕ_0 and by solving Equation (3.20) and taking the errors of the parameters properly into account, get the value of $\langle\beta\rangle$ corresponding to the average expansion speed of the emitter from the beginning of its expansion up to the upper bound of the time interval considered. The results so obtained are listed in Table 3.6. Moreover, we can also compute the value of $\langle\beta\rangle$ between the two time intervals considered above. For $\cos\vartheta = 1$, namely along the line of sight, we obtain $\langle\beta\rangle = 0.90^{+0.06}_{-0.31}$ and $\langle\Gamma\rangle = 2.34^{+1.29}_{-1.10}$. In conclusion, no matter what the details of the approximation adopted, the Lorentz gamma factor is always moderate, i.e., $\Gamma \lesssim 4$.

Chapter 4

High-energy emission from GRBs

In this chapter the reader will be introduced to the study of the GRB emission in high-energy domain of the spectrum. A possible origin of such an emission is given within the theoretical fireshell model as following from accretion onto a black hole.

4.1 Rationale

The *Fermi* space observatory has the widest spectral coverage. In total the onboard detectors operate in a range from 8 keV to 300 GeV. Thus, in order to study high-energy[1] counterpart of gamma-ray bursts we limit our sample with a condition to use data obtained by *Fermi*-LAT. Nevertheless, a comprehensive investigation is only possible with a usage of the whole amount of knowledge on every particular event. For this reason we actively use data by other missions and instruments, especially the information on redshift.

There are two approaches we can implement regarding the GeV band emission. The first approach is model independent and based on careful selection of the working sample by constraining the general list of observed GRBs. We give at the first place. The second approach instead is model-dependent and the working sample is therefore selected on the base of physical model in hand. We give this approach later.

Nevertheless, we can show that these two ways give the working samples which are comparable in size because the constraints in the model-independent approach are put with a possibility of further physical interpretation.

4.1.1 GRB population with high-energy counterpart

It is appropriate at first to give updated numbers on GRB population observed by *Fermi* space observatory, see Table 4.1.

The statistics to the date of July 20th 2018 is the following: *Fermi*-GBM telescope detected 2367 gamma-ray bursts (100%) among which there are 398 short (16.8%) and 1969 long (83.2%) duration GRBs, both are with and without measured redshift

---

[1] In gamma-ray astronomy the term "high energy" is defined for events occurring within energy interval of 30 MeV–100 GeV and it is usually associated with a detection technique which differs from ones of "low" 0.51–10 MeV, "medium" 10–30 MeV, "very high" 100 GeV–100 TeV, and "ultra high" > 100 TeV energies.

End time	GBM	$T_{90} < 2$ s.	$T_{90} \geq 2$ s.	LAT	$T_{90} < 2$ s.	$T_{90} \geq 2$ s.
July 2011	733	122 (16.6%)	611 (83.4%)	35 (4.8%)	5	30
Dec. 2016	1981	324 (16.4%)	1657 (83.6%)	122 (6.2%)	13	109
Dec. 2017	2232	366 (16.4%)	1866 (83.6%)	141 (6.3%)	13	128
July 2018	2367	398 (16.8%)	1969 (83.2%)	169 (7.1%)	14	155

Table 4.1. GRBs detection statistics for all-sky *Fermi*-GBM (8 keV–40 MeV) and *Fermi*-LAT (20 MeV–100 GeV) since the beginning of operational era. The first and the last rows correspond respectively to the time span of *The First Fermi-LAT GRBs Catalog* [10] and *The Second Fermi-LAT GRBs Catalog* [13]. Percentages in parentheses are related to the total number of bursts by GBM. Numbers were retrieved from online *Fermi*-GBM Burst Catalog and *Fermi*-LAT Bursts list.

values; out of this total number of bursts the *Fermi*-LAT telescope detected 169 bursts (7.1%) among which there are 14 short and 155 long duration GRBs, both are with and without measured redshift values. All numbers were retrieved from online *Fermi*-GBM Burst Catalog[2] and *Fermi*-LAT Bursts list.[3] As can be compared with *The First Fermi-LAT GRBs Catalog* [10], where during three years of observation *Fermi*-GBM detected 733 bursts and among this number *Fermi*-LAT confirmed 35 bursts (4.8%) detection with high energy counterpart, the bursts number accumulated according to the observational time increased by appropriate factor, although the correlation of rates (4.8% versus 7.1%) increased, and could be by virtue of recent improvements in event selection procedure [13].

4.1.2   Detectability of high-energy counterpart of GBRs

According to Ackermann et al. (2012) [9], for the sample of 620 GBM-triggered bursts (August 2008–December 2010), roughly half was within 65° of LAT boresight *z*-axis at the time of GBM trigger, namely 288 bursts (46%). The relative sky coverage of two instruments (2.4 steradian versus entire unocculted sky) made possible to expect this ratio and also allows to suppose similar ratio for larger sample collected up to the end of July 2018, namely the GRBs population regardless redshift presence.

The detection or non-detection is undoubtedly a matter of sensitivity of the *Fermi*-LAT detector and moreover the sensitivity itself depends on several essential parameters including photon energy, incident angle of photon, etc. Hence, we can make a statement that the brightness of bursts and the detection dependence on boresight angle both affect on detectability of high-energy counterpart of the bursts.

4.1.3   Brightness of GRBs with high-energy counterpart

If one compares the *Fermi*-GBM reported fluence $[\text{erg} \cdot \text{cm}^{-2}]$ values for those short and long GRBs which show also the presence of high-energy photons detected by *Fermi*-LAT (122 bursts to December 2016), then it will be possible to notice that short duration bursts have fluence values in a range (from 10^{-7} to 10^{-5} erg·cm^{-2}) comparable on systematical level with those of long duration events, see Figure 4.1.

---

[2] https://heasarc.gsfc.nasa.gov/W3Browse/fermi/fermigbrst.html

[3] https://fermi.gsfc.nasa.gov/ssc/observations/types/grbs/lat_grbs/
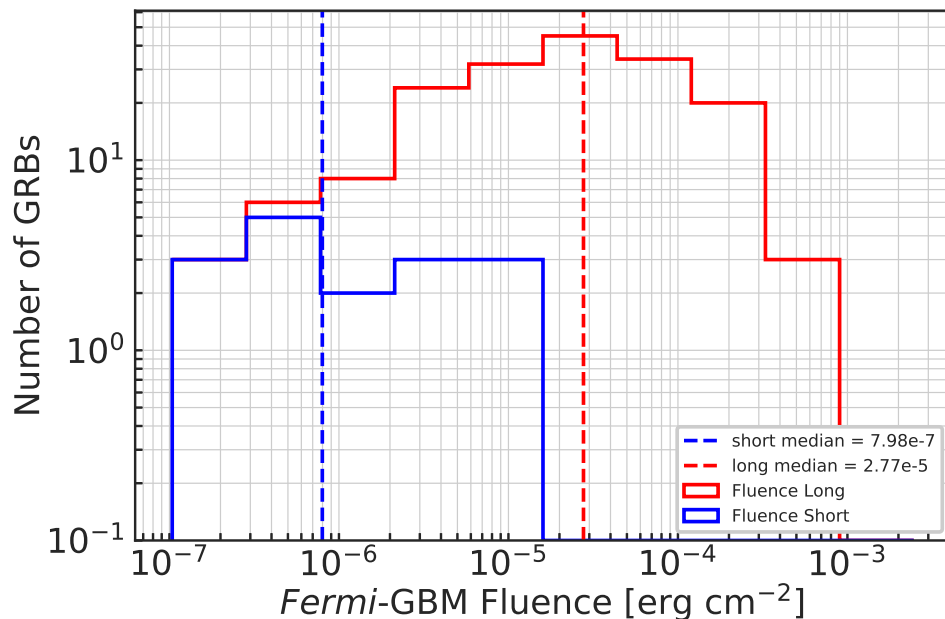
Figure 4.1. Histogram of 186 short and long bursts (August 2008–July 2018) as a function of GBM observed fluences [10–1000 keV]. Data on fluence values are retrieved from *Fermi*-GBM Burst Catalog cross-correlated to the *Fermi*-LAT Bursts list.

One should keep in mind that observed fluence value is an observed flux integrated over the duration of each burst and for long GRBs the T_{90} values are longer by 1-2 orders of magnitude (from tens to hundreds of seconds). Thus, only the burst duration in keV–MeV band creates the difference in fluence values, while observed flux values for both short and long GRBs show similar behavior.

4.1.4 Photons with maximum energy

Regarding the high energy photons from both short and long GRBs, one should notice that GeV counterpart lasts longer than the one of keV–MeV band and the clear temporal correlation on their duration is not found. It means that both short and long GRBs show equally prolonged emission in GeV high energy domain. Note that for high energy domain the term T_{90} for burst duration is not applicable directly. This means nothing but the fact that arrival time interval $T_{\mathrm{LAT,100}}$ for high-energy photons of long GRBs can be as rapid as the ones of short bursts, and *vice versa* GeV emission of short events can end as late as of long GRBs, see Table 4.3. Moreover, the phenomenological difference by keV–MeV duration for short and long GRBs vanishes since in GeV energy domain we are not able to distinguish the difference in their times of photons arrival as well as their photon counts. In its turn this means that arrival photons can be numerous or few without clear distinction between short or long events.

As an example we consider two brightest bursts of short and long GRBs, 090510A and 130427A, see Table 4.2. We retrieve publicly available *Fermi*-LAT data through

the query form[4] following the recommendations on Pass 8 Data (`P8R2`) event classification and selecting the set of photons that are best suited for the photon probability analysis under performance. The event and spacecraft data were constrained by the celestial coordinates (R.A. and Dec., J2000 epoch) of the object, the *region of interest* (ROI) defined as a circle of radius $10°$ centered at the γ-ray position of the burst, the time interval starting 100 s before the *Fermi*-GBM trigger and spanning to 10 000 s after the trigger and given in *mission elapsed time* (MET) units,[5] the energy range treated as the minimum and maximum boundary energy values (100–300 000 MeV) with an upper bound being well above the observable maximum energy of the photons. We remove a possible contamination from the Earth limb by cutting off all the events with zenith angle $> 90°$ and use only the time intervals in which the data acquisition by spacecraft was stable (`DATA_QUAL>0 && LAT_CONFIG==1`), so-called *good time intervals* (GTI). Consistently with the event selection we use models for a galactic interstellar emission `gll_iem_v06` and an isotropic emission `iso_P8R2_SOURCE_V6` to account for the contribution of diffuse γ-ray background.[6]

For GRB 130427A there are 762 photons as total number of counts detected by *Fermi*-LAT with the last photon arrived at 9976 s after trigger time. Out of total number there are 219 photons above 100 MeV (with last arrival photon at 9806 s) and of which 75 photons are above 1 GeV (with last arrival photon at 9597 s), both numbers with confidence level 90% to belong to the burst, Figure 4.2 upper plot.

For GRB 090510A there are 341 photons as total number of counts detected by *Fermi*-LAT with the last photon arrived at 7069 s after trigger time. Out of total number there are 84 photons above 100 MeV (with last arrival photon at 5036 s) and of which 30 photons are above 1 GeV (with last arrival photon at 99 s), both numbers with confidence level 90% to belong to the burst, Figure 4.2 lower plot.

From the above it can be seen that for photons > 100 MeV (with C.L. 90%) the difference between count rates is not more than the factor of three and the difference in duration values is not more than the factor of two. In other words, the difference is within the numerical factors of order unity. But one should be aware that we compare two of the brightest representatives of short and long bursts. Therefore to draw a conservative conclusion it is appropriate to look at the whole sample in hand.

In Figure 4.3 we build a histogram for $T_{\mathrm{LAT},100}$ listed in the Second LAT GRB Catalog [13]. One can clearly see that 17 short GRBs occupy intervals with median value $T_{\mathrm{LAT},100}^{\mathrm{short,med}} = 10.02$ s while 169 long bursts are more prolonged with median value $T_{\mathrm{LAT},100}^{\mathrm{long,med}} = 467.55$ s. Other differences can be traced in Table 4.3, where it is shown the numbers for long events being systematically larger by one order in magnitude (the latest $p > 0.9$ photon, mean, median). Nevertheless one should take into the account GRB population number difference being also one order of magnitude in favor of long bursts. And finally one should notice that in [100 MeV–100 GeV] band there is no more such a clear bimodality as for keV–MeV band [355] and two populations here overlap significantly.

Another phenomenological "hard-to-soft" correlation for spectra cannot be ap-

---

[4] `https://fermi.gsfc.nasa.gov/cgi-bin/ssc/LAT/LATDataQuery.cgi`

[5] MET is interpreted as a floating-point number of seconds since the mission epoch, specifically the midnight at the start of January 1st 2001.

[6] `https://fermi.gsfc.nasa.gov/ssc/data/access/lat/BackgroundModels.html`
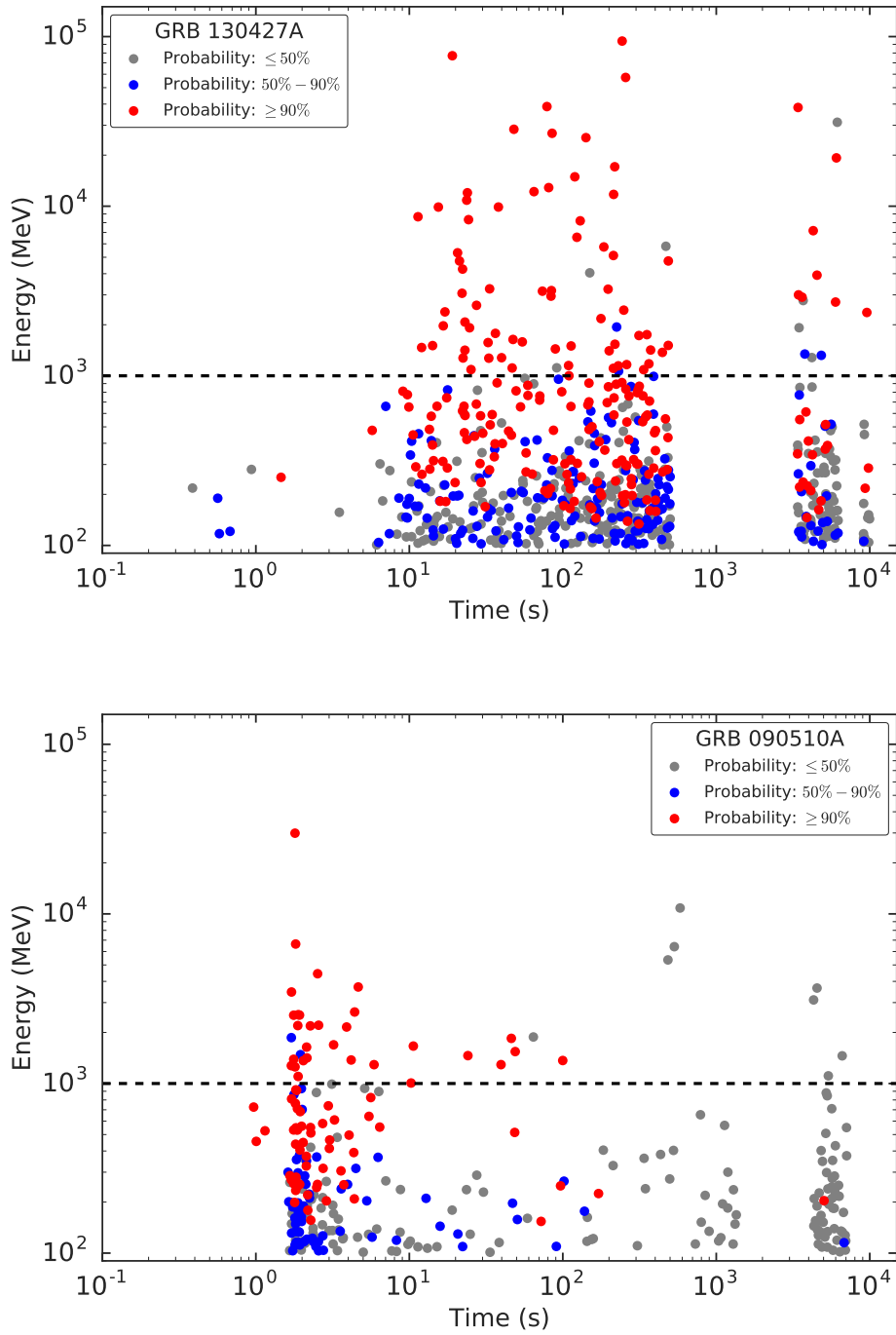
Figure 4.2. Photons of GRB 130427A (upper plot) and GRB 090510A (lower plot) in high-energy domain (100 MeV–100 GeV) observed by *Fermi*-LAT detector. Colour-coded probability values indicate how reliable the photon belongs to the event. The sharp edges on arrival time of the photons are due to the stop of operational mode of the instrument when satellite was passing over South Atlantic Anomaly (SAA).

GRB	Total photons detected	Last photon arrival	Photons $\geq$ 100 MeV (90% C.L.)	Last photon arrival	Photons $\geq$ 1 GeV (90% C.L.)	Last photon arrival
090510A	341	7069 s	84	5036 s	30	100 s
130427A	762	9976 s	219	9806 s	75	9597 s

Table 4.2. High-energy photons (100 MeV–100 GeV) detected by LAT from short-hard GRB 090510A and long-soft GRB 130427A. Here "90% C.L." stands for 90% *confidence level* that detected photon belongs to the burst. Time values are given relative to T_0 meaning the GBM trigger time.

GRB type	Type population	$T_{\text{LAT},0}^{\min}$ T_0+ (s)	$T_{\text{LAT},1}^{\max}$ T_0+ (s)	$T_{\text{LAT},100}^{\min}$ T_0+ (s)	$T_{\text{LAT},100}^{\max}$ T_0+ (s)	$T_{\text{LAT},100}^{\text{mean}}$ (s)	$T_{\text{LAT},100}^{\text{median}}$ (s)
Short	17	0.04	2889.0	0.15	2224.24	194.14	10.02
Long	169	0.02	55389.75	0.58	34667.46	1683.39	467.55
Total	186	0.02	55389.75	0.15	34667.46	1436.58	386.85

Table 4.3. Statistics on LAT GRBs duration. The minimal start time $T_{\text{LAT},0}^{\min}$ and the maximal end time $T_{\text{LAT},1}^{\max}$ are relative to T_0 trigger time of GBM. The values of $T_{\text{LAT},100}$ are related to total duration of the emission within [100 MeV–100 GeV] with $p \gtrsim 0.9$ probability of the photons to be associated with particular GRB. All values are given in observer's frame. Data retrieved from [13].

plied because we are working in different energy range where such a correlation is not easy to trace, mainly due to poor statistics. There is also not a clear connection between "hard-to-soft" correlation in keV–MeV band and other observational patterns in high-energy band. These and other questions are extensively studied in recent publication [13].

4.2   Sampling and criteria

4.2.1   Model-independent approach

A list is constructed from GRBs with high-energy counterparts observed by *Fermi*-LAT from August 2008 to December 2017. We cross-correlate the online *Fermi*-GBM catalog[7] (see recent publication [355]) with online *Fermi*-LAT table of GRBs.[8] Our sample is restricted to the ones with a measured value of spectroscopic redshift. The selection gives a number of **30 GRBs**, of which 11 bursts present in The First *Fermi*-LAT GRB Catalog [10]. We retrieve all the appropriate information on the multiwavelength follow-up by x-ray, optical/near-infrared and radio telescopes from the *Swift* light curve repository [143, 144], the `GCN` circulars[9] as well as the literature and list it in table.

In the Table 4.4 there listed is a basic information on sample GRBs detected by *Fermi*-LAT within August 2008–December 2017 and its multiwavelength follow-up. Written in boldface and highlighted are (by columns): "GRB" is a short duration

---

[7] `https://heasarc.gsfc.nasa.gov/W3Browse/fermi/fermigbrst.html`

[8] `https://fermi.gsfc.nasa.gov/ssc/observations/types/grbs/lat_grbs/`

[9] `https://gcn.gsfc.nasa.gov/`
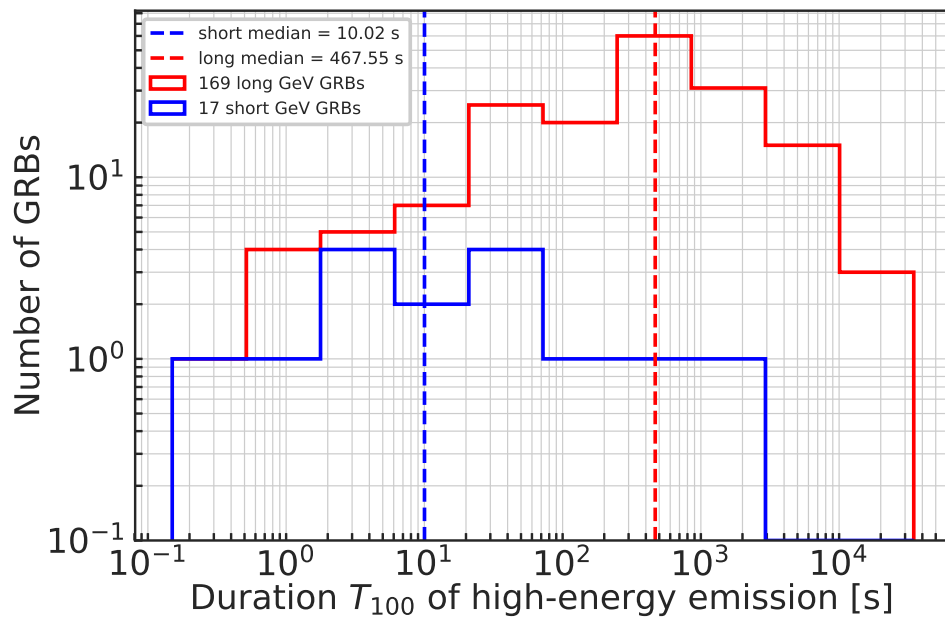
Figure 4.3. Distribution for the arrival durations of high-energy photons from bursts listed in the Second LAT GRB Catalog [13].

burst; "z" is a redshift determined photometrically; "T_{90}" is time duration defined through observation by instrument other than *Fermi*-GBM; "θ" are boresight angles (in degrees) exceeding the nominal LAT sensitivity detection threshold of $\theta_{max} \approx 75°$ at trigger. Signs "Y", "N" and "−" stand, respectively, for "detected", "not detected" and "not observed" regarding the x-ray, optical/near-infrared and radio afterglows of each GRB. The values of T_{90} (in seconds) are retrieved from the *Fermi*-GBM Burst Catalog [355] where they were calculated within the conventional energy range (50–300 keV).

Out of 30 GRBs in our sample all of them have x-ray and optical/near-infrared follow-up observations, and 21 bursts have radio follow-up observations. These observations resulted in 30 x-ray afterglows, 30 optical/near-infrared afterglows, and 15 radio afterglows, representing multiwavelength follow-up detection efficiency of 100%, 100%, and 50%, respectively.

Regarding the *Fermi*-LAT boresight angle θ at the trigger (see Table 4.4), one can distinguish that 5 bursts occurred at $\theta \lesssim 30°$, a fraction of 16 events triggered at $30° \lesssim \theta \lesssim 60°$, and the rest of 9 GRBs were detected at boresight angle $\gtrsim 60°$. As was stated above, this points to the LAT sensitivity being able to catch dimmer sources closer to the boresight and showing that only brighter events can be detected close to the edge of the FoV.

As the redshift is a major criterion for sample selection and derivation of physical quantities, then we present additional details. All but one (GRB 080916C)[10] distances

---

[10] The redshift of the object GRB 080916C was determined through series of photometric observations by GROND instrument, where Lyman-α break at $z = 4.35 \pm 0.15$ serves as the best

GRB	z	T_{90}	θ	X-ray	Opt/NIR	Radio	Comments	References
080916C	4.35	62.98	48.8	Y	Y	N	photometric z	[195, 178, 509, 248, 415, 505, 86, 353, 346]
090323A	3.57	133.89	57.2	Y	Y	Y		[83, 376, 246, 416, 540, 228, 243, 220, 544]
090328A	0.736	61.70	64.5	Y	Y	Y		[67, 334, 245, 247, 316, 365, 448, 538, 160]
090510A	0.903	0.96	13.6	Y	Y	N	short burst	[439, 211, 377, 229, 202, 264, 266, 382, 381, 159]
090902B	1.822	19.33	50.8	Y	Y	Y		[105, 40, 120, 251, 508, 380, 210, 547, 74]
090926A	2.1062	13.76	48.1	Y	Y	N		[301, 39, 536, 551, 197, 370, 93, 69, 345]
091003A	0.8969	20.22	12.3	Y	Y	—		[104, 437, 333, 504, 196, 214, 430, 569]
091208B	1.0633	12.48	55.6	Y	Y	—		[570, 412, 332, 394, 121, 63, 577, 539, 412]
100414A	1.368	26.50	69.0	Y	Y	Y		[103, 154, 510, 396, 275, 150, 542, 76, 240, 161]
100728A	1.567	165.38	59.9	Y	Y	—	late redshift	[260, 560, 62, 141, 367, 379]
110731A	2.83	7.49	3.4	Y	Y	N		[517, 198, 51, 372, 366, 36, 305, 587]
120624B	2.1974	271.36	70.8	Y	Y	Y		[131, 199, 553, 293, 113, 122, 52, 28]
120711A	1.405	44.03	134.5	Y	Y	N	delayed obs	[518, 200, 512, 32, 271, 140, 216, 218, 217]
120729A	0.8	25.47	82.7	Y	Y	N	delayed obs	[514, 438, 537, 369, 557, 233, 118, 280, 499]
130427A	0.3399	138.24	47.3	Y	Y	Y	SN 2013cq	[285, 574, 153, 561, 595, 317, 339, 594, 511, 588, 406, 559]
130518A	2.488	48.58	41.0	Y	Y	Y		[489, 102, 572, 385, 142, 527, 526, 65]
130702A	0.145	58.88	75.2	Y	Y	Y	SN 2013dx	[498, 284, 115, 352, 96, 81, 119, 425, 209, 116, 495, 411, 545]
130907A	1.238	250.0	105.5	Y	Y	Y	delayed obs	[127, 555, 398, 283, 493, 59, 189, 98, 546, 19]
131108A	2.4	18.18	23.8	Y	Y	Y		[126, 580, 583, 435, 506, 79, 191, 529, 407]
131231A	0.6439	31.23	38.1	Y	Y	—		[581, 101, 238, 501, 310, 225, 307, 408]
141028A	2.332	31.49	27.5	Y	Y	—		[578, 440, 41, 250, 496, 193, 530, 324]
150314A	1.758	10.69	47.1	Y	Y	Y		[123, 585, 22, 213, 212, 573, 311, 278]
150403A	2.06	22.27	55.2	Y	Y	—		[433, 592, 296, 291, 57, 265, 190]
150514A	0.807	10.81	38.5	Y	Y	—		[128, 443, 257, 252, 314, 582]
160509A	1.17	369.67	32.0	Y	Y	Y		[515, 441, 297, 249, 286, 70, 16, 71, 347]
160623A	0.367	107.78	83.3	Y	Y	Y		[308, 66, 300, 552, 344, 47, 426, 60, 541, 348, 358]
160625B	1.406	453.39	41.5	Y	Y	Y		[579, 133, 56, 138, 338, 364, 531, 94, 204, 543, 17, 349]
170214A	2.53	122.88	33.0	Y	Y	Y		[261, 299, 434, 31, 48, 533, 304, 492, 322]
170405A	3.51	78.59	52.2	Y	Y	—		[125, 230, 554, 524, 276, 303, 205, 532, 95]
171010A	0.3285	107.27	114.6	Y	Y	Y	SN 2017htp	[242, 132, 423, 386, 109, 50, 302, 567, 268, 323, 227, 279, 226]

Table 4.4. Basic information on model-independent sample of 30 GRBs with measured redshift and high-energy photons (100 MeV–100 GeV) detected by *Fermi*-LAT within August 2008–December 2017 and its multiwavelength follow-up. See further details in the text.

were identified through spectroscopic observations in optical/near-infrared band by ground-based telescopes of predominantly large size. For 5 events the redshift measurements were implemented through bright emission lines in the spectra of their host galaxies [260, 131, 498, 308, 242]; the number of 8 bursts exhibited redshifts from the spectral absorption in their afterglows spectra due to Lyman-α forest [195, 83, 301, 517, 489, 126, 433, 125]; and the rest of redshifts were identified due to various elemental lines of emission or absorption, see Table 4.4. One should note that Lyman-α signature is appropriate only for distant bursts (sample min $z = 2.06$), being indicative for proper high-z determination.

Moreover, there are 3 gamma-ray bursts with GeV emission from our sample which were further accompanied by brightening of supernovae: GRB 130427A-SN 2013cq [130], GRB 130702A-SN 2013dx [494], GRB 171010A-SN 2017htp [132]. In particular, for the object GRB 130427A-SN 2013cq there was a supernova prediction [467] proposed in accordance to the Induced Gravitational Collapse (IGC) scenario [450] of the theoretical fireshell paradigm, see recent publications [465, 566, 473]. An interest arouses to explore these three GRB-SN with GeV emission as ensemble and contrast it to the rest GRB-SN population.

Below we give the details on sample GRBs with some observational peculiarities which can be retraced in the Table 4.4.

Radio observation of GRB 080916C was performed ≈ 9.5 months after the trigger [346] and resulted as awaited with no detection. Its redshift $z = 4.35 \pm 0.15$ was defined through the photometric observations with the 7-channel GROND instrument at the 2.2-meter MPI/ESO telescope [195].

GRB 090510A is the only short duration burst present in our sample. Nevertheless, it demonstrated very bright emission activity across the whole electromagnetic spectrum—high-energy gamma-ray, low-energy gamma-ray, x-ray, optical/near-infrared—with the only non-detection in radio band [159]. There are extensive investigations in the literature focused on this peculiar short burst.

A follow-up observations of GRB 100728A were performed in several runs by the optical GROND instrument [194] at the 2.2-meter MPI/ESO telescope. Initially, very faint source was detected on images obtained ~ 7 hours after trigger, and 24 minutes of total exposure resulted with estimation of the upper-limits [379]. A late observational run was performed 105 days after trigger and lasted in total 4427 seconds for $g'r'i'z'$ filters and 3600 seconds for near-infrared JHK filters. These deep observations allowed to detect an extended object with $0.4''$ offset with respect to GRB 100728A. The spectrum of discovered galaxy was taken two years after in 2012 by VLT/X-Shooter with 2400 seconds exposure. The emission lines due to [O II] 3729 Å and H$_\alpha$ 6563 Å occur at a common redshift $z = 1.567$ being the distance to GRB host galaxy [260]. No observations were performed in radio band.

GRB 120711A was triggered by *INTEGRAL* observatory [192] making possible a multiwavelength observations. The follow-up campaign resulted in measurement of the flux in x-ray and optical/near-infrared bands and determination of the redshift $z = 1.405$, see reference [518]. The value of LAT boresight angle at the moment of trigger was $134.5°$, see reference [200], so the GRB occurred out of instrument FoV. Nevertheless, this burst was bright enough to result in a *Fermi* spacecraft

---

explanation for deviation of measurements in i' to r' bands from the power-law slope $\beta = 0.38 \pm 0.20$.

Autonomous Rapid Repoint (ARR) maneuver. Late-time observation from 0.8 ks to ~ 7 ks showed photons up to 2 GeV with 7σ significance [512]. Such burst duration is one of the longest for a GRB in GeV domain. Radio observations revealed no counterpart at longer wavelength [217].

Similar condition with a high value of LAT boresight angle 82.7° was for the object GRB 120729A, see reference [438]. Provided by x-ray position a rapid follow-up by various ground-based telescopes identified an optical transient and a redshift of $z = 0.80$, see reference [514]. A post-processing of LAT data with known coordinates from data query server shows 5σ significance (TS=33.14) of the high-energy photons to be attributed with GRB 120729A. Hence, the presence of GeV emission concluded via data analysis.[11]

GRB 130907A has not triggered *Fermi* because the spacecraft was passing over the South Atlantic Anomaly and the boresight angle at operations resume was 105.5°, see reference [555]. Therefore, its total duration was defined through the observation by *INTEGRAL*-SPI/ACS being about 250 seconds [490]. The burst entered LAT FoV at $\sim T_0 + 3400$ s, and further likelihood analysis resulted in a detection of the source with 6σ significance[12] (TS=38) at the position provided by ground-based telescope in optical band. A position compatible 55 GeV photon was observed at $\sim T_0 + 18$ ks [555]. The redshift of GRB 130907A is $z = 1.238$ provided by NOT instrument [127].

Occurred at boresight angle $\theta = 83.3°$ the object GRB 160623A entered LAT FoV ~ 400 s after the trigger and was active up to ~ 12 ks [552]. Initially proposed as a galactic transient [519] due to the position close to the Galactic plane L.=84.17, B.=-2.69, later was dispelled as the redshift $z = 0.367$ to the source was measured [308, 66]. More than 15 photons above 1 GeV were detected, and likelihood analysis results in very high significance (TS=201.22).

GRB 171010A was outside FoV ($\theta = 114.6°$) at the time of GRB trigger and was observed by LAT with an autonomous repoint of the spacecraft [423]. The highest detected photon is 7 GeV observed 768 s after the GBM trigger. Further likelihood analysis shows high statistical significance of TS=224.61 being a strong confirmation for high-energy counterpart.[13]

For 9 GRBs (091003A, 091208B, 100728A, 131231A, 141028A, 150403A, 150514A, 170214A, 170405A) there were no follow-up observations in radio band, and for other 6 GRBs (080916C, 090510A, 090926A, 110731A, 120711A, 120729A) radio follow-up resulted in no detection, see Table 4.4.

4.2.2 Model-dependent approach: fireshell sample selection

We address the specific role of the GeV radiation in order to further characterize the nine subclassess of GRBs within the fireshell paradigm, presented in [471] and updated in [472]. In Table 4.5 we have indicated, for each GRB subclass, their name, their progenitors characterizing "in-state" and "out-state" of the merging process. In all cases the progenitors are binary systems composed of various combinations of

---

[11] `https://fermi.gsfc.nasa.gov/ssc/observations/types/grbs/lat_grbs/120729456`

[12] `https://fermi.gsfc.nasa.gov/ssc/observations/types/grbs/lat_grbs/130907904`

[13] `https://fermi.gsfc.nasa.gov/ssc/observations/types/grbs/lat_grbs/171010792`

Class	Type	Previous Alias	*In-state*	*Out-state*	$E_{\rm p,i}$ (MeV)	$E_{\gamma,\rm iso}$ (erg)	$E_{\rm iso,Gev}$ (erg)
Binary Driven	I	BdHN	$CO_{\rm core}$-NS	νNS-BH	~ 0.2–2	$\sim 10^{52}$–10^{54}	$\gtrsim 10^{52}$
Hypernova	II	XRF	$CO_{\rm core}$-NS	νNS-NS	~ 0.01–0.2	$\sim 10^{50}$–10^{52}	–
(BdHN)	III	HN	$CO_{\rm core}$-NS	νNS-NS	~ 0.01	$\sim 10^{48}$–10^{50}	–
	IV	BH-SN	$CO_{\rm core}$-BH	νNS-BH	$\gtrsim 2$	$> 10^{54}$	$\gtrsim 10^{53}$
	I	S-GRF	NS-NS	MNS	~ 0.2–2	$\sim 10^{49}$–10^{52}	–
Binary	II	S-GRB	NS-NS	BH	~ 2–8	$\sim 10^{52}$–10^{53}	$\gtrsim 10^{52}$
Merger	III	GRF	NS-WD	MNS	~ 0.2–2	$\sim 10^{49}$–10^{52}	–
(BM)	IV	FB-KN*	WD-WD	NS/MWD	< 0.2	$< 10^{51}$	–
	V	U-GRB	NS-BH	BH	$\gtrsim 2$	$> 10^{52}$	–

Table 4.5. Summary of the GRB subclasses in *fireshell* model. In addition to the subclass name, we recall as well the "in-state" representing the progenitors and the "out-state" as well as the $E_{\rm p,i}$ and $E_{\gamma,\rm iso}$ for each subclass. We finally indicate the GeV emission in the last column which for the long GRBs is only for the BdHNe I and BdHNe IV (BH-SN), in the case of short bursts is only for S-GRBs and in all of them the GeV emission has energy more than $\sim 10^{52}$ erg.

$CO_{\rm core}$, undergoing a SN explosion, of the νNS created in such SN explosion, of NS, of white dwarfs (WDs), of a BH, see also 1.2 for summary of fireshell paradigm.

For our goal we consider sources detected by *Fermi*-LAT instrument with their essential information of the cosmological redshift. In particular we characterize the difference between XRFs, BdHNe and BH-SN.

Two possible progenitor systems of long GRBs have been previously identified in [471]: a binary system composed of a $CO_{\rm core}$, exploding as SN Ic, and a NS companion (see, e.g., [456, 450, 165]); and an analogous binary system where the binary companion of the exploding $CO_{\rm core}$ is an already formed BH. Binary X-ray sources such as Cygnus-X1 are possible progenitors of these last systems.

Firstly, we address the system with the NS binary companion. As the SN ejecta from the exploding $CO_{\rm core}$ engulfs the close NS binary companion [34, 33] a hypercritical accretion process occurs with the emission of $\nu\bar{\nu}$ pairs and, for tight binaries, the formation of an e^+e^- plasma [450]. The presence of a NS companion explains the observed removing the outer layers of the $CO_{\rm core}$ [165].

According the interpretation, when the orbital period of the binary system is $\gtrsim 5$ min, the hypercritical accretion is not sufficient to trigger the collapse of the NS companion into a BH. Therefore, a MNS is formed creating a binary with the νNS originated in the SN explosion of the $CO_{\rm core}$. The absence of the formation of the BH justifies their observed peak energy in the range 4 keV$< E_{\rm p,i} < 300$ keV and isotropic energy in the range of $10^{48} \lesssim E_{\rm iso} \lesssim 10^{52}$ erg and have been indicated as X-ray flash (XRF) in contrast with the more energetics long GRBs [465, 34, 33, 471].

However, when the orbital period is as short as ≈ 5 minutes, the hypercritical accretion proceeds at higher rates and the companion NS reaches its critical mass leading to 1) the formation of a BH in a binary system with the νNS [164], 2) the emission of a GRB with $E_{\rm iso} \gtrsim 10^{52}$ erg and $E_{\rm p,i} \gtrsim 0.2$ MeV, and 3) the onset of the GeV emission when present is observed following the formation of the newly-born BH. These systems have been indicated as BdHNe [465, 34, 164, 33, 471]. The BH formation and the associated GRB emission occur seconds after the onset of the SN explosion (see, e.g., the case of GRB 090618 in [235]).

An extended list of Binary-driven Hypernovae GRBs was introduced in [421]

which was further updated to the total number of 345 events [472]. The number of 193 sources have been identified after the launch of *Fermi* all with the given redshift, with their in-states represented by a CO_{core}-NS binary and their out-state represented by a νNS, originated in the SN explosion of a CO_{core} and a companion BH, their spectral peak energy has the range 0.2 MeV$< E_{p,i} < 2$ MeV, isotropic energy $10^{52} < E_{iso} < 10^{54}$ erg and their isotropic GeV emission is $\sim 10^{52}$ erg.

Concerning the subclass with progenitor a CO_{core}-BH binary and their out-state represented by a νNS, originated in the SN explosion of a CO_{core} and a companion BH. Their spectral peak energy is larger than 2 MeV, isotropic energy, $E_{iso} > 10^{54}$ erg and their isotropic GeV emission is $\sim 10^{53}$ erg.

Such large values of the energy has been interpreted as obtained on the ground of previously existing BH or the formation of a newly born BH which prompts to analyze the role of the GeV emission as a further confirmation of the BH formation process.

In our classification we have considered 48 XRFs, long GRBs associated with SN with $E_{iso} < 10^{52}$ erg and $E_{p,i} < 300$ keV observed after the launch of *Fermi* [472]. In our approach they originate from a progenitor of the binary CO_{core}-NS in which due to large binary separation, typically more than 10^{11} cm, the critical mass of NS is not reached and the BH is not formed [471]. Our assumption that GeV radiation originates from BH leads to an absence of GeV radiation from XRFs.

Indeed, only 7 XRFs—fulfilling the criteria—were observed by *Fermi*: 3 outside the boresight angle and 4 inside; in none of them GeV emission has been observed, offering a support linking the GeV emission exclusively to the rotational energy of the BH.

Clearly, an important result inferred from the structure of BdHNe follows from the observation of high-energy photons. We address the 193 BdHNe with known redshifts [472]: out of them we are interested only in the **21 BdHNe**—fulfilling the selection criteria—with the boresight angle of *Fermi*-LAT less than 75° at the trigger time and having TS value > 25 to exclude at 5σ the GeV photons from background sources.

4.2.3   Samples matching

If one compares a model-independent sample with the one of the fireshell paradigm selection, then the following should be noticed: independent sample (30 GRBs) is bigger than fireshell sample (21 GRBs). In order to balance them we take into account that:

- The independent sample is made up to the end on 2017—so, the fireshell paradigm does not contain 3 GRBs; another criterion is a boresight angle at the trigger which exceeds the one adapted $\theta_{max} \approx 75°$—hence, the fireshell model does not contain additional 4 GRBs;[14]

- There is only one mismatch regarding the requirement on energetics—object GRB 130702A—with an isotropic-equivalent energy $E_{iso} \approx (6.5 \pm 0.1) \times 10^{50}$ erg. We dedicate the next Section 4.2.4 to describe this burst in details;

---

[14] One burst was already excluded because occurred in 2017—GRB 171010A.

- In the fireshell model sample there is an exclusion of the short duration GRB 090510—the only short gamma-ray burst with both the high-energy counterpart and the redshift measured. According to the fireshell classification the Binary-driven Hypernovae (BdHNe) are only long duration GRBs; short bursts with high energetics are named "authentic" short, being a subclass of two-fold short classification, see the reference [471].

Apart these variances our two samples are identical. Hence, in the rest of the chapter we will refer to a sample from the *fireshell* model and use the naming BdHN instead of GRB which in general should not cause any confusion.

4.2.4 The case of GRB 130702A

At 00:05:23.079 UT on July 2nd 2013 an object GRB 130702A triggered *Fermi*-GBM (trigger 394416326, full name 130702004) [96]. Its light curve shows typical FRED-like behavior[15] with a duration $T_{90} \approx 59$ s [50–300 keV]. The burst was also observed by *Konus*-WIND [184] and *INTEGRAL*-SPI/ACS space telescopes and together with *Fermi*-GBM they have triangulated an event to annulus with 3σ significance [231]. Much more accurate was the position based on 3.4 ks observation in Photon Counting mode performed by *Swift*-XRT on Target of Opportunity (ToO) request [119]; later the XRT confirmed the fading activity of x-ray afterglow based on additional 6.2 ks observation [117] as well as did the *Swift*-UVOT [425]. Final localization at RA(J2000)= $14^{h}29^{m}14.78^{s}$ Dec(J2000)= $+15°46'26.4''$ was obtained by optical 48-inch telescope [498].

The burst was also active in high-energy domain triggering *Fermi*-LAT instrument [81]. The possibility to be detected at boresight angle $\theta \approx 75°$ at trigger demonstrates the burst was bright. Being already outside the nominal field of view (FoV) of the LAT ($\sim 65°$) the object re-entered the FoV at $T_0 + 250$ s to exit again at $T_0 + 2200$ s. More than 5 photons above 100 MeV were observed within $10°$ of the source location and the highest photon energy is a 1.5 GeV event observed at $T_0 + 260$ s. A standard likelihood analysis results with Test Statistics value TS= 29.7, i.e., 5σ significance of the signal.[16]

Observational campaign taken by ground-based telescopes involved many observatories with small, middle and large aperture telescopes. They were in charge of obtaining the location [498], photometry [209, 287, 575, 116, 495, 58, 413, 427, 571] and the spectrum [284, 115, 352, 494, 134] of transient event GRB 130702A. The numerous observations were possible due to the precise localization, and rather than *Swift*-XRT provided ones, the position of this burst was first identified by ground-based optical telescope [498] based on searching ≈ 71 deg^2 surrounding of localization provided *solely* by *Fermi*-GBM. The redshift of GRB 130702A is defined as $z = 0.145 \pm 0.001$ based on [Ca II] absorption line and H$_\alpha$ 6562.8 Å, [O II] 3727.5 Å and [O III] 4959.0/5006.8 Å emission lines [284, 115, 352]. An equivalent luminosity distance is calculated as $d_L = 680$ Mpc.

Radio observatories performed a successful follow-up [411, 545, 99, 72]. Their observations taken within 2.01^d–3.05^d post-trigger confirmed the presence of a radio

---

[15] `http://www.ioffe.ru/LEA/GRBs/GRB130702A/`

[16] `https://fermi.gsfc.nasa.gov/ssc/observations/types/grbs/lat_grbs/130702004`

afterglow in several bands.

This burst is later accompanied by a brightening of the Type Ic supernova SN 2013dx in optical band.[17] The observation at 5.97^d post-trigger revealed color evolution pointing to the emerging supernova [494], which further got an independent confirmation [68, 134, 253]. Its spectral features were reported to be comparable to previous GRB-associated supernovae such as SN 2006aj and SN 1998bw at the similar epoch.

An excellent overview of the photometric and spectroscopic observations is given in publication [497]. There it is noted that while the x-ray and optical counterparts behave typically for GRB afterglows, they were, however, scaled down by a factor of ~ 10 compared to other *Swift* detected bursts.

From the point of energy release in γ-ray band of the prompt phase an isotropic-equivalent energy is calculated as $E_{\gamma,\mathrm{iso}} \approx (6.5 \pm 0.1) \times 10^{50}$ erg (90% upper limit [18]). This estimate places GRB 130702A among less energetic than typical bursts of $E_{\mathrm{iso}} \gtrsim 10^{52}$ erg if put on $E_{\mathrm{p,i}}$-E_{iso} diagram, so-called, Amati relation.[18] However if compare to other GRB-SN events such as canonical GRB 980425-SN 1998bw with $E_{\gamma,\mathrm{iso}} = 1.0 \times 10^{48}$ erg [417] and GRB 060218-SN 2006aj with $E_{\gamma,\mathrm{iso}} = 6.2 \times 10^{49}$ erg [61] then we see that supernova SN 2013dx is very bright.

A detailed study of the host galaxy of GRB 130702A revealed its type as a dwarf and metal-poor satellite of a massive, metal-rich galaxy [244]. The offset of exploded GRB-SN from the center of bright ($r = 18.1$ mag) red massive galaxy is $\sim 7.6''$ (19.1 kpc in projection) while for a much fainter ($r = 23$ mag) dwarf galaxy the offset is $\sim 0.6''$ (1.5 kpc in projection) measured from its center. The authors accurately measured galaxies' redshift values through studying their H_α profiles and place 2σ upper limit on their line-of-sight velocity dispersion $\lesssim 60$ km s^{-1} showing that these two galaxies are indeed physically connected as local group. By fitting stellar population synthesis models to the above objects together with the third bright blue galaxy having similar redshift (as given by SDSS photometric study), they estimated masses of three galaxies and suggested that the bright red galaxy should dominate the local gravitational potential due to the largest mass. Calculated star-formation rate (SFR) for dwarf galaxy gives a value ~ 0.05 $M_\odot$ yr^{-1}. The peculiarity authors found and underline is that GRB 130702A—being long duration burst—was detected for the first time as occurring in dwarf metal-poor galaxy, and if the trend is universal then it is raising the question of superimposed faint dwarf and bright giant galaxies of the previously detected L-SGRBs.

Another combined spectroscopic observations resulted in extensive study of the burst with a particular focus to SN 2013dx [135]. Based on similarity in the peak luminosity and the photospheric velocities with other GRB-SN population, the physical parameters of SN 2013dx were obtained via empirical method of rescaling the parameters of already known SNe. Authors estimated a synthesized ^{56}Ni mass to be ~ 0.2 $M_\odot$, total ejecta mass $M_{ej} \sim 7$ $M_\odot$ and kinetic energy $E_K \sim 35 \times 10^{51}$ erg. Properly examining the field galaxies around the target one they surprisingly found that 65% of them have the same redshift, hence representing not single host galaxy but the galaxy group or cluster. This conclusion goes in parallel with the previously

---

[17]http://simbad.u-strasbg.fr/simbad/sim-basic?Ident=sn+2013dx&submit=SIMBAD+search
[18] http://www.iasfbo.inaf.it/~amati/grb130702a.pdf

GRB 130702A-SN 2013dx		
Parameter	Value	Comments & references
location	$14^{\rm h}29^{\rm m}14.78^{\rm s}$; $+15°46'26.4''$	RA(J2000); Dec(J2000) [498]
host	dwarf	galaxy type [244]
offset	$\sim 0.6''$	from the galaxy center [244]
z	0.145 ± 0.001	[Ca II], H_α, [O II], [O III] [284, 115, 352]
d_L	680 Mpc	luminosity distance
T_{90}	59 s	50–300 keV burst duration [96]
$E_{\gamma,{\rm iso}}$	$(6.5 \pm 0.1) \times 10^{50}$ erg	isotropic energy, 90% upper limit [18]
θ	75°	initial LAT boresight angle [81]
TS	29.7	$> 5\sigma$ likelihood Test Statistic
$M_{\rm Ni}$	$\sim 0.2\ M_\odot$	estimate of synthesized ^{56}Ni mass [135]
M_{ej}	$\sim 7\ M_\odot$	estimate of total ejecta mass [135]
E_K	$\sim 35 \times 10^{51}$ erg	estimate of SN total kinetic energy [135]

Table 4.6. Main observed and derived parameters of GRB 130702A-SN 2013dx.

mentioned idea of superimposed galaxies and partly enriches it.

Another study [523] presents an extensive optical/near-infrared photometry and optical spectra with the modeling of the underlying SN component. The estimates for SN explosion parameters give $M_{\rm Ni} = 0.37 \pm 0.01\ M_\odot$, $M_{ej} = 3.1 \pm 0.1\ M_\odot$ and $E_K = (8.2 \pm 0.4) \times 10^{51}$ erg. The comparison of SN 2013dx with other GRB-SN and just SNe populations resulted with no clear correlation between $M_{\rm Ni}$, M_{ej}, E_K and GRB isotropic energy $E_{\gamma,{\rm iso}}$, even when considering beaming correction.

Recent study [558] performed a multicolour modeling of SN 2013dx based on wealth observational data of 88 days campaign. In order to separate SN from GRB emission authors have carefully treated data in optical band accounting for the contribution from GRB afterglow, emission from host galaxy as well as light extinction in both host and Milky Way galaxies. The numerical calculations were performed with one-dimensional radiative hydrodynamics code and resulted with the following estimates: progenitor mass $M_{\rm WR} = 25\ M_\odot$, energy of the outburst $E_{\rm outburst} = 3.5 \times 10^{52}$ erg, mass of the remnant $M_{\rm remnant} = 6\ M_\odot$, and SN radiative efficiency $\eta > 0.1\%$ upper bound. It should be underlined that authors derived these values not via rescaling the results from previous simulations of other SN but performed a modeling tailored to data of SN 2013dx. They concluded that central engine of GRB 130702A-SN 2013dx is of similar nature to those of GRB 111209A-SN 2011kl and GRB 130831A-SN 2013fu although their isotropic energy values are higher by several orders.

For the purpose of convenience we summarized main observed and derived quantities in Table 4.6.

We turn our attention to the object GRB 130702A because its isotropic-equivalent energy is surprisingly low [18] and due to criterion on energy it gets out of the BdHNe list with GeV emission resulted from the fireshell model sample selection. That is the main contradiction since all the other features are consistent with the definition of Binary-driven Hypernovae subclass of the long GRBs.

The Induced Gravitational Collapse (IGC) scenario suggests a SN explosion in

binary progenitor and indeed the brightening of SN was observed. According to the fireshell paradigm the subclass of BdHNe should be active in high-energy domain; the signal with high significance was indeed observed and GeV photons were caught by *Fermi*-LAT. But according to the fireshell paradigm the GeV photons and the SN occurrence should be attributed to BdHNe with isotropic energy $E_{\gamma,\mathrm{iso}} > 10^{52}$ erg.

Here one cannot argue and refer to the missing part of the γ-ray signal because the *Fermi*-GBM was observing the burst from the beginning and measured single pulsed FRED-like curve which is common for many GRBs. Early precise positioning allowed a big observational campaign which stated that afterglow of GRB 130702A behave typically in x-ray and optical bands. This excludes any possibility for claiming the exceptional density of the event surroundings that could absorb part of the radiation.

Detailed study of the galaxy field rather opens a prospect for more comprehensive study of the host environment with new facts and does not crucially contradict to previous findings. A sensitive studies of SN 2013dx resulted with numbers which are similar to other GRB-SN population. An estimated upper bound on kinetic energy does not reach watershed value of 10^{52} erg needed to operate BdHNe system in order to have the energy budget sufficient to drive a hypercritical accretion with following collapse of a NS to a BH. The latter has a role of the engine for high-energy photons generation and acceleration and it is a key element in BdHNe scenario.

Thus, to the present moment there is no reasonable explanation within fireshell paradigm given to the phenomenon of this low energetic burst. We conclude that the object GRB 130702A associated with SN 2013dx, located at redshift $z = 0.145$ with estimated isotropic-equivalent energy $E_{\mathrm{iso}} \approx (6.5 \pm 0.1) \times 10^{50}$ erg and with counterparts on entire electromagnetic spectrum including an activity in high-energy domain represents by itself an exceptional outlier for the *fireshell* model.

4.2.5 Release of the Second *Fermi*-LAT catalog of GRBs

A decade of *Fermi* space telescope mission was summarized by series of articles and one of that is dedicated to Large Area Telescope observations on Gamma-Ray Bursts—The Second *Fermi*-LAT catalog of GRBs [13].

The catalog[19] summarizes information on total of 186 GRBs, where 17 bursts show emission only within 30–100 MeV range and number of 169 events are detected above 100 MeV. A study covered each GRB in the following aspects: emission onset, duration and temporal properties, spectral characteristics, photons with the highest energy.

The second catalog data support and broaden the characteristics previously reported in the first catalog, namely that the high-energy emission is delayed and lasts longer than low-energy γ-radiation. Another similar conclusion is given for *Fermi*-LAT detected bursts as they are representatives of the brightest and more energetic GRB population.

When compared with The First *Fermi*-LAT GRB Catalog [10] covering time span August 2008–July 2011 the new release has more bursts due to detection technique improved as well an inclusion of 30–100 MeV range detected bursts. However, few

---

[19] https://heasarc.gsfc.nasa.gov/W3Browse/fermi/fermilgrb.html

GRB	z	T_{90} (s)	θ (deg)	References
180720B (598)	0.654	48.9	49.1	[565, 442]
180728A (728)	0.117	6.4	35.0	[446, 222, 550]
180914B *KW	1.096	280.0	**94.0**	23246, 23240 *KW
181010A (247)	1.39	9.7	48.1	[556, 562]
181020A (792)	2.938	15.1	50.0	[166, 549]

Table 4.7. GRBs with measured z and high-energy photons within January–December 2018.

events were excluded in the new catalog (GRB 091208B and GRB 110709A) because of poor photon statistics. Nevertheless, we leave GRB 091208B in our sample as the fitting we perform and interpretation we work within are both able to deal with an event having few counts.

We update the above Table 4.4 in Section 4.2.1 with events occurred within January–July 2018 by scanning through the all triggered bursts. To have a comprehensive list we have used several sources of information including online catalogs[20] [21] [22] to retrieve and cross-correlate data on each GRB.

In Table 4.7 we present GRB list with measured redshift values and high-energy photons within January–December 2018. The values of redshift z and duration T_{90} are retrieved from GCN and literature. The boresight angle θ with respect to *Fermi*-LAT instrument is an off-axis angle defined at the trigger moment. The description of highlighted elements is the same as for the Table 4.4.

4.2.6 Updated list of BdHNe

In order to update BdHNe sample [421, 472] with new information of the last 2 years we summarize the observations of 2017–2018 with a focus on BdHNe and the model-dependent criteria used above.

There are 197 (2017) and 164 (2018) events in total classified as GRBs and reported in GCN circulars. Among them 17 (2017) and 16 (2018) bursts have the measured redshift values. These 33 GRBs are represented by 31 long and 2 short duration bursts. In total of 31 long events the *Fermi*-GBM triggered in 16 cases while the rest objects were observed by different instruments—*Konus*-WIND and *Swift*-BAT, etc.

The values of isotropic-equivalent energy E_{iso} are calculated using the spectral parameters (α, β, $E_{p,i}$, etc.) of the model best-fitting the T_{90} interval defined within [50–300] keV band and reported in appropriate GCN, preferentially by *Fermi*-GBM team. Note that the preference for duration info and best-fit was given to *Fermi*-GBM, then if absent—to *Konus*-WIND, then if absent—to *Swift*-BAT, and the motivation for such a gradation stands on different energy bands used to define T_{90} value.

The final statistics for the period 2017–2018 is the following: there are not more than 30 BdHNe and 8 of them fell within *Fermi*-LAT FoV at the moment of trigger.

---

[20] https://gcn.gsfc.nasa.gov/gcn3_archive.html
[21] https://heasarc.gsfc.nasa.gov/W3Browse/fermi/fermigbrst.html
[22] http://www.mpe.mpg.de/~jcg/grbgen.html

BdHN	z	T_{90} (s)	$E_{\gamma,\mathrm{iso}}$ ($\times 10^{52}$ erg)	θ (deg)	GeV photons	E_{LAT} ($\times 10^{52}$ erg)	TS	References
170214A	2.53	122.9	$\cdots$	33.2	Yes	53 ± 4	1571	[299, 261, 13]
170405A	3.51	78.6	241.01	52.0	Yes	16 ± 7	56	[125, 230, 13]
171222A	2.409	80.4	20.73	43.0	No	—	—	[124, 503]
180703A	0.6678	20.7	3.15	44.0	No	—	—	[234, 424]
180720B	0.654	48.9	19.08	49.1	Yes	2.2 ± 0.2	975	[565, 442, 13]
180728A	0.117	6.4	$\cdots$	35.0	No			[446, 222, 550]
181010A	1.39	9.7	$\cdots$	48.1	No			[556, 562]
181020A	2.938	15.1	$\cdots$	50.0	Yes			[166, 549]

Table 4.8. List of BdHNe within 2017–2018 with boresight angle $\theta \lesssim 75°$ at the trigger.

Among these 8 BdHNe seen by LAT the number of 4 bursts do not show any evidence for GeV photons, whereas in 4 cases there is an emission of high-energy photons.

In Table 4.8 we present the list narrowed to the BdHNe which fell within *Fermi*-LAT FoV at the trigger. Additional information includes whether the high-energy photons were detected, and if so, the calculated value of energy E_{LAT} is given together with test statistic (TS) value of the signal to be associated with GRB. The bursts observed by other instruments lack the information on *Fermi*-LAT boresight angle and consequently no observations in high-energy domain were carried out. Therefore, consideration of that events is not possible even their energy values are sufficient ($E_{\gamma,\mathrm{iso}} \gtrsim 10^{52}$ erg) and GRBs are classified as BdHNe.

4.3   Analysis

We perform standard analysis through means of *FermiTools* software developed by the Fermi Science Support Center.[23] Both GBM[24] and LAT[25] data on selected GRBs are publicly available and provided for scientific community on continuous stand with all the necessary supportive information on mission and telescope condition.

Using these databases along with information from online GBM burst catalog[26] and LAT burst table[27] we selected GRBs from our list.

The data reduction and analysis of the *Fermi*-GBM data was briefly described in Section 2.1, paragraphs "Time-integrated analysis" and "Time-resolved analysis".

For GBM analysis we retrieved the time-tagged event (TTE) data and response files (RSP) giving an advantage, if present, to responses determined for multiple time intervals (RSP2), hence, accounting for the spacecraft slewing. Standard data reduction and analysis procedure[28] includes a selection of the detectors with reliable count rate, a determination of the working energy band (8–900 keV for NaI and 250–40 000 keV for BGO detectors), a subtraction of the background, a selection of time intervals with the *prompt* emission signal and its potential binning

---

[23] https://fermi.gsfc.nasa.gov/ssc/
[24] https://heasarc.gsfc.nasa.gov/FTP/fermi/data/gbm/bursts/
[25] https://heasarc.gsfc.nasa.gov/FTP/fermi/data/lat/
[26] https://heasarc.gsfc.nasa.gov/W3Browse/fermi/fermigbrst.html
[27] https://fermi.gsfc.nasa.gov/ssc/observations/types/grbs/lat_grbs/
[28] https://fermi.gsfc.nasa.gov/ssc/data/analysis/scitools/rmfit_tutorial.html

in order to have secure predominance of the signal over the noise. The last step is a detector combined fitting given the various model functions—Power-Law, Band, Cutoff Power-Law, Blackbody, Broken Power-Law, etc.

The fit results—light curves and spectra—could be represented in the traditional for astronomical community form. The best-fit model is determined through the chosen statistics (χ^2 [64] for Gaussian-like high number of counts or C-Stat for Poisson-like poor number of counts).

Further analysis requires an interpretation of the spectra and light curves with the best-fit model for various combinations of the fitting procedure: time-integrated and time-resolved regarding the signal evolution; spectral hardness regarding the energy band slices; combination of the counts regarding the binning of initial signal; etc. From the spectra one can derive the necessary information on quantity and quality of the photons.

The data reduction and analysis of the *Fermi*-LAT data[29] was partially described in Section 2.3.1, Paragraph "Clustering of luminosity light curves" and Section 4.1.4, Paragraph "Photons with maximum energy".

An analysis of LAT data consists of data retrieve using a query form given the burst date, time interval, position and energy band in interest. The further steps are the burst localization and generation of the files appropriate for the analysis. The latter includes a modeling of the residual and isotropic γ-ray background through the calculation of an exposure map and a usage of adequate model for galactic and extragalactic diffuse components.

The spectral analysis is performed for two phases: prompt emission and extended emission. Consequently, there are *binned* and *unbinned* modes of analysis performed with a belief that an emission in low-energy domain (keV–MeV *prompt* emission) has an influence and connection to LAT photons. The statistical method in use is a *likelihood*, which gives a probability of obtaining the data given an input model with parameters to be estimated. The spectral model parameters are varied in order to maximize the likelihood function, and equivalently to minimize the χ^2 value. The necessary steps to fit spectrum of the source are: 1) selection of spatial regions—source region (larger) and region of interest (smaller)—to be analyzed; 2) selection of the spectral model, including source itself, nearby sources, diffuse emission model, functional form of the source spectra and values of the spectral parameters; 3) pre-computation of the quantities for likelihood through the computation of varied parameter values; 4) the fit, which is performed in simultaneous fitting of a number of sources and requires a repeatedly calculating the likelihood for different trial parameter sets until a value sufficiently near the maximum is found.

The goodness-of-fit for above spectral fitting can be defined by a probability of obtaining the observed value, when χ^2 is a valid statistic. And this is the case when we know the photon distribution.[30]

Following the recipes in *Fermi*-LAT catalog [10] for time-resolved spectral analysis we divide the data from each GRB into logarithmically spaced bins and performed

---

[29] https://fermi.gsfc.nasa.gov/ssc/data/analysis/scitools/lat_grb_analysis.html

[30] In high-energy domain the spectra of GRBs is usually described by Power-Law function accompanied with an implicit assumption of Gaussian distribution of the errors.

a likelihood analysis. If the output TS value of each bin is smaller than 16 we merge the time bin with the next one and repeat the likelihood analysis. Doing this procedure results in appropriate flux values which further used to build a light curve. Provided by redshift we convert flux into luminosity component and further work in the rest-frame of each source.

The values of E_{LAT} are calculated by multiplying the average luminosity in each time bin by the corresponding rest-frame time duration and then summing up all bins. We must point out that at late time the GeV emission observation can be prevented due to the instrument threshold of the LAT and is expected to give a minor contribution to the E_{LAT}. Therefore these values are lower limits to the GeV isotropic energies.

After obtaining the luminosity light curves of all 25 sources we performed their simultaneous fit. By assuming a power-law we fix a decay index to be the same for the set and let the amplitudes to vary through scaling.

$$L_n(t) = A_n t^{\alpha}, \tag{4.1}$$

In order to avoid unconstrained values we put an additional criterion which does not allow to use curves made of limited data, i.e., two data points. This reduced the working sample to 20 sources. The motivation for such a limitation is required by needs of further individual fit. Another pre-fit preparation includes an exclusion of early rising trend in light curves which is in practice coeval with the prompt phase in lower energy band. By implementing the latter operation we automatically avoid a break parameter and concentrate on later decay phase only.

The fitting technique used is the Levenberg-Marquardt method for χ^2 minimization [175]. Shortly, when fitting one curve to one equation, we minimize χ^2. When fitting N curves to N equations simultaneously, then we should minimize the sum of the χ^2 values. Consequently:

$$\chi^2 = \sum_{n=1}^{N} \chi_n^2, \tag{4.2}$$

$$\chi_n^2 = \sum_{i=1}^{M} \frac{1}{\sigma_{ni}^2} (L_{ni} - L_n(t_{ni}, A_n, \alpha))^2, \tag{4.3}$$

where n represents each of the sources, and i represents each data point in a given source, A_n is the amplitude of a power-law function for the nth GRB, α is the common power-law index shared for all the bursts. Thus, for the nth burst, at time t_{ni}, the observed luminosity is L_{ni}, and the predicted luminosity is $L_n(t_{ni}, A_n, \alpha)$. The value of χ^2 represents the difference between the best power-laws fitting and all the observed data, it is a sum of individual χ_n^2, which shows the difference between power-law fitting and the observed value of each GRB.

Source	z	$E_{\text{p,i}}$ (MeV)	E_{iso} ($\times 10^{52}$ erg)	E_{LAT} ($\times 10^{52}$ erg)	θ (deg)	TS
080916C	4.35	2.27 ± 0.13	407 ± 86	$\gtrsim 408 \pm 57$	48.8	1450
090323A	3.57	2.9 ± 0.7	438 ± 53	$\gtrsim 48.85 \pm 0.59$	57.2	150
090328A	0.736	1.13 ± 0.08	14.2 ± 1.4	$\gtrsim 3.04 \pm 0.01$	64.6	107
090902B	1.822	2.19 ± 0.03	292 ± 29	$\gtrsim 110 \pm 5$	50.8	1832
090926A	2.106	0.98 ± 0.01	228 ± 23	$\gtrsim 151 \pm 7$	48.1	1983
091003A	0.897	0.92 ± 0.04	10.7 ± 1.8	$\gtrsim 1.29 \pm 0.03$	12.3	108
091127A	0.49	0.05 ± 0.01	0.81 ± 0.18	$\gtrsim 0.05 \pm 0.03$	25.8	34
091208B	1.063	0.25 ± 0.04	2.10 ± 0.11	$\gtrsim 0.41 \pm 0$	55.6	20
100414A	1.368	1.61 ± 0.07	55.0 ± 0.5	$\gtrsim 8.79 \pm 0.31$	69.0	81
100728A	1.567	1.00 ± 0.45	72.5 ± 2.9	$\gtrsim 1.15 \pm 0.2$	59.9	32
110731A	2.83	1.21 ± 0.04	49.5 ± 4.9	$\gtrsim 31.4 \pm 7.4$	3.4	460
120624B	2.197	1.39 ± 0.35	347 ± 16	$\gtrsim 28 \pm 2$	70.8	312
130427A	0.334	1.11 ± 0.01	92 ± 13	$\gtrsim 5.69 \pm 0.05$	47.3	163
130518A	2.488	1.43 ± 0.38	193 ± 1	$\gtrsim 3.5 \pm 0.6$	41.5	50
131108A	2.40	1.27 ± 0.05	51.2 ± 3.8	$\gtrsim 50.43 \pm 5.86$	23.8	870
131231A	0.642	0.27 ± 0.01	21.50 ± 0.02	$\gtrsim 2.18 \pm 0.02$	38.0	110
141028A	2.33	0.77 ± 0.05	76.2 ± 0.6	$\gtrsim 7.36 \pm 0.46$	27.5	105
150314A	1.758	0.86 ± 0.01	70.10 ± 3.25	$\gtrsim 1.93 \pm 0.89$	47.1	27
150403A	2.06	0.95 ± 0.04	87.30 ± 7.74	$\gtrsim 7.55 \pm 5.19$	55.2	37
150514A	0.807	0.13 ± 0.01	1.14 ± 0.03	$\gtrsim 0.42 \pm 0.05$	38.5	33.9
160509A	1.17	0.80 ± 0.02	84.5 ± 2.3	$\gtrsim 35.92 \pm 0.26$	32.0	234
160625B	1.406	1.3 ± 0.1	337 ± 1	$\gtrsim 29.90 \pm 3.51$	41.5	961
170214A	2.53	0.89 ± 0.04	392 ± 3	$\gtrsim 79.51 \pm 6.34$	33.2	1571
170405A	3.51	1.20 ± 0.42	241.01 ± 52.02	$\gtrsim 23.91 \pm 1.62$	52.0	56
180720B	0.654	1.06 ± 0.24	68.2 ± 2.2	$\gtrsim 3.04 \pm 0.6$	49.1	975

Table 4.9. List of 25 long GRBs inside *Fermi*-LAT boresight angle and with GeV photons detected. Columns list: the source name, a redshift z, a spectral energy peak $E_{\text{p,i}}$, an isotropic-equivalent energy of the prompt emission E_{iso}, an energy of the LAT detected photons E_{LAT}, a position of the source from the LAT boresight θ, a likelihood test statistic (TS). A symbol "$\gtrsim$" indicates the value is a lower limit.

4.4   Results and discussion

4.4.1   Towards universal decay of luminosity light curves

We summarize the analysis results in Table 4.9. Regarding the simultaneous fit, there are 20 bursts each with its power-law function. This means, there are 21 parameters, including 20 derived amplitudes and 1 common value of decay index. The fit is resulted with a value of the latter as $\alpha = 1.19 \pm 0.04$, i.e.,:

$$L_n = A_n \; t^{-1.19 \pm 0.04}, \tag{4.4}$$

The light curves are plotted in Figure 4.4 and the amplitudes of each GRB, A_n, with the uncertainty are shown in Table 4.10.

Having the power-law parameters of the light curve for each BdHNe, we check

BdHNe	A_n (Amplitude)	uncertainty of A_n	$L_{@10s}$	uncertainty of $L_{@10s}$
080916C	5.201×10^{53}	$^{+1.605}_{-1.307} \times 10^{53}$	3.341×10^{52}	$^{+1.963}_{-1.800} \times 10^{52}$
090323A	3.847×10^{53}	$^{+1.436}_{-1.169} \times 10^{53}$	2.472×10^{52}	$^{+1.542}_{-1.397} \times 10^{52}$
090328A	2.408×10^{52}	$^{+1.087}_{-0.773} \times 10^{52}$	1.547×10^{51}	$^{+1.042}_{-0.889} \times 10^{51}$
090902B	2.091×10^{53}	$^{+5.845}_{-4.599} \times 10^{52}$	1.343×10^{52}	$^{+7.696}_{-7.055} \times 10^{51}$
090926A	2.141×10^{53}	$^{+5.887}_{-4.838} \times 10^{52}$	1.376×10^{52}	$^{+7.850}_{-7.259} \times 10^{51}$
091003A	5.715×10^{51}	$^{+1.735}_{-1.520} \times 10^{51}$	3.671×10^{50}	$^{+2.147}_{-2.004} \times 10^{50}$
100414A	3.529×10^{52}	$^{+1.399}_{-1.142} \times 10^{52}$	2.267×10^{51}	$^{+1.446}_{-1.306} \times 10^{51}$
100728A	4.241×10^{51}	$^{+1.978}_{-1.512} \times 10^{51}$	2.725×10^{50}	$^{+1.863}_{-1.622} \times 10^{50}$
110731A	4.807×10^{52}	$^{+1.707}_{-1.442} \times 10^{52}$	3.088×10^{51}	$^{+1.894}_{-1.739} \times 10^{51}$
120624B	2.459×10^{53}	$^{+8.261}_{-6.167} \times 10^{52}$	1.580×10^{52}	$^{+9.518}_{-8.513} \times 10^{51}$
130427A	2.053×10^{52}	$^{+5.124}_{-4.091} \times 10^{51}$	1.318×10^{51}	$^{+7.370}_{-6.815} \times 10^{50}$
131231A	1.637×10^{52}	$^{+7.818}_{-5.446} \times 10^{51}$	1.052×10^{51}	$^{+7.273}_{-6.116} \times 10^{50}$
141028A	3.590×10^{52}	$^{+1.225}_{-1.109} \times 10^{52}$	2.306×10^{51}	$^{+1.396}_{-1.310} \times 10^{51}$
131108A	6.077×10^{52}	$^{+9.089}_{-8.894} \times 10^{51}$	3.904×10^{51}	$^{+2.037}_{-1.947} \times 10^{51}$
150403A	4.671×10^{52}	$^{+2.034}_{-1.595} \times 10^{52}$	3.001×10^{51}	$^{+1.989}_{-1.760} \times 10^{51}$
160509A	4.812×10^{52}	$^{+1.733}_{-1.313} \times 10^{52}$	3.091×10^{51}	$^{+1.905}_{-1.698} \times 10^{51}$
160625B	2.378×10^{53}	$^{+8.093}_{-5.854} \times 10^{52}$	1.528×10^{52}	$^{+9.241}_{-8.199} \times 10^{51}$
170214A	4.105×10^{53}	$^{+11.093}_{-8.857} \times 10^{52}$	2.637×10^{52}	$^{+1.499}_{-1.38} \times 10^{52}$
170405A	5.996×10^{52}	$^{+1.573}_{-1.4} \times 10^{52}$	3.852×10^{51}	$^{+2.175}_{-2.045} \times 10^{51}$
180720B	1.370×10^{52}	$^{+5.877}_{-4.386} \times 10^{51}$	8.794×10^{50}	$^{+5.795}_{-5.051} \times 10^{50}$

Table 4.10. Fitting parameters of the relation between 0.1–100 GeV luminosity versus time when measured in the rest frame of 20 BdHNe with GeV emission: amplitude of the BdHNe 0.1–100 GeV luminosity, A_n, and its uncertainty, the inferred 0.1–100 GeV luminosity at 10 s from the fitting and its uncertainty. The common power-law index is $\alpha = 1.19 \pm 0.04$. GRBs 091208B, 130518A, 150314A, 150514A have only two data points in their GeV luminosity light curves, therefore, were excluded from calculation.
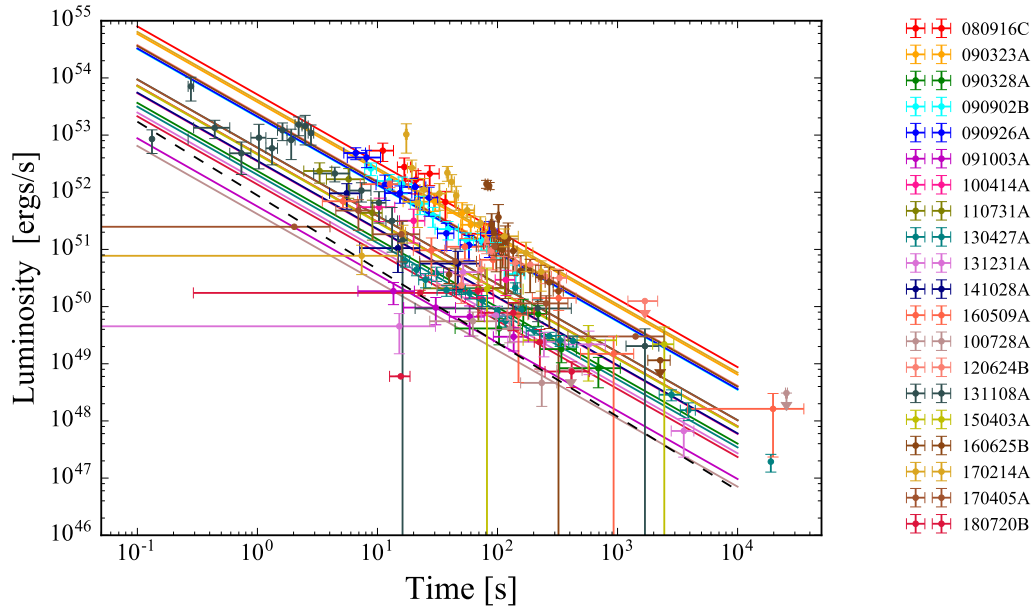
Figure 4.4. The rest-frame 0.1–100 GeV isotropic luminosity light curves of 20 selected BdHNe with LAT emission. The solid red line marks the common power-law behavior of the GeV emission for BdHNe with slope $\alpha = 1.19 \pm 0.04$; the shaded gray area encloses all the luminosity light curves of the selected BdHNe. The dashed black line marks the common power-law behavior of the GeV emission in S-GRBs with $\gamma = 1.29 \pm 0.06$ slope. Plot reproduced from [475].

the correlation between the GeV luminosity at 10 s from Equation (4.4) using the fit parameters and the isotropic energy $E_{\gamma,\mathrm{iso}}$ from prompt emission analysis. The power-law fitting gives, see Figure 4.5:

$$L_{10\mathrm{s}} = (3.20 \pm 1.01) \times 10^{51} \ E_{\mathrm{iso}}^{1.53 \pm 0.405}, \tag{4.5}$$

and the fitting parameters for each GRB including their uncertainties are shown in Table 4.10. Furthermore, we estimate the energy released in the GeV band by each GRB in the 0.1–10^4 s time interval, i.e.:

$$E_{0.1-10^4\mathrm{s}} = A_{\mathrm{GRB}} \int_{0.1}^{10000} t^{-1.19} \ dt \tag{4.6}$$

and the derived $E_{0.1-10^4\mathrm{s}}$ are shown in Table 4.11. The parameters $E_{0.1-10^4\mathrm{s}}$ and $E_{\gamma,\mathrm{iso}}$ (energy of the prompt emission) are also correlated by a power-law relation, see Figure 4.5:

$$E_{0.1-10^4\mathrm{s}} = (3.86 \pm 1.59) \times 10^{53} \ E_{\mathrm{iso}}^{1.468 \pm 0.447}. \tag{4.7}$$

This positive correlations indicates that the BdHNe with higher isotropic energy are also more luminous and more energetic in the GeV emission.
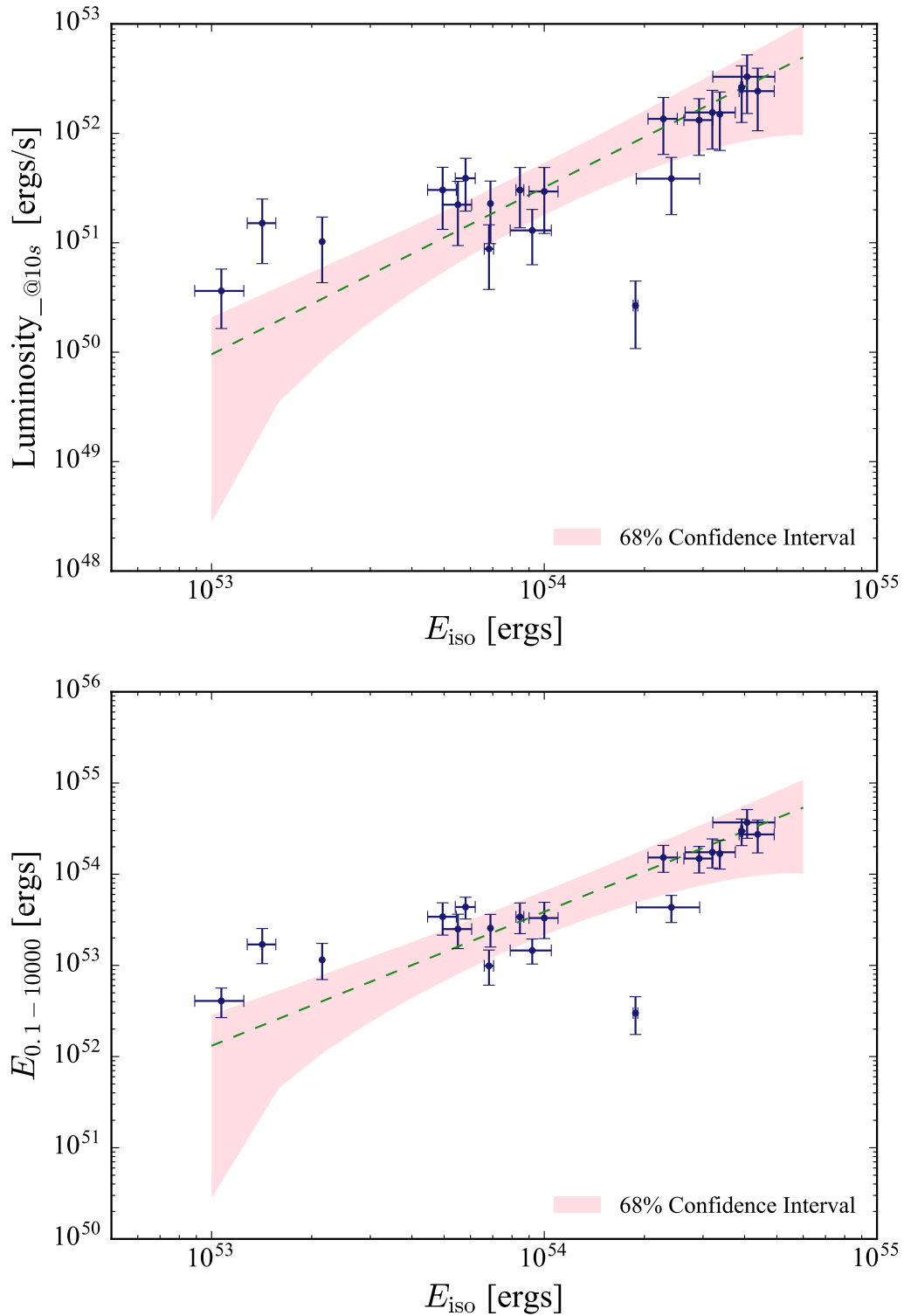
Figure 4.5. Upper panel: the *Fermi*-LAT luminosity at 10 s in the energy range 0.1–
100 GeV versus the isotropic gamma-ray energy from 1 keV to 10 MeV. The BdHNe
are listed in Table 4.10. Lower panel: the *Fermi*-LAT energy during 0.1–10^4 s versus
isotropic gamma-ray energy within 1 keV–10 MeV. See Table 4.11 for the corresponding
values. Plot reproduced from [475].

BdHNe	$E_{0.1-10^4\mathrm{s}}$	pos. uncertainty of $E_{0.1-10^4\mathrm{s}}$	neg. uncertainty of $E_{0.1-10^4\mathrm{s}}$
080916C	3.752×10^{54}	1.460×10^{54}	1.242×10^{54}
090323A	2.775×10^{54}	1.227×10^{54}	1.034×10^{54}
090328A	1.737×10^{53}	8.860×10^{52}	6.723×10^{52}
090902B	1.508×10^{54}	5.529×10^{53}	4.646×10^{53}
090926A	1.545×10^{54}	5.608×10^{53}	4.824×10^{53}
091003A	4.122×10^{52}	1.588×10^{52}	1.411×10^{52}
100414A	2.546×10^{53}	1.176×10^{53}	9.902×10^{52}
100728A	3.060×10^{52}	1.600×10^{52}	1.275×10^{52}
110731A	3.467×10^{53}	1.481×10^{53}	1.281×10^{53}
120624B	1.774×10^{54}	7.294×10^{53}	5.867×10^{53}
130427A	1.481×10^{53}	5.098×10^{52}	4.348×10^{52}
131108A	4.383×10^{53}	1.228×10^{53}	1.142×10^{53}
131231A	1.181×10^{53}	6.297×10^{52}	4.682×10^{52}
141028A	2.589×10^{53}	1.076×10^{53}	9.757×10^{52}
150403A	3.369×10^{53}	1.671×10^{53}	1.361×10^{53}
160509A	3.471×10^{53}	1.497×10^{53}	1.207×10^{53}
160625B	1.716×10^{54}	7.116×10^{53}	5.614×10^{53}
170214A	2.961×10^{54}	1.064×10^{54}	9.032×10^{53}
170405A	4.325×10^{53}	1.529×10^{53}	1.374×10^{53}
180720B	9.874×10^{52}	4.842×10^{52}	3.813×10^{52}

Table 4.11. Results of $E_{0.1-10^4\mathrm{s}}$ and related error of 20 BdHNe. $E_{0.1-10^4\mathrm{s}}$ is total GeV energy in erg emitted during 0.1–10^4 s. GRBs 091208B, 130518A, 150314A, 150514A are excluded since they have only two data points in their GeV luminosity light curves.

4.4.2 Previous studies of the luminosity decay in high-energy domain

While in early phase, coincident with *prompt* activity, the high-energy counterpart shows some variability, its later and long-lasting decay phase evolves smoothly.

Regarding the early phase it is generally believed to be connected/affected by *prompt* counterpart or alternatively to have inner origin. There have been reported [172] that the early phase has steeper decay ($\propto t^{-1.5}$) going further to shallower regime ($\propto t^{-1}$).

A common power law decay for late-time high-energy counterpart has been already pointed in The First *Fermi*-LAT GRB Catalog [10]. These conclusion is drawn on the base of energy flux measurements of 35 GRBs detected during the first two years of operation.

The power law index inferred from our analysis is similar to the one previously obtained from fitting of GeV flux, $f_\nu(t)$, see e.g. Kumar & Barniol Duran (2009) [269] and Panaitescu (2017) [399], in which power-law index is $\alpha = 1.2 \pm 0.2$ and $\alpha = 1.2 \pm 0.4$, respectively. Since luminosity is proportional to flux, i.e. $L = 4\pi d_L^2 (1+z)^{\alpha-2} f_\mu$ this similarity of power-law index is not surprising. The advantage of using luminosity expressed in the rest-frame of the source, instead of flux in arrival time, is that one can determine the intrinsic energy loss of the system which produces the GeV radiation, regardless of difference in the redshift of their sources.

In previous papers [470, 12] we introduced a specific luminosity dependence as a function of the rest-frame time of the GeV emission. This approach followed the corresponding one for the long GRBs originally introduced in [421]. The rest-frame 0.1–100 GeV isotropic luminosity light curves follow a power-law behavior

$$L(t) = A\ t^\gamma \tag{4.8}$$

where t is the rest-frame time and $A = L(@1s)$ is the luminosity at 1$^{\text{st}}$ second after trigger. This has been well established in all S-GRBs, see, e.g. [357, 465, 469].

We recall that in BdHNe there are two possibilities that the hypercritical accretion of the HN ejecta occurs on a NS companion leading to the formation of the BH (BdHN I) or it occurs on an already formed BH (BdHN IV). We are going to see how relating GeV radiation to the loss of rotational energy of the Kerr-Newman can lead to the determination of the mass and spin of the BH in the above 25 GRBs and create a separatix between BdHNe I and BdHNe IV.

4.4.3 Energy extraction from BH as engine for GeV photons generation

There are several possibilities for energy extraction from rotating BH, see, e.g., recent review [535]. One of the ways to explain high-energy emission from BH operates with a term of an *extractable* energy of BH [84]. A general picture for such an extraction is the following.

It is considered that rotating BH can give out part of its rotational energy in accordance with angular momentum conservation law. We then use an assumptionn that extractable energy is converted into electromagnetic radiation of high-energy

domain. This radiation travels with high velocity and reaches Earth being observed by γ-ray telescopes.

Hence, by back-tracking the detected photons we can make an inference on parameters of black hole which is believed to be situated in GRB events.

Of course, there are much more details in between and in the following we try to cover some of the subtleties of the proposed scenario.

An investigations dedicated to the extraction of energy from black holes go back to 1970s with pioneering work by Penrose (1969) [405]. From extensively studied properties of BH it follows the existence of so-called *irreducible* mass [84], therefore the rest part can be, in principle, considered as extractable.

Another operative assumption comes from generally accepted view on how the BH are created. There are plethora of works concentrated on a detailed study of gravitational collapse, but almost all of them consider a neutron star (NS) as being the progenitor of black holes.

Not going deep into the details we just glance through the scenario we propose within fireshell paradigm in order to motivate the further usage of NS. The more general scenario tells us that the subclass of GRBs called BdHNe which are energetic representatives of long duration bursts are originated in binary system of massive CO_{core} star and compact NS. The former collapses to supernova (SN) with ejecta expanding with non-relativistic velocity. Part of this ejecta accretes on the NS, making it to overcome the critical mass known to be attributed to such a compact object. Passing a mass limit the NS should collapse into the BH. And this moment is the one of our direct interest because we claim that GRB is exactly the consequence of these transformations.

Now to match extractable energy of black hole with progenitor neutron star the most evident bridge is a critical mass of NS. This parameter depends on nuclear composition which in its turn affects the balance between gravitational force inwards and pressure outwards, the so-called *equation of state* (EoS). We use critical mass parameter from Cipolletta (2015) [85] and solove numerically the equations adapting the limit of maximal spin for uniformly rotating NS, following the requirement of angular momentum conservation law. As well we avoid infinity solution for rotating black hole, i.e., in accordance with maximum spin value derived for Kerr BH, see the next paragraphs.

Table 4.12, Table 4.13 and Table 4.14 list calculated parameters of BH mass and spin for two kinds of EoS (TM1 and NL3 from [85]). We note that finding an extremum value on family of solutions in some cases violate requirement on maximum spin $\alpha_{\max} = 0.71$. Therefore, we detach these BdHNe from the main part and calculate only their masses with explicitly fixed spin parameter, see Table **??**. Thus, our initial sample is split into two subsamples and their interpretation is of the main purpose of the paradigm.

If compare mass values given in these three tables then one should notice the following trend: the BH masses in the main larger table is of the order of 2–3 $M_\odot$ while smaller subsample BH masses range $\gtrsim 9$ $M_\odot$. The conclusion which comes immediately is that the latter 3 BH events cannot be produced from NS collapse, at least not for the production of high-energy emission from GRBs. Then the only solution the paradigm can suggest is that BH was already present as binary companion of CO_{core} massive star.

Source	TM1		NL3	
	α	$M(\alpha)$	α	$M(\alpha)$
		$(M_\odot)$		$(M_\odot)$
BdHN I 090328A	$0.532^{+0.017}_{-0.019}$	$2.439^{+0.019}_{-0.019}$	$0.483^{+0.017}_{-0.018}$	$3.012^{+0.016}_{-0.016}$
BdHN I 091003A	$0.459^{0.031}_{-0.028}$	$2.372^{0.024}_{-0.023}$	$0.414^{+0.027}_{-0.030}$	$2.956^{+0.020}_{-0.020}$
BdHN I 091127	$0.130^{0.015}_{-0.017}$	$2.218^{0.004}_{-0.003}$	$0.115^{+0.013}_{-0.015}$	$2.825^{+0.003}_{-0.003}$
BdHN I 091208B	$\lesssim 0.222$	$\gtrsim 2.244$	$\lesssim 0.197$	$\gtrsim 2.847$
BdHN I 131231A	$0.6050^{+0.0003}_{-0.0003}$	$2.5314^{+0.0006}_{-0.0006}$	$0.5547^{+0.0004}_{-0.0004}$	$3.0863^{+0.0005}_{-0.0005}$
BdHN I 150514A	$0.176^{+0.004}_{-0.004}$	$2.230^{+0.001}_{-0.001}$	$0.156^{+0.003}_{-0.004}$	$2.834^{+0.001}_{-0.001}$

Table 4.12. The BH spin parameter α and mass M within the TM1 and the NL3 nuclear models, as inferred from the values of E_{LAT} for 6 BdHNe I, out of the 25 long GRBs in Table. 4.9, providing BH spin parameters $\alpha < 0.71$, consistent with the maximum spin parameter of a rotating NS, see for details [85].

Source	α	$M(\alpha)$
		$(M_\odot)$
BdHN I 090902B	$\lesssim 1$	$\gtrsim 7.68 \pm 0.65$
BdHN I 090926A	$\lesssim 1$	$\gtrsim 7.24 \pm 0.57$
BdHN I 100414A	0.71	$\gtrsim 4.63 \pm 0.03$
BdHN I 100728A	0.71	$\gtrsim 5.32 \pm 0.23$
BdHN I 110731A	0.71	$\gtrsim 5.88 \pm 0.90$
BdHN I 120624B	$\lesssim 1$	$\gtrsim 7.16 \pm 0.34$
BdHN I 130427A	0.71	$\gtrsim 7.10 \pm 0.95$
BdHN I 130518A	$\lesssim 1$	$\gtrsim 3.75 \pm 0.03$
BdHN I 131108A	0.71	$\gtrsim 7.40 \pm 0.07$
BdHN I 141028A	0.71	$\gtrsim 6.07 \pm 0.08$
BdHN I 150314A	0.71	$\gtrsim 5.24 \pm 0.30$
BdHN I 150403A	0.71	$\gtrsim 6.90 \pm 0.94$
BdHN I 160509A	0.71	$\gtrsim 8.76 \pm 0.19$
BdHN I 160625B	$\lesssim 1$	$\gtrsim 7.00 \pm 0.09$
BdHN I 170405A	$\lesssim 1$	$\gtrsim 5.06 \pm 1.02$
BdHN I 180720B	0.71	$\gtrsim 5.18 \pm 0.2$

Table 4.13. The number of 16 BdHNe I, out of the 25 long GRBs in Table 4.9, requiring $M > M_{\mathrm{max}}^{J\neq 0}$. The masses M have been obtained from Eq. 4 in [476] by fixing $\alpha = \alpha_{\mathrm{max}} = 0.71$ for 10 and $\alpha = 1$ for 6 GRBs. The inferred values for mass of each system is smaller than the maximum mass that the BH can attain, namely $M \approx 9 M_\odot$, therefore, we these systems are possibly BdHNe I.

Source	α	$M(\alpha)$
		$(\mathrm{M}_\odot)$
BdHN IV 080916C	$\lesssim 1$	$\gtrsim 15.58 \pm 2.73$
BdHN IV 090323A	$\lesssim 1$	$\gtrsim 9.30 \pm 1.02$
BdHN IV 170214A	$\lesssim 1$	$\gtrsim 9.00 \pm 0.18$

Table 4.14. The 3 BdHNe IV, out of the 25 long GRBs in Table 4.9, requiring $M > M_{\max}^{J \neq 0}$. The masses M have been obtained from Eq. 4 in [476] by fixing $\alpha = 1$. The inferred values for mass of each system is bigger than the maximum critical-mass of the NS, for TM1 model $M_{crit}(\alpha_{max}) = 2.62 M_\odot$ and for NL3 model $M_{crit}(\alpha_{max}) = 3.38 M_\odot$. Moreover, the mass is larger than the maximum mass that the BH can attain in BdHNe I. These sources cannot be associated with NS, therefore we the hypercritical accretion occurs onto an already formed BH.

We can do few more interesting inferences with simple considerations on the observable population in hand.

Turning back to Section 4.1.2 we also check the ability of GRBs within FoV to emit GeV photons. To stay within fireshell paradigm we use its largest collection of BdHNe [472, 422] and scan it in order to find bursts of our interest. There are 329 BdHNe spanning the time duration within 1997–2016 but only 193 events of the list occurred within operational era of *Fermi* observatory. Among them there are 54 bursts triggered within *Fermi*-LAT FoV. As being already found there are 25 GRBs forming our working sample with GeV photons. Hence, the remaining 29 sources are still within FoV but with no activity in high-energy domain.

These 29 bursts are represented across wide range of redshifts, fluences, durations and energetics, though being initially within BdHNe list requires from them to have isotropic-equivalent energy $E_{\gamma,\mathrm{iso}} > 10^{52}$ erg.

The numbers go in accordance with previously reported by *Fermi*-LAT team [9] with a little deviation which we refer to the small size of our sample. Ending up with such a trend regardless the sample size we could play still with interpretation and suppose that the non-appearance of GeV photons is related to the geometry onsite the GRB.

If look at the ratio of BdHNe (LAT detected versus total within FoV) and make an assumption of emitting region as cones on both sides of the source (in analogy with Blazars) then from

$$(1 - cos\ \theta) \propto \frac{N_{\mathrm{LAT}}}{N_{\mathrm{total}}}\ , \tag{4.9}$$

we result with $\theta \approx \pi/3$, a wide emitting region of conical size. And one can further use this in order to speculate effects of rotation and some accretion disc around BH or other central object.

Another interesting consequences can be considered from previously derived values of BH together with obtained (and claimed to be universal) PL decay in luminosity light curves. Namely, by assuming the decay to be strictly bound to the mass of BH, i.e., to extractable energy in terms of mass, one can construct the

appropriate relation:

$$L \propto -\frac{dE_{\text{extr}}}{dt} \approx -\frac{dM}{dt} \ . \tag{4.10}$$

Integrating the above equation with respect to time and keeping in mind the temporal PL decay of luminosity in Equation 4.4 and the property of the irreducible mass to remain constant we get

$$M = M_0 + 5At^{-0.2} - 5At_0^{-0.2} \ , \tag{4.11}$$

where M_0 is the initial mass of BH.

Further, following mass-energy equation:

$$J = 2M_{\text{irr}} \sqrt{M^2 - M_{\text{irr}}^2} \ . \tag{4.12}$$

Therefore

$$a = \frac{J}{M} \ . \tag{4.13}$$

As a result we get a simple equation describing the spin down (or slowing down) of roatting BH due to energy loss through radiation.

Further investigations in great details are of course needed and many other important effects should be taken into the account. The purpose here was to demonstrate how the high-energy emission can be related to the rotational energy of BH.

4.5 Other correlations in GRBs with GeV emission: work in progress.

4.5.1 Search for a correlation of GeV-Radio emission in GRBs

Our comment will focus on point in Lloyd-Ronning et al. (2019) [295] where authors study the correlations in GRBs with and without radio afterglow. That work extends previous study [294] and covers time span between 1997–2018 with a total number of 119 bursts with follow-up observations in radio band, among which there are 78 and 41 events showing, respectively, the presence (radio loud) or the absence (radio quiet) of the afterglow in the long wavelength end of the spectrum. In particular, regarding the bursts with GeV emission authors were stating that the high-energy extended emission is *only present* in the radio loud sample with energies $E_{\text{iso}}^{\gamma} \gtrsim 10^{52}$ erg. We will study this point in details and make our approach not from the side of radio follow-up, but from the point of the high-energy photons. Therefore, rephrasing the statement for our case should be: extended GeV emission *have to* be accompanied by radio emission for bursts with $E_{\text{iso}}^{\gamma} \gtrsim 10^{52}$ erg.

GRB	Redshift	Radio	GRB	Redshift	Radio
080916C	4.35	N	130907A	1.238	Y
081024B	–	N	131108A	2.4	Y
081203A	2.1	N	131231A	0.6439	–

Continued on next page

Table 4.15 – Continued from previous page

GRB	Redshift	Radio	GRB	Redshift	Radio
090102A	1.55	N	141028A	2.332	−
090323A	3.57	Y	150314A	1.758	Y
090328A	0.736	Y	150403A	2.06	−
090510A	0.903	N	150514A	0.807	−
090902B	1.822	Y	160509A	1.17	Y
090926A	2.1062	N	160521B	−	N
091003A	0.8969	−	160623A	0.367	Y
091127A	0.4903	N	160625B	1.406	Y
100414A	1.368	Y	160816A	−	Y?
100728A	1.567	−	160821A	−	N
110731A	2.83	N	160910A	−	Y
120624B	2.1974	Y	161015A	−	N
120711A	1.405	N	170214A	2.53	−
120729A	0.8	N	170405A	3.51	−
130427A	0.3399	Y	170728B	−	N
130518A	2.488	Y	171010A	0.3285	Y
130702A	0.145	Y	180720B	0.654	Y

Table 4.15. Master table. Total 40 GRBs. Regarding redshift: 33 measured, 7 not measured. Regarding radio band observations: 18 radio loud, 14 radio quiet, 8 no follow-up. Signs "Y", "N" and "−" stand, respectively, for "detected", "not detected" and "not observed" regarding the radio afterglow for each GRB.

We will base our approach on data from The Second *Fermi*-LAT GRB Catalog [13] (hereafter "second catalog"). It represents bursts in 0.1–100 GeV band detected within 10 years from July 2008 to August 2018. We will examine a whole GRB set (Table 4.15) as well as sample with measured redshift value (Table 4.16) for the presence of follow-up observations with radio telescopes. We just note here that will not consider an emission in 30–100 MeV band uniquely detected by *Fermi*-LAT.

First of all, the Table 4.15 shows that there are GRBs having high-energy emission and radio follow-up observations resulted with both positive (radio loud) and negative (radio quiet) signal detection. In total of 32 follow-up campaigns (25 with known redshifts), the number of 18 GRBs are radio loud (16 with redshifts), while in 14 cases GRBs appeared to be radio quiet (9 with redshifts). However, Lloyd-Ronning et al. (2018) [295] found only 9 GRBs with redshifts where 8 bursts are radio loud and only 1 event (GRB 130518A) is radio quiet. GRBs with high-energy emission in our Table 4.16 as well as those [356] used by authors are both presented up to the end of 2017, but two samples give different numbers on radio follow-up information. This shows nothing but the fact that the authors excluded those GRBs with energy $E_{\rm iso} < 10^{52}$ erg. Nevertheless, we can still utilize larger sample.

GRBs with measured redshift values is used as a sample for further interpretation needs due to possibility to estimate physical parameters. Additionally there is opportunities for the study of host galaxies, because they are believed to contribute to the emission in long wavelength range.

GRB	z	T_{90}	T_{90}^{RF}	$T_{0,\mathrm{RF}}^{\mathrm{LAT}}$	θ	Radio	T_{05}^{GBM}	T_{95}^{GBM}	T_0^{LAT}	T_1^{LAT}	T_{100}^{LAT}
080916C	4.35	62.98	11.77	0.56	48.8	N	1.3	64.3	3.0	1531.8	1500 ± 200
090323A	3.57	133.89	29.30	2.04	57.2	Y	8.7	142.6	9.3	5321.6	5312 ± 8
090328A	0.736	61.70	35.54	8.29	64.5	Y	4.4	66.1	14.4	6150.6	6140 ± 70
090510A	0.903	0.96	0.50	0.0	13.6	N	−0.048	0.9	0.0	170.0	170 ± 2
090902B	1.822	19.33	6.85	0.18	50.8	Y	2.8	22.1	0.5	884.2	880 ± 60
090926A	2.1062	13.76	4.43	0.71	48.1	N	2.2	15.9	2.2	4419.5	4420 ± 50
091003A	0.8969	20.22	10.66	0.53	12.3	—	0.83	21.1	1.0	392.0	390 ± 10
091208B	1.0633	12.48	6.05	—	55.6	—	—	—	—	—	—
100414A	1.368	26.50	11.19	7.90	69.0	Y	1.9	28.4	18.7	5506.1	5490 ± 30
100728A	1.567	165.38	64.43	96.84	59.9	—	13.0	178.7	248.6	1340.5	1090 ± 40
110731A	2.83	7.49	1.20	0.29	3.4	N	0.003	7.5	1.1	436.0	430 ± 10
120624B	2.1974	271.36	84.87	23.05	70.8	Y	−260	14.3	73.7	1103.9	1030 ± 30
120711A	1.405	44.03	4.59	163.53	134.5	N	62	106.5	393.3	5431.6	5000 ± 800
120729A	0.8	25.47	14.15	220.5	82.7	N	−1.0	24.5	396.9	432.0	40 ± 10
130427A	0.3399	138.24	103.17	0.07	47.3	Y	4.1	142.3	0.1	34366.2	34400 ± 300
130518A	2.488	48.58	13.93	7.68	41.0	Y	9.9	58.5	26.8	343.6	320 ± 10
130702A	0.145	58.88	51.43	237.82	75.2	Y	0.77	59.7	272.3	1283.3	1000 ± 100
130907A	1.238	250.0	111.71	1616.80	105.5	Y	—	210.0	3618.4	4010.9	400 ± 300
131108A	2.4	18.18	5.35	0.0	23.8	Y	0.32	18.5	0.0	678.1	680 ± 40
131231A	0.6439	31.23	19.00	14.05	38.1	—	13.0	44.5	23.1	4824.2	4800 ± 700
141028A	2.332	31.49	9.45	3.27	27.5	—	6.7	38.2	10.9	500.5	490 ± 80
150314A	1.758	10.69	3.88	0.04	47.1	Y	0.61	11.3	0.1	3064.3	3100 ± 100
150403A	2.06	22.27	7.28	130.56	55.2	—	3.3	25.6	399.5	970.5	600 ± 200
150514A	0.807	10.81	5.98	244.83	38.5	—	0.003	10.8	442.4	597.6	200 ± 200
160509A	1.17	369.67	170.35	4.42	32.0	Y	8.2	377.9	9.6	5687.4	6000 ± 1000
160623A	0.367	107.78	78.84	293.71	83.3	Y	−1.3	106.5	401.5	35069.0	35000 ± 1000
160625B	1.406	453.39	188.44	10.64	41.5	Y	190.0	641.8	25.6	840.5	810 ± 20
170214A	2.53	122.88	34.81	11.19	33.0	—	13.0	135.4	39.5	752.0	713 ± 8
170405A	3.51	78.59	17.42	3.95	52.2	—	7.4	86.0	17.8	868.0	850 ± 60
171010A	0.3285	107.27	80.75	252.62	114.6	Y	17.0	123.9	335.6	2984.8	2650 ± 50
180720B	0.654	48.90	29.56	7.13	50.0	Y	4.4	53.3	11.8	625.0	613 ± 9

Table 4.16. Basic information on sample of GRBs with measured redshift, high-energy photons (100 MeV–100 GeV) detected by *Fermi*-LAT within August 2008–July 2018 and its follow-up in radio band. Highlighted in "yellow" were not included into the BdHNe sample with GeV emission. See other details in the text.

We give a sample list of GRBs with measured redshift and high-energy photons (0.1–100 GeV) detected within August 2008–July 2018 by *Fermi*-LAT instrument, see Table 4.16. There the signs "Y", "N" and "−" stand, respectively, for "detected", "not detected" and "not observed" regarding the information on radio afterglows of each GRB collected from various sources. The values of T_{90}, T_{05}^{GBM}, T_{95}^{GBM}, T_0^{LAT}, T_1^{LAT} and T_{100}^{LAT} (in seconds) are retrieved from the *Fermi*-GBM Burst Catalog [355] where they were calculated for conventional energy range (50–300 keV) and the Second *Fermi*-LAT Gamma-Ray Burst Catalog [13]. The values of T_{90}^{RF} and $T_{0,\mathrm{RF}}^{\mathrm{LAT}}$ are calculated for the rest-frame of the source.

Since there was not given any GRBs list evaluated [295], we cross-correlate *Fermi*-LAT bursts with the ones used by the authors [356] and by searching for radio afterglow campaigns across the literature and GCN circulars we found the following. If one refers to the Second *Fermi*-LAT GRB catalog [13] then the object GRB 130518A, which was stated as having no extended emission, actually has one, see three last columns of Table 4.16. Its duration is ≈ 6 times longer than T_{90} of the prompt phase. Moreover, according to the catalog the emission above 100 MeV lasts longer than keV–MeV band emission on systematical base. Among 169 GRBs of the Second *Fermi*-LAT Catalog showing photons in 0.1–100 GeV band there are less than 10% of objects whose emission lasts shorter than prompt phase duration including few cases when photons arrived with great delay due to either Earth occultation or late repointing by LAT.

As for the main message of the considered article [295], we built a correlation plot for the intrinsic prompt duration and redshift, although our GeV-Radio sample is much smaller, containing only 24 bursts (20.2%) versus 119 of the above mentioned work.

In Figure 4.6 we search for a trend in GRB samples by fitting them with power-law function through the Levenberg-Marquardt algorithm [175]. There is an anticorrelation between the intrinsic burst duration and redshift for the bright (both radio loud and radio quiet) sample having decay index -0.68 ± 0.57. Its value lies within statistical uncertainty with respect to the one obtained by authors of the main article [295]. When fitting separately radio loud (purple) and radio quiet (green) samples give indices -0.52 and $+0.16$, respectively. Bursts with GeV emission, measured redshift but without radio follow-up (blue empty circles) are built for the purpose of comparison and shows no explicit relation to any of samples. It can be stated that although our bright sample is strictly limited it yet keeps the decay trend of the larger sample, the one without regard to the presence of the high-energy photons. If one potentially includes the bursts without radio follow-up then the fitting will come closer to authors' result though not significantly, -0.72 ± 0.55. Additionally we built histograms of the intrinsic duration (Figure 4.7) and redshift (Figure 4.8) which both go in accordance with the ones of the larger sample [295].

We can conclude that even if the correlations given in our sample in general support the results of the main publication, however, taken separately, will not reach the same inferences due to small size, at least these inferences turn out to be not so evident.
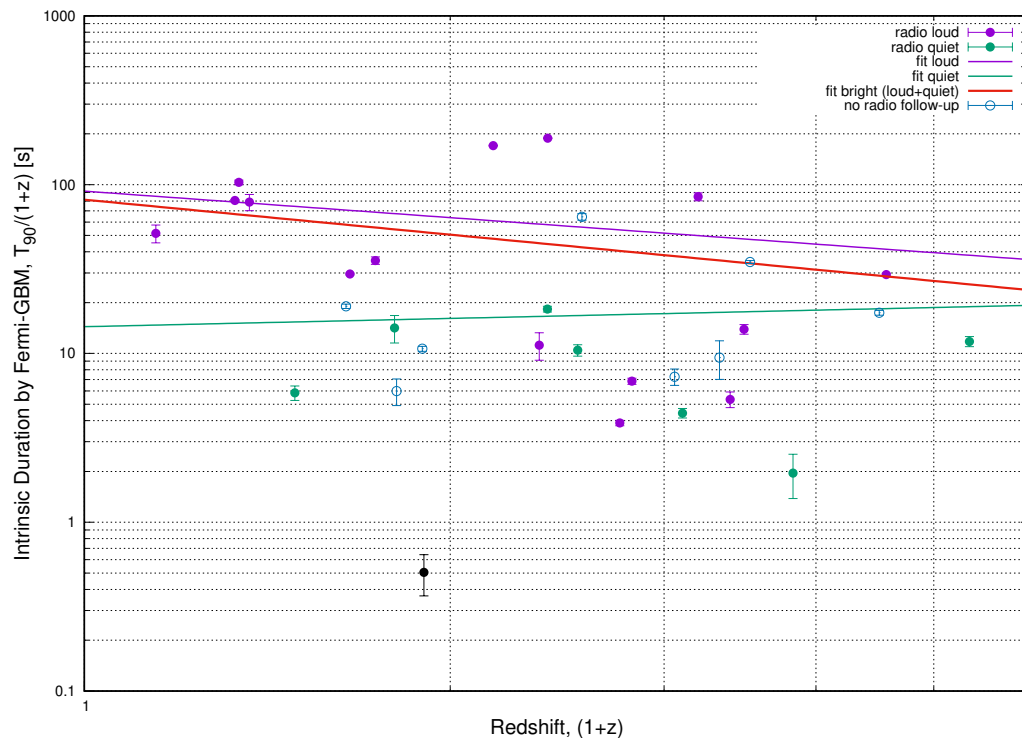
Figure 4.6. A correlation between intrinsic duration of the prompt phase and redshift. There are 24 GRBs with high-energy photons, measured redshift and radio follow-up observations, among which 16 are radio loud (purple) and 8 are radio quiet (green). Additionally there are 8 bursts with no follow-up campaigns (blue empty circles) and only one short GRB 090510A with redshift and high-energy photons (black).
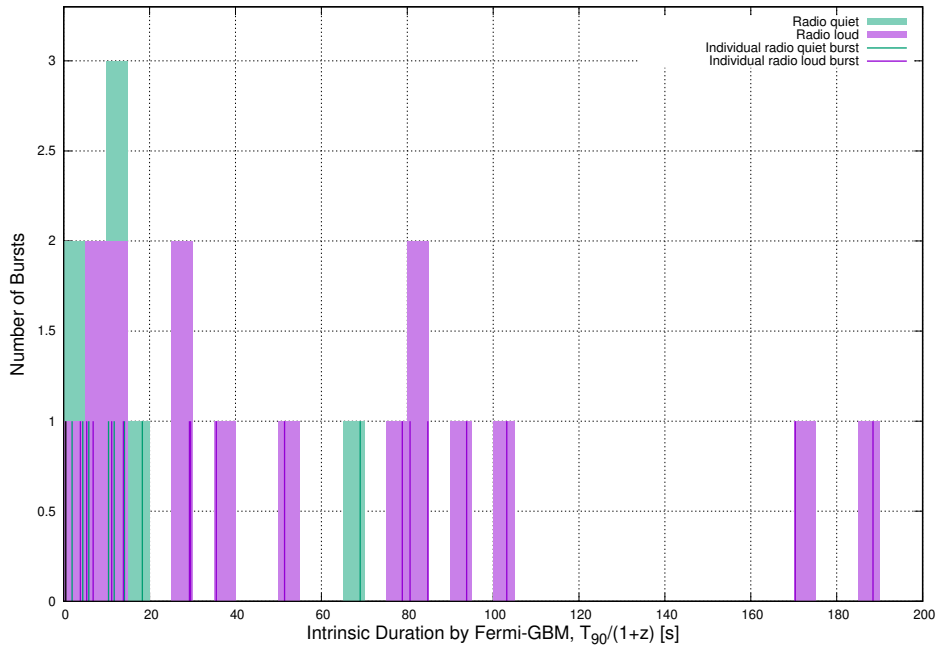
Figure 4.7. Histogram of the intrinsic prompt duration for 24 GRBs with high-energy photons, redshift and radio follow-up resulting with radio loud (purple) and radio quiet (green) bursts. Individual bursts are marked with ticks at their intrinsic durations. Short GRB 090510A is shown with black tick at the intrinsic duration 0.5 seconds. Time binning for histogram is 5 seconds.
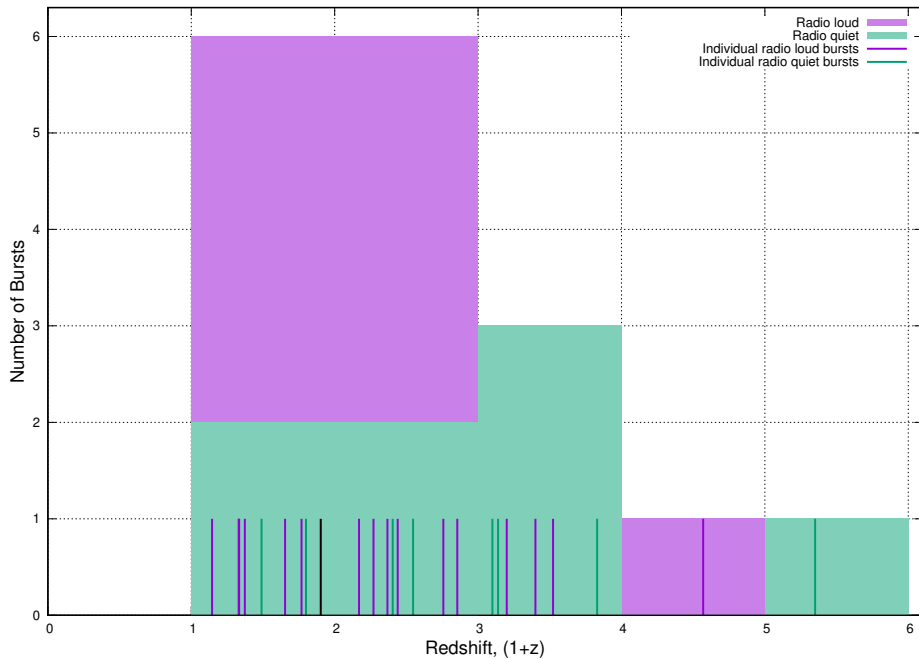
Figure 4.8. Histogram of the redshift $(1 + z)$ distribution for 24 GRBs with high-energy photons, redshift and radio follow-up resulting with radio loud (purple) and radio quiet (green) bursts. Individual bursts are marked with ticks at their redshifts. Short GRB 090510A is shown with black tick at $(1+z) = 1.903$. Redshift binning for histogram is equal to unity.

Total S-GRBs	$\theta < 75°$	$\theta = 75°$	$\theta > 75°$	no θ
398	207	6	147	38

Table 4.17. Distribution of short GRBs with regard to LAT boresight angle.

4.5.2   Energies of short GRBs

In order to estimate energies for GRBs without redshift we take an average value of those short and long bursts with measured redshift. The mean value for the redshift of short GRBs is around unity, while the mean redshift value of long bursts is around two. Within a decade of the *Fermi* operational era there were reported 30 short GRBs with redshifts measured, among them there is only one GRB 090510 with both measured redshift and GeV photons detected [10, 13]. This means a number of > 350 short bursts does not have redshift and roughly same number without GeV photons were observed.

Fixing the redshift at unity value we calculate E_{iso} given a spectral model. For every GRB its '`Flnc_Best_Fitting_Model`' parameter from GBM catalog indicates the model best fitting the data for a spectrum accumulated over T_{90} duration of the burst [355]. The calculated values of $E_{\mathrm{iso}}^{z=1}$ are listed in Table B.1 and Table B.2, and Figure 4.9 shows the energy distribution of the sample with such an assumption.

4.5.3   Distribution of LAT boresight angles at the trigger moment for short GRBs

We scan throughout (in order of priority) the `Fermi LAT Second GRB Catalog`,[31] the `Fermi GBM Trigger Catalog`[32] and `GCN archive`[33] looking for the LAT boresight angle with regard to the best location of every burst. We give in Table B.1 a short GRB name, its T_{90} duration in seconds, the estimate of isotropic-equivalent energy E_{iso} in erg given the redshift of unity as mean value for short bursts, and the boresight angle θ in degrees of the *Fermi*-LAT at the trigger.

There are 360 short GRBs with known θ at the trigger (Table 4.17) of which 207 bursts were detected at $\theta < 75°$, number of 6 short GRBs were triggered at $\theta = 75°$ and events in amount of 147 were detected at $\theta > 75°$. In Figure 4.10 we show this distribution where marked as red are the events triggered in LAT instrument giving high-energy photons above 100 MeV. Note that the large offset GRB 170127C still had a strong signal after late repointing.

---

[31]`https://heasarc.gsfc.nasa.gov/W3Browse/all/fermilgrb.html`
[32]`https://heasarc.gsfc.nasa.gov/W3Browse/fermi/fermigtrig.html`
[33]`https://gcn.gsfc.nasa.gov/`
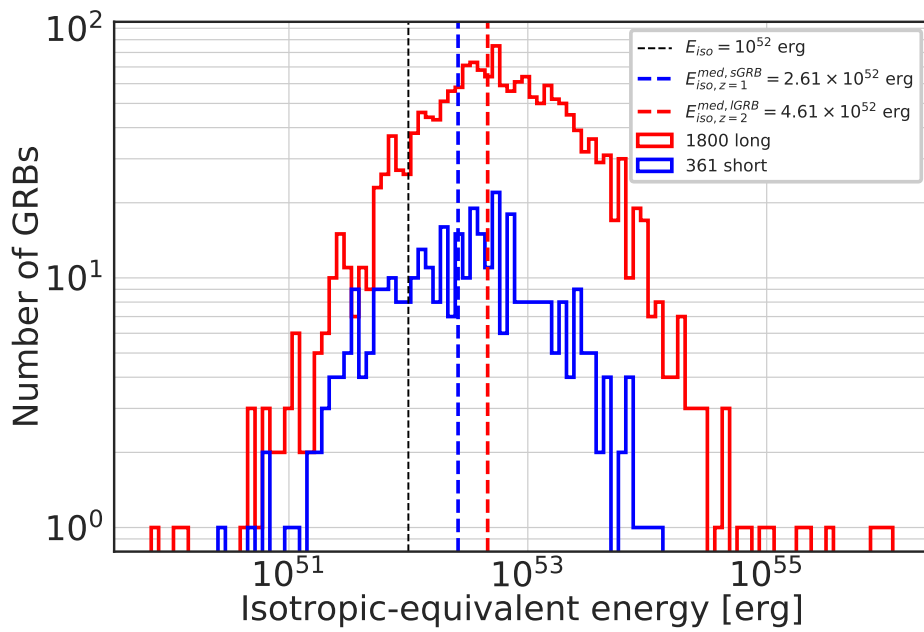
Figure 4.9. Histogram of E_{iso} for short and long GRBs for a decade of *Fermi* mission. The values of isotropic-equivalent energy are calculated by assuming average redshifts for short ($z = 1.0$) and long ($z = 2.0$) bursts. Dashed black line indicates $E_{\mathrm{iso}} = 10^{52}$ erg. Dashed blue and orange lines indicate median $E_{\mathrm{iso}}^{\mathrm{z}=1}$ correspondingly for short and long GRBs. Parameters are listed in Table B.1.
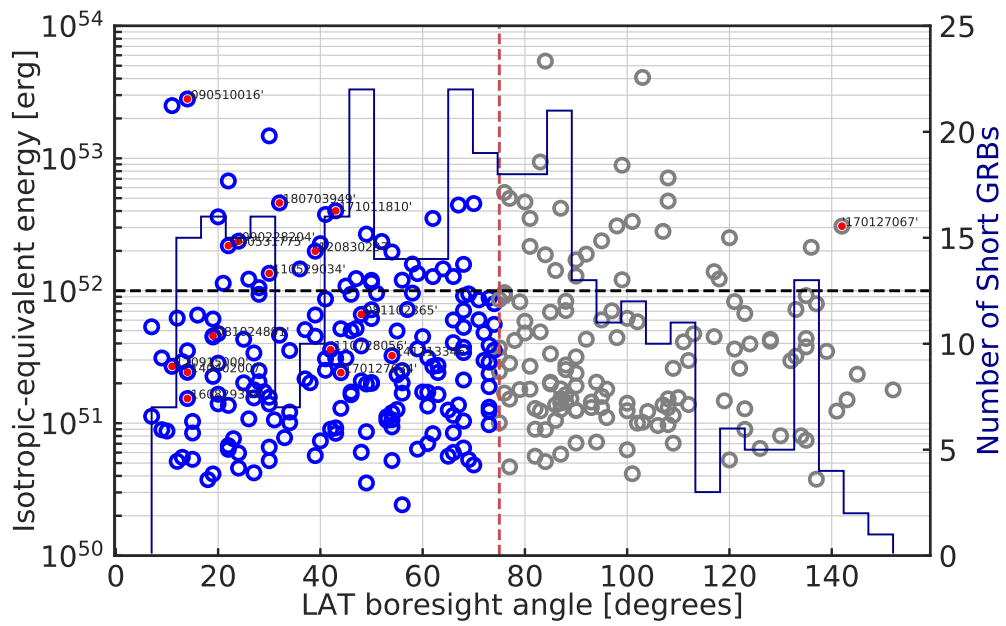
Figure 4.10. Distribution of short GRBs by boresight angle θ and isotropic-equivalent energy E_{iso}. Vertical dashed line indicates $\theta = 75°$ threshold angle, horizontal dashed line indicates $E_{\mathrm{iso}} = 10^{52}$ erg. Labeled red points indicate S-GRBs from the Second LAT Catalog [13] with parameters given in B.2. A large offset of S-GRB 170127067 still had high-energy emission at late repointing. The histogram shows the same distribution stacked in 30 bins.

Chapter 5

Conclusion

In the last chapter we summarize the work presented in the given manuscript.

This thesis is mainly focused on careful data analysis of different parts of high-energy (sub-keV–GeV) spectra of gamma-ray bursts. All the interpretation works are based on the theoretical ground of the *fireshell* paradigm which is being continuously developed for over 20 years: there is a detailed study of the early γ-ray prompt phase microphysics [462, 461, 463, 458, 457, 456], as well as currently developing microphysics of the x-ray and optical afterglow phases [472, 460, 477] and mechanisms for generation of high-energy photons [470, 476, 475, 478, 473]. Thus, the author sees his contribution to the model development from the perspective of providing a reliable and comprehensive analysis on the observational data of gamma-ray bursts.

The thesis summarizes the following results:

- In Chapter 2 we analyzed data from 3 short GRBs—081024B, 090510A, 140402A—with an aim to study their connection to the progenitor binary neutron star system which further coalescing into a Kerr-Newman black hole. We mark three distinct components inherent to so-defined "authentic" short GRB subclass: proper-GRB emission, prompt emission and high-energy band emission. We define the GeV emission as one of the main signatures for black hole formation. Under such an assumption we calculate GRB energetics and show the consistency of energy requirement (GRB 090510A) to the black hole angular momentum which is used for energy extraction through matter accretion process. By building-up the high-energy luminosity light curves for two additional short bursts (GRB 081024B and GRB 140402A) we further strengthen the standpoint for existence of common power-law behavior following from the idea of black hole with certain range of mass and spin parameters. The following results were obtained and reflected in the subsequent publications [470, 12]:
  1. The role of the amount of energy $E_{\mathrm{iso}} \approx 10^{52}$ erg was discussed;
  2. Energy requirement of the GeV emission for S-GRBs was estimated and the consistency for the amount of energy extracted through accretion on Kerr black hole has been shown;
  3. GRB 090510 is defined as a prototype of genuine short GRB subclass and

the indication for a rapidly rotating black hole was shown;

4. Theoretical redshift values for S-GRBs was calculated through consideration of expanding plasma dynamics;

5. A common power-law decay for high-energy luminosity light curves of S-GRBs was obtained pointing to the similarity in mass and spin parameters of the proposed central black hole;

6. Non-detectability of x-ray afterglow for S-GRBs was discussed.

- In Chapter 3 we analyzed data from 16 long GRBs with a focus on flaring structure in the early x-ray afterglow phase. Our aim was to strengthen the point that flares presented only in some of the long bursts are carrying information on the dynamics of the main prompt phase. This line was inferred from the correlation of parameters extracted from the flare data and the one of energetics, namely the isotropic-equivalent energy of the prompt phase. Additionally, we found a thermal components in the time-resolved spectra of the flares and interpreted them as coming from collision of the GRB with surrounding supernova ejecta within the Induced-Gravitational Collapse (IGC) scenario of the Binary-driven Hypernova (BdHN) system of the fireshell paradigm. The following results were obtained and reflected in the subsequent publication [472]:

  1. The correlations of the flare occurrence time, its duration, its peak luminosity and total energy in x-ray band were found with regard to an isotropic-equivalent energy of the prompt phase radiation for each of sample bursts;

  2. A correlation between energies of the flare-plateau-afterglow phase in x-ray afterglow and one of the γ-ray prompt phase was found for each sample burst;

  3. For each sample GRB a thermal component in the time-resolved spectra of the x-ray flare was identified and interpreted as due to collision of GRB with supernova ejecta with subsequent transparency at radii $\sim 10^{12}$ cm with $\Gamma \lesssim 4$.

- In Chapter 4 we analyzed a sample of 54 GRBs with high-energy emission detected by *Fermi*-LAT telescope. Our goal was to connect GeV photons generation to the black hole activity. We work under the assumption of the black hole generating the high-energy emission via extraction of its rotational energy. We constrain the black hole mass and spin parameters and infer the geometry of the GeV emission site as conical region perpendicular to the orbital plane of the binary progenitors. The following results were obtained and reflected in the subsequent publication [475]:

  1. Black hole mass and spin parameters were calculated following the works on rotational energy extraction mechanism;

  2. New families of the fireshell paradigm were introduced and in total now account as 9 subsclasses.

  3. Interpretation of the GeV photons non-observability for energetic GRBs occurred within *Fermi*-LAT field of view was given as due to specific morphology of the emission site.

  4. Luminosity light curves behavior for high-energy emission of the long GRBs was shown as having universal decay trend and interpreted as due to the spin down rate of the resulting black hole.

Appendix A

K-correction

Let us recall the basic point of the *K*-correction. All the observed GRBs have a different redshift. In order to compare them it is necessary to refer each one of them to its cosmological rest frame. Similarly to the observed flux, each instrument is characterized by its fixed energy window $[\epsilon_{obs,1}; \epsilon_{obs,2}]$. The observed flux f_{obs}, defined as the energy per unit area and time in a fixed instrumental energy window $[\epsilon_{obs,1}; \epsilon_{obs,2}]$, is expressed in terms of the observed photon number spectrum n_{obs}, i.e., as the number of observed photons per unit energy, area and time:

$$f_{obs,[\epsilon_{obs,1};\epsilon_{obs,2}]} = \int_{\epsilon_{obs,1}}^{\epsilon_{obs,2}} \epsilon\, n_{obs}(\epsilon)d\epsilon\,. \tag{A.1}$$

It then follows that the luminosity L of the source, i.e., the total emitted energy per unit time in a given bandwidth (expressed by definition in the source cosmological rest frame), is related to f_{obs} through the luminosity distance $D_L(z)$:

$$L_{[\epsilon_{obs,1}(1+z);\epsilon_{obs,2}(1+z)]} = 4\pi D_L^2(z)f_{obs,[\epsilon_{obs,1};\epsilon_{obs,2}]}\,. \tag{A.2}$$

The above Equation (A.2) gives the luminosities in different cosmological rest frame energy bands, depending on the source redshift. To express the luminosity L in a fixed cosmological rest frame energy band, e.g., $[E_1; E_2]$, common to all sources, we can rewrite Equation (A.2) as:

$$L_{[E_1;E_2]} = 4\pi D_L^2 f_{obs,\left[\frac{E_1}{1+z};\frac{E_2}{1+z}\right]} = 4\pi D_L^2 k[\epsilon_{obs,1}; \epsilon_{obs,2}; E_1; E_2; z]f_{obs,[\epsilon_{obs,1};\epsilon_{obs,2}]}\,, \tag{A.3}$$

where we have defined the *K*-correction factor:

$$k[\epsilon_{obs,1}; \epsilon_{obs,2}; E_1; E_2; z] = \frac{f_{obs,\left[\frac{E_1}{1+z};\frac{E_2}{1+z}\right]}}{f_{obs,[\epsilon_{obs,1};\epsilon_{obs,2}]}} = \frac{\displaystyle\int_{E_1/(1+z)}^{E_2/(1+z)} \epsilon\, n_{obs}(\epsilon)d\epsilon}{\displaystyle\int_{\epsilon_{obs,1}}^{\epsilon_{obs,2}} \epsilon\, n_{obs}(\epsilon)d\epsilon}\,. \tag{A.4}$$

If the energy range $[\frac{E_1}{1+z}; \frac{E_2}{1+z}]$ is not fully inside the instrumental energy band $[\epsilon_{obs,1}; \epsilon_{obs,2}]$, It may well happen that we need to extrapolate n_{obs} within the integration boundaries $[\frac{E_1}{1+z}; \frac{E_2}{1+z}]$.

Finally we express each luminosity in a rest frame energy band which coincides with the energy window of each specific instrument.

Appendix B

Tables

B.1 Full list of short GRBs observed by *Fermi*-GBM

GRB name	T_{90} (s)	$E_{peak}^{z=1}$	$E_{iso}^{z=1}$	θ
	(s)	(keV)	(erg)	(degrees)
080723913	0.192	641.679	6.70615e+50	
080725541	0.96	2965.18	4.87635e+51	
080802386	0.576	1244.78	4.81246e+51	
080815917	0.832	0	3.68838e+51	
080831053	0.576	0	4.57116e+50	
080905499	0.96	0	1.05504e+52	28
080919790	0.512	0	7.8143e+50	
081012045	1.216	2370.44	7.99603e+51	74
081024245	0.832	0	1.5236e+51	
081024891	0.64	3545.56	4.56215e+51	19
081101491	0.128	442.788	5.21599e+50	30
081102365	1.728	1285.07	6.62857e+51	48
081105614	1.28	0	1.26962e+51	87
081107321	1.664	141.622	3.58689e+51	
081113230	0.576	455.594	1.22532e+51	
081115891	0.32	0	8.61698e+50	
081119184	0.32	0	7.25741e+50	
081122614	0.192	358.561	3.48905e+50	
081204517	0.192	598.864	8.06488e+50	
081209981	0.192	2247.43	7.32888e+51	
081213173	0.256	0	9.22377e+50	
081216531	0.768	2224.98	2.38226e+52	95
081223419	0.576	363.589	2.49374e+51	28
081226044	0.832	1166.97	1.55926e+51	110
081226509	0.192	681.076	1.07855e+51	26
081229187	0.768	1033.82	1.34468e+51	
081230871	0.512	0	5.31384e+50	
090108020	0.704	259.755	2.20409e+51	

Continued on next page

Table B.1 – Continued from previous page

GRB name	T_{90} (s)	$E_{peak}^{z=1}$	$E_{iso}^{z=1}$	θ
	(s)	(keV)	(erg)	(degrees)
090108322	0.192	0	3.28744e+51	
090109332	1.728	0	1.23781e+52	
090120627	1.856	5041.05	5.67479e+51	
090206620	0.32	919.76	2.21293e+51	
090219074	0.448	0	1.23427e+51	141
090228204	0.448	1722.89	2.36772e+52	24
090305052	1.856	2118.26	2.2667e+52	40
090308734	1.664	1227.6	1.19893e+52	50
090328713	0.192	3957.59	5.57168e+51	74
090331681	0.832	1503.68	5.35737e+51	
090405663	0.448	1863.64	1.4081e+51	
090412061	0.896	0	1.31967e+51	73
090418816	0.32	0	3.11433e+51	
090427644	1.024	0	2.43776e+51	14
090429753	0.64	1857.87	5.01014e+52	
090510016	0.96	9454.12	2.80464e+53	14
090520832	0.768	0	1.6791e+52	
090531775	0.768	3364.75	2.18837e+52	22
090616157	1.152	0	1.95155e+51	
090617208	0.192	1362.16	3.97977e+51	
090620901	0.96	0	5.1056e+51	
090621922	0.384	1038.57	1.52736e+51	108
090717111	0.384	0	2.1605e+51	
090802235	0.048	703.651	1.80665e+51	96
090814368	0.192	1428.8	3.11827e+51	61
090819607	0.192	811.168	7.4192e+50	
090907808	0.832	791.744	4.62427e+51	
090909854	1.152	0	2.35391e+52	52
090924625	0.352	1241.33	1.68492e+51	56
090927422	0.512	0	3.33944e+51	85
091006360	0.192	358.276	4.76063e+50	
091012783	0.704	1321.02	1.14154e+52	
091018957	0.192	618.001	8.02501e+50	134
091019750	0.208	429.059	2.4216e+50	56
091126333	0.192	684.205	1.44536e+51	93
091223191	0.576	0	2.06468e+51	
091224373	0.768	0	8.94052e+50	84
100101988	1.984	1596.86	5.18463e+51	47
100107074	0.576	0	1.05274e+51	53
100117879	0.256	650.862	1.0517e+51	86
100204858	1.92	0	4.15572e+50	101
100206563	0.176	1063.65	3.09658e+51	45
100208386	0.192	0	2.31901e+51	55

Continued on next page

Table B.1 – Continued from previous page

GRB name	T_{90} (s)	$E_{peak}^{z=1}$	$E_{iso}^{z=1}$	θ
	(s)	(keV)	(erg)	(degrees)
100216422	0.192	772.045	1.00677e+51	75
100223110	0.256	2084.1	9.16017e+51	76
100301068	0.96	801.046	8.39528e+50	43
100328141	0.384	2410.06	1.58952e+52	58
100411516	0.512	0	9.74811e+50	73
100417166	0.192	491.73	5.3387e+50	15
100516396	0.64	0	5.3121e+50	69
100525744	1.472	1111.47	2.97386e+51	72
100612545	0.576	2095.02	8.86773e+52	99
100616773	0.192	0	2.59808e+51	122
100625773	0.24	966.378	3.96609e+51	124
100629801	0.832	443.396	3.20591e+51	133
100706693	0.128	1669.48	1.41471e+51	100
100719311	1.6	0	3.08616e+51	43
100805300	0.064	0	1.78482e+51	152
100811108	0.384	2261.5	1.46385e+52	64
100827455	0.576	1470.51	1.23574e+52	47
100929916	0.32	2244.31	6.02272e+51	95
101021063	1.536	0	5.87903e+51	80
101026034	0.256	955.138	1.22482e+51	104
101027230	1.344	0	6.59423e+50	30
101031625	0.384	661.811	1.10354e+51	96
101116481	0.576	874.683	5.52262e+50	13
101129652	0.384	2809.88	1.22314e+52	26
101129726	0.576	1670.26	8.66833e+51	41
101204343	0.128	1168.81	1.29486e+51	44
101208203	0.192	1125.41	1.3726e+51	67
101216721	1.917	305.804	8.32354e+51	88
101224227	1.728	0	1.88799e+51	73
110131780	0.384	0	2.08516e+51	48
110212550	0.064	954.631	2.02623e+51	50
110213876	0.448	0	1.29147e+51	82
110227009	1.728	489.412	1.03809e+51	68
110409179	0.128	996.759	1.2343e+51	73
110420946	0.128	691.676	8.98107e+50	123
110422029	0.32	0	2.02169e+51	38
110424758	0.672	0	1.2568e+51	65
110509475	0.64	0	3.83465e+51	48
110517453	0.576	0	1.65493e+51	20
110526715	0.448	1137.68	4.05884e+51	66
110529034	0.512	1980.89	1.35369e+52	30
110605780	1.536	433.6	1.52902e+51	87
110705151	0.192	2047.35	1.87069e+52	84

Continued on next page

Table B.1 – Continued from previous page

GRB name	T_{90} (s)	$E_{peak}^{z=1}$	$E_{iso}^{z=1}$	θ
	(s)	(keV)	(erg)	(degrees)
110717180	0.112	917.138	1.1444e+51	109
110728056	0.704	1222.81	3.58737e+51	42
110801335	0.384	0	3.48831e+51	139
110916016	1.792	0	1.24821e+51	90
111001804	0.384	0	2.36932e+51	73
111011094	1.472	702.368	1.71177e+51	61
111022854	0.192	741.978	7.63363e+50	23
111024896	0.96	599.261	9.00965e+50	82
111103948	0.32	2555.94	4.21658e+51	78
111112908	0.224	1866.39	4.50258e+51	60
111117510	0.432	1087.23	3.52182e+51	14
111207512	0.768	0	4.21956e+50	27
111222619	0.288	1481.52	2.12798e+52	136
120101354	0.128	400.537	3.53881e+50	49
120129312	1.28	2422.78	8.4702e+50	66
120205285	0.576	0	5.63433e+50	65
120210650	1.344	0	1.55286e+51	27
120212353	0.864	0	2.05661e+51	28
120222021	1.088	259.993	4.89235e+51	83
120302722	1.6	0	1.00079e+51	102
120314412	1.28	0	2.01732e+51	25
120327418	0.256	483.667	6.45025e+50	126
120410585	1.088	1099.51	1.52004e+51	77
120415891	0.96	1608.88	1.99829e+51	50
120429003	1.664	563.001	1.42187e+51	87
120509619	0.704	0	1.2677e+51	55
120519721	1.056	1638.02	1.29e+52	90
120524134	0.704	123.262	6.30015e+50	100
120603439	0.384	1294.74	3.17986e+51	75
120608489	0.96	732.983	2.83991e+51	20
120609580	1.792	0	4.61897e+51	32
120612687	0.256	1941.78	3.17056e+51	90
120616630	0.048	0	1.39705e+51	30
120619884	0.96	0	4.47695e+51	19
120629565	0.704	0	9.00474e+50	42
120811014	0.448	2522.57	1.42328e+52	86
120814201	0.896	2060.28	7.97105e+51	137
120814803	0.192	0	5.6964e+50	39
120817168	0.16	2696.71	1.34896e+52	59
120822628	1.536	0	1.12741e+51	7
120830297	0.896	2179.73	1.99039e+52	39
120831901	0.384	1433.09	1.5938e+51	95
120915000	0.576	1563.63	2.68801e+51	11

Continued on next page

Table B.1 – Continued from previous page

GRB name	T_{90} (s)	$E_{peak}^{z=1}$	$E_{iso}^{z=1}$	θ
	(s)	(keV)	(erg)	(degrees)
120916085	1.28	0	4.84042e+50	70
121004211	1.536	0	3.74094e+51	68
121012724	0.448	1158.74	3.70712e+51	75
121014638	0.576	0	1.14665e+51	66
121023322	0.512	2671.36	9.68755e+51	76
121112806	1.28	0	7.21682e+51	57
121116459	0.832	0	8.28323e+51	121
121124606	0.256	0	1.37417e+51	86
121127914	0.64	1929.43	1.22734e+52	118
130127743	0.144	1445.79	1.78776e+51	27
130204484	0.192	0	2.50958e+51	41
130219626	1.536	532.833	5.12625e+50	84
130307126	0.384	3505.53	9.4659e+51	69
130325005	0.64	0	3.74901e+50	18
130404877	0.96	0	8.43522e+50	15
130416770	0.192	2138.18	5.4185e+53	84
130503214	0.88	0	6.76768e+50	22
130504314	0.384	2654.32	3.5156e+52	62
130515056	0.256	992.969	4.16273e+51	128
130617564	0.768	0	4.36004e+51	135
130622615	0.96	349.361	1.97773e+51	49
130626452	1.728	0	1.5291e+51	89
130628860	0.512	2307.86	9.57568e+51	51
130701761	1.6	2410.75	4.5504e+52	70
130705398	0.128	0	2.03737e+51	85
130706900	0.128	844.681	7.0299e+50	61
130716442	0.768	0	9.4048e+51	46
130802730	0.064	0	1.64461e+51	88
130804023	0.96	1022.48	1.13884e+52	21
130808253	0.256	0	1.47506e+51	119
130912358	0.512	1996.31	5.82931e+51	102
130919173	0.96	232.702	1.15504e+52	50
130924910	1.792	0	1.46181e+52	36
131004904	1.152	235.821	1.31239e+51	93
131006367	0.128	0	1.31034e+51	95
131126163	0.128	1220.55	4.75818e+52	108
131128629	1.984	0	6.04378e+51	71
131217108	0.768	3269.73	1.21079e+52	99
140105065	1.088	2094.97	4.81227e+51	72
140105748	0.576	812.675	1.57114e+51	30
140109771	0.704	0	3.76854e+51	135
140129499	0.128	0	1.37203e+51	107
140209313	1.408	287.801	4.98317e+52	77

Table B.1 – Continued from previous page

GRB name	T_{90} (s)	$E_{peak}^{z=1}$	$E_{iso}^{z=1}$	θ
	(s)	(keV)	(erg)	(degrees)
140329272	0.064	791.022	7.77454e+50	33
140402007	0.32	2091.38	2.42366e+51	14
140428906	0.32	1810.31	4.11581e+51	111
140501139	0.256	0	1.25105e+51	90
140511095	1.408	656.873	1.06215e+51	54
140518709	0.704	0	8.03697e+50	130
140526571	0.064	0	1.03078e+51	15
140605377	0.512	1360.91	6.5596e+51	39
140610487	0.96	0	2.38431e+51	90
140619490	0.448	484.942	7.43203e+50	135
140624423	0.096	702.159	9.38637e+50	54
140626843	1.792	352.201	3.63146e+51	121
140710537	0.384	0	2.75189e+51	88
140720158	0.32	755.169	5.63174e+50	82
140724533	0.896	0	3.51571e+52	81
140807500	0.512	1607.24	6.89827e+51	85
140901821	0.176	2705.45	3.08713e+52	98
141011282	0.08	1228.3	3.54085e+51	34
141031998	0.16	0	1.2137e+51	34
141102112	0.016	0	7.06485e+50	109
141105406	1.28	840.779	4.30145e+51	25
141111435	1.728	0	6.49996e+50	68
141113346	0.448	0	3.23457e+51	54
141122087	1.28	822.701	7.20403e+50	94
141124277	0.512	0	4.29226e+51	128
141126233	0.896	0	2.49672e+51	56
141128962	0.272	342.787	5.83865e+50	87
141202470	1.408	1317.2	2.16357e+52	81
141205337	1.28	0	6.7288e+51	123
141208632	0.96	0	1.89035e+52	92
141213300	0.768	237.916	1.44293e+51	88
141230871	0.224	0	1.20011e+51	54
150101270	0.48	0	5.15486e+50	12
150101641	0.08	0	5.22752e+50	54
150118927	0.288	1345.34	4.3074e+51	92
150128624	0.096	0	1.50125e+51	143
150208929	0.128	0	2.49967e+53	11
150214293	0.192	1422.33	1.7161e+51	46
150301045	0.416	0	9.60873e+50	106
150312403	0.32	601.755	4.58252e+50	24
150316400	1.984	0	3.61539e+52	20
150320462	0.064	1802.32	2.34129e+51	145
150325696	0.08	630.78	5.9515e+50	24

Continued on next page

Table B.1 – Continued from previous page

GRB name	T_{90} (s)	$E^{z=1}_{peak}$	$E^{z=1}_{iso}$	θ
	(s)	(keV)	(erg)	(degrees)
150412507	0.576	0	6.03277e+50	48
150412931	0.64	1140.18	1.79459e+51	79
150506630	0.512	1986.11	4.75079e+51	20
150506972	0.384	2172.93	2.67827e+52	49
150522944	1.024	467.013	6.34836e+50	22
150601904	0.768	0	4.13604e+50	19
150604434	0.896	1561.11	9.40498e+51	28
150605782	0.176	0	4.68211e+50	77
150609316	0.256	0	6.00612e+50	66
150628767	0.64	975.561	1.64578e+51	63
150629564	1.92	3875.5	3.76577e+52	41
150705588	0.704	0	9.21624e+50	43
150715136	0.384	1894.89	6.17414e+51	50
150721431	0.32	0	9.38947e+52	83
150728151	1.728	823.455	5.2911e+51	68
150805746	1.408	0	2.03946e+51	94
150810485	1.28	2721.97	1.27922e+52	62
150811849	0.64	2750.03	2.80788e+52	107
150819440	0.96	1047.75	3.33379e+52	101
150901924	0.256	0	5.27632e+50	120
150906944	0.32	1141.7	1.72664e+51	29
150912600	0.32	703.727	1.64105e+51	46
150922234	0.144	1031.3	3.06248e+51	41
150923297	0.192	0	1.00869e+51	34
150923429	0.192	0	2.12115e+51	68
150923864	1.792	286.987	4.53491e+51	39
151022577	0.32	527.06	1.01586e+51	103
151202565	0.704	2308.26	6.19357e+51	100
151222340	0.768	2637.45	1.39353e+52	117
151228129	0.256	1680.08	4.5052e+51	117
151229486	0.16	0	1.81361e+51	87
151231568	0.832	929.077	7.19034e+51	50
160211119	0.96	0	2.9198e+51	13
160224911	0.384	0	2.44995e+51	75
160314473	1.664	0	7.08357e+50	90
160406503	0.432	1426.48	2.8314e+51	77
160408268	1.056	1780.2	5.34214e+51	7
160411062	0.672	0	9.76435e+50	108
160428412	0.576	2948.56	6.55056e+51	16
160603719	0.384	986.839	7.05746e+51	97
160612842	0.288	2729.4	5.08298e+51	37
160624477	0.384	0	5.52041e+52	76
160714097	0.32	0	9.59781e+51	58

Table B.1 – Continued from previous page

GRB name	T_{90} (s)	$E_{peak}^{z=1}$	$E_{iso}^{z=1}$	θ
	(s)	(keV)	(erg)	(degrees)
160726065	0.768	730.066	5.16395e+51	44
160804180	0.64	1391.09	7.08502e+51	88
160804968	0.192	6023.97	4.97966e+51	46
160806584	1.664	277.307	4.72923e+51	113
160820496	0.448	1519.29	3.41596e+51	68
160821937	1.088	0	1.34785e+51	61
160822672	0.04	1322.46	2.72925e+51	63
160826938	1.792	0	3.56017e+51	74
160829334	0.512	1168.57	1.53575e+51	14
161015400	0.192	0	1.97971e+51	85
161026373	0.112	568.534	3.39019e+51	27
161110179	1.792	0	1.08504e+52	45
161115745	0.032	0	8.73127e+50	10
161218222	0.32	3972.47	1.28078e+52	66
161230298	0.448	1063.54	8.33036e+50	62
170111760	0.832	1821.19	1.91254e+51	90
170121133	1.6	0	3.88009e+51	73
170124528	0.448	877.269	1.309e+51	108
170127067	0.128	1707.91	3.07379e+52	142
170127634	1.728	1243.83	2.40694e+51	44
170203486	0.336	0	1.24265e+51	100
170206453	1.168	695.983	4.43889e+52	67
170219002	0.096	3888.32	7.22153e+51	133
170222209	1.664	1668.2	2.51439e+52	120
170304003	0.16	172.802	6.36723e+50	59
170305256	0.448	546.378	3.64113e+51	59
170325331	0.576	1150.26	1.71834e+51	60
170403583	0.48	1086.51	1.80719e+51	81
170506169	0.832	1857.32	4.42685e+51	98
170511648	1.28	0	2.1611e+51	37
170604603	0.32	1981.54	6.01399e+51	66
170709334	1.856	1113.2	8.79543e+51	73
170711713	1.152	4686.04	8.53714e+51	71
170714049	0.224	0	1.05949e+51	31
170726249	1.792	412.772	3.10623e+51	9
170816599	1.6	2674.26	4.07915e+53	103
170818137	0.576	0	2.5944e+51	109
170826369	0.256	1445	2.6916e+51	81
170827818	0.832	639.669	2.68354e+51	62
170912985	0.48	0	1.11858e+51	53
170915520	0.64	1180.5	2.25852e+51	19
170918139	0.128	0	7.10877e+52	108
170926782	0.896	221.505	9.15256e+51	68

Table B.1 – Continued from previous page

GRB name	T_{90} (s)	$E_{peak}^{z=1}$	$E_{iso}^{z=1}$	θ
	(s)	(keV)	(erg)	(degrees)
171030729	0.096	0	1.23894e+51	83
171108656	0.032	200.448	4.68532e+52	80
171207055	0.176	1364.45	1.40136e+51	20
171219279	1.152	0	6.11454e+51	19
171223818	0.384	0	1.20202e+52	56
171230119	1.28	3844.33	2.88727e+51	73
180123820	0.32	0	6.74539e+52	22
180128215	0.208	0	2.01722e+51	56
180130744	0.256	0	3.77766e+50	137
180131528	0.96	0	1.36354e+51	22
180201706	0.192	0	1.47761e+53	30
180201780	0.64	0	7.08773e+51	68
180204109	1.152	1705.76	1.58221e+52	68
180206203	0.448	0	4.79763e+51	80
180225417	0.896	1949.55	4.96947e+51	55
180227211	0.288	0	4.19608e+52	87
180311074	0.96	0	9.18617e+51	135
180313978	0.08	599.462	7.35399e+50	40
180402406	0.448	2653.58	1.70886e+52	90
180402481	0.256	670.755	1.28506e+51	123
180404848	0.544	0	1.38347e+51	112
180417689	0.256	0	2.41335e+51	63
180511364	0.128	1488	8.62698e+50	49
180511437	1.984	215.067	1.96105e+52	54
180523782	1.984	2869.04	6.21393e+51	12
180525151	0.544	2023.86	1.68771e+51	76
180602938	0.008	769.01	8.92689e+50	9
180617872	1.92	316.63	2.53838e+51	88
180625941	0.704	1152.03	2.96277e+51	132
180626392	0.96	862.47	2.97544e+51	112
180703949	1.536	273.749	4.60329e+52	32
180715741	1.664	1121.59	8.24943e+51	79
180715755	0.704	1804.56	8.58977e+51	75

Table B.1. List of 398 short ($\lesssim 2$ s) GRBs within August 2008–July 2018 detected by *Fermi*-GBM with estimated isotropic-equivalent energy E_{iso} when given $z = 1.0$ as an average redshift for short bursts. Highlighted in red are short GRBs from the Second LAT Catalog, see Table B.2. The information on boresight angle θ in degrees was retrieved from LAT catalog, GBM trigger catalog and `GCN` archive.

B.2   Short bursts from the Second *Fermi*-LAT GRB catalog

GRB name	T_{90} (s)	$E_{peak}^{z=1}$	$E_{iso}^{z=1}$	θ
	(s)	(keV)	(erg)	(degrees)
081024891	0.64	3545.56	4.56215e+51	19
081102365	1.728	1285.07	6.62857e+51	48
090227772	0.304	0	0	73
090228204	0.448	1722.89	2.36772e+52	24
090510016	0.96	9454.12	2.80464e+53	14
090531775	0.768	3364.75	2.18837e+52	22
110529034	0.512	1980.89	1.35369e+52	30
110728056	0.704	1222.81	3.58737e+51	42
120830297	0.896	2179.73	1.99039e+52	39
120915000	0.576	1563.63	2.68801e+51	11
140402007	0.32	2091.38	2.42366e+51	14
141113346	0.448	0	3.23457e+51	54
160702A				72
160829334	0.512	1168.57	1.53575e+51	14
170127C				142
171011810	0.48	0	4.01258e+52	43
180703949	1.536	273.749	4.60329e+52	32

Table B.2. List of 14 short GRBs from the second *Fermi*-LAT catalog. Three bursts were observed in LLE mode only [30–100 MeV].

Bibliography

[1] AARTSEN, M. G., ET AL. Search for Prompt Neutrino Emission from Gamma-Ray Bursts with IceCube. *The Astrophysical Journal Letters*, **805** (2015), L5. `arXiv:1412.6510`, `doi:10.1088/2041-8205/805/1/L5`.

[2] AARTSEN, M. G., ET AL. An All-sky Search for Three Flavors of Neutrinos from Gamma-ray Bursts with the IceCube Neutrino Observatory. *The Astrophysical Journal*, **824** (2016), 115. `arXiv:1601.06484`, `doi:10.3847/0004-637X/824/2/115`.

[3] AARTSEN, M. G., ET AL. Extending the Search for Muon Neutrinos Coincident with Gamma-Ray Bursts in IceCube Data. *The Astrophysical Journal*, **843** (2017), 112. `arXiv:1702.06868`, `doi:10.3847/1538-4357/aa7569`.

[4] ABBASI, R., ET AL. Search for Muon Neutrinos from Gamma-ray Bursts with the IceCube Neutrino Telescope. *The Astrophysical Journal*, **710** (2010), 346. `arXiv:0907.2227`, `doi:10.1088/0004-637X/710/1/346`.

[5] ABBASI, R., ET AL. An absence of neutrinos associated with cosmic-ray acceleration in γ-ray bursts. *Nature*, **484** (2012), 351. `arXiv:1204.4219`, `doi:10.1038/nature11068`.

[6] ABDO, A. A., ET AL. Fermi Observations of GRB 090902B: A Distinct Spectral Component in the Prompt and Delayed Emission. *The Astrophysical Journal Letters*, **706** (2009), L138. `arXiv:0909.2470`, `doi:10.1088/0004-637X/706/1/L138`.

[7] ABDO, A. A., ET AL. Fermi Detection of Delayed GeV Emission from the Short Gamma-Ray Burst 081024B. *The Astrophysical Journal*, **712** (2010), 558. `arXiv:1002.3205`, `doi:10.1088/0004-637X/712/1/558`.

[8] ABLES, J. G. Fourier transform photography: a new method for X-ray astronomy. *Proceedings of the Astronomical Society of Australia*, **1** (1968), 172.

[9] ACKERMANN, M., ET AL. Constraining the High-energy Emission from Gamma-Ray Bursts with Fermi. *The Astrophysical Journal*, **754** (2012), 121. `arXiv:1201.3948`, `doi:10.1088/0004-637X/754/2/121`.

[10] ACKERMANN, M., ET AL. The First Fermi-LAT Gamma-Ray Burst Catalog. *The Astrophysical Journal Supplement Series*, **209** (2013), 11. `arXiv:1303.2908`, `doi:10.1088/0067-0049/209/1/11`.

[11] ACKERMANN, M., ET AL. Fermi-LAT Observations of the Gamma-Ray Burst GRB 130427A. *Science*, **343** (2014), 42. `arXiv:1311.5623`, `doi:10.1126/science.1242353`.

[12] AIMURATOV, Y., ET AL. GRB 081024B and GRB 140402A: Two Additional Short GRBs from Binary Neutron Star Mergers. *The Astrophysical Journal*, **844** (2017), 83. `arXiv:1704.08179`, `doi:10.3847/1538-4357/aa7a9f`.

[13] AJELLO, M., ET AL. A Decade of Gamma-Ray Bursts Observed by Fermi-LAT: The Second GRB Catalog. *The Astrophysical Journal*, **878** (2019), 52. `arXiv:1906.11403`, `doi:10.3847/1538-4357/ab1d4e`.

[14] AKSENOV, A. G., RUFFINI, R., AND VERESHCHAGIN, G. V. Thermalization of Nonequilibrium Electron-Positron-Photon Plasmas. *Physical Review Letters*, **99** (2007), 125003. arXiv:0707.3250, doi:10.1103/PhysRevLett.99.125003.

[15] AKSENOV, A. G., RUFFINI, R., AND VERESHCHAGIN, G. V. Thermalization of the mildly relativistic plasma. *Physical Review D*, **79** (2009), 043008. arXiv:0901.4837, doi:10.1103/PhysRevD.79.043008.

[16] ALEXANDER, K. D., LASKAR, T., AND BERGER, E. GRB 160509A: VLA Detection. *GCN*, **19414** (2016).

[17] ALEXANDER, K. D., LASKAR, T., FONG, W., AND BERGER, E. GRB 160625B: VLA Detection. *GCN*, **19606** (2016).

[18] AMATI, L., ET AL. GRB 130702A in the Ep,i–Eiso plane. *GCN*, **15025** (2013).

[19] ANDERSON, G. E., FENDER, R. P., STALEY, T. D., AND ROWLINSON, B. A. GRB 130907A: AMI radio detection. *GCN*, **15211** (2013).

[20] ATTEIA, J.-L., ET AL. A second catalog of gamma-ray bursts - 1978-1980 localizations from the interplanetary network. *The Astrophysical Journal Supplement Series*, **64** (1987), 305. doi:10.1086/191198.

[21] ATWOOD, W. B., ET AL. The Large Area Telescope on the Fermi Gamma-Ray Space Telescope Mission. *The Astrophysical Journal*, **697** (2009), 1071. arXiv:0902.1089, doi:10.1088/0004-637X/697/2/1071.

[22] AXELSSON, M., KOCEVSKI, D., AND RACUSIN, J. GRB 150314A: Fermi-LAT detection. *GCN*, **17576** (2015).

[23] BAND, D., ET AL. BATSE observations of gamma-ray burst spectra. I - Spectral diversity. *The Astrophysical Journal*, **413** (1993), 281. doi:10.1086/172995.

[24] BAND, D. L., ET AL. Prospects for GRB Science with the Fermi Large Area Telescope. *The Astrophysical Journal*, **701** (2009), 1673. arXiv:0906.0991, doi:10.1088/0004-637X/701/2/1673.

[25] BARTHELMY, S. D., ET AL. The Burst Alert Telescope (BAT) on the SWIFT Midex Mission. *Space Science Reviews*, **120** (2005), 143. arXiv:astro-ph/0507410, doi:10.1007/s11214-005-5096-3.

[26] BARTHELMY, S. D., ET AL. A small revision to the GRB-naming convention. *GCN*, **10251** (2009).

[27] BARTHELMY, S. D., ET AL. GRB 131030A: BAT refined. *GCN*, **15456** (2013).

[28] BATHURST, C., FRAIL, D. A., AND CENKO, S. B. GRB 120624B: VLA observations. *GCN*, **13474** (2012).

[29] BAUMGARTNER, W. H., ET AL. GRB 140419A: BAT refined. *GCN*, **16127** (2014).

[30] BEAR, E. AND SOKER, N. Neutron Star Natal Kick and Jets in Core Collapse Supernovae. *The Astrophysical Journal*, **855** (2018), 82. arXiv:1710.00819, doi:10.3847/1538-4357/aaad07.

[31] BEARDMORE, A. P., ET AL. GRB 170214A: XRT observation. *GCN*, **20679** (2017).

[32] BEARDMORE, A. P. AND EVANS, P. A. GRB 120711A: XRT. *GCN*, **13442** (2012).

[33] BECERRA, L., BIANCO, C. L., FRYER, C. L., RUEDA, J. A., AND RUFFINI, R. On the Induced Gravitational Collapse Scenario of Gamma-ray Bursts Associated with Supernovae. *The Astrophysical Journal*, **833** (2016), 107. arXiv:1606.02523, doi:10.3847/1538-4357/833/1/107.

[34] BECERRA, L., CIPOLLETTA, F., FRYER, C. L., RUEDA, J. A., AND RUFFINI, R. Angular Momentum Role in the Hypercritical Accretion of Binary-driven Hypernovae. *The Astrophysical Journal*, **812** (2015), 100. `arXiv:1505.07580`, `doi:10.1088/0004-637X/812/2/100`.

[35] BERGER, E. Short-Duration Gamma-Ray Bursts. *Annual Review of Astronomy and Astrophysics*, **52** (2014), 43. `arXiv:1311.2603`, `doi:10.1146/annurev-astro-081913-035926`.

[36] BERSIER, D. GRB 110731A: FTN+FTS afterglow observations. *GCN*, **12216** (2011).

[37] BIANCO, C. L. AND RUFFINI, R. Exact versus Approximate Solutions in Gamma-Ray Burst Afterglows. *The Astrophysical Journal Letters*, **633** (2005), L13. `arXiv:astro-ph/0509621`, `doi:10.1086/498146`.

[38] BIANCO, C. L. AND RUFFINI, R. On the Exact Analytic Expressions for the Equitemporal Surfaces in Gamma-Ray Burst Afterglows. *The Astrophysical Journal Letters*, **620** (2005), L23. `arXiv:astro-ph/0501390`, `doi:10.1086/428500`.

[39] BISSALDI, E. GRB 090926: Fermi GBM detection. *GCN*, **9933** (2009).

[40] BISSALDI, E. AND CONNAUGHTON, V. GRB 090902B: Fermi GBM detection of a bright burst. *GCN*, **9866** (2009).

[41] BISSALDI, E., ET AL. GRB 141028A: Fermi-LAT detection. *GCN*, **16969** (2014).

[42] BISSALDI, E., VIANELLO, G., AND CHIANG, J. GRB 140402A: Fermi-LAT detection of a burst. *GCN*, **16069** (2014).

[43] BLOOM, J. S., DJORGOVSKI, S. G., KULKARNI, S. R., AND FRAIL, D. A. The Host Galaxy of GRB 970508. *The Astrophysical Journal Letters*, **507** (1998), L25. `arXiv:astro-ph/9807315`, `doi:10.1086/311682`.

[44] BLOOM, J. S., FRAIL, D. A., AND SARI, R. The Prompt Energy Release of Gamma-Ray Bursts using a Cosmological k-Correction. *The Astronomical Journal*, **121** (2001), 2879. `arXiv:astro-ph/0102371`, `doi:10.1086/321093`.

[45] BOELLA, G., ET AL. BeppoSAX, the wide band mission for X-ray astronomy. *Astronomy & Astrophysics Supplement*, **122** (1997), 299. `doi:10.1051/aas:1997136`.

[46] BOËR, M., ET AL. Detection of a very bright optical flare from the gamma-ray burst grb 050904 at redshift 6.29. *The Astrophysical Journal Letters*, **638** (2006), L71.

[47] BREEVELD, A. AND MASELLI, A. GRB 160623A: UVOT UL. *GCN*, **19568** (2016).

[48] BREEVELD, A. A. AND BEARDMORE, A. P. GRB 170214A: UL. *GCN*, **20682** (2017).

[49] BREEVELD, A. A. AND PAGANI, C. GRB 140402A: UVOT UL. *GCN*, **16077** (2014).

[50] BREEVELD, A. A. AND SIEGEL, M. H. GRB 171010A: UVOT. *GCN*, **22004** (2017).

[51] BREGEON, J., MCENERY, J., AND OHNO, M. GRB110731A. *GCN*, **12218** (2011).

[52] BREMER, M., WINTERS, J. M., KONIG, S., DE UGARTE POSTIGO, A., AND CASTRO-TIRADO, A. J. GRB 120624B: mm detection at PdBI. *GCN*, **13421** (2012).

[53] BRIGGS, M. S., ET AL. The Accuracy of GBM GRB Locations. In *American Institute of Physics Conference Series* (edited by C. Meegan, C. Kouveliotou, and N. Gehrels), vol. 1133, pp. 40–42 (2009). `doi:10.1063/1.3155935`.

[54] BRIGGS, M. S., ET AL. BATSE Observations of the Large-Scale Isotropy of Gamma-Ray Bursts. *The Astronomical Journal*, **459** (1996), 40. `arXiv:astro-ph/9509078`, `doi:10.1086/176867`.

[55] BURLON, D., ET AL. Precursors in Swift Gamma Ray Bursts with Redshift. *The Astrophysical Journal Letters*, **685** (2008), L19. `arXiv:0806.3076, doi:10.1086/ 592350`.

[56] BURNS, E. GRB 160625B: Fermi GBM initial observations. *GCN*, **19581** (2016).

[57] BURROWS, D. N., ET AL. GRB 150403A: XRT refined. *GCN*, **17668** (2015).

[58] BUTLER, N., ET AL. GRB 130702A: RATIR optical and NIR observations. *GCN*, **14980** (2013), 1.

[59] BUTLER, N., ET AL. GRB 130907A: RATIR optical/NIR. *GCN*, **15208** (2013).

[60] BUTLER, N., ET AL. GRB 160623A: RATIR Optical/NIR. *GCN*, **19567** (2016).

[61] CAMPANA, S., ET AL. The association of GRB 060218 with a supernova and the evolution of the shock wave. *Nature*, **442** (2006), 1008. `arXiv:astro-ph/0603279, doi:10.1038/nature04892`.

[62] CANNIZZO, J. K., ET AL. GRB 100728A: Swift detection. *GCN*, **11004** (2010).

[63] CANO, Z., ET AL. GRB 091208B: Faulkes North and South. *GCN*, **10262** (2009).

[64] CASH, W. Parameter estimation in astronomy through application of the likelihood ratio. *The Astrophysical Journal*, **228** (1979), 939. `doi:10.1086/156922`.

[65] CASTRO-TIRADO, A. J., BREMER, M., AND WINTERS, J.-M. GRB 130518A: mm detection at PdBI. *GCN*, **14689** (2013).

[66] CASTRO-TIRADO, A. J., ET AL. GRB 160623A: afterglow spectroscopy by GTC and independent redshift determination. *GCN*, **19710** (2016).

[67] CENKO, S. B., BLOOM, J. S., MORGAN, A. N., AND PERLEY, D. A. GRB 090328: Gemini South redshift. *GCN*, **9053** (2009).

[68] CENKO, S. B., ET AL. GRB 130702A: P200 spectroscopic confirmation of associated supernova. *GCN*, **14998** (2013), 1.

[69] CENKO, S. B., PERLEY, D. A., COBB, B. E., BLOOM, J. S., AND BUTLER, N. R. GRB 090926A: late-time Gemini south observations and possible jet break. *GCN*, **10049** (2009).

[70] CENKO, S. B., TROJA, E., AND TEGLER, S. GRB 160509A: DCT Imaging / Afterglow Confirmation. *GCN*, **19416** (2016).

[71] CENKO, S. B., VOGEL, S., PERLEY, D. A., AND FRUCHTER, A. GRB 160509A: Further VLA Observations. *GCN*, **19428** (2016).

[72] CHANDRA, P. GMRT radio detection of GRB 130702A. *GCN*, **15002** (2013), 1.

[73] CHANDRA, P., CENKO, S. B., FRAIL, D. A., AND HARRISON, F. GRB 081024B: VLA radio observation. *GCN*, **8451** (2008).

[74] CHANDRA, P. AND FRAIL, D. A. GRB 090902B: VLA radio. *GCN*, **9889** (2009).

[75] CHANDRA, P. AND FRAIL, D. A. A Radio-selected Sample of Gamma-Ray Burst Afterglows. *The Astrophysical Journal*, **746** (2012), 156. `arXiv:1110.4124, doi: 10.1088/0004-637X/746/2/156`.

[76] CHANDRA, P., FRAIL, D. A., CENKO, S. B., AND HARRISON, F. GRB 100413A: radio afterglow detection with the expanded VLA. *GCN*, **10649** (2010).

[77] CHARISI, M., MÁRKA, S., AND BARTOS, I. Catalogue of isolated emission episodes in gamma-ray bursts from Fermi, Swift and BATSE. *Monthly Notices of the Royal Astronomical Society*, **448** (2015), 2624. `arXiv:1409.2491`, `doi:10.1093/mnras/stu2667`.

[78] CHERUBINI, C., GERALICO, A., RUEDA, H. J. A., AND RUFFINI, R. e^--e^+ pair creation by vacuum polarization around electromagnetic black holes. *Physical Review D*, **79** (2009), 124002. `arXiv:0905.3274`, `doi:10.1103/PhysRevD.79.124002`.

[79] CHESTER, M. M. AND STROH, M. C. GRB 131108A: UVOT. *GCN*, **15476** (2013).

[80] CHESTER, M. M., ET AL. GRB 070318: A Case of Prompt Emission from the External Shock? In *American Institute of Physics Conference Series* (edited by M. Galassi, D. Palmer, and E. Fenimore), vol. 1000, pp. 421–424 (2008). `doi:10.1063/1.2943500`.

[81] CHEUNG, T., ET AL. GRB 130702A/Fermi394416326: LAT. *GCN*, **14971** (2013).

[82] CHINCARINI, G., ET AL. The First Survey of X-Ray Flares from Gamma-Ray Bursts Observed by Swift: Temporal Properties and Morphology. *The Astrophysical Journal*, **671** (2007), 1903. `arXiv:astro-ph/0702371`, `doi:10.1086/521591`.

[83] CHORNOCK, R., PERLEY, D. A., CENKO, S. B., AND BLOOM, J. S. GRB 090323 Gemini-South redshift. *GCN*, **9028** (2009).

[84] CHRISTODOULOU, D. AND RUFFINI, R. Reversible Transformations of a Charged Black Hole. *Physical Review D*, **4** (1971), 3552. `doi:10.1103/PhysRevD.4.3552`.

[85] CIPOLLETTA, F., CHERUBINI, C., FILIPPI, S., RUEDA, J. A., AND RUFFINI, R. Fast rotating neutron stars with realistic nuclear matter equation of state. *Physical Review D*, **92** (2015), 023007. `arXiv:1506.05926`, `doi:10.1103/PhysRevD.92.023007`.

[86] CLEMENS, C., ROSSI, A., GREINER, J., AND MCBREEN, S. GRB 080916C: GROND detection of the optical afterglow candidate. *GCN*, **8257** (2008).

[87] CLEVELAND, W. AND DEVLIN, S. Locally weighted regression: An approach to regression analysis by local fitting. *Journal of the American Statistical Association*, **83** (1988), 596. Available from: `http://www.jstor.org/stable/2289282`.

[88] CLINE, T. L. Recent observations of cosmic gamma-ray bursts. In *Seventh Texas Symposium on Relativistic Astrophysics* (edited by P. G. Bergman, E. J. Fenyves, and L. Motz), vol. 262 of *Annals of the New York Academy of Sciences*, pp. 159–163 (1975). `doi:10.1111/j.1749-6632.1975.tb31429.x`.

[89] CLINE, T. L. AND DESAI, U. D. Progress in Gamma-Ray Burst astronomy. In *The Context and Status of Gamma-Ray Astronomy* (edited by B. G. Taylor) (1974).

[90] CLINE, T. L., DESAI, U. D., KLEBESADEL, R. W., AND STRONG, I. B. Energy Spectra of Cosmic Gamma-Ray Bursts. *The Astrophysical Journal Letters*, **185** (1973), L1. `doi:10.1086/181309`.

[91] CLINE, T. L., ET AL. Detection of a fast, intense and unusual gamma-ray transient. *The Astrophysical Journal Letters*, **237** (1980), L1. `doi:10.1086/183221`.

[92] COBB, B. E. GRB 070318, SMARTS optical/IR. *GCN*, **6296** (2007).

[93] COBB, B. E. GRB 090926a, SMARTS optical/IR. *GCN*, **10113** (2009).

[94] COBB, B. E. GRB 160625B: SMARTS optical/IR. *GCN*, **19616** (2016).

[95] COBB, B. E. GRB 170405A: SMARTS optical/IR. *GCN*, **21003** (2017).

[96] COLLAZZI, A. C. AND CONNAUGHTON, V. GRB 130702A / Fermi394416326: Fermi GBM detection. *GCN*, **14972** (2013).

[97] CONNAUGHTON, V. AND BRIGGS, M. GRB 081024B: Fermi gamma-ray burst monitor detection. *GCN*, **8408** (2008).

[98] CORSI, A. GRB 130907A: VLA detection. *GCN*, **15200** (2013).

[99] CORSI, A., PERLEY, D. A., AND CENKO, S. B. GRB 130702A: VLA detection. *GCN*, **14990** (2013).

[100] COSTA, E., ET AL. Discovery of an X-ray afterglow associated with the γ-ray burst of 28 February 1997. *Nature*, **387** (1997), 783. `arXiv:astro-ph/9706065`, `doi:10.1038/42885`.

[101] CUCCHIARA, A. GRB 131231A: Gemini-South redshift. *GCN*, **15652** (2014).

[102] CUCCHIARA, A. AND CENKO, S. B. GRB 130518A: Gemini. *GCN*, **14687** (2013).

[103] CUCCHIARA, A. AND FOX, D. B. GRB 100414A: Gemini-N. *GCN*, **10606** (2010).

[104] CUCCHIARA, A., FOX, D. B., CENKO, S. B., TANVIR, N., AND BERGER, E. GRB 091003: Gemini-N. *GCN*, **10031** (2009).

[105] CUCCHIARA, A., FOX, D. B., TANVIR, N., AND BERGER, E. GRB 090902B: Gemini-N. *GCN*, **9873** (2009).

[106] CUCCHIARA, A., ET AL. A Photometric Redshift of z ˜ 9.4 for GRB 090429B. *The Astrophysical Journal*, **736** (2011), 7. `arXiv:1105.4915`, `doi:10.1088/0004-637X/736/1/7`.

[107] CUMMINGS, J. R. GRB 140402A BAT refined analysis. *GCN*, **16073** (2014).

[108] CUMMINGS, J. R., ET AL. GRB 070318: Swift detection of a burst with an optical afterglow. *GCN*, **6210** (2007).

[109] D'AI, A., ET AL. GRB 171010A: Swift-XRT afterglow detection. *GCN*, **21989** (2017).

[110] DAI, X., ET AL. Optical and x-ray observations of grb 060526: a complex afterglow consistent with an achromatic jet break. *The Astrophysical Journal*, **658** (2007), 509.

[111] DAMOUR, T., HANNI, R. S., RUFFINI, R., AND WILSON, J. R. Regions of magnetic support of a plasma around a black hole. *Physical Review D*, **17** (1978), 1518. `doi:10.1103/PhysRevD.17.1518`.

[112] DAMOUR, T. AND RUFFINI, R. Quantum Electrodynamical Effects in Kerr-Newmann Geometries. *Physical Review Letters*, **35** (1975), 463. `doi:10.1103/PhysRevLett.35.463`.

[113] D'AVANZO, P., ET AL. GRB 120624B: HAWKI NIR. *GCN*, **13391** (2012).

[114] D'AVANZO, P., D'ELIA, V., AND COVINO, S. GRB081008: VLT. *GCN*, **8350** (2008).

[115] D'AVANZO, P., ET AL. GRB 130702A: further TNG. *GCN*, **14984** (2013).

[116] D'AVANZO, P., MELANDRI, A., ANDREUZZI, G., AND MAINELLA, G. GRB 130702A: TNG optical observations. *GCN*, **14977** (2013).

[117] D'AVANZO, P., MELANDRI, A., AND EVANS, P. A. GRB 130702A: further Swift-XRT observations. *GCN*, **14982** (2013), 1.

[118] D'AVANZO, P., MELANDRI, A., STEELE, I., MUNDELL, C. G., AND PALAZZI, E. GRB 120729A: break in the optical light curve. *GCN*, **13551** (2012).

[119] D'AVANZO, P., ET AL. Fermi GRB 130702A: Swift XRT and UVOT observations. *GCN*, **14973** (2013).

[120] DE PALMA, F., BREGEON, J., AND TAJIMA, H. GRB 090902B: Fermi LAT detection. *GCN*, **9867** (2009).

[121] DE PASQUALE, M. AND PAGANI, C. GRB091208B: Swift/UVOT refined analysis. *GCN*, **10267** (2009).

[122] DE UGARTE POSTIGO, A., ET AL. GRB 120426B: HAWKI. *GCN*, **13395** (2012).

[123] DE UGARTE POSTIGO, A., ET AL. GRB150314A: OSIRIS/GTC. *GCN*, **17583** (2015).

[124] DE UGARTE POSTIGO, A., ET AL. GRB 171222A: Redshift from 10.4m GTC/OSIRIS. *GCN*, **22272** (2017), 1.

[125] DE UGARTE POSTIGO, A., ET AL. GRB170405A: OSIRIS/GTC. *GCN*, **20990** (2017).

[126] DE UGARTE POSTIGO, A., ET AL. GRB 131108A: GTC redshift. *GCN*, **15470** (2013).

[127] DE UGARTE POSTIGO, A., ET AL. GRB 130907A: NOT redshift. *GCN*, **15187** (2013).

[128] DE UGARTE POSTIGO, A., XU, D., MALESANI, D., AND TANVIR, N. R. GRB 150514A: VLT/X-shooter redshift. *GCN*, **17822** (2015).

[129] DE UGARTE POSTIGO, A., ET AL. The distribution of equivalent widths in long GRB afterglow spectra. *Astronomy & Astrophysics*, **548** (2012), A11. `arXiv:1209.0891`, `doi:10.1051/0004-6361/201219894`.

[130] DE UGARTE POSTIGO, A., ET AL. GRB 130427A: spectroscopic detection of the SN from the 10.4m GTC. *GCN*, **14646** (2013).

[131] DE UGARTE POSTIGO, A., ET AL. The obscured hyper-energetic GRB 120624B hosted by a luminous compact galaxy at z = 2.20. *Astronomy & Astrophysics*, **557** (2013), L18. `arXiv:1309.1167`, `doi:10.1051/0004-6361/201322065`.

[132] DE UGARTE POSTIGO, A., ET AL. GRB 171010A: VLT spectroscopic identification of the associated SN 2017htp. *GCN*, **22096** (2017).

[133] D'ELIA, V., MELANDRI, A., AND MALESANI, D. GRB 160625B: TNG redshift confirmation. *GCN*, **19601** (2016).

[134] D'ELIA, V., ET AL. GRB 130702A: TNG spectroscopic observations of the emerging supernova. *GCN*, **15000** (2013), 1.

[135] D'ELIA, V., ET AL. SN 2013dx associated with GRB 130702A: a detailed photometric and spectroscopic monitoring and a study of the environment. *Astronomy & Astrophysics*, **577** (2015), A116. `arXiv:1502.04883`, `doi:10.1051/0004-6361/201425381`.

[136] DICKE, R. H. Scatter-Hole Cameras for X-Rays and Gamma Rays. *The Astrophysical Journal Letters*, **153** (1968), L101. `doi:10.1086/180230`.

[137] DINGUS, B. L., ET AL. EGRET Observations of Three Gamma-Ray Bursts at Energies $\gtrsim$ 30 MeV. In *Gamma-Ray Bursts* (edited by G. J. Fishman), vol. 307 of *American Institute of Physics Conference Series*, p. 22 (1994). `doi:10.1063/1.45796`.

[138] DIRIRSA, F., RACUSIN, J., MCENERY, J., AND DESIANTE, R. GRB 160625B: Fermi-LAT detection of a bright burst. *GCN*, **19580** (2016).

[139] DJORGOVSKI, S. G., KULKARNI, S. R., BLOOM, J. S., AND FRAIL, D. A. GRB 970228: redshift and properties of the host galaxy. *GCN*, **289** (1999), 1.

[140] ELLIOTT, J., KLOSE, S., AND GREINER, J. GRB 120711A: GROND photometric redshift. *GCN*, **13438** (2012).

[141] EVANS, P. A. AND CANNIZZO, J. K. GRB 100728A: XRT. *GCN*, **11014** (2010).

[142] EVANS, P. A., DE PASQUALE, M., STROH, M. C., AND SIEGEL, M. H. GRB 130518A: Swift XRT and UVOT possible afterglow. *GCN*, **14678** (2013).

[143] EVANS, P. A., ET AL. An online repository of Swift/XRT light curves of γ-ray bursts. *Astronomy & Astrophysics*, **469** (2007), 379. `arXiv:0704.0128, doi:10.1051/0004-6361:20077530`.

[144] EVANS, P. A., ET AL. Methods and results of an automatic analysis of a complete sample of Swift-XRT observations of GRBs. *Monthly Notices of the Royal Astronomical Society*, **397** (2009), 1177. `arXiv:0812.3662, doi:10.1111/j.1365-2966.2009.14913.x`.

[145] FALCONE, A., ET AL. GRB 060204B: swift detection of a burst. *GCN*, **4655** (2006).

[146] FALCONE, A. D., ET AL. The First Survey of X-Ray Flares from Gamma-Ray Bursts Observed by Swift: Spectral Properties and Energetics. *The Astrophysical Journal*, **671** (2007), 1921. `arXiv:0706.1564, doi:10.1086/523296`.

[147] FATKHULLIN, T., MOSKVITIN, A., AND CASTRO-TIRADO, A. J. GRB 081024B: BTA deep optical observations. *GCN*, **8456** (2008).

[148] FAZIO, G. G. Gamma Ratiation from Celestial Objects. *Annual Review of Astronomy and Astrophysics*, **5** (1967), 481. `doi:10.1146/annurev.aa.05.090167.002405`.

[149] FENIMORE, E. E., ET AL. The Trigger Algorithm for the Burst Alert Telescope on Swift. In *Gamma-Ray Burst and Afterglow Astronomy 2001: A Workshop Celebrating the First Year of the HETE Mission* (edited by G. R. Ricker and R. K. Vanderspek), vol. 662 of *American Institute of Physics Conference Series*, pp. 491–493 (2003). `arXiv:astro-ph/0408514, doi:10.1063/1.1579409`.

[150] FILGAS, R., KRUEHLER, T., AND GREINER, J. GRB 100414A: GROND detection of the optical afterglow. *GCN*, **10607** (2010).

[151] FISHMAN, G. J., ET AL. Burst and Transient Source Experiment (BATSE) for the Gamma Ray Observatory (GRO). *International Cosmic Ray Conference*, **3** (1985).

[152] FISHMAN, G. J., ET AL. The first BATSE gamma-ray burst catalog. *The Astrophysical Journal Supplementary Series*, **92** (1994), 229. `doi:10.1086/191968`.

[153] FLORES, H., ET AL. GRB 130427A: VLT/X-shooter redshift. *GCN*, **14491** (2013).

[154] FOLEY, S. GRB 100414A: Fermi GBM detection. *GCN*, **10595** (2010).

[155] FONG, W. AND BERGER, E. The Locations of Short Gamma-Ray Bursts as Evidence for Compact Object Binary Progenitors. *The Astrophysical Journal*, **776** (2013), 18. `arXiv:1307.0819, doi:10.1088/0004-637X/776/1/18`.

[156] FONG, W., BERGER, E., MARGUTTI, R., AND ZAUDERER, B. A. A Decade of Short-duration Gamma-Ray Burst Broadband Afterglows: Energetics, Circumburst Densities, and Jet Opening Angles. *The Astrophysical Journal*, **815** (2015), 102. `arXiv:1509.02922, doi:10.1088/0004-637X/815/2/102`.

[157] FONG, W., ET AL. GRB 140402A: Deep limit on the optical afterglow from Magellan observations. *GCN*, **16080** (2014).

[158] FONG, W., ET AL. Demographics of the Galaxies Hosting Short-duration Gamma-Ray Bursts. *The Astrophysical Journal*, **769** (2013), 56. `arXiv:1302.3221, doi:10.1088/0004-637X/769/1/56`.

[159] FRAIL, D. A. AND CHANDRA, P. GRB 090510, radio limits. *GCN*, **9354** (2009).

[160] FRAIL, D. A., CHANDRA, P., AND CENKO, B. GRB 090328. *GCN*, **9060** (2009).

[161] FRAIL, D. A., CHANDRA, P., CENKO, S. B., AND HARRISON, F. GRB 100414A : EVLA radio detection. *GCN*, **10698** (2010).

[162] FRAIL, D. A. AND KULKARNI, S. R. GRB 970508. *IAU Circulars*, **6662** (1997).

[163] FRONTERA, F., ET AL. The Gamma-Ray Burst Catalog Obtained with the Gamma-Ray Burst Monitor Aboard BeppoSAX. *The Astrophysical Journal Supplement Series*, **180** (2009), 192. `arXiv:0809.5174, doi:10.1088/0067-0049/180/1/192`.

[164] FRYER, C. L., OLIVEIRA, F. G., RUEDA, J. A., AND RUFFINI, R. Neutron-Star-Black-Hole Binaries Produced by Binary-Driven Hypernovae. *Physical Review Letters*, **115** (2015), 231102. `arXiv:1505.02809, doi:10.1103/PhysRevLett.115.231102`.

[165] FRYER, C. L., RUEDA, J. A., AND RUFFINI, R. Hypercritical Accretion, Induced Gravitational Collapse, and Binary-Driven Hypernovae. *The Astrophysical Journal Letters*, **793** (2014), L36. `arXiv:1409.1473, doi:10.1088/2041-8205/793/2/L36`.

[166] FYNBO, J. P. U., ET AL. GRB 181020A: VLT/X-shooter spectroscopy and redshift. *GCN*, **23356** (2018), 1.

[167] GALAMA, T. J., ET AL. GRB 970508. *IAU Circulars*, **6655** (1997).

[168] GALLI, M., ET AL. AGILE mini-calorimeter gamma-ray burst catalog. *Astronomy & Astrophysics*, **553** (2013), A33. `arXiv:1303.0114, doi:10.1051/0004-6361/201220833`.

[169] GEHRELS, N. Use of νF_ν spectral energy distributions for multiwavelength astronomy. *Nuovo Cimento B*, **112** (1997), 11.

[170] GEHRELS, N., KNIFFEN, D. A., AND ORMES, J. F. The Compton Gamma Ray Observatory. In *Current Topics in Astrofundamental Physics* (edited by N. Sanchez and A. Zichichi) (1992).

[171] GEHRELS, N., ET AL. The Swift Gamma-Ray Burst Mission. *The Astrophysical Journal*, **611** (2004), 1005. `doi:10.1086/422091`.

[172] GHISELLINI, G., GHIRLANDA, G., NAVA, L., AND CELOTTI, A. GeV emission from gamma-ray bursts: a radiative fireball? *Monthly Notices of the Royal Astronomical Society*, **403** (2010), 926. `arXiv:0910.2459, doi:10.1111/j.1365-2966.2009.16171.x`.

[173] GIACCONI, R. An Education in Astronomy. *Annual Review of Astronomy and Astrophysics*, **43** (2005), 1. `doi:10.1146/annurev.astro.43.090303.091253`.

[174] GIACCONI, R. AND ROSSI, B. A 'Telescope' for Soft X-Ray Astronomy. *Journal of Geophysical Research*, **65** (1960), 773. `doi:10.1029/JZ065i002p00773`.

[175] GILL, P. E., MURRAY, W., AND WRIGHT, M. H. *Practical optimization* (1981).

[176] GIULIANI, A., ET AL. AGILE Detection of Delayed Gamma-ray Emission From the Short Gamma-Ray Burst GRB 090510. *The Astrophysical Journal*, **708** (2010), L84. `arXiv:0908.1908, doi:10.1088/2041-8205/708/2/L84`.

[177] GOLDSTEIN, A., ET AL. The BATSE 5B Gamma-Ray Burst Spectral Catalog. *The Astrophysical Journal Supplement Series*, **208** (2013), 21. `arXiv:1311.7135, doi:10.1088/0067-0049/208/2/21`.

[178] GOLDSTEIN, A. AND VAN DER HORST, A. GRB 080916C: GBM. *GCN*, **8245** (2008).

[179] GOLDSTEIN, A., ET AL. The Fermi GBM Gamma-Ray Burst Spectral Catalog: The First Two Years. *The Astrophysical Journal Supplement Series*, **199** (2012), 19. `arXiv:1201.2981, doi:10.1088/0067-0049/199/1/19`.

[180] GOLENETSKII, S., ET AL. GRB 131030A: Konus-wind. *GCN*, **15413** (2013).

[181] GOLENETSKII, S., ET AL. GRB 140419A: Konus-Wind. *GCN*, **16134** (2014).

[182] GOLENETSKII, S., ET AL. GRB 080607: Konus-wind. *GCN*, **7862** (2008).

[183] GOLENETSKII, S., ET AL. Konus-wind observation of GRB 091005. *GCN*, **9344** (2009), 1.

[184] GOLENETSKII, S., ET AL. Konus-wind observation of GRB 130702A. *GCN*, **14986** (2013), 1.

[185] GOLENETSKII, S., ET AL. GRB 151027A: Konus-Wind. *GCN*, **1851** (2015).

[186] GOLENETSKII, S. V. On the spatial distribution of gamma-ray burst sources. *Advances in Space Research*, **8** (1988), 653. `doi:10.1016/0273-1177(88)90472-3`.

[187] GOLENETSKII, S. V., ILINSKII, V. N., AND MAZETS, E. P. Recurrent bursts in GBS0526 - 66, the source of the 5 March 1979 gamma-ray burst. *Nature*, **307** (1984), 41. `doi:10.1038/307041a0`.

[188] GOLENETSKII, S. V., MAZETS, E. P., APTEKAR, R. L., AND ILINSKII, V. N. Correlation between luminosity and temperature in gamma-ray burst sources. *Nature*, **306** (1983), 451. `doi:10.1038/306451a0`.

[189] GORBOVSKOY, E., ET AL. GRB 130907A: MASTER refined. *GCN*, **15220** (2013).

[190] GORBOVSKOY, E., ET AL. GRB 150403A: MASTER-net. *GCN*, **17680** (2015).

[191] GOROSABEL, J., MOTTOLA, S., DE UGARTE POSTIGO, A., HELLMICH, S., AND PROFFE, G. GRB 131108A: 1.23m CAHA optical candidate. *GCN*, **15469** (2013).

[192] GOTZ, D., ET AL. GRB 120711A: INTEGRAL. *GCN*, **13434** (2012).

[193] GRAHAM, J. F., KANN, D. A., SCHADY, P., AND GREINER, J. GRB 141028A: GROND Afterglow confirmation (MASTER source). *GCN*, **16977** (2014).

[194] GREINER, J. The Benefit of Simultaneous Seven-filter Imaging: 10 Years of GROND Observations. *Publications of the Astronomical Society of the Pacific*, **131** (2019), 015002. `arXiv:1812.00636`, `doi:10.1088/1538-3873/aaec5d`.

[195] GREINER, J., ET AL. The redshift and afterglow of the extremely energetic gamma-ray burst GRB 080916C. *Astronomy & Astrophysics*, **498** (2009), 89. `arXiv:0902.0761`, `doi:10.1051/0004-6361/200811571`.

[196] GRONWALL, C. AND STARLING, R. L. C. GRB 091003: Swift UVOT detection of a candidate UV afterglow. *GCN*, **9987** (2009).

[197] GRONWALL, C. AND VETERE, L. GRB 090926A: Swift/UVOT detection of an optical afterglow. *GCN*, **9938** (2009).

[198] GRUBER, D. GRB 110731A: Fermi GBM observation. *GCN*, **12221** (2011).

[199] GRUBER, D., BURGESS, J. M., AND CONNAUGHTON, V. GRB 120624B: Fermi GBM detection. *GCN*, **13377** (2012).

[200] GRUBER, D. AND PELASSA, V. GRB 120711A: Fermi GBM. *GCN*, **13437** (2012).

[201] GRUBER, D., ET AL. The Fermi GBM Gamma-Ray Burst Spectral Catalog: Four Years of Data. *The Astrophysical Journal Supplement Series*, **211** (2014), 12. `arXiv:1401.5069`, `doi:10.1088/0067-0049/211/1/12`.

[202] GRUPE, D. AND HOVERSTEN, E. GRB 090510: XRT refined. *GCN*, **9341** (2009).

[203] GUIDORZI, C. GRB 081024B: Swift-XRT late-time observations. *GCN*, **8513** (2008).

[204] Guidorzi, C., Kobayashi, S., Mundell, C. G., and Gomboc, A. GRB 160625B: LCOGT FTN observations. *GCN*, **19640** (2016).

[205] Guidorzi, C., Kobayashi, S., Steele, I. A., Gomboc, A., and Mundell, C. G. GRB 170405A: LCO FTN observations. *GCN*, **20994** (2017).

[206] Guidorzi, C., Mao, J., and Margutti, R. GRB 081024B: new Swift-XRT observations. *GCN*, **8454** (2008).

[207] Guidorzi, C. and Margutti, R. GRB 081024B: XRT. *GCN*, **8416** (2008).

[208] Guidorzi, C., Margutti, R., and Mao, J. GRB 081024B. *GCN*, **8410** (2008).

[209] Guidorzi, C., Mundell, C. G., Steele, I. A., and Singer, L. P. Fermi394416326: FTN detection. *GCN*, **14968** (2013).

[210] Guidorzi, C., et al. GRB 090902B: Faulkes North. *GCN*, **9875** (2009).

[211] Guiriec, S., Connaughton, V., and Briggs, M. GRB 090510: Fermi GBM detection. *GCN*, **9336** (2009).

[212] Hagen, L. M. Z. GRB 150314A: Swift/UVOT Detection. *GCN*, **17580** (2015).

[213] Hagen, L. M. Z., et al. GRB 150314A: Swift detection. *GCN*, **17573** (2015).

[214] Haislip, J., et al. GRB 091003: Skynet/DSO observations. *GCN*, **9989** (2009).

[215] Hanabata, Y., et al. GRB 081024B: suzaku WAM observation of the prompt emission. *GCN*, **8444** (2008).

[216] Hancock, P., Murphy, T., Gaensler, B., Bell, M., and Burlon, D. GRB 120711A: ATCA 34GHz upper limit. *GCN*, **13451** (2012).

[217] Hancock, P., et al. GRB 120711A: ATCA 34GHz final UL. *GCN*, **13485** (2012).

[218] Hancock, P., et al. GRB 120711A: ATCA 34GHz UL. *GCN*, **13463** (2012).

[219] Hansen, B. M. S. and Lyutikov, M. Radio and X-ray signatures of merging neutron stars. *Monthly Notices of the Royal Astronomical Society*, **322** (2001), 695. arXiv:astro-ph/0003218, doi:10.1046/j.1365-8711.2001.04103.x.

[220] Harrison, F., Cenko, B., Frail, D. A., Chandra, P., and Kulkarni, S. GRB 090323: radio afterglow detection. *GCN*, **9043** (2009).

[221] Hartmann, D. and Epstein, R. I. The angular distribution of gamma-ray bursts. *The Astrophysical Journal*, **346** (1989), 960. doi:10.1086/168076.

[222] Heintz, K. E., et al. GRB 180728A: No evidence of SN in early VLT/X-shooter spectra. *GCN*, **23067** (2018), 1.

[223] Higdon, J. C. and Lingenfelter, R. E. Gamma-ray bursts. *Annual Review of Astronomy and Astrophysics*, **28** (1990), 401. doi:10.1146/annurev.aa.28.090190.002153.

[224] Ho, C., Epstein, R. I., and Fenimore, E. E. *Gamma-ray Bursts* (1992).

[225] Holland, S. T. and Mangano, V. GRB 131231A: Swift/UVOT observations of the optical afterglow. *GCN*, **15673** (2014).

[226] Horesh, A., Perley, D. A., and Cenko, S. B. GRB 171010A: VLA Observations. *GCN*, **22015** (2017).

[227] Horesh, A., et al. GRB 171010A: AMI radio detection. *GCN*, **22013** (2017).

[228] Hoversten, E. A. GRB 090323: UVOT detection of afterglow. *GCN*, **9032** (2009).

[229] HOVERSTEN, E. A., ET AL. GRB 090510: Swift detection. *GCN*, **9331** (2009).

[230] HUI, C. M. AND MEEGAN, C. GRB 170405A: Fermi GBM. *GCN*, **20986** (2017).

[231] HURLEY, K., ET AL. IPN localization of GRB 130702A (= Fermi 394416326). *GCN*, **14974** (2013), 1.

[232] HURLEY, K., ET AL. The InterPlanetary Network Supplement to the Second Fermi GBM Catalog of Cosmic Gamma-Ray Bursts. *The Astrophysical Journal Supplement Series*, **229** (2017), 31. `doi:10.3847/1538-4365/229/2/31`.

[233] IM, M. AND HONG, J. GRB 120729A: UKIRT observation. *GCN*, **13544** (2012).

[234] IZZO, L., ET AL. GRB 180703A: VLT/MUSE host galaxy redshift measurement. *GCN*, **23889** (2019), 1.

[235] IZZO, L., ET AL. A double component in GRB 090618: a proto-black hole and a genuinely long gamma-ray burst. *Astronomy & Astrophysics*, **543** (2012), A10. `arXiv:1202.4374`, `doi:10.1051/0004-6361/201117436`.

[236] JAKOBSSON, P., FYNBO, J. P. U., VREESWIJK, P. M., AND DE UGARTE POSTIGO, A. GRB 080805: VLT redshift update. *GCN*, **8077** (2008).

[237] JAUNSEN, A. O., FYNBO, J. P. U., ANDERSEN, M. I., AND VREESWIJK, P. GRB 070318: absorption-line redshift. *GCN*, **6216** (2007).

[238] JENKE, P. AND XIONG, S. GRB 131231A: Fermi GBM. *GCN*, **15644** (2014).

[239] JENKE, P. A. AND YU, H.-F. GRB 140402A: Fermi GBM. *GCN*, **16070** (2014).

[240] KAMBLE, A. P., ET AL. GRB 100414A : WSRT radio detection. *GCN*, **10697** (2010).

[241] KANEKO, Y., ET AL. The Complete Spectral Catalog of Bright BATSE Gamma-Ray Bursts. *The Astrophysical Journal Supplement Series*, **166** (2006), 298. `arXiv:astro-ph/0601188`, `doi:10.1086/505911`.

[242] KANKARE, E., ET AL. GRB 171010A: ePESSTO NTT redshift. *GCN*, **22002** (2017).

[243] KANN, D. A., LAUX, U., AND STECKLUM, S. GRB 090323 TLS detection - still bright. *GCN*, **9033** (2009).

[244] KELLY, P. L., FILIPPENKO, A. V., FOX, O. D., ZHENG, W., AND CLUBB, K. I. Evidence that Gamma-Ray Burst 130702A Exploded in a Dwarf Satellite of a Massive Galaxy. *The Astrophysical Journal Letters*, **775** (2013), L5. `arXiv:1307.5103`, `doi:10.1088/2041-8205/775/1/L5`.

[245] KENNEA, J. GRB 090328: possible Swift/XRT detection. *GCN*, **9045** (2009).

[246] KENNEA, J., EVANS, P., AND GOAD, M. GRB 090323: XRT. *GCN*, **9024** (2009).

[247] KENNEA, J., EVANS, P., AND GOAD, M. GRB 090328: updated position/optical afterglow candidate. *GCN*, **9046** (2009).

[248] KENNEA, J. A. GRB 080916C: Swift/XRT detection of possible afterglow. *GCN*, **8253** (2008).

[249] KENNEA, J. A. GRB 160509A: Preliminary XRT positon. *GCN*, **19407** (2016).

[250] KENNEA, J. A., RACUSIN, J. L., AND PAGANI, C. GRB 141028A: Swift/XRT detection of the X-ray afterglow. *GCN*, **16978** (2014).

[251] KENNEA, J. A. AND STRATTA, G. GRB 090902B: Swift/XRT. *GCN*, **9868** (2009).

[252] KENNEA, J. A., ET AL. GRB 150514A: Swift-XRT afterglow. *GCN*, **17818** (2015).

[253] KHORUNZHEV, G., ET AL. GRB 130702A: RTT150 optical observations. *GCN*, **15243** (2013), 1.

[254] KLEBESADEL, R., ET AL. A catalog of gamma-ray bursts with earth crossing times. *The Astrophysical Journal Letters*, **259** (1982), L51. `doi:10.1086/183846`.

[255] KLEBESADEL, R. W. *The durations of gamma-ray bursts*, pp. 161–168 (1992).

[256] KLEBESADEL, R. W., STRONG, I. B., AND OLSON, R. A. Observations of Gamma-Ray Bursts of Cosmic Origin. *The Astrophysical Journal Letters*, **182** (1973), L85. `doi:10.1086/181225`.

[257] KOCEVSKI, D. AND ARIMOTO, M. GRB 150514A: Fermi-LAT. *GCN*, **17816** (2015).

[258] KOUVELIOTOU, C., ET AL. Identification of two classes of gamma-ray bursts. *The Astrophysical Journal Letters*, **413** (1993), L101. `doi:10.1086/186969`.

[259] KRIMM, H. A., ET AL. GRB 081210: Swift detection of a burst with optical afterglow. *GCN*, **8648** (2008).

[260] KRÜHLER, T., GREINER, J., AND KANN, D. A. GRB 100728A: GROND host detection and X-shooter redshift. *GCN*, **14500** (2013).

[261] KRÜHLER, T., SCHADY, P., GREINER, J., AND TANVIR, N. R. GRB 170214A: VLT/X-shooter spectroscopy and tentative redshift. *GCN*, **20686** (2017).

[262] KRÜHLER, T., TANVIR, N. R., MALESANI, D., XU, D., AND FYNBO, J. P. U. GRB 140301A: VLT/X-shooter redshift. *GCN*, **15900** (2014).

[263] KRÜHLER, T., ET AL. Correlated optical and x-ray flares in the afterglow of xrf 071031. *The Astrophysical Journal*, **697** (2009), 758.

[264] KUIN, N. P. M. AND HOVERSTEN, E. A. GRB 090510: UVOT. *GCN*, **9342** (2009).

[265] KUIN, N. P. M. AND LIEN, A. Y. GRB 150403A: UVOT. *GCN*, **17673** (2015).

[266] KUIN, N. P. M., OATES, S., DE PASQUALE, M., HOVERSTEN, E. A., AND MARSHALL, F. GRB 090510: Swift/UVOT host galaxy candidates. *GCN*, **9351** (2009).

[267] KULKARNI, S. R., ET AL. GRB 970228. *IAU Circulars*, **6732** (1997).

[268] KUMAR, B., SAHU, D. K., ANUPAMA, G. C., AND SINGH, A. GRB 171010A : Optical observations from HCT. *GCN*, **22012** (2017).

[269] KUMAR, P. AND BARNIOL DURAN, R. On the generation of high-energy photons detected by the Fermi Satellite from gamma-ray bursts. *Monthly Notices of the Royal Astronomical Society*, **400** (2009), L75. `arXiv:0905.2417`, `doi:10.1111/j.1745-3933.2009.00766.x`.

[270] KUMAR, P. AND ZHANG, B. The physics of gamma-ray bursts & relativistic jets. *Physics Reports*, **561** (2015), 1. `arXiv:1410.0679`, `doi:10.1016/j.physrep.2014.09.008`.

[271] LACLUYZE, A., ET AL. GRB 120711A: Skynet observations. *GCN*, **13430** (2012).

[272] LAMB, D. Q. The Distance Scale to Gamma-Ray Bursts. *Publications of the Astronomical Society of the Pacific*, **107** (1995), 1152. `doi:10.1086/133673`.

[273] LAMB, D. Q. AND QUASHNOCK, J. M. Gamma-Ray Bursts as a Probe of Large-Scale Structure in the Universe. *The Astrophysical Journal Letters*, **415** (1993), L1. `doi:10.1086/187018`.

[274] LANDAU, L. D. AND LIFSHITZ, E. M. *The classical theory of fields* (1975).

[275] LANDSMAN, W. AND CANNIZZO, J. GRB 100414A: Swift/UVOT observations. *GCN*, **10609** (2010).

[276] LAPORTE, S. GRB170405A, Swift-UVOT Detection. *GCN*, **21000** (2017).

[277] LAROS, J. G., FENIMORE, E. E., FIKANI, M. M., KLEBESADEL, R. W., AND BARAT, C. The soft gamma-ray burst GB790107. *Nature*, **322** (1986), 152. `doi: 10.1038/322152a0`.

[278] LASKAR, T. AND BERGER, E. GRB 150314A: VLA. *GCN*, **17591** (2015).

[279] LASKAR, T., COPPEJANS, D. L., AND MARGUTTI, R. GRB 171010A: VLA Detection. *GCN*, **22014** (2017).

[280] LASKAR, T., ZAUDERER, A., AND BERGER, E. GRB 120729A: EVLA observations. *GCN*, **13547** (2012).

[281] LAZZATI, D. Precursor activity in bright, long BATSE gamma-ray bursts. *Monthly Notices of the Royal Astronomical Society*, **357** (2005), 722. `arXiv:astro-ph/0411753`, `doi:10.1111/j.1365-2966.2005.08687.x`.

[282] LEDOUX, C., VREESWIJK, P., SMETTE, A., JAUNSEN, A., AND KAUFER, A. VLT/UVES observations of GRB 060607. *GCN*, **5237** (2006).

[283] LEE, W. H., ET AL. GRB 130907A: RATIR optical/NIR. *GCN*, **15192** (2013).

[284] LELOUDAS, G., ET AL. GRB 130702A: NOT spectroscopy and redshift of the nearby bright galaxy. *GCN*, **14983** (2013).

[285] LEVAN, A. J., CENKO, S. B., PERLEY, D. A., AND TANVIR, N. R. GRB 130427A: Gemini-North redshift. *GCN*, **14455** (2013).

[286] LEVAN, A. J., TANVIR, N. R., CENKO, S. B., AND PERLEY, D. GRB 160509A Gemini North candidate afterglow. *GCN*, **19410** (2016).

[287] LEVATO, H., ET AL. Fermi GBM trigger 394416326: MASTER early optical limit. *GCN*, **14970** (2013), 1.

[288] LI, L., ET AL. A Comprehensive Study of Gamma-Ray Burst Optical Emission. I. Flares and Early Shallow-decay Component. *The Astrophysical Journal*, **758** (2012), 27. `arXiv:1203.2332`, `doi:10.1088/0004-637X/758/1/27`.

[289] LIEN, A., ET AL. The Third Swift Burst Alert Telescope Gamma-Ray Burst Catalog. *The Astrophysical Journal*, **829** (2016), 7. `arXiv:1606.01956`, `doi: 10.3847/0004-637X/829/1/7`.

[290] LIEN, A. Y., ET AL. GRB 140206A: Swift detection of a burst. *GCN*, **15784** (2014).

[291] LIEN, A. Y., ET AL. GRB 150403A: Swift detection of a burst with an optical counterpart. *GCN*, **17665** (2015).

[292] LITHWICK, Y. AND SARI, R. Lower Limits on Lorentz Factors in Gamma-Ray Bursts. *The Astrophysical Journal*, **555** (2001), 540. `arXiv:astro-ph/0011508`, `doi:10.1086/321455`.

[293] LITTLEJOHNS, O. M., ET AL. GRB 120624B: Swift-XRT. *GCN*, **13394** (2012).

[294] LLOYD-RONNING, N. M. AND FRYER, C. L. On the lack of a radio afterglow from some gamma-ray bursts - insight into their progenitors? *Monthly Notices of the Royal Astronomical Society*, **467** (2017), 3413. `arXiv:1609.04686`, `doi:10.1093/mnras/stx313`.

[295] LLOYD-RONNING, N. M., GOMPERTZ, B., PE'ER, A., DAINOTTI, M., AND FRUCHTER, A. A Comparison between Radio Loud and Quiet Gamma-Ray Bursts, and Evidence for a Potential Correlation between Intrinsic Duration and Redshift in the Radio Loud Population. *The Astrophysical Journal*, **871** (2019), 118. `arXiv:1809.04190`, `doi:10.3847/1538-4357/aaf6ac`.

[296] LONGO, F., BISSALDI, E., ARIMOTO, M., AND ZHU, S. GRB 150403A: Fermi-LAT detection. *GCN*, **17667** (2015).

[297] LONGO, F., ET AL. GRB 160509A: Fermi-LAT prompt detection of a very bright burst. *GCN*, **19403** (2016).

[298] LONGO, F., ET AL. AGILE detection of GRB 090510. *GCN*, **9343** (2009), 1.

[299] MAILYAN, B. AND MEEGAN, C. GRB 170214A: Fermi GBM. *GCN*, **20675** (2017).

[300] MAILYAN, B., TOELGE, K., AND ROBERTS, O. GRB 160623A: Fermi GBM detection/observation. *GCN*, **19555** (2016).

[301] MALESANI, D., ET AL. GRB 090926A: VLT/X-shooter redshift. *GCN*, **9942** (2009).

[302] MALESANI, D., HEINTZ, K. E., CALISSENDORFF, P., AND LOSADA, I. R. GRB 171010A: NOT optical observations. *GCN*, **22000** (2017).

[303] MALESANI, D., HEINTZ, K. E., AND PURSIMO, T. GRB 170405A: NOT optical observations. *GCN*, **20988** (2017).

[304] MALESANI, D., KROGAGER, J.-K., AND RANJAN, A. GRB 170214A: NOT optical afterglow confirmation. *GCN*, **20683** (2017).

[305] MALESANI, D., ET AL. GRB 110731A: NOT photometry. *GCN*, **12220** (2011).

[306] MALESANI, D., ET AL. GRB 140206A: NOT redshift. *GCN*, **15800** (2014).

[307] MALESANI, D., XU, D., LOSADA, I. R., AND DUVAL, F. GRB 131231A: afterglow confirmation from the NOT. *GCN*, **15642** (2013).

[308] MALESANI, D., ET AL. GRB 160623A: astro-, photometry, z. *GCN*, **19708** (2016).

[309] MANGANO, V., ET AL. GRB 080607: Swift detection. *GCN*, **7847** (2008).

[310] MANGANO, V., PAGE, K., AND MALESANI, D. GRB 131231A. *GCN*, **15648** (2014).

[311] MAO, J., LUN, B., AND BAI, J.-M. GRB 150314A: GMG. *GCN*, **17614** (2015).

[312] MARGUTTI, R., ET AL. Lag-luminosity relation in γ-ray burst X-ray flares: a direct link to the prompt emission. *Monthly Notices of the Royal Astronomical Society*, **406** (2010), 2149. `arXiv:1004.1568`, `doi:10.1111/j.1365-2966.2010.16824.x`.

[313] MARISALDI, M., ET AL. GRB 080607: AGILE-MCAL observation of the prompt emission. *GCN*, **7866** (2008).

[314] MARSHALL, F. E. AND CANNIZZO, J. K. GRB 150514A: Swift/UVOT Detection. *GCN*, **17820** (2015).

[315] MARSHALL, F. E., ET AL. GRB 140419A: Swift detection of a burst with optical afterglow. *GCN*, **16118** (2014).

[316] MARSHALL, F. E., ET AL. GRB 090328A: Swift detection. *GCN*, **207** (2009).

[317] MASELLI, A., ET AL. GRB 130427A: Swift detection of a very bright burst with a likely bright optical counterpart. *GCN*, **14448** (2013).

[318] MASELLI, A., ET AL. GRB 151027A: Swift detection of a burst with a bright optical afterglow. *GCN*, **18478** (2015).

[319] MASELLI, A. AND D'AVANZO, P. GRB 140619B: Swift-XRT. *GCN*, **16424** (2014).

[320] MASUMITSU, T., ET AL. GRB 151027A: MAXI/GSC detection. *GCN*, **18525** (2015).

[321] MATZ, S. M., ET AL. High-energy emission in gamma-ray bursts. *The Astrophysical Journal Letters*, **288** (1985), L37. `doi:10.1086/184417`.

[322] MAZAEVA, E., POZANENKO, A., KLUNKO, E., AND VOLNOVA, A. GRB 170214A: Mondy optical upper limit. *GCN*, **20687** (2017).

[323] MAZAEVA, E., ET AL. GRB 171010A: afterglow and SN 2017htp. *GCN*, **22113** (2017).

[324] MAZAEVA, E., ET AL. GRB 141028A: Mondy observations. *GCN*, **17035** (2014).

[325] MAZETS, E. P. AND GOLENETSKII, S. V. Recent results from the gamma-ray burst studies in the KONUS experiment. *Astrophysics and Space Science*, **75** (1981), 47. `doi:10.1007/BF00651384`.

[326] MAZETS, E. P., GOLENETSKII, S. V., GURIAN, I. A., AND ILINSKII, V. N. The 5 March 1979 event and the distinct class of short gamma bursts Are they of the same origin. *Astrophysics and Space Science*, **84** (1982), 173. `doi:10.1007/BF00713635`.

[327] MAZETS, E. P., GOLENTSKII, S. V., ILINSKII, V. N., APTEKAR, R. L., AND GURYAN, I. A. Observations of a flaring X-ray pulsar in Dorado. *Nature*, **282** (1979), 587. `doi:10.1038/282587a0`.

[328] MAZETS, E. P., ET AL. Catalog of cosmic gamma-ray bursts from the KONUS experiment data. Part I and II. *Astrophysics and Space Science*, **80** (1981), 3. `doi:10.1007/BF00649140`.

[329] MAZETS, E. P., ET AL. Catalog of cosmic gamma-ray bursts from the KONUS experiment data. Part III. *Astrophysics and Space Science*, **80** (1981), 85. `doi:10.1007/BF00649141`.

[330] MAZETS, E. P., ET AL. Catalog of cosmic gamma-ray bursts from the KONUS experiment data. Part IV. *Astrophysics and Space Science*, **80** (1981), 119. `doi:10.1007/BF00649142`.

[331] MCBREEN, S. GRB 090516: Fermi GBM observation. *GCN*, **9415** (2009).

[332] MCBREEN, S. GRB 091208B: Fermi GBM observation. *GCN*, **10266** (2009).

[333] MCENERY, J., CHIANG, J., AND HANABATA, Y. GRB 091003A: Fermi LAT detection. *GCN*, **9985** (2009).

[334] MCENERY, J., CUTINI, S., OHNO, M., AND KOERDING, E. Fermi LAT and GBM detections of GRB090328. *GCN*, **9044** (2009).

[335] MEEGAN, C., ET AL. The Fermi Gamma-ray Burst Monitor. *The Astrophysical Journal*, **702** (2009), 791. `arXiv:0908.0450`, `doi:10.1088/0004-637X/702/1/791`.

[336] MEEGAN, C. A., ET AL. Spatial distribution of gamma-ray bursts observed by BATSE. *Nature*, **355** (1992), 143. `doi:10.1038/355143a0`.

[337] MEEGAN, C. A., ET AL. The Third BATSE Gamma-Ray Burst Catalog. *The Astrophysical Journal Supplement Series*, **106** (1996), 65. `doi:10.1086/192329`.

[338] MELANDRI, A., ET AL. GRB 160625B: Swift-XRT afterglow. *GCN*, **19585** (2016).

[339] MELANDRI, A., GUIDORZI, C., GOMBOC, A., JAPELJ, J., AND MUNDELL, C. G. GRB 130427A: Faulkes telescope north detection. *GCN*, **14452** (2013).

[340] MELANDRI, A., ET AL. Grb 090313 and the origin of optical peaks in gamma-ray burst light curves: implications for lorentz factors and radio flares. *The Astrophysical Journal*, **723** (2010), 1331.

[341] MÉSZÁROS, P. Theories of Gamma-Ray Bursts. *Annual Review of Astronomy and Astrophysics*, **40** (2002), 137. `arXiv:arXiv:astro-ph/0111170, doi:10.1146/annurev.astro.40.060401.093821`.

[342] MÉSZÁROS, P. Gamma-ray bursts. *Reports on Progress in Physics*, **69** (2006), 2259. `arXiv:astro-ph/0605208, doi:10.1088/0034-4885/69/8/R01`.

[343] METZGER, M. R., COHEN, J. G., CHAFFEE, F. H., AND BLANDFORD, R. D. GRB 970508. *IAU Circulars*, **6676** (1997).

[344] MINGO, B., ET AL. GRB 160623A: Swift-XRT afterglow. *GCN*, **19558** (2016).

[345] MOIN, A., FRAIL, D. A., TINGAY, S., AND MACQUART, J.-P. GRB 090926A: ATCA. *GCN*, **10020** (2009).

[346] MOIN, A., ET AL. GRB 080916C: ATCA. *GCN*, **10019** (2009).

[347] MOOLEY, K. P., ET AL. GRB 160509A: AMI 15 GHz UL. *GCN*, **19532** (2016).

[348] MOOLEY, K. P., ET AL. GRB 160623A: AMI detection 15 GHz. *GCN*, **19609** (2016).

[349] MOOLEY, K. P., ET AL. GRB 160625B: AMI detection 15 GHz. *GCN*, **19610** (2016).

[350] MORADI, R., RUEDA, J. A., RUFFINI, R., AND WANG, Y. The newborn black hole in GRB 191014C manifests that is alive. *arXiv e-prints*, (2019), arXiv:1911.07552. `arXiv:1911.07552`.

[351] MUCCINO, M., RUFFINI, R., BIANCO, C. L., IZZO, L., AND PENACCHIONI, A. V. GRB 090227B: The Missing Link between the Genuine Short and Long Gamma-Ray Bursts. *The Astrophysical Journal*, **763** (2013), 125. `arXiv:1205.6600, doi:10.1088/0004-637X/763/2/125`.

[352] MULCHAEY, J., KASLIWAL, M. M., ARCAVI, I., BELLM, E., AND KELSON, D. GRB130702A: redshift of afterglow candidate iPTF13bxl. *GCN*, **14985** (2013).

[353] NAGAYAMA, T. GRB 080916C: IRSF/SIRUS NIR observation. *GCN*, **8274** (2008).

[354] NARAYAN, R., PACZYNSKI, B., AND PIRAN, T. Gamma-ray bursts as the death throes of massive binary stars. *The Astrophysical Journal Letters*, **395** (1992), L83. `arXiv:astro-ph/9204001, doi:10.1086/186493`.

[355] NARAYANA BHAT, P., ET AL. The Third Fermi GBM Gamma-Ray Burst Catalog: The First Six Years. *The Astrophysical Journal Supplement Series*, **223** (2016), 28. `arXiv:1603.07612, doi:10.3847/0067-0049/223/2/28`.

[356] NAVA, L. High-energy emission from gamma-ray bursts. *International Journal of Modern Physics D*, **27** (2018), 1842003. `arXiv:1804.01524, doi:10.1142/S0218271818420038`.

[357] NAVA, L., ET AL. Clustering of LAT light curves: a clue to the origin of high-energy emission in gamma-ray bursts. *Monthly Notices of the Royal Astronomical Society*, **443** (2014), 3578. `arXiv:1406.6693, doi:10.1093/mnras/stu1451`.

[358] NAYANA, A. J., CHANDRA, P., RAO, A. R., BHATTACHARYA, D., AND BHALERAO, V. Possible radio detection of GRB160623A with the GMRT. *GCN*, **19848** (2016).

[359] NORRIS, J. P., CLINE, T. L., DESAI, U. D., AND TEEGARDEN, B. J. Frequency of fast, narrow gamma-ray bursts. *Nature*, **308** (1984), 434. `doi:10.1038/308434a0`.

[360] Norris, J. P., et al. Attributes of Pulses in Long Bright Gamma-Ray Bursts. *The Astrophysical Journal*, **459** (1996), 393. `doi:10.1086/176902`.

[361] Norris, J. P., et al. Spectral evolution in gamma-ray bursts. *Advances in Space Research*, **6** (1986), 19. `doi:10.1016/0273-1177(86)90231-0`.

[362] Nousek, J. A., et al. Evidence for a Canonical Gamma-Ray Burst Afterglow Light Curve in the Swift XRT Data. *The Astrophysical Journal*, **642** (2006), 389. `arXiv:astro-ph/0508332`, `doi:10.1086/500724`.

[363] Nysewander, M., et al. Prompt Observations of the Early-Time Optical Afterglow of GRB 060607A. *The Astrophysical Journal*, **693** (2009), 1417. `arXiv:0708.3444`, `doi:10.1088/0004-637X/693/2/1417`.

[364] Oates, S. GRB 160625B: Swift/UVOT Detection. *GCN*, **19589** (2016).

[365] Oates, S. R. GRB 090328: Swift UVOT observations. *GCN*, **9048** (2009).

[366] Oates, S. R. GRB110731A: Swift/UVOT observations. *GCN*, **12222** (2011).

[367] Oates, S. R. and Cannizzo, J. K. GRB 100728A: UVOT UL. *GCN*, **11016** (2010).

[368] Oates, S. R. and Page, M. J. GRB130907A: Swift/UVOT. *GCN*, **15195** (2013).

[369] Oates, S. R. and Ukwatta, T. N. GRB120729A: UVOT. *GCN*, **13539** (2012).

[370] Oates, S. R. and Vetere, L. GRB090926A: Swift/UVOT. *GCN*, **9948** (2009).

[371] Oates, S. R., et al. A statistical study of gamma-ray burst afterglows measured by the Swift Ultraviolet Optical Telescope. *Monthly Notices of the Royal Astronomical Society*, **395** (2009), 490. `arXiv:0901.3597`, `doi:10.1111/j.1365-2966.2009.14544.x`.

[372] Oates, S. R., et al. GRB 110731A: Swift detection of a burst with an optical counterpart. *GCN*, **12215** (2011).

[373] Oda, M. High-Resolution X-Ray Collimator with Broad Field of View for Astronomical Use. *Applied Optics*, **4** (1965), 143. `doi:10.1364/AO.4.000143`.

[374] Oda, M. X-ray and γ-ray astronomy. *Internat. Cosmic Ray Conference*, **1** (1965), 68.

[375] Ohmori, N., et al. GRB 090510: Suzaku WAM observation of the prompt emission. *GCN*, **9355** (2009), 1.

[376] Ohno, M., Cutini, S., McEnery, J., Chiang, J., and Koerding, E. Fermi GBM and LAT detections of GRB 090323. *GCN*, **9021** (2009).

[377] Ohno, M. and Pelassa, V. GRB 090510: Fermi LAT detection. *GCN*, **9334** (2009).

[378] Olausen, S. A. and Kaspi, V. M. The McGill Magnetar Catalog. *The Astrophysical Journal Supplement Series*, **212** (2014), 6. `arXiv:1309.4167`, `doi:10.1088/0067-0049/212/1/6`.

[379] Olivares, E. F., et al. GRB 100728A: GROND detection of the NIR afterglow candidate. *GCN*, **11020** (2010).

[380] Olivares, F., et al. GRB 090902B: GROND NIR observations. *GCN*, **9874** (2009).

[381] Olivares, F., Klose, S., Kruehler, T., and Greiner, J. GRB 090510: GROND observations. *GCN*, **9352** (2009).

[382] Olofsson, G., et al. GRB 090510: NOT confirmation. *GCN*, **9338** (2009).

[383] Omodei, N. Fermi-LAT observation of GRB 081024B. *GCN*, **8407** (2008).

[384] OMODEI, N., ET AL. GRB 090510: Fermi-LAT follow-up analysis. *GCN*, **9350** (2009), 1.

[385] OMODEI, N. AND MCENERY, J. GRB 130518A: LAT detection. *GCN*, **14675** (2013).

[386] OMODEI, N., VIANELLO, G., AND AHLGREN, B. GRB 171010A: Fermi-LAT detection. *GCN*, **21985** (2017).

[387] PACIESAS, W. S., ET AL. The Fourth BATSE Gamma-Ray Burst Catalog (Revised). *The Astrophysical Journal Supplement Series*, **122** (1999), 465. `arXiv:astro-ph/9903205`, `doi:10.1086/313224`.

[388] PACIESAS, W. S., ET AL. The Fermi GBM Gamma-Ray Burst Catalog: The First Two Years. *The Astrophysical Journal Supplement Series*, **199** (2012), 18. `arXiv:1201.3099`, `doi:10.1088/0067-0049/199/1/18`.

[389] PACZYNSKI, B. Estimating redshifts for γ-ray bursts. *Nature*, **355** (1992), 521. `doi:10.1038/355521a0`.

[390] PACZYNSKI, B. How Far Away Are Gamma-Ray Bursters? *Publications of the Astronomical Society of the Pacific*, **107** (1995), 1167. `arXiv:astro-ph/9505096`, `doi:10.1086/133674`.

[391] PAGANI, C. GRB 140402A: Swift-XRT observations. *GCN*, **16078** (2014).

[392] PAGANI, C. GRB 140402A: Swift-XRT observations. *GCN*, **16075** (2014).

[393] PAGANI, C., ET AL. GRB 080805: Swift detection of a burst. *GCN*, **8059** (2008).

[394] PAGANI, C., ET AL. GRB 091208B: Swift detection of a burst. *GCN*, **10256** (2009).

[395] PAGE, K. L., ET AL. Swift Observations of GRB 140301A. *GCN*, **460** (2014).

[396] PAGE, K. L., RACUSIN, J. L., KENNEA, J. A., AND CANNIZZO, J. K. GRB 100414A: Swift-XRT detection of a possible X-ray afterglow. *GCN*, **10601** (2010).

[397] PAGE, K. L., ET AL. Multiwavelength observations of the energetic GRB 080810: detailed mapping of the broad-band spectral evolution. *Monthly Notices of the Royal Astronomical Society*, **400** (2009), 134. `arXiv:0907.4578`, `doi:10.1111/j.1365-2966.2009.15462.x`.

[398] PAGE, M. J., ET AL. GRB 130907A: Swift detection of a burst with an optical counterpart. *GCN*, **15183** (2013).

[399] PANAITESCU, A. Seven-year Collection of Well-monitored Fermi-LAT Gamma-Ray Burst Afterglows. *The Astrophysical Journal*, **837** (2017), 13. `arXiv:1605.09367`, `doi:10.3847/1538-4357/837/1/13`.

[400] PATRICELLI, B., ET AL. Analysis of GRB 080319B and GRB 050904 within the Fireshell Model: Evidence for a Broader Spectral Energy Distribution. *The Astrophysical Journal*, **756** (2012), 16. `arXiv:1206.5605`, `doi:10.1088/0004-637X/756/1/16`.

[401] PÉLANGEON, A., ET AL. Intrinsic properties of a complete sample of HETE-2 gamma-ray bursts. A measure of the GRB rate in the Local Universe. *Astronomy & Astrophysics*, **491** (2008), 157. `arXiv:0811.3304`, `doi:10.1051/0004-6361:200809709`.

[402] PENACCHIONI, A. V., ET AL. GRB 110709B in the induced gravitational collapse paradigm. *Astronomy & Astrophysics*, **551** (2013), A133. `arXiv:1301.6014`, `doi:10.1051/0004-6361/201220679`.

[403] PENACCHIONI, A. V., ET AL. Evidence for a proto-black hole and a double astrophysical component in GRB 101023. *Astronomy & Astrophysics*, **538** (2012), A58. `arXiv:1112.2970`, `doi:10.1051/0004-6361/201118403`.

[404] PENG, Z. Y., ET AL. The Temporal and Spectral Characteristics of "Fast Rise and Exponential Decay" Gamma-ray Burst Pulses. *The Astrophysical Journal*, **718** (2010), 894. `arXiv:1006.1612`, `doi:10.1088/0004-637X/718/2/894`.

[405] PENROSE, R. Gravitational Collapse: the Role of General Relativity. *Nuovo Cimento Rivista Serie*, **1** (1969), 252.

[406] PERLEY, D. A. GRB 130427A: CARMA 3mm observations. *GCN*, **14494** (2013).

[407] PERLEY, D. A. GRB 131108A: CARMA 3mm detection. *GCN*, **15478** (2013).

[408] PERLEY, D. A. GRB 131231A: CARMA 3mm detection. *GCN*, **15680** (2014).

[409] PERLEY, D. A., CAO, Y., AND CENKO, S. B. GRB 141221A: Keck spectroscopy. *GCN*, **17228** (2014).

[410] PERLEY, D. A., HILLENBRAND, L., AND PROCHASKA, J. X. GRB 151027A: Keck-HIRES redshift. *GCN*, **18487** (2015).

[411] PERLEY, D. A. AND KASLIWAL, M. GRB 130702A: CARMA. *GCN*, **14979** (2013).

[412] PERLEY, D. A., ET AL. GRB 091208B: Keck HIRES redshift. *GCN*, **10272** (2009).

[413] PERLEY, D. A., SINGER, L. P., AND CENKO, S. B. GRB 130702A: continued P60 observations. *GCN*, **14981** (2013), 1.

[414] PERLEY, D. A., ET AL. The Swift Gamma-Ray Burst Host Galaxy Legacy Survey. I. Sample Selection and Redshift Distribution. *The Astrophysical Journal*, **817** (2016), 7. `arXiv:1504.02482`, `doi:10.3847/0004-637X/817/1/7`.

[415] PERRI, M., PREGER, B., AND ET AL. GRB 080916C: Swift-XRT. *GCN*, **8261** (2008).

[416] PERRI, M. AND STRATTA, G. GRB 090323: Swift-XRT. *GCN*, **9031** (2009).

[417] PIAN, E., ET AL. BEPPOSAX Observations of GRB 980425: Detection of the Prompt Event and Monitoring of the Error Box. *The Astrophysical Jounal*, **536** (2000), 778. `arXiv:astro-ph/9910235`, `doi:10.1086/308978`.

[418] PIRAN, T. Gamma-ray bursts and the fireball model. *Physics Reports*, **314** (1999), 575. `arXiv:astro-ph/9810256`, `doi:10.1016/S0370-1573(98)00127-6`.

[419] PIRAN, T. The physics of gamma-ray bursts. *Reviews of Modern Physics*, **76** (2004), 1143. `arXiv:astro-ph/0405503`, `doi:10.1103/RevModPhys.76.1143`.

[420] PISANI, G. B., ET AL. Novel distance indicator for gamma-ray bursts associated with supernovae. *Astronomy & Astrophysics*, **552** (2013), L5. `arXiv:1304.1764`, `doi:10.1051/0004-6361/201220829`.

[421] PISANI, G. B., ET AL. On the Universal Late X-Ray Emission of Binary-driven Hypernovae and Its Possible Collimation. *The Astrophysical Journal*, **833** (2016), 159. `arXiv:1610.05619`, `doi:10.3847/1538-4357/833/2/159`.

[422] PISANI, G. B., ET AL. The first ICRANet catalog of binary-driven hypernovae. In *European Physical Journal Web of Conferences*, vol. 168, p. 04002 (2018). `doi:10.1051/epjconf/201816804002`.

[423] POOLAKKIL, S. AND MEEGAN, C. GRB 171010A: Fermi GBM. *GCN*, **21992** (2017).

[424] POOLAKKIL, S. AND MEEGAN, C. GRB 180703A: Fermi GBM detection. *GCN*, **22896** (2018), 1.

[425] PORTERFIELD, B., SIEGEL, M., AND D'AVANZO, P. GRB 130702A: continued UVOT observations. *GCN*, **14991** (2013).

[426] Pozanenko, A., et al. GRB 160623A: Mondy observations. *GCN*, **19561** (2016).

[427] Pozanenko, A., Volnova, A., Burhonov, O., and Molotov, I. GRB 130702A (= Fermi 394416326): correction of the GCN #14988 title. *GCN*, **14989** (2013), 1.

[428] Preece, R. D., et al. The BATSE Gamma-Ray Burst Spectral Catalog. I. High Time Resolution Spectroscopy of Bright Bursts Using High Energy Resolution Data. *The Astrophysical Journal Supplement Series*, **126** (2000), 19. `arXiv:astro-ph/9908119`, `doi:10.1086/313289`.

[429] Preparata, G., Ruffini, R., and Xue, S.-S. The dyadosphere of black holes and gamma-ray bursts. *Astronomy & Astrophysics*, **338** (1998), L87. `arXiv:astro-ph/9810182`.

[430] Pritchard, T. A., Hoversten, E. A., and Starling, R. L. C. GRB 091003: Swift/UVOT detection of an optical afterglow. *GCN*, **9990** (2009).

[431] Prochaska, J. X., et al. The Galaxy Hosts and Large-Scale Environments of Short-Hard Gamma-Ray Bursts. *The Astrophysical Journal*, **642** (2006), 989. `arXiv:astro-ph/0510022`, `doi:10.1086/501160`.

[432] Protassov, R., van Dyk, D. A., Connors, A., Kashyap, V. L., and Siemiginowska, A. Statistics, Handle with Care: Detecting Multiple Model Components with the Likelihood Ratio Test. *The Astrophysical Journal*, **571** (2002), 545. `arXiv:astro-ph/0201547`, `doi:10.1086/339856`.

[433] Pugliese, V., et al. GRB 150403A: VLT/X-shooter redshift. *GCN*, **17672** (2015).

[434] Racusin, J. L., Vianello, G., and Perkins, J. GRB 170214A: Fermi-LAT detection. *GCN*, **20676** (2017).

[435] Racusin, J. L., et al. GRB 131108A: Fermi-LAT. *GCN*, **15464** (2013).

[436] Racusin, J. L., et al. GRB 081008: Swift detection. *GCN*, **8344** (2008).

[437] Rau, A. GRB 091003A: Fermi GBM detection. *GCN*, **9983** (2009).

[438] Rau, A. GRB 120729A: Fermi GBM observation. *GCN*, **13560** (2012).

[439] Rau, A., McBreen, S., and Kruehler, T. GRB090510: VLT/FORS2 spectroscopic redshift. *GCN*, **9353** (2009).

[440] Roberts, O. J. GRB 141028A: Fermi GBM detection. *GCN*, **16971** (2014).

[441] Roberts, O. J., Fitzpatrick, G., and Veres, P. GRB 160509A: Fermi GBM Detection. *GCN*, **19411** (2016).

[442] Roberts, O. J. and Meegan, C. GRB 180720B: Fermi GBM observation. *GCN*, **22981** (2018), 1.

[443] Roberts, O. J., Zhang, B.-B., and Meegan, C. GRB 150514A: Fermi GBM Detection. *GCN*, **17819** (2015).

[444] Romano, P., et al. Panchromatic study of GRB 060124: from precursor to afterglow. *Astronomy & Astrophysics*, **456** (2006), 917. `arXiv:astro-ph/0602497`, `doi:10.1051/0004-6361:20065071`.

[445] Rossi, A., Afonso, P., and et al. GRB 090516: GROND. *GCN*, **9382** (2009).

[446] Rossi, A., et al. GRB 180728A: VLT/X-shooter redshift of a nearby energetic GRB. *GCN*, **23055** (2018), 1.

[447] Rosswog, S., Ramirez-Ruiz, E., and Davies, M. B. High-resolution calculations of merging neutron stars - III. Gamma-ray bursts. *Monthly Notices of the Royal Astronomical Society*, **345** (2003), 1077. `arXiv:astro-ph/0306418`, `doi:10.1046/j.1365-2966.2003.07032.x`.

[448] Rowlinson, A. and Page, K. GRB 090328: XRT refined. *GCN*, **9052** (2009).

[449] Rowlinson, B. A., et al. GRB 090516: Swift detection. *GCN*, **9374** (2009).

[450] Rueda, J. A. and Ruffini, R. On the Induced Gravitational Collapse of a Neutron Star to a Black Hole by a Type Ib/c Supernova. *The Astrophysical Journal Letters*, **758** (2012), L7. `arXiv:1206.1684`, `doi:10.1088/2041-8205/758/1/L7`.

[451] Rueda, J. A., et al. GRB 170817A-GW170817-AT 2017gfo and the observations of NS-NS, NS-WD and WD-WD mergers. *Journal of Cosmology and Astroparticle Physics*, **2018** (2018), 006. `arXiv:1802.10027`, `doi:10.1088/1475-7516/2018/10/006`.

[452] Ruffini, R. Black Holes, Supernovae and Gamma Ray Bursts. In *Thirteenth Marcel Grossmann Meeting: On Recent Developments in Theoretical and Experimental General Relativity, Astrophysics and Relativistic Field Theories* (edited by K. Rosquist), pp. 242–314 (2015). `doi:10.1142/9789814623995_0016`.

[453] Ruffini, R., et al. GRB 050315: A step in the proof of the uniqueness of the overall GRB structure. In *Gamma-Ray Bursts in the Swift Era* (edited by S. S. Holt, N. Gehrels, and J. A. Nousek), vol. 836 of *American Institute of Physics Conference Series*, pp. 103–108 (2006). `arXiv:astro-ph/0601708`, `doi:10.1063/1.2207866`.

[454] Ruffini, R., et al. The Blackholic energy: long and short Gamma-Ray Bursts (New perspectives in physics and astrophysics from the theoretical understanding of Gamma-Ray Bursts, II). In *XIth Brazilian School of Cosmology and Gravitation* (edited by M. Novello and S. E. Perez Bergliaffa), vol. 782 of *American Institute of Physics Conference Series*, pp. 42–127 (2005). `arXiv:astro-ph/0503476`, `doi:10.1063/1.2032728`.

[455] Ruffini, R., Bianco, C. L., Chardonnet, P., Fraschetti, F., and Xue, S.-S. On the Structures in the Afterglow Peak Emission of Gamma-Ray Bursts. *The Astrophysical Journal Letters*, **581** (2002), L19. `arXiv:astro-ph/0210648`, `doi:10.1086/345804`.

[456] Ruffini, R., Bianco, C. L., Fraschetti, F., Xue, S.-S., and Chardonnet, P. On a Possible Gamma-Ray Burst-Supernova Time Sequence. *The Astrophysical Journal Letters*, **555** (2001), L117. `arXiv:astro-ph/0106534`, `doi:10.1086/323177`.

[457] Ruffini, R., Bianco, C. L., Fraschetti, F., Xue, S.-S., and Chardonnet, P. On the Interpretation of the Burst Structure of Gamma-Ray Bursts. *The Astrophysical Journal Letters*, **555** (2001), L113. `arXiv:astro-ph/0106532`, `doi:10.1086/323176`.

[458] Ruffini, R., Bianco, C. L., Fraschetti, F., Xue, S.-S., and Chardonnet, P. Relative Spacetime Transformations in Gamma-Ray Bursts. *The Astrophysical Journal Letters*, **555** (2001), L107. `arXiv:astro-ph/0106531`, `doi:10.1086/323175`.

[459] Ruffini, R., et al. On the Instantaneous Spectrum of Gamma-Ray Bursts. *International Journal of Modern Physics D*, **13** (2004), 843. `arXiv:astro-ph/0405284`, `doi:10.1142/S0218271804004980`.

[460] Ruffini, R., et al. A GRB Afterglow Model Consistent with Hypernova Observations. *The Astrophysical Journal*, **869** (2018), 101. `arXiv:1712.05000`, `doi:10.3847/1538-4357/aaeac8`.

[461] Ruffini, R., Salmonson, J. D., Wilson, J. R., and Xue, S.-S. On evolution of the pair-electromagnetic pulse of a charged black hole. *Astronomy & Astrophysics Supplement*, **138** (1999), 511. `arXiv:astro-ph/9905021`, `doi:10.1051/aas:1999330`.

[462] Ruffini, R., Salmonson, J. D., Wilson, J. R., and Xue, S.-S. On the pair electromagnetic pulse of a black hole with electromagnetic structure. *Astronomy & Astrophysics*, **350** (1999), 334. `arXiv:astro-ph/9907030`.

[463] Ruffini, R., Salmonson, J. D., Wilson, J. R., and Xue, S.-S. On the pair-electromagnetic pulse from an electromagnetic black hole surrounded by a baryonic remnant. *Astronomy & Astrophysics*, **359** (2000), 855. `arXiv:astro-ph/0004257`.

[464] Ruffini, R., Song, D. J., and Stella, L. On the statistical distribution off massive fermions and bosons in a Friedmann universe. *Astronomy & Astrophysics*, **125** (1983), 265.

[465] Ruffini, R., et al. GRB 130427A and SN 2013cq: A Multi-wavelength Analysis of An Induced Gravitational Collapse Event. *The Astrophysical Journal*, **798** (2015), 10. `arXiv:1405.5723`, `doi:10.1088/0004-637X/798/1/10`.

[466] Ruffini, R. and Wilson, J. R. Relativistic magnetohydrodynamical effects of plasma accreting into a black hole. *Physical Review D*, **12** (1975), 2959. `doi:10.1103/PhysRevD.12.2959`.

[467] Ruffini, R., et al. GRB 130427A: predictions about the occurrence of a supernova. *GCN*, **14526** (2013).

[468] Ruffini, R., et al. On binary-driven hypernovae and their nested late X-ray emission. *Astronomy & Astrophysics*, **565** (2014), L10. `arXiv:1404.3946`, `doi:10.1051/0004-6361/201423812`.

[469] Ruffini, R., et al. GRB 140619B: a short GRB from a binary neutron star merger leading to black hole formation. *The Astrophysical Journal*, **808** (2015), 190. `arXiv:1412.1018`, `doi:10.1088/0004-637X/808/2/190`.

[470] Ruffini, R., et al. GRB 090510: A Genuine Short GRB from a Binary Neutron Star Coalescing into a Kerr-Newman Black Hole. *The Astrophysical Journal*, **831** (2016), 178. `arXiv:1607.02400`, `doi:10.3847/0004-637X/831/2/178`.

[471] Ruffini, R., et al. On the Classification of GRBs and Their Occurrence Rates. *The Astrophysical Journal*, **832** (2016), 136. `arXiv:1602.02732`, `doi:10.3847/0004-637X/832/2/136`.

[472] Ruffini, R., et al. Early X-Ray Flares in GRBs. *The Astrophysical Journal*, **852** (2018), 53. `arXiv:1704.03821`, `doi:10.3847/1538-4357/aa9e8b`.

[473] Ruffini, R., et al. On the GeV emission of the type I BdHN GRB 130427A. *ArXiv e-prints*, (2018). `arXiv:1812.00354`.

[474] Ruffini, R., et al. On the Rate and on the Gravitational Wave Emission of Short and Long GRBs. *The Astrophysical Journal*, **859** (2018), 30. `doi:10.3847/1538-4357/aabee4`.

[475] Ruffini, R., et al. On the role of the Kerr-Newman black hole in the GeV emission of long gamma-ray bursts. *ArXiv e-prints*, (2018). `arXiv:1803.05476`.

[476] Ruffini, R., et al. On the Short GRB GeV emission from a Kerr Black hole. *ArXiv e-prints*, (2018). `arXiv:1802.07552`.

[477] Ruffini, R., et al. On the Ultra-relativistic Prompt Emission, the Hard and Soft X-Ray Flares, and the Extended Thermal Emission in GRB 151027A. *The Astrophysical Journal*, **869** (2018), 151. `arXiv:1712.05001`, `doi:10.3847/1538-4357/aaee68`.

[478] RUFFINI, R., ET AL. The inner engine of GeV-radiation-emitting gamma-ray bursts. *arXiv e-prints*, (2018), arXiv:1811.01839. `arXiv:1811.01839`.

[479] RUFFINI, R., ET AL. On the GeV Emission of the Type I BdHN GRB 130427A. *The Astrophysical Journal*, **886** (2019), 82. `arXiv:1812.00354`, `doi:10.3847/1538-4357/ab4ce6`.

[480] RYBICKI, G. B. AND LIGHTMAN, A. P. *Radiative Processes in Astrophysics* (1986).

[481] RYDE, F. Is Thermal Emission in Gamma-Ray Bursts Ubiquitous? *The Astrophysical Journal Letters*, **625** (2005), L95. `arXiv:astro-ph/0504450`, `doi:10.1086/431239`.

[482] RYDE, F. AND PE'ER, A. Quasi-blackbody Component and Radiative Efficiency of the Prompt Emission of Gamma-ray Bursts. *The Astrophysical Journal*, **702** (2009), 1211. `arXiv:0811.4135`, `doi:10.1088/0004-637X/702/2/1211`.

[483] SAHU, K. C., ET AL. The optical counterpart to γ-ray burst GRB970228 observed using the Hubble Space Telescope. *Nature*, **387** (1997), 476. `arXiv:astro-ph/9705184`, `doi:10.1038/387476a0`.

[484] SAKAMOTO, T., ET AL. The First Swift BAT Gamma-Ray Burst Catalog. *The Astrophysical Journal Supplement Series*, **175** (2008), 179. `arXiv:0707.4626`, `doi:10.1086/523646`.

[485] SAKAMOTO, T., ET AL. GRB 090516A: Konus-wind and Swift/BAT joint spectral analysis. *GCN*, **9422** (2009).

[486] SAKAMOTO, T., ET AL. The Second Swift Burst Alert Telescope Gamma-Ray Burst Catalog. *The Astrophysical Journal Supplement Series*, **195** (2011), 2. `arXiv:1104.4689`, `doi:10.1088/0067-0049/195/1/2`.

[487] SAKAMOTO, T., ET AL. GRB 140206A, BAT refined analysis. *GCN*, **15805** (2014).

[488] SALMONSON, J. D. AND WILSON, J. R. A Model of Short Gamma-Ray Bursts: Heated Neutron Stars in Close Binary Systems. *The Astrophysical Journal*, **578** (2002), 310. `arXiv:astro-ph/0203349`, `doi:10.1086/342311`.

[489] SANCHEZ-RAMIREZ, R., GOROSABEL, J., CASTRO-TIRADO, A. J., CEPA, J., AND GOMEZ-VELARDE, G. GRB 130518A: 10.4m GTC/OSIRIS redshift. *GCN*, **14685** (2013).

[490] SAVCHENKO, V., ET AL. GRB 130907A: INTEGRAL/SPI-ACS. *GCN*, **15204** (2013).

[491] SCHADY, P. AND GUIDORZI, C. GRB081024B: Swift/UVOT. *GCN*, **8413** (2008).

[492] SCHADY, P. AND KRUEHLER, T. GRB 170214A: GROND. *GCN*, **20684** (2017).

[493] SCHMIDL, S., ET AL. GRB 130907A: Tautenburg detections. *GCN*, **15194** (2013).

[494] SCHULZE, S., ET AL. GRB130702A: NOT observation - the detection of an emerging supernova. *GCN*, **14994** (2013).

[495] SCHULZE, S., ET AL. GRB 130702A: NOT optical observations. *GCN*, **14978** (2013).

[496] SIEGEL, M. H. AND PAGANI, C. GRB 141028A: UVOT. *GCN*, **16979** (2014).

[497] SINGER, L. P., ET AL. Discovery and Redshift of an Optical Afterglow in 71 deg^2: iPTF13bxl and GRB 130702A. *The Astrophysical Journal Letters*, **776** (2013), L34. `arXiv:1307.5851`, `doi:10.1088/2041-8205/776/2/L34`.

[498] SINGER, L. P., ET AL. Fermi394416326: iPTF detection. *GCN*, **14967** (2013).

[499] SMITH, I. A., TILANUS, R. P. J., TANVIR, N. R., AND FRAIL, D. A. GRB 120729A: JCMT SCUBA-2 sub-mm observation. *GCN*, **13554** (2012).

[500] Sonbas, E., et al. GRB 141221A: Swift detection of a burst with an optical counterpart. *GCN*, **17206** (2014).

[501] Sonbas, E., Racusin, J. L., Kocevski, D., and McEnery, J. GRB 131231A: Fermi-LAT detection of a burst. *GCN*, **15640** (2013).

[502] Stamatikos, M., et al. GRB 090812: Swift detection of a burst with an optical counterpart. *GCN*, **9768** (2009).

[503] Stanbro, M., Hui, C. M., and Meegan, C. GRB 171222A: Fermi GBM detection. *GCN*, **22277** (2017), 1.

[504] Starling, R. L. C. and Beardmore, A. P. GRB 091003: Swift XRT analysis. *GCN*, **9986** (2009).

[505] Stratta, G., et al. GRB 080916C: Swift Observation. *GCN*, **166** (2008).

[506] Stroh, M. C. and Kennea, J. A. GRB 131108A: Swift detection of a possible X-ray afterglow. *GCN*, **15468** (2013).

[507] Swenson, C. A. and Roming, P. W. A. Gamma-Ray Burst Flares: X-Ray Flaring. II. *The Astrophysical Journal*, **788** (2014), 30. `arXiv:1310.2628`, `doi: 10.1088/0004-637X/788/1/30`.

[508] Swenson, C. A. and Siegel, M. H. GRB090902B: UVOT. *GCN*, **9869** (2009).

[509] Tajima, H., Bregeon, J., Chiang, J., and Thayer, G. GRB 080916C: Fermi LAT observation. *GCN*, **8246** (2008).

[510] Takahashi, H., Ohno, M., and Omodei, N. GRB100414A: Fermi LAT detection. *GCN*, **10594** (2010).

[511] Takahashi, J., Morihana, K., Honda, S., and Takagi, Y. GRB 130427A: Nishi-Harima NIR observations. *GCN*, **14495** (2013).

[512] Tam, P. H. T., Li, K. L., and Kong, A. K. H. GRB 120711A: Fermi LAT detection. *GCN*, **13444** (2012).

[513] Tanvir, N., et al. GRB 090423: VLT/ISAAC spectroscopy. *GCN*, **9219** (2009).

[514] Tanvir, N. R. and Ball, J. GRB 120729A Gemini-N redshift. *GCN*, **13532** (2012).

[515] Tanvir, N. R., et al. GRB 160509A Gemini-North redshift. *GCN*, **19419** (2016).

[516] Tanvir, N. R., Levan, A. J., Cucchiarra, A., Perley, D., and Cenko, S. B. GRB 140419A: Gemini-N redshift. *GCN*, **16125** (2014).

[517] Tanvir, N. R., Wiersema, K., Levan, A. J., Cenko, S. B., and Geballe, T. GRB 110731A Gemini-N redshift. *GCN*, **12225** (2011).

[518] Tanvir, N. R., et al. GRB 120711A gemini-s likely redshift. *GCN*, **13441** (2012).

[519] Tiengo, A., Vianello, G., Esposito, P., and Salvaterra, R. Swift detection of a dust-scattered halo around GRB 160623A. *GCN*, **19559** (2016).

[520] Tinney, C., et al. GRB 980425. *IAU Circulars*, **6896** (1998).

[521] Toelge, K., Yu, H.-F., and Meegan, C. A. GRB 151027A: Fermi GBM observation. *GCN*, **18492** (2015).

[522] Tonry, J. L., Hu, E. M., Cowie, L. L., and McMahon, R. G. GRB 970228. *IAU Circulars*, **6620** (1997).

[523] Toy, V. L., et al. Optical and Near-infrared Observations of SN 2013dx Associated with GRB 130702A. *The Astrophysical Journal*, **818** (2016), 79. `arXiv:1508.00575`, `doi:10.3847/0004-637X/818/1/79`.

[524] Troja, E., et al. GRB 170405A: Swift detection of a burst with an optical counterpart. *GCN*, **20984** (2017).

[525] Troja, E., et al. Swift and Fermi Observations of X-Ray Flares: The Case of Late Internal Shock. *The Astrophysical Journal*, **803** (2015), 10. `arXiv:1411.1415`, `doi:10.1088/0004-637X/803/1/10`.

[526] Troja, E., et al. GRB 130518A: continued RATIR. *GCN*, **14684** (2013).

[527] Troja, E., et al. GRB 130518A: RATIR optical and NIR. *GCN*, **14679** (2013).

[528] Troja, E., et al. GRB 131030A: Swift detection. *GCN*, **15402** (2013).

[529] Troja, E., et al. GRB 131108A: RATIR optical and NIR. *GCN*, **15475** (2013).

[530] Troja, E., et al. GRB 141028A: RATIR Optical and NIR. *GCN*, **16980** (2014).

[531] Troja, E., et al. GRB 160625B: RATIR Optical and NIR. *GCN*, **19588** (2016).

[532] Troja, E., et al. GRB 170405A: RATIR Optical and NIR. *GCN*, **20996** (2017).

[533] Troja, E., et al. GRB170214A: RATIR Optical and NIR. *GCN*, **20681** (2017).

[534] Tsang, D., Read, J. S., Hinderer, T., Piro, A. L., and Bondarescu, R. Resonant Shattering of Neutron Star Crusts. *Physical Review Letters*, **108** (2012), 011102. `arXiv:1110.0467`, `doi:10.1103/PhysRevLett.108.011102`.

[535] Tursunov, A. and Dadhich, N. Fifty Years of Energy Extraction from Rotating Black Hole: Revisiting Magnetic Penrose Process. *Universe*, **5** (2019), 125. `arXiv:1905.05321`, `doi:10.3390/universe5050125`.

[536] Uehara, T., Takahashi, H., and McEnery, J. GRB 090926: Fermi LAT detection. *GCN*, **9934** (2009).

[537] Ukwatta, T. N., et al. GRB 120729A: Swift detection of a burst with an optical afterglow. *GCN*, **13530** (2012).

[538] Updike, A., Klose, S., Clemens, C., and Greiner, J. GRB 090328: GROND detection of the Optical/NIR afterglow. *GCN*, **9054** (2009).

[539] Updike, A., Rossi, A., and Greiner, J. GRB 091208B: GROND observations. *GCN*, **10271** (2009).

[540] Updike, A. C., Filgas, R., Kruehler, T., Greiner, J., and McBreen, S. GRB 090323: GROND detection of the afterglow and photo-z. *GCN*, **9026** (2009).

[541] Urata, Y., Huang, K., and Petitpas, G. GRB 160623A: SMA submm afterglow observations. *GCN*, **19584** (2016).

[542] Urata, Y. and Huang, K. Y. GRB 100414A: CFHT. *GCN*, **10641** (2010).

[543] Valeev, A. F., Moskvitin, A. S., Beskin, G. M., Vlasyuk, V. V., and Sokolov, V. V. GRB 160625B: SAO RAS monitoring. *GCN*, **19642** (2016).

[544] van der Horst, A. J. GRB 090323: WSRT radio detection. *GCN*, **9047** (2009).

[545] van der Horst, A. J. GRB 130702A: WSRT radio detection. *GCN*, **14987** (2013).

[546] van der Horst, A. J. GRB 130907A: WSRT radio detection. *GCN*, **15207** (2013).

[547] van der Horst, A. J., Kamble, A. P., Wijers, R. A. M. J., and Kouveliotou, C. GRB 090902B: WSRT radio observation. *GCN*, **9883** (2009).

[548] VAN PARADIJS, J., ET AL. Transient optical emission from the error box of the γ-ray burst of 28 February 1997. *Nature*, **386** (1997), 686. `doi:10.1038/386686a0`.

[549] VERES, P. GRB 181020A: Fermi GBM detection. *GCN*, **23352** (2018), 1.

[550] VERES, P., MEEGAN, C., AND MAILYAN, B. GRB 180728A: Fermi GBM observation. *GCN*, **23053** (2018), 1.

[551] VETERE, L., EVANS, P. A., AND GOAD, M. R. GRB090926A: UVOT-enhanced XRT position. *GCN*, **9936** (2009).

[552] VIANELLO, G., ET AL. GRB160623A: Fermi-LAT. *GCN*, **19553** (2016).

[553] VIANELLO, G. AND KOCEVSKI, D. GRB 120624B: Fermi-LAT. *GCN*, **13379** (2012).

[554] VIANELLO, G. AND KOCEVSKI, D. GRB 170405A: Fermi-LAT. *GCN*, **20987** (2017).

[555] VIANELLO, G., KOCEVSKI, D., RACUSIN, J., AND CONNAUGHTON, V. GRB 120916A: Fermi-LAT detection of a burst. *GCN*, **15196** (2013).

[556] VIELFAURE, J. B., ET AL. GRB 181010A: VLT/X-shooter redshift. *GCN*, **23315** (2018), 1.

[557] VIRGILI, F. J., JAPELJ, J., MUNDELL, C. G., AND MELANDRI, A. GRB120729A - Faulkes telescope north optical afterglow candidate. *GCN*, **13531** (2012).

[558] VOLNOVA, A. A., ET AL. Multicolour modelling of SN 2013dx associated with GRB 130702A. *Monthly Notices of the Royal Astronomical Society*, **467** (2017), 3500. `arXiv:1612.07626, doi:10.1093/mnras/stw3297`.

[559] VOLVACH, A., VOLVACH, L., AND POZANENKO, A. GRB 130427A: CrAO RT-22 36 GHz observation. *GCN*, **14505** (2013).

[560] VON KIENLIN, A. GRB 100728A: Fermi GBM observation. *GCN*, **11006** (2010).

[561] VON KIENLIN, A. GRB 130427A: Fermi GBM observation. *GCN*, **14473** (2013).

[562] VON KIENLIN, A. GRB 181010A: Fermi GBM observation. *GCN*, **23320** (2018), 1.

[563] VON KIENLIN, A. AND BHAT, P. N. GRB 140206A: GBM. *GCN*, **15796** (2014).

[564] VON KIENLIN, A., ET AL. The Second Fermi GBM Gamma-Ray Burst Catalog: The First Four Years. *The Astrophysical Journal Supplement Series*, **211** (2014), 13. `arXiv:1401.5080, doi:10.1088/0067-0049/211/1/13`.

[565] VREESWIJK, P. M., ET AL. GRB 180720B: VLT/X-shooter redshift. *GCN*, **22996** (2018), 1.

[566] WANG, Y., ET AL. Two Predictions of Supernova: GRB 130427A/SN 2013cq and GRB 180728A/SN 2018fip. *The Astrophysical Journal*, **874** (2019), 39. `arXiv:1811.05433, doi:10.3847/1538-4357/ab04f8`.

[567] WATSON, A. M., ET AL. GRB 171010A: RATIR Optical and NIR Observations. *GCN*, **22011** (2017).

[568] WENGER, M., ET AL. The SIMBAD astronomical database. The CDS reference database for astronomical objects. *Astronomy & Astrophysics Supplement*, **143** (2000), 9. `arXiv:astro-ph/0002110, doi:10.1051/aas:2000332`.

[569] WIERSEMA, K., TANVIR, N., LEVAN, A., AND BENN, C. GRB 091003: WHT ACAM observations. *GCN*, **9995** (2009).

[570] WIERSEMA, K., TANVIR, N. R., CUCCHIARA, A., LEVAN, A. J., AND FOX, D. GRB 091208B: gemini-north redshift. *GCN, Circular Service, No. 10263, #1 (2009)*, **10263** (2009).

[571] Xin, L. P., et al. GRB 130702A: Xinglong TNT optical observation. *GCN*, **14992** (2013), 1.

[572] Xiong, S. GRB 130518A: Fermi GBM detection. *GCN*, **14674** (2013).

[573] Xu, D., et al. GRB 150314A: NOT optical observations. *GCN*, **17582** (2015).

[574] Xu, D., et al. GRB 130427A: NOT photometry and redshift. *GCN*, **14478** (2013).

[575] Xu, D., Esamdin, A., Ma, L., and Zhang, X. GRB 130702A / Fermi394416326 : nanshan optical observations. *GCN*, **14975** (2013), 1.

[576] Xu, D., et al. GRB 131030A: NOT redshift. *GCN*, **15407** (2013).

[577] Xu, D., et al. GRB091208B: NOT optical observations. *GCN*, **10269** (2009).

[578] Xu, D., et al. GRB 141028A: VLT/X-shooter redshift. *GCN*, **16983** (2014).

[579] Xu, D., et al. GRB 160625B: VLT/X-shooter redshift. *GCN*, **19600** (2016).

[580] Xu, D., Malesani, D., and Pursimo, T. GRB 131108A: NOT optical observations. *GCN*, **15471** (2013).

[581] Xu, D., et al. GRB 131231A: VLT/X-shooter redshift. *GCN*, **15645** (2014).

[582] Yates, R., Knust, F., Kann, D. A., and Greiner, J. GRB 150514A: GROND Bright Afterglow Confirmation. *GCN*, **17821** (2015).

[583] Younes, G. GRB 131108A: Fermi GBM observation. *GCN*, **15477** (2013).

[584] Yu, H.-F. GRB 141221A: Fermi GBM observation. *GCN*, **17216** (2014).

[585] Yu, H.-F. GRB 150314A: Fermi GBM observation. *GCN*, **17579** (2015).

[586] Yuan, F., et al. GRB 081008: From Burst to Afterglow and the Transition Phase in Between. *The Astrophysical Journal*, **711** (2010), 870. `arXiv:1002.0581`, `doi:10.1088/0004-637X/711/2/870`.

[587] Zauderer, A., Berger, E., and Frail, D. A. GRB 110731A / EVLA upper limits. *GCN*, **12227** (2011).

[588] Zauderer, B. A., Berger, E., Chakraborti, S., and Soderberg, A. GRB 130427A: VLA 5 GHz detection. *GCN*, **14480** (2013).

[589] Zevin, M., et al. Forward Modeling of Double Neutron Stars: Insights from Highly-Offset Short Gamma-Ray Bursts. *arXiv e-prints*, (2019), arXiv:1910.03598. `arXiv:1910.03598`.

[590] Zhang, B. *The Physics of Gamma-Ray Bursts* (2018). `doi:10.1017/9781139226530`.

[591] Zhang, B., et al. Physical Processes Shaping Gamma-Ray Burst X-Ray Afterglow Light Curves: Theoretical Implications from the Swift X-Ray Telescope Observations. *The Astrophysical Journal*, **642** (2006), 354. `arXiv:astro-ph/0508321`, `doi:10.1086/500723`.

[592] Zhang, B.-B. GRB 150403A: Fermi GBM Detection. *GCN*, **17674** (2015).

[593] Zhang, Z. B., et al. Spectrum-energy Correlations in GRBs: Update, Reliability, and the Long/Short Dichotomy. *Publications of the Astronomical Society of the Pacific*, **130** (2018), 054202. `doi:10.1088/1538-3873/aaa6af`.

[594] Zhao, X.-H., Mao, J., Xin, Y. X., and Bai, J.-M. GRB 130427A: GMG optical observation. *GCN*, **14466** (2013).

[595] Zhu, S., et al. GRB 130427A: Fermi-LAT detection of a burst. *GCN*, **14471** (2013).

[596] Ziaeepour, H. Z., et al. GRB 060607: Swift detection of a burst with bright optical counterpart. *GCN*, **5233** (2006).